ESTUDIOS SOBRE EL CONTROL TRADUCCIONAL EN MODELOS NEURONALES Y SU MODULACIÓN POR PDCD4

Tesis Doctoral
Programa de Desarrollo de las Ciencias Básicas
Área Biología

Mag. Guillermo Eastman
Departamento de Genómica
Instituto de Investigaciones Biológicas Clemente Estable

Julio 2021

Programa de Desarrollo de las Ciencias Básicas
Área Biología

Tesis de Doctorado

"Estudios sobre el control traduccional en modelos neuronales y su modulación por PDCD4"

Mag. Guillermo Eastman
Departamento de Genómica
Instituto de Investigaciones Biológicas Clemente Estable (IIBCE)

Julio 2021

Orientador: Dr. José Sotelo-Silveira
Co-Orientador: Dr. George Bloom (EE.UU.)

Tribunal

Dr. Rodney Colina	(PRESIDENTE)
Dr. Alexander de Luna	(VOCAL)
Dra. Patricia Lagos	(VOCAL)

AGENCIA NACIONAL DE INVESTIGACIÓN E INNOVACIÓN
PEDECIBA MEC-UDELAR
ASBMB American Society for Biochemistry and Molecular Biology
Ministerio de Educación y Cultura | Dirección Nacional de Innovación, Ciencia y Tecnología

Apoyo Financiero

ÍNDICE

I. RESUMEN

El control de la expresión génica a nivel traduccional es un aspecto clave para el correcto funcionamiento celular y es en particular importante en modelos neuronales debido al alto grado de compartimentalización y sus grandes dimensiones. Por esta razón, en la presente tesis nos hemos propuesto investigar distintos eventos de regulación traduccional en modelos neuronales utilizando aproximaciones genómicas como Ribo-Seq y RNA-Seq.

En primer lugar, estudiamos el rol de PDCD4 en la regulación traduccional y sus posibles ARNm blancos en un modelo neuronal. Resultados previos obtenidos en nuestro laboratorio mostraron que PDCD4 se expresa en altos niveles en distintos tipos neuronales y ejerce una regulación negativa sobre el crecimiento axonal. Utilizando células PC12 diferenciadas a neuronas como modelo celular *in vitro* tipo neuronal, pudimos verificar el efecto inhibitorio de PDCD4 en el crecimiento neurítico. También, mediante RNA-Seq y Ribo-Seq observamos el control que PDCD4 ejerce a nivel traduccional y exploramos sus blancos traduccionales. Así, reportamos una lista de 267 ARNm blancos de PDCD4 cuyos niveles traduccionales se ven significativamente aumentados en ausencia de este factor. El análisis de dichos blancos nos permitió reconocer una firma génica asociada al crecimiento neurítico y axonal que podría justificar la regulación observada. La regulación ejercida sobre alguno de dichos blancos fue confirmada por western blot y por cuantificación en fracciones polisomales.

En segundo lugar, optimizamos y aplicamos la técnica de Ribo-Seq en distintos modelos neuronales como cultivos *in vitro* de neuronas corticales primarias y corteza cerebral de ratón. En el primer caso evitamos la recuperación de la fracción polisomal lo cual nos permitió trabajar con una menor cantidad de material biológico de partida, una de las principales limitantes de la técnica. También, comparamos nuestro protocolo de producción de huellas ribosomales con el protocolo original, ya que éstos difieren en la enzima utilizada en el ensayo de digestión: Benzonasa y RNAsa I, respectivamente. Pudimos observar diferencias principalmente a nivel del tamaño de las huellas, su presencia en la región 3'-UTR y en la periodicidad de mapeo. También, en base a tres criterios complementarios, definimos un set de genes cuya detección se ve favorecida con una enzima y no con la otra. El análisis funcional de estos genes no reveló grandes diferencias a considerar aunque se destaca la presencia de genes no codificantes y entre ellos especies de ARN pequeños.

En último lugar nos propusimos estudiar los eventos de regulación traduccional presentes en modelos murinos transgénicos de la enfermedad de Alzheimer, donde los mecanismos neuronales que determinan los eventos de neurodegeneración no se conocen en detalle. Para

esto utilizamos dos modelos murinos transgénicos de la enfermedad, en edades tempranas, preferentemente asintomáticas (ratones CVN: *App* KM670/671NL, ED693/694QN; *Nos2*$^{-/-}$ y ratones Tg2576: *App* KM670/671NL). Utilizando RNA-Seq y Ribo-Seq cuantificamos los niveles de expresión transcripcional y traduccional de más de 14.000 genes en la corteza cerebral y detectamos genes expresados diferencialmente en ambos niveles, en particular en el modelo CVN, completamente asintomático a la edad utilizada. El análisis funcional reveló principalmente una inhibición de procesos neurodegenerativos y la activación de procesos tipo neuroprotectores como transmisión sináptica, cantidad de neuronas y neuroglias, procesos de mielinización, entre otros. Además se detectó una firma génica asociada a la activación de una subpoblación microglial asociada a la enfermedad y que responde a la acumulación de Aβ, así como la activación de genes asociados al metabolismo de Aβ y APP.

En conclusión, en la presente tesis pudimos determinar por primera vez un set completo de blancos traduccionales de PDCD4, entre los cuales reconocimos una firma génica asociada al crecimiento neurítico y axonal que explica el rol que este factor tiene sobre dichos procesos. También, aplicamos el protocolo de Ribo-Seq sobre diversos modelos neuronales *in vitro* e *in vivo*, así como comparamos las huellas ribosomales producidas con distintas ARNasas. En último lugar, exploramos eventos de regulación traduccional en modelos transgénicos de la enfermedad de Alzheimer y observamos, por primera vez, la regulación traduccional que controla la expresión de muchos genes previamente asociados a la enfermedad. Pensamos que los aportes realizados por la presente tesis permitirán en un futuro explorar de manera precisa la regulación traduccional en diversos modelos neuronales mediante técnicas ómicas de última generación.

II. INTRODUCCIÓN

El estricto control de la expresión génica involucra variados mecanismos y etapas sucesivas de regulación. Entre ellas, la regulación de los niveles de traducción de ARN mensajeros (ARNm) es uno de los aspectos más relevantes (ejemplos en [1,2]). En particular si consideramos los modelos neuronales, donde se observa tanto un alto nivel de polarización como grandes dimensiones celulares, los mecanismos que controlan la expresión génica en tiempo y espacio adquieren una relevancia aún mayor. Estos dos factores agregan un nivel extra de complejidad en la regulación de la expresión génica, donde se destaca la regulación traduccional local [3–9]. Por ejemplo, los mecanismos de regulación traduccional pueden ser ejercidos de manera central, afectando los niveles traduccionales en el soma neuronal, o de una manera completamente distinta afectando niveles traduccionales locales, regulando la síntesis proteica en distintos dominios neuronales: axón, dendritas, terminal presináptica y postsináptica. Respecto a la síntesis proteica local, nuestro grupo [9–17] junto con otros [4,6,18–28], han realizado significativos aportes al área, aunque todavía resta por conocer en detalle cómo se regulan estos procesos. Estudiar en profundidad los mecanismos de regulación traduccional generales y locales es un objetivo clave para comprender una gran variedad de procesos que ocurren en el intrincado panorama tridimensional de las células neuronales.

A continuación procederemos a describir tres aspectos relevantes para el marco teórico de la presente tesis. En primer lugar, se describe la estrategia de Ribo-Seq como una aproximación novedosa para el estudio del compartimiento traduccional a nivel ómico ya que la misma representa un insumo transversal a los distintos objetivos planteados. Luego nos centramos en la regulación del proceso traduccional que ocurre tanto mediado por factores proteicos, como PDCD4, y en el contexto de patologías neurodegenerativas. Así, describimos PDCD4 como un modulador traduccional cuyo rol neuronal exploraremos en la presente tesis. Finalmente introducimos aspectos relevantes para entender posibles eventos de regulación traduccional que puedan ocurrir en enfermedades neurodegenerativas, como nos planteamos estudiar en el caso del mal de Alzheimer.

Ribo-Seq: Una estrategia ómica para el estudio de la traducción

Hace poco más de 10 años se publicaba el primer trabajo que describe el uso de una novedosa aproximación metodológica basada en la tecnología de secuenciación masiva y que

permite el estudio global de los niveles traduccionales de los ARNm con una resolución a nivel de sub codones [29]. En los años siguientes, los continuos avances tecnológicos aplicados a técnicas de biología molecular y el desarrollo de nuevas y mejores capacidades para secuenciar fragmentos de ácidos nucleicos, han permitido un uso masivo y extensivo de la técnica conocida como *ribosome profiling* o Ribo-Seq.

Como parte de uno de los primeros pasos en el desarrollo de esta tesis nos propusimos realizar una revisión actualizada de la metodología y sus aplicaciones. Se adjunta a continuación la publicación de dicha revisión en formato de mini-review donde describimos la metodología, discutimos los aspectos protocolares más relevantes y listamos diversos programas y paquetes computacionales diseñados para la visualización, análisis e interpretación de los datos producidos por Ribo-Seq. También discutimos algunos de los principales hallazgos que se han descrito mediante el uso de esta metodología en distintos sistemas y modelos biológicos.

Trabajo publicado I: Following Ribosome Footprints to Understand Translation at a Genome Wide Level

Se adjunta a continuación.

Computational and Structural Biotechnology Journal 16 (2018) 167–176

COMPUTATIONAL AND STRUCTURAL BIOTECHNOLOGY JOURNAL

journal homepage: www.elsevier.com/locate/csbj

Mini Review

Following Ribosome Footprints to Understand Translation at a Genome Wide Level

Guillermo Eastman [a], Pablo Smircich [a,b], José R. Sotelo-Silveira [a,c,*]

[a] Department of Genomics, Instituto de Investigaciones Biológicas Clemente Estable, MEC, Av. Italia 3318, Montevideo, CP 11600, Uruguay
[b] Laboratory of Molecular Interactions, Facultad de Ciencias, Universidad de la República, Iguá 4225, Montevideo, CP 11400, Uruguay
[c] Department of Cell and Molecular Biology, Facultad de Ciencias, Universidad de la República, Iguá 4225, Montevideo, CP 11400, Uruguay

ARTICLE INFO

Article history:
Received 16 January 2018
Received in revised form 6 April 2018
Accepted 10 April 2018
Available online 01 May 2018

Keywords:
Ribo-seq
Translation
Translatome
Transcriptome
Ribosome profiling

ABSTRACT

Protein translation is a key step in gene expression. The development of Ribosome Profiling has allowed the global analysis of this process at sub-codon resolution. In the last years the method has been applied to several models ranging from bacteria to mammalian cells yielding a surprising amount of insight on the mechanism and the regulation of translation. In this review we describe the key aspects of the experimental protocol and comment on the main conclusions raised in different models.

Contents

1. Introduction

The decreasing cost of obtaining Next Generation Sequencing (NGS) data [1–3] together with the huge information sets arising from these technologies is revolutionizing several research fields of life sciences (see an example in [4] or in disease biology [5,6]). Ingenuity is continuously leading to the development of new methods, a very interesting

* Corresponding author at: Department of Genomics, Instituto de Investigaciones Biológicas Clemente Estable, Av. Italia 3318, Montevideo, CP 11600, Uruguay.
E-mail addresses: geastman@iibce.edu.uy (G. Eastman), psmircich@iibce.edu.uy (P. Smircich), jsotelosilveira@iibce.edu.uy
URL: http://www.iibce.edu.uy (J.R. Sotelo Silveira).

https://doi.org/10.1016/j.csbj.2018.04.001

case is an application named Ribosome Profiling (RP), or Ribo-Seq, developed by Ingolia & Weissman in 2009 [7] where the deep sequencing of mRNA fragments covered by ribosomes during translation yielded an original view of translation at a genome wide scale. The footprints of active ribosomes are obtained using an RNAse protection assay, where controlled digestion generates small mRNA fragments/footprints of approximately 30 nucleotides [8]. Therefore, after data processing, translation can be observed at an unprecedented resolution in a variety of biological settings. Before performing the digestion, ribosomes are halted over the mRNAs using translation inhibitory drugs or by quick deep freezing the sample to avoid ribosome run-off. The resulting fragments, *i.e*. the ribosome footprints, are purified and used to construct sequencing libraries to feed short read sequencers. In this scenario, a transcriptome wide picture of the translating ribosomes location over mRNAs is obtained, together with an estimation of the mRNAs translation rates. These expression levels estimated by RP define what is called *translatome*, in analogy to the term transcriptome. Translatome estimations of gene expression levels correlate better with proteomic data than transcriptome-derived estimations (see below). This increased correlation evidences the existence of mechanisms operating in the control of translation that fine tune the synthesis of cellular proteins.

In the context of the rich data obtained in a RP experiment, an interesting outcome was the definition of two concepts: translational efficiency and periodicity. The first concept refers to how much an mRNA is translated considering the level of its coding mRNA, so it is an important parameter yielding information on translation regulation. Translational efficiency is calculated as the ratio between translation (derived from counts of footprints per mRNA) over transcription (derived from RNA-seq mRNA levels) of particular mRNA. The second, refers to the three bases mapping periodicity observed for the reads derived from footprints as a consequence of ribosome movement along mRNA. Since the ribosome moves codon by codon, the 5′-end of the ribosome footprints tend to map at the same position of each codon throughout the whole coding sequence.

Several aspects concerning protocol have been discussed, revised and modified since the original protocol was established. Some aim to adapt the protocol to different biological models, like eukaryotic or prokaryotic cells, specific tissues, *etc*. Other aspects have been intensely discussed, for example what the appropriate method to stop translation is or how to define the correct translation frame from ribosome footprints. Nevertheless, RP protocol is currently a widely used approach to study gene expression in different biological models from virus and bacteria to complex mammalian tissues (examples in [9–11]). In this mini-review we will discuss the main and critical steps in the RP protocol, its uses and main findings obtained in different biological models and the contributions to our knowledge of cellular and molecular biology.

2. Ribosome Profiling Protocol

2.1. Protocol Description

Ribosome Profiling comprise mainly five steps: sample preparation, RNAse protection assay, isolation of ribosome footprints, high-throughput sequencing and bioinformatic analysis (Fig. 1A) [12]. Sample preparation refers to steps necessary to process the biological sample and obtain a post mitochondrial supernatant where lysis conditions ensure to preserve *in vivo* ribosome positioning and RNA integrity. Among others, alternative inputs could be tissue homogenates, isolated tagged ribosomes or a bacterial cell lysate. Critical aspects concerning this step are: ensuring enough biological material to produce quantifiable ribosome footprints and avoiding ribosome run-off. For the last, either drugs inhibitors of translation or physical methods like flash-freezing using liquid nitrogen and dry ice can be used. Indeed, fast freezing becomes crucial in cases where using translation inhibitors are to be avoided.

The RNAse protection assay, also called nuclease footprinting, is another critical step in RP protocol. Several RNAses had been used, mainly RNAse I and micrococcal nuclease (MNAse) in eukaryotic cell models and bacterial cells, respectively. At this step, controlling factors like reaction time and enzyme concentration are critical to ensure an appropriate mRNA digestion, for example it has been stablished that the ratio between RNA and RNAse controls footprints size [13].

The third step is one of the most laborious in terms of protocol. Different strategies had been used to isolate ribosome protected fragments or ribosome footprints, but all of them imply a ribosome/poly-ribosome purification step. Even though commercial columns are available to purify monosomes, the most used approach is the differential sedimentation of ribosomes through a sucrose cushion during ultracentrifugation. The use of this technique of subcellular fractionation ensures the purification of monosomes with bound ribosome footprints. Once monosomes are purified, a polyacrylamide gel electrophoresis in denaturing conditions is run to separate the complex sample by length. Using appropriate size markers, the gel is cut at the corresponding length of 28-30 nt using a dark field transilluminator, even if footprints are not visible as it is usually the case. After disrupting the gel slices, precipitation and re-purification of ribosome footprints, samples are ready to proceed to library preparation.

Library preparation implies a set of protocol steps common in many high-throughput sequencing experiments like end repair, 3′ adaptor ligation, reverse transcription and PAGE cDNA purification, circularization of cDNA and PCR amplification. After checking length and concentration of the ribosome footprints library, they can be submitted to sequencing according to user-preferred sequencing technologies. Due to footprints small size, neither long reads nor paired-end reads are needed. Nevertheless, due to ribosomal rRNA presence in the footprints fraction purified, depletion of rRNA, coupled with extra sequencing depth are usually needed.

Finally, the bioinformatic analysis of data is the most user-dependent step. A typical analysis would include quality control of raw reads, mapping, count normalization and gene expression levels estimation. It could also include, for example, differential gene expression analysis if two biological conditions are contrasted. Table 1 show a list of some of the software available to perform classical analysis over RP data. Nevertheless, how deeply the data is interrogated is on user's hands, here we will discuss some of these downstream analyses later.

2.2. Protocol Variants, User Decisions

Up to this point we have reviewed the main steps in RP protocol considering the classical approaches most used in literature. Henceforth we will mention some protocol variants and why they could be used if is necessary (Fig. 1B). Considering the chronological order of the protocol, we will start with one of the steps where more variants are described in the literature: how to stop translation at the moment the experimental design requires to do so. Efficient stop of translation avoids ribosome run off, sharpening the picture taken of the translatome at a given time point. In the original protocol, a classical translation inhibitor like cycloheximide was used to specifically target translation elongation. However, as it does not interfere with pre-initiation complex scanning and translation initiation, treatment with cycloheximide causes a significant accumulation of ribosomes at initiation sites of mRNAs actively translated. This could represent a source of bias since a lot of ribosome footprints will be generated by initiating ribosomes while elongation is stopped. This issue was highly covered in the literature, with some authors proposing that this accumulation is actually due to an enrichment of slow codons after the initiation and others are in line with the bias hypothesis that generates a skewed distribution. Alternatively, it is possible to stop translation using liquid nitrogen and dry ice [12]. In this scenario, ribosomes are flash-frozen and stopped just by reducing

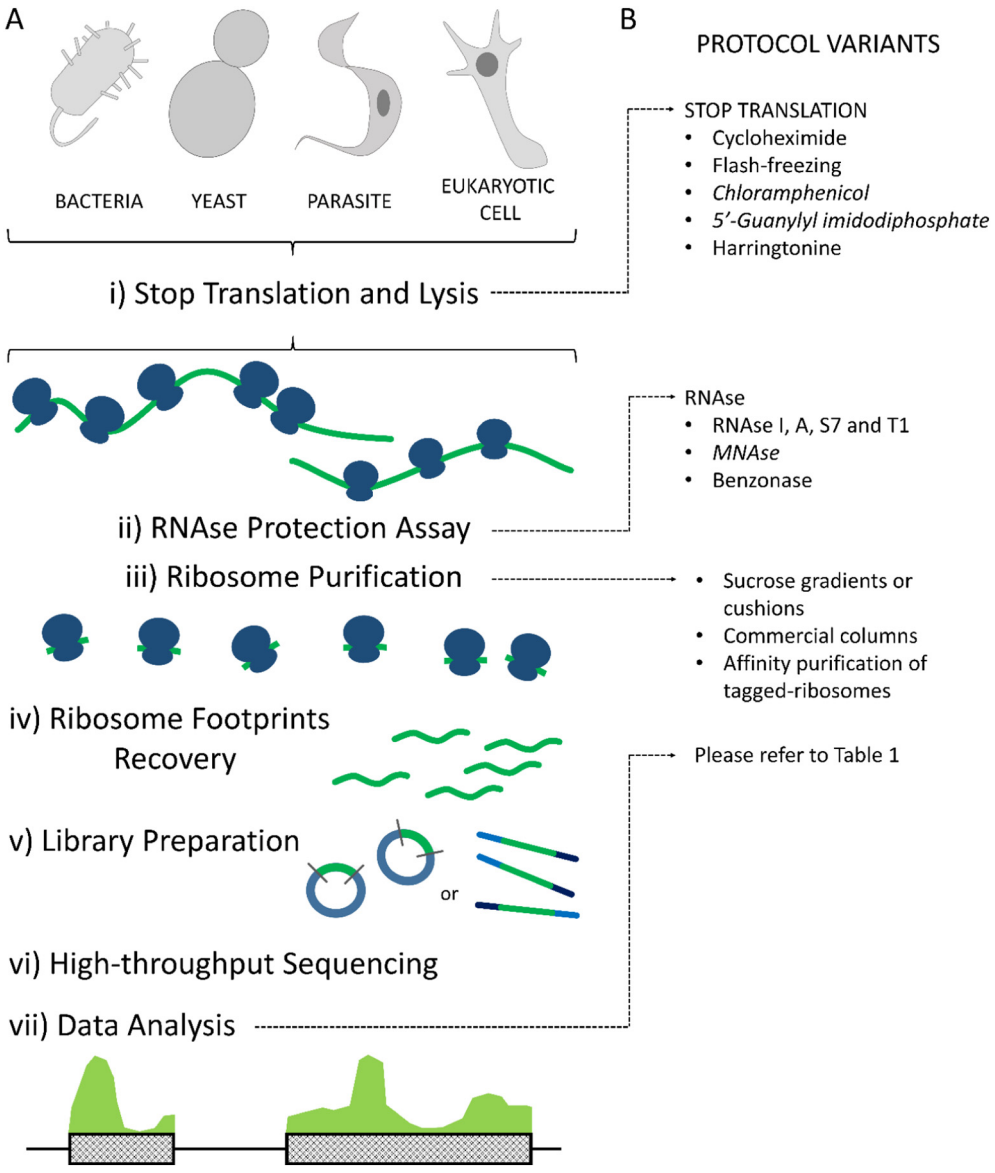

Fig. 1. Ribosome Profiling protocol description. A general description of RP protocol is shown in A, representing the main steps described in the text. The protocol variants discussed are summarized in B, linked to the corresponding step where would be applied. Variants that correspond to prokaryotes are marked in italic.

kinetic energy to a minimum. This alternative seems to not affect ribosome density and expression measurements but it's not the most extended approach, maybe because of availability of liquid nitrogen in the laboratories. When working with prokaryotes, besides flash-freezing, drugs like chloramphenicol and 5′-Guanylyl imidodiphosphate had been used [9]. Finally, it is worth mentioning that other drugs that target translation had been used to reveal specific aspects of translation. One of the most extended example is the use of harringtonine or the combined use of cycloheximide and harringtonine. Since harringtonine it is an inhibitor of translation initiation, the use of this drug alone could reveal translation initiation sites exclusively. Also, if harringtonine is first applied, and cycloheximide is applied after at different time points, it is possible to measure very specific translation properties like translation elongation speed [14,15].

The second step we mentioned it is the RNAse protection assay. In this step enzyme selection is critical [16]. In first place the biological model (eukaryotic or prokaryotic) already limits the options. In the literature, enzymes used for eukaryotic systems are mainly RNAse I, A, S7, T1 and MNAse, also used in prokaryotes. Since the method has been mainly applied to eukaryotic cells, RNAse I is the more common enzyme selected. In this case, the amount of RNA that is digested and other reaction conditions are well established, but when a *new* RNAse is being used, parameters like enzyme units and time of the digestion needs to be specifically determined to ensure a correct ribosome footprint production. It has been useful the use of enzymes, like Benzonase, or the above mentioned MNAse, that produce digestion products that allow a more straight forward ligation of the linkers required to prepare NGS molecular libraries [17–20] simplifying the library preparation protocol.

Once cells are harvested, lysed and the RNAse protection assay is carried out, the next step is to collect ribosomes and specifically purify ribosome footprints. As we mentioned above, ribosome purification could be one of the most laborious step. Despite commercial columns are available to purify ribosomes, more classical strategies tend to be used, like monosome separation by ultracentrifugation in sucrose cushions or gradients. While sucrose gradients fractionation is challenging, sucrose cushions give similar results with less technical challenges. Other approaches to collect ribosomes are available, like genetic manipulation to add epitope tags to ribosomes, allowing affinity purification [21–23]. In any case, after ribosome isolation, footprints purification is

Table 1
Software available to analyze, interpret and visualize RP-derived data.
A list of some of the software used to analyze RP data is briefly described, indicating its main features and the adequate environment to use it.

Name	Functions/description	Enviroment	Ref.
riboSeqR	Parsing data, align reads, plotting functions, frameshift detection and inferring alternative ORFs.	R	[101]
RiboProfiling	Quality assessment, read start position recalibration, counting of reads on CDS, 3′UTR, and 5′UTR, plotting of count data: pairs, log fold-change, codon frequency and coverage assessment, principal component analysis on codon coverage.	R	[102]
RiboGalaxy	On-line tools for the analysis and visualization of ribo-seq data (some of them use riboSeqR)	Galaxy webserver	[103]
Plastid	A handful of scripts for common high-throughput sequencing and ribosome profiling analyses, like: determining P-sites offsets	Python Library	[104]
Ribomap	Generates isoform-level ribosome profiles from ribosome profiling data	Unix	[105]
RiboTraper	Identifies translated regions	Unix	[106]
Rfoot	Identifies RNA regions protected by non-ribosomal protein complex present in Ribo-Seq data	Perl	[107]
anota	Analysis of differential translation and results visualization	R	[108]
RiboDiff	An statistical tool to detect changes in protein translation efficiency	Unix	[109]
Xtail	An analysis pipeline that identifies differentially translated genes in pairwise comparisons	R	[110]
RiboTools	Detection of translational ambiguities, stop codon readthrough events and codon occupancy. Provides plots for the visualization of these events.	Galaxy webserver	[111]
Proteoformer	Genome-wide visualization of ribosome occupancy and a translation initiation site calling algorithm. A protein database can be incorporated to increase protein identification	Galaxy webserver	[112]
ORFscore	Small ORF identification	In SPECTtre [106]; python	[75]
ORF-RATER	Coding sequence annotation	Python	[113]
FLOSS	A metric for distinguishing between 80S footprints and nonribosomal sources using footprint size distributions	In SPECTtre [106]; python	[61]
tRanslatome	Analysis of transcriptome, translatome and proteome data: Differentially expressed genes detection, gene ontology enrichment comparison and analysis of regulatory elements	R	[114]
TranslatomeDB	Differential gene expression, translation ratio, elongation velocity index and translational efficiency. Also comparision with other RP experiments can be done	Online	[115]
systemPipeR	Filter/trim sequences, quality control, alignments, counting, peak detection, differentially expressed genes detection, enrichment, classification, several reports and graphs	R	[116]

the immediate follow step. Since the RNAses used are endonucleases, they digest “unprotected” mRNA while also cutting fragments of rRNA exposed in ribosome's surface. This digestion produces a very complex mix of RNA fragments of diverse length that is separated by a denaturing PAGE. Using appropriate size markers (26 and 34 nt), the band corresponding to ribosome footprints is excised from the gel and the RNA is isolated. Interestingly, a new population of small footprints of 20 nt in length was recently described [24]. This small population would not be recovered if we use the size markers mentioned above. In this context, depending on the experiment being performed and on the research goals, size selection can be modified accordingly.

Since the original sample contains a lot of ribosomes, a very important fraction of the generated fragments comes from rRNA. This contamination, still present in ribosome footprints expected band, is an important issue. One possible strategy is to continue with the protocol ignoring this contamination and go deep in sequencing to obtain enough mRNA derived sequences to achieve RNA-seq like coverage. However, this contamination can represent up to 90% of the sample, so a subtracting strategy is usually necessary. Ribosomal RNA removal can be achieved through streptavidin affinity purification using specific biotinylated rRNA probes available for mouse and human. If the biological model it is not mouse or human, synthesis of specific rRNA complementary oligos can be considered, provided by previous knowledge of the region of the rRNA protected in the model used. The later can be obtained by sequencing at low depth to determine the most abundant protected fragments derived from rRNA. Because different enzymes can produce different protected rRNA due to allosteric impediments or cleavage site sequence specificity, determining the identity of contaminating rRNAs could be necessary.

When footprints are collected, library construction and high-throughput sequencing are the next in line. Depending on the RNAse used, end repair could be necessary prior to linker ligation. While conventional protocols require PCR amplification and purification of the amplified PCR product by PAGE, as mentioned above some enzymes simplify these steps. Finally, sequencing is performed. While several platforms are available to perform high-throughput sequencing, long reads are not necessary as footprints are naturally short. Usually the depth of coverage to be achieved is dependent on how much rRNA is contaminating your footprints and how many mRNAs you will need to quantify.

Finally, data interpretation implies a complete *in silico* analysis (see Table 1), although this is the step more flexible and open to user aims, it represents several challenges due to the particular features of RP. For example, reads are short in length, may have relatively high error rates and depending on library construction protocol could have high bias. Also, some fragments tend to be enriched, because accumulated ribosomes at translation initiation sites or pausing sites, leading to high read counts. Beyond this, most of the available tool to process and analyze experiments of RNA-Seq are suitable to use analyzing data from RP, specifically the ones used to short length reads and/or single-end reads. Nevertheless, some aspects need to be considered due to the peculiarities of the data set analyzed. For example, gene isoforms studies are difficult since ribosome footprints are short reads and mapping over splice junctions tend to be unreliable. Briefly, bioinformatic analysis implies in general: quality and adaptor trimming, mapping against a specific data base of rRNA or ncRNAs to remove contamination, unmapped reads are aligned to an mRNA data base, counting reads, normalize counts and proceed to check statistical differences between conditions. As said above, diverse analysis can be done with data, just to mention some: check footprints periodicity, upstream Open Reading Frame (uORF) search, detection of different translation initiation sites, codon usage and search for translation pauses, among others. Even though general-purpose RNA-seq tools may be suitable, some specific software has been developed to apply to RP data set that explicitly consider the influence of transcript levels on translatome determinations (see examples in Table 1).

3. Biological Models and Contributions

Up to date, the RP protocol has been applied to a large variety of biological models from viruses and bacteria to yeast, mammalian cells and tissues, and embryos. In this section we will present the main contributions done in each model, and also what we have learned about the translation mechanism using this methodology. In addition, in Table 2 several RP works were grouped by the main topic analyzed, indicating in each case the different organisms used.

Table 2
Brief summary of RP works in several models, grouped by the main analyzed topic.

Topic	Organism	Ref.
Genomic/translation characterization	Virus	[11,86–88]
	Mycobacterium abscessus	[35]
	Mammalian cells	[14]
Translation initiation sites	*Caulobacter crescentus*	[26]
	Mammalian cells	[59]
Translation elongation	*Saccharomyces cerevisiae*	[24]
	Caenorhabditis elegan	[79]
Translational pausing	*Escherichia coli*	[9,27,32]
	Bacillus subtilis	[9]
	Saccharomyces cerevisiae	[46,67]
Codon usage	*Escherichia coli*	[37]
	Saccharomyces cerevisiae	[47,49,50]
Small ORF	*Saccharomyces cerevisiae*	[51]
	Zebra fish	[75]
	Drosophila melanogaster	[77]
	Mammalian cells	[65]
Translation dynamics on different stages	*Plasmodium falciparum*	[81,82]
	Trypanosoma cruzi	[17]
	Trypanosoma brucei	[83,84]
Stress response	*Escherichia coli*	[41]
	Mycoplasma gallisepticum	[34]
	Arabidopsis thaliana	[80]
	Saccharomyces cerevisiae	[7]
lncRNAs translation	Mammalian cells	[60–64]

3.1. Bacteria: Translational Pausing, Codon Use and Antibiotics

In bacteria, ribosome profiling was applied in first place to *Escherichia coli* and *Bacillus subtilis* [9] to study the causes of translational pausing. The authors observed that the presence of Shine-Dalgarno-like features in coding sequences are the major determinants of translation rates in these models. Instead of codon usage or the presence of rare tRNAs, interactions between rRNA and these Shine-Dalgarno-like features in mRNA can impact on ribosomal movement along mRNA, which in turn affect footprints location and abundance [25]. Later, Schrader et al. [26] also applied RP, in *Caulobacter crescentus* and arrived to the same conclusion: ribosomes tend to pause at internal Shine-Dalgarno-like sequences in coding genes. Although the later hypothesis regarding underling mechanisms of translation pausing in bacteria is still controversial (see an example in [27]), with authors supporting classical hypothesis of tRNA abundance as main modulator of translation speed, this is still a new possible mechanism for regulating translation uncovered by the RP strategy.

In another study Oh et al. [28], investigated a chaperone trigger factor and how this protein regulates outer membrane proteins, using a RP protocol modified later in [29]. Balakrishnan et al. [30] studied translation initiation on *E. coli* using RP, while translation elongation was covered by Elgamal et al. [31], where authors find translational pauses associated to elongation factor P and amino acids motifs upstream to ribosome P-site (also found in [32]). Other bacteria where RP was applied are *Mycoplasma gallisepticum* [33,34], *Mycobacterium abscessu* [35] and *Staphylococcus aureus* [36]. RP as a powerful technique to measure translation rates at subcodon resolution, has allowed scientist to focus on the relationship between translation efficiency and codon usage deriving in the optimization bacterial vectors for expression of heterologous recombinant proteins [37,38].

Also, RP has given new insights on the antibiotics mechanisms to inhibit translation [39]. Other studies have been using RP to investigate mechanisms for biofilm formation in *B. subtilis* [40], ethanol effects on translation [41] and mRNA cleavage by the endonuclease RelE [42].

3.2. Yeast: Start Codons, uORFs and Translational Pauses

Since RP was firstly described in the budding yeast *Saccharomyces cerevisiae* [7], a lot of research has been done using this model and by re-analyzing that public data sets generated. In the original article, Ingolia et al. [7] explored translation response to starvation. In this seminal paper the terms translation efficiency and periodicity were defined for first time in this context (see Introduction). While translation efficiency is usually calculated in every experiment using RP, periodicity is not assessed so often, because it depends on RNAse amount used and digestion time.

For first time, integrating all data obtained, correlations between expression levels estimated by RNA-Seq (transcriptional levels), RP (translational levels) and proteomics (protein levels) could be obtained, reflecting the contribution of translational regulation in the fine tuning of final proteins levels (please see examples in Fig. 2). In this sense, other efforts have been made to correlate translation ratios and protein abundance. For example, Wang et al. [43] by incorporating mRNA length as a key factor, found a strong multivariate linear correlation between protein levels and translation ratios estimated by ribosome-nascent chain complex sequencing (RNC-Seq). The correlation between translational and protein levels estimated by RP and proteomics, respectively, may be improved if elongation velocity index are incorporated in the analysis, according to the authors [44] (please see Section 3.3.2).

Also, start codons were also precisely determined in this work, and initiation at non-AUG codons was observed as response to starvation. In the same way, detection of ribosome footprints at 5'-UTRs reveals translational activity in these regions mainly explained by the presence of uORFs. In this way, a new approach to uORF study and its relationship with translation regulation was stablished, revealing a completely new and complex field previously not covered in detail.

To highlight some of these contributions yeast models provided, we can mention that distinct population of ribosome footprints were discovered and were assigned to distinct stages of translating ribosomes [24]. Furthermore, 80S ribosomes (monosomes) were detected as translationally active, translating specific mRNAs encoding low abundance and regulatory proteins, among others [45]. In addition, codon usage, tRNA levels and how they influence translation was highly covered [46–50]. The hypothesis that arise more strongly in yeast is that biochemical interactions between the nascent peptide and the ribosomal exit tunnel (in particular the initial part of the tunnel) are major determinants on ribosome stalling [46]. A stalling signal of proline and arginine was detected, as others showed for bacteria [31,32]. On the other hand, also the correlation between tRNA concentrations and codon decoding time was evaluated, finding a significant negative correlation, supporting the idea that translation efficiency is influenced by tRNAs levels in the cells [48]. Also, RP was used to explore the genome-wide translation of small ORFs (<100 amino acids) and long non coding RNAs (lncRNAs) [51], ribosome rescue in 3′-UTR [52], the yeast meiotic program with important contributions to the area [53], and also how translation contributes to regulate gene-expression in yeast in an evolutionary view [54].

3.3. Mammalian Cells: uORFs, Pauses, Initiation Sites and lncRNAs

In mammalian cells, the first study carried out applied RP strategy to reveal aspects of microRNA's (miRNA) function in the cell [55]. The authors observed that miRNA predominantly affect mRNA levels, with only a modest influence on translational efficiency. This study revealed for first time that mRNA destabilization is the major consequence of miRNA regulation. So, from here to the end of this section we will present some interesting research and their results in mammalian cells mainly, but also in other eukaryotic models.

A significant study in terms of results, conclusions and repercussions, was done by the group who publish the RP protocol, but using mouse embryonic stem cells (mESC) [14]. In this model, the authors identified thousands of pause sites and unannotated translation products like amino-terminal extension and uORFs with potential regulatory roles. In parallel, authors combine harringtonine and cycloheximide use to monitoring kinetic of translation as we describe below, evidencing a

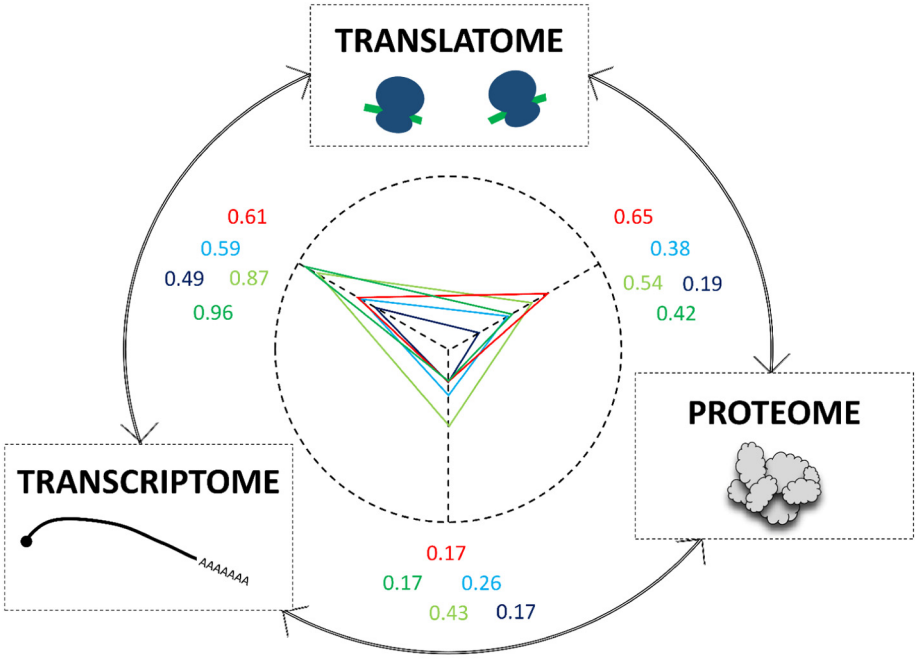

Authors	Journal	Year	Organism	Correlation score
Ingolia	Science	2009	Yeast	R^2
Smircich	BMC Genomics	2015	Trypanosoma cruzi	Pearson R^2
Cenik	Genome Research	2015	Lymphoblastoid cell lines	Spearman ρ
Wang & Sun	Genome Biol Evol	2015	Yeast	Pearson R^2
Miranda-CasoLuengo & Staunton	BMC Genomics	2016	Mycobacterium abscessus	Pearson R^2

Fig. 2. Correlations among RNA-Seq, RP and proteome-derived expression data sets. Genome-wide correlations of individual gene expression levels estimated by RNA-Seq, RP and proteome techniques are shown. Each correlation value is referenced to its corresponding author, indicating also journal, year, organism involved and correlation test used, by the same color code.

ribosome translation rate of 5.6 amino acids per second, consistent with previous values [56], and that is independent of length, protein abundance, classes of mRNAs or codon use.

3.3.1. uORFs

Ingolia et al. [14], using harringtonine in mESC, could identify translation initiation sites, where AUG was present in almost 75% of canonical sites, but in <25% in upstream sites, where others near-AUG codons were observed, like CUG and GUG (see also Section 3.3.3). Considering the initiation site defined, the reading frame associated was also investigated and classified based on their relationship to the annotated ORF. In this characterization, many uORF were detected, as well as alternate protein products with amino-terminal extensions or truncations. The authors also study the widespread translation of uORFs detected and their change during differentiation, highlighting the important regulatory role that these elements have affecting translation, particularly when the cell is under stress conditions [57]. A well-known example is the uORF translation regulation that affects GCN4 expression in yeast under starvation [7].

3.3.2. Translational Pauses and Elongation Speed

Regarding translational stall sites, Ingolia et al. [14] observed in mESC a consensus peptide motif of glutamate (preferentially GAA codon) or aspartate in the A site of pauses, preceded by a proline or glycine, and then another proline (preferentially represented by CC[A/T] codons); while no evidence of rare codons enrichment was seen in pausing sites. Also, Dana and Tuller [58], re-analyzed the data focusing on elongation speed and ribosome profiles. Their analysis suggest that elongation speed is indeed determined by the tRNA pool, local mRNA folding and local charge of amino acids encoded; an idea that seems to be extended in different articles, as was mentioned before (see also [46]). Nevertheless, the authors mention that they detect an unknown source of biases in the data that can interfere in ribosome profiles over mRNAs. Nevertheless, by experimentally assessing elongation velocity, recently Lian & Guo et al. [44] found that these general conclusions we have described may not be applicable to all individual cases. In this work, information from RNA-Seq, RP and also RNC-mRNA was used to define and calculate an elongation velocity index at individual genes in human cells. This index was correlated with several mRNA features and also with biological conditions, where authors find an elongation speed deceleration on malignant phenotype associated genes.

3.3.3. Translation Initiation Sites (TIS)

Combining more data sets, Michel et al. [59] designed a method to estimate the probability of ribosomes initiating at individual start codons. This tool is able to discriminate between weak or strong initiation sites based on the accepted leaky scanning model of translation initiation in eukaryotes. For example, analyzing the codon preference in TIS in human and mouse, a > 50% of AUG TIS and also almost 50% of AUG preference in downstream TIS was observed. Composition of upstream TIS was more diverse: 25% are AUG codons, 30% CUG and 40% include other AUG-variants like UUG, GUG, AGG, ACG, among others [15].

3.3.4. Long Non Coding RNAs

With no doubt, another striking finding of the work done by Ingolia et al. [14] in mESC was the detection of high levels of ribosome footprints in long intragenic noncoding RNAs (lincRNAs), with marked initiation sites evidenced by harringtonine. They classify these RNAs as sprcRNA: short, polycistronic ribosome-associated coding RNAs. If lincRNA encode or not a message to be translated by the ribosomes is a matter addressed specifically in two publications [60,61]. Guttman et al. [60] defined a Ribosome Release Score, that discriminate between

coding and noncoding transcripts. Using this score, authors claim that the ribosome occupancy observed on lincRNAs *per se* is not an indicator of active translation and describe possible reasons why noncoding RNAs show ribosome footprints. One of these possibilities is that these footprints actually come from ribonucleo protein particles or others RNA-protein complexes. Alternatively, footprints could be generated by real engagement of ribosomes over ncRNAs that will not be functional at the end. This interesting controversy was going to take an unexpected turn when just over a year later, again Ingolia and Weissman described a different metric to analyze footprints, that now classify lncRNAs as coding [61]. This new metric called FLOSS (fragment length organization similarity score) measure the magnitude of disagreement between length distribution of a set of transcripts of interest and annotated protein-coding transcripts. Based on FLOSS and other lines of evidence, the authors proposed that lncRNAs has ribosome footprints that show features of translation. In addition alternative hypothesis were discussed: *i*) translating ribosome could act as a potent helicase to remodel RNA structures and remove RNA-binding proteins; *ii*) translated sequences may also act as cis-acting elements over lncRNAs that originate them and *iii*) the authors discuss about a possible contribution of the proteins synthetized by noncanonical translation to serve as possible antigens presented to the cellular immune system, expanding the universe of epitopes either in a viral infection or in a tumoral context. In any case, the fact that some ncRNAs are associated with ribosomes, translationally active or not, generates both challenging and interesting questions that wait to be answered (see examples in [62–64]).

Using the data produced by RP on mESC, a lot of downstream analysis has been conducted. For example, an approach to search and predict putatively functional small ORF was developed to identify new classes of bioactive peptides [65]. Another example is the work done by Zupanic et al. [66], where the authors developed a method to study mRNA translation regulation analyzing individual ribosome profiles. Incorporating RNA-Seq data to correct bias and artifacts, they look for changes in ribosome density along mRNAs to detect mechanisms of regulation, like premature termination or new transcript isoforms.

Regarding bias, several articles have studied this important issue on RP data. Some improvements have been done in terms of understand the bias source, and be able to correct it accurately [58,67,68].

The movement of the ribosome over the mRNA has been studied analyzing in deep mapping periodicity leading to undercover mechanisms underlying translational frameshifts [59]. Also regions in the human genome that are dually decoded were identified (~1% of human genome approx.), either from different mRNAs as from the same, expanding our vision about translation regulation and even about central dogma [4,59].

In HeLa cells, RP was applied to explore the translational landscape of cell cycle, and a widespread translation regulation was seen over cell cycle progression [69,70]. Surprisingly, evidence of functional bicistronic mRNAs with antiviral functions in the innate immune system was also revealed by RP in a human cell line [71]. Furthermore RP was used in humans to investigate genetic variants in lymphoblastoid cells derived from a diverse group of 30 individuals and how some genetic differences may modulate ribosome occupancy [72].

The mTOR pathway is a very important target of different drugs and has been implicated in several diseases, including cancer. Since this complex regulates cell growth and proliferation by regulating mRNA translation, it is interesting to use RP protocol to elucidate translation control executed by mTOR. This was done by Sabatini's [73] and Ruggero's [74] labs, and what they found was a surprising simple model of the mRNA features that mediates mTORC1-dependent translation: an established 5′ terminal oligopyrimidine (TOP) motifs. 5′-UTR length or complexity was not associated with mTORC1 translation regulation. The later also identify another motif called PRTE (pyrimidine-rich translational element) in 5′-UTR of mTOR targets mRNAs, which in conjunction with TOP motif were founded in almost 90% of mTOR-sensitive genes. A common result of both works, which undoubtedly draws attention, is the low regulatory spectrum found in terms of number of messengers: mTOR-regulated mRNAs were 253 and 144, respectively for each publication, a low number of targets considering the central role of mTOR pathway in cellular metabolism and previous results of translation control resolution using RP. It is still an open question whether this number changes in different cell types or conditions, since there are still several factors downstream of mTOR that influences what is being translated.

3.4. Others Biological Models: Zebrafish, Drosophila, C. elegans, Trypanosomatids and Virus

Besides bacteria, yeast and mammalian cell lines, the RP method was used to study translation regulation in others biological models as zebrafish [63,75], the fruit fly *Drosophila* [76–78], *C. elegans* [79], *Arabidopsis* [80] and also parasites like *Plasmodium falciparum* [81,82], *Trypanosoma brucei* [83,84] and *T. cruzi* [17]. Trypanosomatids undergo a complex life cycle with several distinct developmental forms, each having particular morphologic and metabolic profiles. However, these organisms accomplish the associated gene expression changes without transcriptional control [85]. Indeed, translation regulation proved to be a key mechanism controlling protein levels as revealed by drastic changes in translational efficiency for many developmentally regulated genes. For instance, the transition from a dividing to a non-diving parasite form was accompanied by a decrease in the translational efficiency of ribosomal proteins which in turn may explain the observed global decrease in protein synthesis. However, proteins required in the non-dividing stage scape this general trend and are actively translated as shown for the trans-sialidase family of virulence factors in *T. cruzi* [17]. Besides, the data allowed the curation of the available genomes in these non-model organisms [84].

Also, RP was applied to study translation in virus like human cytomegalovirus and Kaposi's sarcoma-associated herpesvirus, both herpesvirus, and also in Cricket paralysis virus and Influenza A virus (see [11,86–88], respectively).

4. Applications, Challenges and Perspectives

Besides classical applications we have been discussing above, like determine translation gene expression levels, pause associated motifs, codon translational rates, uORF and frameshift events detection, among others, here we will mention specific protocols that had evolved from initial RP experiments, like how to determine TIS by Qian lab [15,89]. In first place, they describe an approach named global translation initiation sequencing (or GTI-Seq) that combine the use of lactimidomycin and cycloheximide to detect both initiation and elongation ribosomes along transcripts, in human and mouse. The other, but similar approach, named QTI-Seq (Quantitative Translation Initiation Sequencing) evaluating not only TIS qualitatively, but also quantitatively, so statistical comparisons can be made between two conditions. In bacteria also exist an approach to identify TIS genome-wide named tetracycline-inhibited RP [90].

Research on mitochondrial and chloroplast translation is also possible using RP [91–93]. Recently, an specific application of RP named mitochondrial ribosome (mitoribosome) profiling was developed [94]. In this case, the approach developed in yeast consist in the immunoprecipitation of mitoribosomes from cell lysates to perform RNAse digestion. A similar approach but targeting reticulum-bound ribosomes was also used, in mammalian cells, to study translation related to intracellular traffic of membranes [19].

Throughout this minireview we have shown how the RP method has provided the scientific community with a powerful system to study the translation mechanisms and regulation, and more generally a more complete picture of regulation of gene expression in several models.

However even when the seminal paper will turn 10 years old next year many aspects of the technique are not completely resolved, as

can be shown in the continuous development of new experimental protocols and analysis tools. Variations of the method are emerging to address particular cases, such as the development of protocols to assess localized translation. For instance, Williams et al. [95] reported proximity-specific ribosome profiling to target translation of nuclear encoded mitochondrial genes by tagging ribosomes in close contact with the outer mitochondrial membrane. In this context, localized translation can be investigated in more difficult scenarios like protein synthesis in neuronal projections [96–98], specifically Holt lab performed ribosome tagging and analyzed mRNA associated to tagged polysomes in the pre-synaptic area of a minute portion of the brain [99] but the low input in mRNA would impair ribosome profiling. So, it is still necessary to develop methods that will allow the study of systems where input material is a limiting factor. Some work is starting to appear in this field [100].

Some intriguing questions have not been yet pursued, particularly there are just a few reports where RP has been applied to disturbed systems, for example drug treated cells or pathological cells, as neurodegenerative diseases tissue or cancer cells where translation me be playing a key role in the etiology of the abnormal molecular processes.

Acknowledgements

We would like to acknowledge Dr. David Munroe for his inspiration, advices and support for the development of RP protocol and encouragement to study translation regulation.

This work received financial support from: Master and PhD fellowships from Agencia Nacional de Investigación e Innovación (ANII) and Comisión Académica de Posgrado (CAP) to GE (POS_NAC_2012_1_8584 and POS_NAC_2016_1_129959), Comisión Sectorial de Investigación Científica (CSIC) for JRSS (CSIC grupos ID=108725 #144) and for GE (CSIC Iniciación #370), ANII to JRSS (FCE_1_2017_1_136082) and to PS (FCE_3_2016_1_126317), and from Programa de Desarrollo de las Ciencias Básicas (PEDECIBA).

References

[1] Sboner A, Mu XJ, Greenbaum D, Auerbach RK, Gerstein MB. The real cost of sequencing: higher than you think! Genome Biol 2011;12:125. https://doi.org/10.1186/gb-2011-12-8-125.
[2] Buermans HPJ, Dunnen den JT. Next generation sequencing technology: advances and applications. Biochim Biophys Acta 2014;1842:1932–41. https://doi.org/10.1016/j.bbadis.2014.06.015.
[3] Muir P, Li S, Lou S, Wang D, Spakowicz DJ, Salichos L, et al. Erratum to: the real cost of sequencing: scaling computation to keep pace with data generation. Genome Biol 2016;17:78. https://doi.org/10.1186/s13059-016-0961-9.
[4] Mouilleron H, Delcourt V, Roucou X. Death of a dogma: eukaryotic mRNAs can code for more than one protein. Nucleic Acids Res 2016;44:14–23. https://doi.org/10.1093/nar/gkv1218.
[5] Vogelstein B, Papadopoulos N, Velculescu VE, Zhou S, Diaz LA, Kinzler KW. Cancer genome landscapes. Science 2013;339:1546–58. https://doi.org/10.1126/science.1235122.
[6] Campbell BB, Light N, Fabrizio D, Zatzman M, Fuligni F, de Borja R, et al. Comprehensive analysis of hypermutation in human cancer. Cell 2017;171:1042–1056.e10. https://doi.org/10.1016/j.cell.2017.09.048.
[7] Ingolia NT, Ghaemmaghami S, Newman JRS, Weissman JS. Genome-wide analysis in vivo of translation with nucleotide resolution using ribosome profiling. Science 2009;324:218–23. https://doi.org/10.1126/science.1168978.
[8] Steitz JA. Polypeptide chain initiation: nucleotide sequences of the three ribosomal binding sites in bacteriophage R17 RNA. Nature 1969;224:957–64.
[9] Li G-W, Oh E, Weissman JS. The anti-Shine-Dalgarno sequence drives translational pausing and codon choice in bacteria. Nature 2012;484:538–41. https://doi.org/10.1038/nature10965.
[10] Castelo-Szekely V, Arpat AB, Janich P, Gatfield D. Translational contributions to tissue specificity in rhythmic and constitutive gene expression. Genome Biol 2017;18:116. https://doi.org/10.1186/s13059-017-1222-2.
[11] Stern-Ginossar N, Weisburd B, Michalski A, Le VTK, Hein MY, Huang S-X, et al. Decoding human cytomegalovirus. Science 2012;338:1088–93. https://doi.org/10.1126/science.1227919.
[12] Ingolia NT, Brar GA, Rouskin S, McGeachy AM, Weissman JS. The ribosome profiling strategy for monitoring translation in vivo by deep sequencing of ribosome-protected mRNA fragments. Nat Protoc 2012;7:1534–50. https://doi.org/10.1038/nprot.2012.086.
[13] McGlincy NJ, Ingolia NT. Transcriptome-wide measurement of translation by ribosome profiling. Methods 2017;126:112–29. https://doi.org/10.1016/j.ymeth.2017.05.028.
[14] Ingolia NT, Lareau LF, Weissman JS. Ribosome profiling of mouse embryonic stem cells reveals the complexity and dynamics of mammalian proteomes. Cell 2011;147:789–802. https://doi.org/10.1016/j.cell.2011.10.002.
[15] Lee S, Liu B, Lee S, Huang S-X, Shen B, Qian S-B. Global mapping of translation initiation sites in mammalian cells at single-nucleotide resolution. Proc Natl Acad Sci U S A 2012;109:E2424-2. https://doi.org/10.1073/pnas.1207846109.
[16] Gerashchenko MV, Gladyshev VN. Ribonuclease selection for ribosome profiling. Nucleic Acids Res 2017;45:e6. https://doi.org/10.1093/nar/gkw822.
[17] Smircich P, Eastman G, Bispo S, Duhagon MA, Guerra-Slompo EP, Garat B, et al. Ribosome profiling reveals translation control as a key mechanism generating differential gene expression in Trypanosoma cruzi. BMC Genomics 2015;16:197. https://doi.org/10.1186/s12864-015-1563-8.
[18] Marcon BH, Holetz FB, Eastman G, Origa-Alves AC, Amorós M, de Aguiar AM, et al. Downregulation of the protein synthesis machinery is a major regulatory event during early adipogenic differentiation of human adipose-derived stromal cells. Stem Cell Res 2017. https://doi.org/10.1016/j.scr.2017.10.027.
[19] Reid DW, Nicchitta CV. Primary role for endoplasmic reticulum-bound ribosomes in cellular translation identified by ribosome profiling. J Biol Chem 2012;287:5518–27. https://doi.org/10.1074/jbc.M111.312280.
[20] Reid DW, Shenolikar S, Nicchitta CV. Simple and inexpensive ribosome profiling analysis of mRNA translation. Methods 2015;91:69–74. https://doi.org/10.1016/j.ymeth.2015.07.003.
[21] Sanz E, Yang L, Su T, Morris DR, McKnight GS, Amieux PS. Cell-type-specific isolation of ribosome-associated mRNA from complex tissues. Proc Natl Acad Sci U S A 2009;106:13939–44. https://doi.org/10.1073/pnas.0907143106.
[22] Heiman M, Schaefer A, Gong S, Peterson JD, Day M, Ramsey KE, et al. A translational profiling approach for the molecular characterization of CNS cell types. Cell 2008;135:738–48. https://doi.org/10.1016/j.cell.2008.10.028.
[23] Shigeoka T, Jung J, Holt CE, Jung H. Axon-TRAP-RiboTag: affinity purification of translated mRNAs from neuronal axons in mouse in vivo. Methods Mol Biol 1649;2018:85–94. https://doi.org/10.1007/978-1-4939-7213-5_5.
[24] Lareau LF, Hite DH, Hogan GJ, Brown PO. Distinct stages of the translation elongation cycle revealed by sequencing ribosome-protected mRNA fragments. Elife 2014;3:e01257. https://doi.org/10.7554/eLife.01257.
[25] O'Connor PBF, Li G-W, Weissman JS, Atkins JF, Baranov PV. rRNA:mRNA pairing alters the length and the symmetry of mRNA-protected fragments in ribosome profiling experiments. Bioinformatics 2013;29:1488–91. https://doi.org/10.1093/bioinformatics/btt184.
[26] Schrader JM, Zhou B, Li G-W, Lasker K, Childers WS, Williams B, et al. The coding and noncoding architecture of the Caulobacter crescentus genome. PLoS Genet 2014;10:e1004463. https://doi.org/10.1371/journal.pgen.1004463.
[27] Mohammad F, Woolstenhulme CJ, Green R, Buskirk AR. Clarifying the translational pausing landscape in bacteria by ribosome profiling. Cell Rep 2016;14:686–94. https://doi.org/10.1016/j.celrep.2015.12.073.
[28] Oh E, Becker AH, Sandikci A, Huber D, Chaba R, Gloge F, et al. Selective ribosome profiling reveals the cotranslational chaperone action of trigger factor in vivo. Cell 2011;147:1295–308. https://doi.org/10.1016/j.cell.2011.10.044.
[29] Latif H, Szubin R, Tan J, Brunk E, Lechner A, Zengler K, et al. A streamlined ribosome profiling protocol for the characterization of microorganisms. Biotechniques 2015;58:329–32. https://doi.org/10.2144/000114302.
[30] Balakrishnan R, Oman K, Shoji S, Bundschuh R, Fredrick K. The conserved GTPase LepA contributes mainly to translation initiation in Escherichia coli. Nucleic Acids Res 2014;42:13370–83. https://doi.org/10.1093/nar/gku1098.
[31] Elgamal S, Katz A, Hersch SJ, Newsom D, White P, Navarre WW, et al. EF-P dependent pauses integrate proximal and distal signals during translation. PLoS Genet 2014;10:e1004553. https://doi.org/10.1371/journal.pgen.1004553.
[32] Woolstenhulme CJ, Guydosh NR, Green R, Buskirk AR. High-precision analysis of translational pausing by ribosome profiling in bacteria lacking EFP. Cell Rep 2015;11:13–21. https://doi.org/10.1016/j.celrep.2015.03.014.
[33] Fisunov GY, Evsyutina DV, Arzamasov AA, Butenko IO, Govorun VM. Profiling of mycoplasma gallisepticum ribosomes. Acta Nat 2015;7:107–12.
[34] Fisunov GY, Evsyutina DV, Garanina IA, Arzamasov AA, Butenko IO, Altukhov IA, et al. Ribosome profiling reveals an adaptation strategy of reduced bacterium to acute stress. Biochimie 2017;132:66–74. https://doi.org/10.1016/j.biochi.2016.10.015.
[35] Miranda-CasoLuengo AA, Staunton PM, Dinan AM, Lohan AJ, Loftus BJ. Functional characterization of the Mycobacterium abscessus genome coupled with condition specific transcriptomics reveals conserved molecular strategies for host adaptation and persistence. BMC Genomics 2016;17:553. https://doi.org/10.1186/s12864-016-2868-y.
[36] Basu A, M-NF Yap. Ribosome hibernation factor promotes staphylococcal survival and differentially represses translation. Nucleic Acids Res 2016;44:4881–93. https://doi.org/10.1093/nar/gkw180.
[37] Nakahigashi K, Takai Y, Shiwa Y, Wada M, Honma M, Yoshikawa H, et al. Effect of codon adaptation on codon-level and gene-level translation efficiency in vivo. BMC Genomics 2014;15:1115. https://doi.org/10.1186/1471-2164-15-1115.
[38] Li G-W. How do bacteria tune translation efficiency? Curr Opin Microbiol 2015;24:66–71. https://doi.org/10.1016/j.mib.2015.01.001.
[39] Marks J, Kannan K, Roncase EJ, Klepacki D, Kefi A, Orelle C, et al. Context-specific inhibition of translation by ribosomal antibiotics targeting the peptidyl transferase center. Proc Natl Acad Sci U S A 2016;113:12150–5. https://doi.org/10.1073/pnas.1613055113.
[40] Subramaniam AR, Deloughery A, Bradshaw N, Chen Y, O'Shea E, Losick R, et al. A serine sensor for multicellularity in a bacterium. Elife 2013;2:e01501. https://doi.org/10.7554/eLife.01501.

[41] Haft RJF, Keating DH, Schwaegler T, Schwalbach MS, Vinokur J, Tremaine M, et al. Correcting direct effects of ethanol on translation and transcription machinery confers ethanol tolerance in bacteria. Proc Natl Acad Sci U S A 2014;111:E2576-5. https://doi.org/10.1073/pnas.1401853111.
[42] Hwang J-Y, Buskirk AR. A ribosome profiling study of mRNA cleavage by the endonuclease RelE. Nucleic Acids Res 2017;45:327–36. https://doi.org/10.1093/nar/gkw944.
[43] Wang T, Cui Y, Jin J, Guo J, Wang G, Yin X, et al. Translating mRNAs strongly correlate to proteins in a multivariate manner and their translation ratios are phenotype specific. Nucleic Acids Res 2013;41:4743–54. https://doi.org/10.1093/nar/gkt178.
[44] Lian X, Guo J, Gu W, Cui Y, Zhong J, Jin J, et al. Genome-wide and experimental resolution of relative translation elongation speed at individual gene level in human cells. PLoS Genet 2016;12:e1005901. https://doi.org/10.1371/journal.pgen.1005901.
[45] Heyer EE, Moore MJ. Redefining the translational status of 80S monosomes. Cell 2016;164:757–69. https://doi.org/10.1016/j.cell.2016.01.003.
[46] Sabi R, Tuller T. A comparative genomics study on the effect of individual amino acids on ribosome stalling. BMC Genomics 2015;16(Suppl. 10):S5. https://doi.org/10.1186/1471-2164-16-S10-S5.
[47] Pop C, Rouskin S, Ingolia NT, Han L, Phizicky EM, Weissman JS, et al. Causal signals between codon bias, mRNA structure, and the efficiency of translation and elongation. Mol Syst Biol 2014;10:770. https://doi.org/10.15252/msb.20145524.
[48] Dana A, Tuller T. The effect of tRNA levels on decoding times of mRNA codons. Nucleic Acids Res 2014;42:9171–81. https://doi.org/10.1093/nar/gku646.
[49] Gardin J, Yeasmin R, Yurovsky A, Cai Y, Skiena S, Futcher B. Measurement of average decoding rates of the 61 sense codons in vivo. Elife 2014;3:198. https://doi.org/10.7554/eLife.03735.
[50] Gorochowski TE, Ignatova Z, Bovenberg RAL, Roubos JA. Trade-offs between tRNA abundance and mRNA secondary structure support smoothing of translation elongation rate. Nucleic Acids Res 2015;43:3022–32. https://doi.org/10.1093/nar/gkv199.
[51] Smith JE, Alvarez-Dominguez JR, Kline N, Huynh NJ, Geisler S, Hu W, et al. Translation of small open reading frames within unannotated RNA transcripts in Saccharomyces cerevisiae. Cell Rep 2014;7:1858–66. https://doi.org/10.1016/j.celrep.2014.05.023.
[52] Guydosh NR, Green R. Dom34 rescues ribosomes in 3′ untranslated regions. Cell 2014;156:950–62. https://doi.org/10.1016/j.cell.2014.02.006.
[53] Brar GA, Yassour M, Friedman N, Regev A, Ingolia NT, Weissman JS. High-resolution view of the yeast meiotic program revealed by ribosome profiling. Science 2012;335:552–7. https://doi.org/10.1126/science.1215110.
[54] McManus CJ, May GE, Spealman P, Shteyman A. Ribosome profiling reveals post-transcriptional buffering of divergent gene expression in yeast. Genome Res 2014;24:422–30. https://doi.org/10.1101/gr.164996.113.
[55] Guo H, Ingolia NT, Weissman JS, Bartel DP. Mammalian microRNAs predominantly act to decrease target mRNA levels. Nature 2010;466:835–40. https://doi.org/10.1038/nature09267.
[56] Boström K, Wettesten M, Borén J, Bondjers G, Wiklund O, Olofsson SO. Pulse-chase studies of the synthesis and intracellular transport of apolipoprotein B-100 in Hep G2 cells. J Biol Chem 1986;261:13800–6.
[57] Andreev DE, O'Connor PBF, Fahey C, Kenny EM, Terenin IM, Dmitriev SE, et al. Translation of 5′ leaders is pervasive in genes resistant to eIF2 repression. Elife 2015;4:e03971. https://doi.org/10.7554/eLife.03971.
[58] Dana A, Tuller T. Determinants of translation elongation speed and ribosomal profiling biases in mouse embryonic stem cells. PLoS Comput Biol 2012;8:e1002755. https://doi.org/10.1371/journal.pcbi.1002755.
[59] Michel AM, Andreev DE, Baranov PV. Computational approach for calculating the probability of eukaryotic translation initiation from ribo-seq data that takes into account leaky scanning. BMC Bioinf 2014;15:380. https://doi.org/10.1186/s12859-014-0380-4.
[60] Guttman M, Russell P, Ingolia NT, Weissman JS, Lander ES. Ribosome profiling provides evidence that large noncoding RNAs do not encode proteins. Cell 2013;154:240–51. https://doi.org/10.1016/j.cell.2013.06.009.
[61] Ingolia NT, Brar GA, Stern-Ginossar N, Harris MS, Talhouarne GJS, Jackson SE, et al. Ribosome profiling reveals pervasive translation outside of annotated protein-coding genes. Cell Rep 2014;8:1365–79. https://doi.org/10.1016/j.celrep.2014.07.045.
[62] Cohen SM. Everything old is new again: (linc)RNAs make proteins! EMBO J 2014;33:937–8. https://doi.org/10.1002/embj.201488303.
[63] Chew G-L, Pauli A, Rinn JL, Regev A, Schier AF, Valen E. Ribosome profiling reveals resemblance between long non-coding RNAs and 5′ leaders of coding RNAs. Development 2013;140:2828–34. https://doi.org/10.1242/dev.098343.
[64] Li L-J, Leng R-X, Fan Y-G, Pan H-F, Ye D-Q. Translation of noncoding RNAs: focus on lncRNAs, pri-miRNAs, and circRNAs. Exp Cell Res 2017;361:1–8. https://doi.org/10.1016/j.yexcr.2017.10.010.
[65] Crappé J, Van Criekinge W, Trooskens G, Hayakawa E, Luyten W, Baggerman G, et al. Combining in silico prediction and ribosome profiling in a genome-wide search for novel putatively coding sORFs. BMC Genomics 2013;14:648. https://doi.org/10.1186/1471-2164-14-648.
[66] Zupanic A, Meplan C, Grellscheid SN, Mathers JC, Kirkwood TBL, Hesketh JE, et al. Detecting translational regulation by change point analysis of ribosome profiling data sets. RNA 2014;20:1507–18. https://doi.org/10.1261/rna.045286.114.
[67] Artieri CG, Fraser HB. Accounting for biases in riboprofiling data indicates a major role for proline in stalling translation. Genome Res 2014;24:2011–21. https://doi.org/10.1101/gr.175893.114.
[68] Bartholomäus A, Del Campo C, Ignatova Z. Mapping the non-standardized biases of ribosome profiling. Biol Chem 2016;397:23–35. https://doi.org/10.1515/hsz-2015-0197.
[69] Stumpf CR, Moreno MV, Olshen AB, Taylor BS, Ruggero D. The translational landscape of the mammalian cell cycle. Mol Cell 2013;52:574–82. https://doi.org/10.1016/j.molcel.2013.09.018.
[70] Aramayo R, Polymenis M. Ribosome profiling the cell cycle: lessons and challenges. Curr Genet 2017;63:959–64. https://doi.org/10.1007/s00294-017-0698-3.
[71] Brubaker SW, Gauthier AE, Mills EW, Ingolia NT, Kagan JC. A bicistronic MAVS transcript highlights a class of truncated variants in antiviral immunity. Cell 2014;156:800–11. https://doi.org/10.1016/j.cell.2014.01.021.
[72] Cenik C, Cenik ES, Byeon GW, Grubert F, Candille SI, Spacek D, et al. Integrative analysis of RNA, translation, and protein levels reveals distinct regulatory variation across humans. Genome Res 2015;25:1610–21. https://doi.org/10.1101/gr.193342.115.
[73] Thoreen CC, Chantranupong L, Keys HR, Wang T, Gray NS, Sabatini DM. A unifying model for mTORC1-mediated regulation of mRNA translation. Nature 2012;485:109–13. https://doi.org/10.1038/nature11083.
[74] Hsieh AC, Liu Y, Edlind MP, Ingolia NT, Janes MR, Sher A, et al. The translational landscape of mTOR signalling steers cancer initiation and metastasis. Nature 2012;485:55–61. https://doi.org/10.1038/nature10912.
[75] Bazzini AA, Johnstone TG, Christiano R, Mackowiak SD, Obermayer B, Fleming ES, et al. Identification of small ORFs in vertebrates using ribosome footprinting and evolutionary conservation. EMBO J 2014;33:981–93. https://doi.org/10.1002/embj.201488411.
[76] Dunn JG, Foo CK, Belletier NG, Gavis ER, Weissman JS. Ribosome profiling reveals pervasive and regulated stop codon readthrough in Drosophila melanogaster. Elife 2013;2:e01179. https://doi.org/10.7554/eLife.01179.
[77] Aspden JL, Eyre-Walker YC, Phillips RJ, Amin U, Mumtaz MAS, Brocard M, et al. Extensive translation of small open reading frames revealed by poly-Ribo-Seq. Elife 2014;3:e03528. https://doi.org/10.7554/eLife.03528.
[78] Miettinen TP, Björklund M. Modified ribosome profiling reveals high abundance of ribosome protected mRNA fragments derived from 3′ untranslated regions. Nucleic Acids Res 2015;43:1019–34. https://doi.org/10.1093/nar/gku1310.
[79] Stadler M, Fire A. Wobble base-pairing slows in vivo translation elongation in metazoans. RNA 2011;17:2063–73. https://doi.org/10.1261/rna.02890211.
[80] Juntawong P, Girke T, Bazin J, Bailey-Serres J. Translational dynamics revealed by genome-wide profiling of ribosome footprints in Arabidopsis. Proc Natl Acad Sci U S A 2014;111:E203-2. https://doi.org/10.1073/pnas.1317811111.
[81] Caro F, Ahyong V, Betegon M, DeRisi JL. Genome-wide regulatory dynamics of translation in the plasmodium falciparum asexual blood stages. Elife 2014;3:568. https://doi.org/10.7554/eLife.04106.
[82] Bunnik EM, Chung D-WD, Hamilton M, Ponts N, Saraf A, Prudhomme J, et al. Polysome profiling reveals translational control of gene expression in the human malaria parasite plasmodium falciparum. Genome Biol 2013;14:R128. https://doi.org/10.1186/gb-2013-14-11-r128.
[83] Jensen BC, Ramasamy G, Vasconcelos EJR, Ingolia NT, Myler PJ, Parsons M. Extensive stage-regulation of translation revealed by ribosome profiling of Trypanosoma brucei. BMC Genomics 2014;15:911. https://doi.org/10.1186/1471-2164-15-911.
[84] Vasquez J-J, Hon C-C, Vanselow JT, Schlosser A, Siegel TN. Comparative ribosome profiling reveals extensive translational complexity in different Trypanosoma brucei life cycle stages. Nucleic Acids Res 2014;42:3623–37. https://doi.org/10.1093/nar/gkt1386.
[85] Clayton CE. Life without transcriptional control? From fly to man and back again. EMBO J 2002;21:1881–8. https://doi.org/10.1093/emboj/21.8.1881.
[86] Stern-Ginossar N, Ingolia NT. Ribosome profiling as a tool to decipher viral complexity. Annu Rev Virol 2015;2:335–49. https://doi.org/10.1146/annurev-virology-100114-054854.
[87] Khong A, Bonderoff JM, Spriggs RV, Tammpere E, Kerr CH, Jackson TJ, et al. Temporal regulation of distinct internal ribosome entry sites of the dicistroviridae cricket paralysis virus. Virus 2016;8:25. https://doi.org/10.3390/v8010025.
[88] Bercovich-Kinori A, Tai J, Gelbart IA, Shitrit A, Ben-Moshe S, Drori Y, et al. A systematic view on influenza induced host shutoff. Elife 2016;5:600. https://doi.org/10.7554/eLife.18311.
[89] Gao X, Wan J, Liu B, Ma M, Shen B, Qian S-B. Quantitative profiling of initiating ribosomes in vivo. Nat Methods 2015;12:147–53. https://doi.org/10.1038/nmeth.3208.
[90] Nakahigashi K, Takai Y, Kimura M, Abe N, Nakayashiki T, Shiwa Y, et al. Comprehensive identification of translation start sites by tetracycline-inhibited ribosome profiling. DNA Res 2016;23:193–201. https://doi.org/10.1093/dnares/dsw008.
[91] Rooijers K, Loayza-Puch F, Nijtmans LG, Agami R. Ribosome profiling reveals features of normal and disease-associated mitochondrial translation. Nat Commun 2013;4:2886. https://doi.org/10.1038/ncomms3886.
[92] Zoschke R, Watkins KP, Barkan A. A rapid ribosome profiling method elucidates chloroplast ribosome behavior in vivo. Plant Cell 2013;25:2265–75. https://doi.org/10.1105/tpc.113.111567.
[93] Chotewutmontri P, Barkan A. Dynamics of chloroplast translation during chloroplast differentiation in maize. PLoS Genet 2016;12:e1006106. https://doi.org/10.1371/journal.pgen.1006106.
[94] Couvillion MT, Churchman LS. Mitochondrial ribosome (Mitoribosome) profiling for monitoring mitochondrial translation in vivo. Curr Protoc Mol Biol 2017;119:4.28.1–4.28.25. https://doi.org/10.1002/cpmb.41.
[95] Williams CC, Jan CH, Weissman JS. Targeting and plasticity of mitochondrial proteins revealed by proximity-specific ribosome profiling. Science 2014;346:748–51. https://doi.org/10.1126/science.1257522.
[96] Sotelo-Silveira JR, Holt CE. Introduction to the special issue on local protein synthesis in axons. Dev Neurobiol 2014;74:207–9. https://doi.org/10.1002/dneu.22163.
[97] Sotelo-Silveira JR, Calliari A, Kun A, Koenig E, Sotelo JR. RNA trafficking in axons. Traffic 2006;7:508–15. https://doi.org/10.1111/j.1600-0854.2006.00405.x.

[98] Calliari A, Farías J, Puppo A, Canclini L, Mercer JA, Munroe D, et al. Myosin Va associates with mRNA in ribonucleoprotein particles present in myelinated peripheral axons and in the central nervous system. Dev Neurobiol 2014;74:382–96. https://doi.org/10.1002/dneu.22155.
[99] Shigeoka T, Jung H, Jung J, Turner-Bridger B, Ohk J, Lin JQ, et al. Dynamic axonal translation in developing and mature visual circuits. Cell 2016;166:181–92. https://doi.org/10.1016/j.cell.2016.05.029.
[100] Hornstein N, Torres D, Sharma Das S, Tang G, Canoll P, Sims PA. Ligation-free ribosome profiling of cell type-specific translation in the brain. Genome Biol 2016;17:149. https://doi.org/10.1186/s13059-016-1005-1.
[101] Chung BY, Hardcastle TJ, Jones JD, Irigoyen N, Firth AE, Baulcombe DC, et al. The use of duplex-specific nuclease in ribosome profiling and a user-friendly software package for Ribo-seq data analysis. RNA 2015;21:1731–45. https://doi.org/10.1261/rna.052548.115.
[102] Popa A, Lebrigand K, Paquet A, Nottet N, Robbe-Sermesant K, Waldmann R, et al. RiboProfiling: a bioconductor package for standard Ribo-seq pipeline processing. F1000Res 2016;5:1309. https://doi.org/10.12688/f1000research.8964.1.
[103] Michel AM, Mullan JPA, Velayudhan V, O'Connor PBF, Donohue CA, Baranov PV. RiboGalaxy: a browser based platform for the alignment, analysis and visualization of ribosome profiling data. RNA Biol 2016;13:316–9. https://doi.org/10.1080/15476286.2016.1141862.
[104] Dunn JG, Weissman JS. Plastid: nucleotide-resolution analysis of next-generation sequencing and genomics data. BMC Genomics 2016;17:958. https://doi.org/10.1186/s12864-016-3278-x.
[105] Wang H, McManus J, Kingsford C. Isoform-level ribosome occupancy estimation guided by transcript abundance with Ribomap. Bioinformatics 2016;32:1880–2. https://doi.org/10.1093/bioinformatics/btw085.
[106] Calviello L, Mukherjee N, Wyler E, Zauber H, Hirsekorn A, Selbach M, et al. Detecting actively translated open reading frames in ribosome profiling data. Nat Methods 2016;13:165–70. https://doi.org/10.1038/nmeth.3688.
[107] Ji Z, Song R, Huang H, Regev A, Struhl K. Transcriptome-scale RNase-footprinting of RNA-protein complexes. Nat Biotechnol 2016;34:410–3. https://doi.org/10.1038/nbt.3441.
[108] Larsson O, Sonenberg N, Nadon R. anota: analysis of differential translation in genome-wide studies. Bioinformatics 2011;27:1440–1. https://doi.org/10.1093/bioinformatics/btr146.
[109] Zhong Y, Karaletsos T, Drewe P, Sreedharan VT, Kuo D, Singh K, et al. RiboDiff: detecting changes of mRNA translation efficiency from ribosome footprints. Bioinformatics 2017;33:139–41. https://doi.org/10.1093/bioinformatics/btw585.
[110] Xiao Z, Zou Q, Liu Y, Yang X. Genome-wide assessment of differential translations with ribosome profiling data. Nat Commun 2016;7:11194. https://doi.org/10.1038/ncomms11194.
[111] Legendre R, Baudin-Baillieu A, Hatin I, Namy O. RiboTools: a galaxy toolbox for qualitative ribosome profiling analysis. Bioinformatics 2015;31:2586–8. https://doi.org/10.1093/bioinformatics/btv174.
[112] Crappé J, Ndah E, Koch A, Steyaert S, Gawron D, De Keulenaer S, et al. PROTEOFORMER: deep proteome coverage through ribosome profiling and MS integration. Nucleic Acids Res 2015;43:e29-. https://doi.org/10.1093/nar/gku1283.
[113] Fields AP, Rodriguez EH, Jovanovic M, Stern-Ginossar N, Haas BJ, Mertins P, et al. A regression-based analysis of ribosome-profiling data reveals a conserved complexity to mammalian translation. Mol Cell 2015;60:816–27. https://doi.org/10.1016/j.molcel.2015.11.013.
[114] Tebaldi T, Dassi E, Kostoska G, Viero G, Quattrone A. tRanslatome: an R/Bioconductor package to portray translational control. Bioinformatics 2014;30:289–91. https://doi.org/10.1093/bioinformatics/btt634.
[115] Liu W, Xiang L, Zheng T, Jin J, Zhang G. TranslatomeDB: a comprehensive database and cloud-based analysis platform for translatome sequencing data. Nucleic Acids Res 2018;46:D206–12. https://doi.org/10.1093/nar/gkx1034.
[116] H Backman TW, Girke T. systemPipeR: NGS workflow and report generation environment. BMC Bioinf 2016;17:388. https://doi.org/10.1186/s12859-016-1241-0.

PDCD4, un regulador de la traducción con posibles funciones neuronales

Pocos reguladores traduccionales proteicos nuevos han sido descritos en la literatura recientemente, en particular en modelos neuronales. En este sentido, nuestro laboratorio ha explorado la presencia y el rol de la proteína PDCD4, capaz de regular la traducción, en modelos neuronales *in vitro* e *in vivo*. Estos antecedentes, junto con resultados previos obtenidos por el grupo (ver más adelante), sugieren para PDCD4 un posible rol neuronal.

PDCD4 fue identificado inicialmente como un gen cuya expresión aumentaba durante la apoptosis [30]. Estudios posteriores mostraron que se trata de un gen supresor de tumores involucrado en la regulación de la transcripción y traducción de ARNm, en las vías de transducción de señales celulares y en la apoptosis, entre otros [31]. El gen de PDCD4 codifica para una proteína de 470 aminoácidos [30], muy conservada en vertebrados [31] y de expresión ubicua en los tejidos [32]. Dicha proteína consta de tres dominios, uno amino-terminal de unión al ARN y dos dominios MA-3 de interacción proteína-proteína: uno central (MA-3m) y otro carboxilo-terminal (MA-3c) [31]. A nivel de secuencia, la proteína cuenta con varios sitios plausibles de fosforilación que regulan su actividad, localización subcelular y degradación mediada por el proteasoma [31,33]. El ARNm que codifica para PDCD4 cuenta también con sitios blanco de micro ARN, los cuales regulan su traducción en condiciones fisiológicas alteradas. El caso más estudiado es el del miRNA-21, quien inhibe la traducción de PDCD4 en diversos tipos tumorales [34–37].

Respecto de las funciones a cargo de PDCD4, se ha descrito que interviene en la transformación neoplásica donde se manifiesta como gen supresor de tumores, regulando negativamente la proliferación celular, invasión celular, el crecimiento tumoral y la sobrevida celular luego de daño al ADN [31]. Estas funciones implican el control a nivel transcripcional y traduccional de la expresión génica por parte de PDCD4. A nivel transcripcional se ha visto que PDCD4 regula la actividad de varios factores de transcripción al unirlos de forma directa. Algunos ejemplos son: c-Jun [38,39], sp1 [40], Twist1 [41] y p53 [42]. A nivel traduccional, mediante interacciones ARN-proteína PDCD4 es capaz de reconocer estructuras secundarias en los 5'-UTR de sus ARNm blancos y de esta manera ejercer un control de forma específica [43]. También se ha observado que mediante interacciones proteína-proteína PDCD4 se une tanto con los factores de iniciación eucariotas eIF4A y eIF4G, así como con proteínas que se encuentran en el complejo de iniciación 40S y complejo de preiniciación 43S [44,45]. En condiciones normales, eIF4G une eIF4A e interacciones adicionales activan este último factor para que manifieste su actividad de ARN helicasa, la cual le permite resolver estructuras secundarias presentes en los 5'-UTR y que inhiben la traducción de los ARNm. PDCD4 compite con eIF4G y con el ARNm por la unión a eIF4A [46]. Cuando PDCD4 logra unir a

eIF4A, lo hace de manera estable y bloquea el sitio de unión al ARN de eIF4A, estabilizando una conformación abierta inactiva del complejo de iniciación [43]. De esta forma, la interacción de PDCD4 con eIF4A inhibe su actividad helicasa, lo cual en consecuencia inhibe de forma directa la traducción cap-dependiente de ciertos mensajeros que aún no se conocen con detalle (ver Figura II.1). También ha sido descrito un posible mecanismo por el cual PDCD4 es capaz de inhibir la traducción de ARNm de manera independiente del factor eIF4A [47,48]. Los mensajeros cuya traducción es inhibida por PDCD4, son los que por tanto se denominan blancos traduccionales.

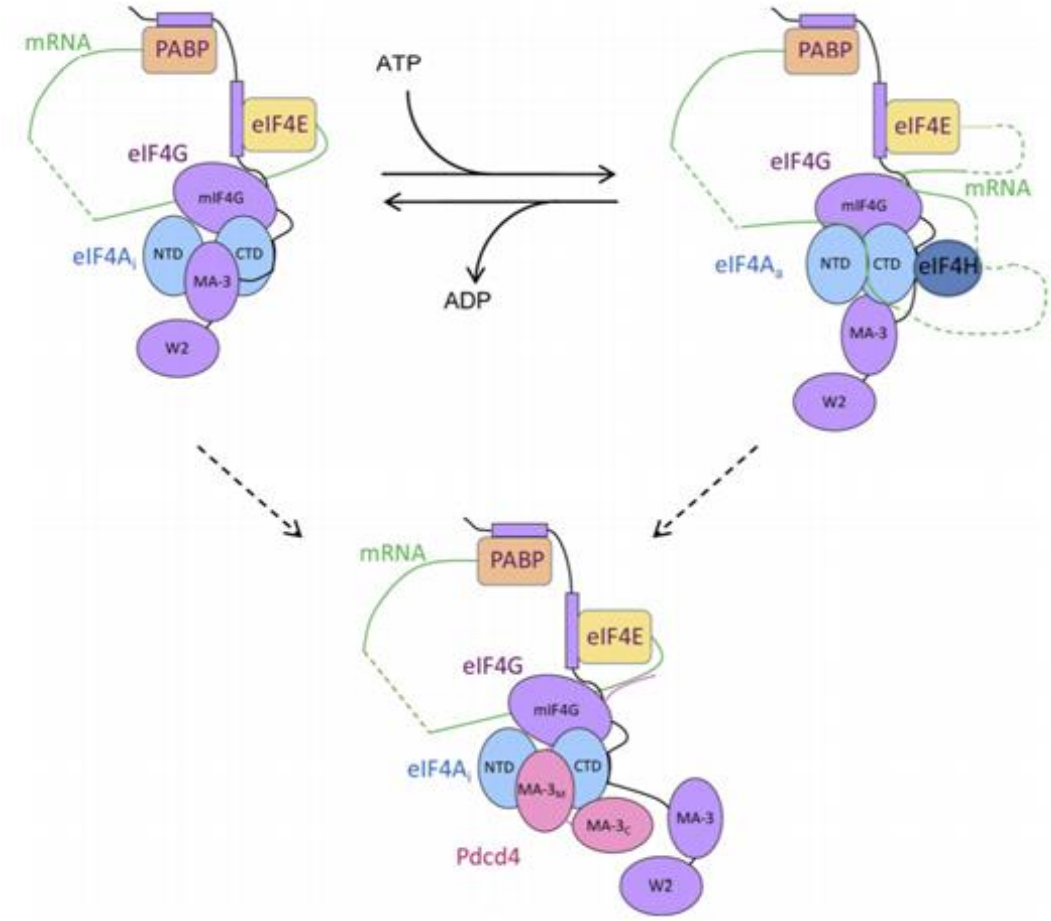

Figura II.1. Modelo molecular planteado para ilustrar la interferencia de PDCD4 con el complejo de preiniciación. El esquema muestra en la parte superior el correcto acople del factor eIF4H al complejo de preiniciación asociado al consumo de ATP. En la parte inferior se muestra la interacción de PDCD4 con eIF4A que desplaza a eIF4G de su posición y determina por tanto la inhibición de la actividad helicasa del factor 4A. Figura adaptada de Waters et al J Biol Chem (2011).

Nuestro grupo ha trabajado en la caracterización del rol de PDCD4 en diversos modelos neuronales. Hemos descrito la expresión de este factor tanto en sistema nervioso central como periférico mediante técnicas como microscopía confocal y RT-PCR [49] así como hemos explorado posibles blancos traduccionales en modelos neuronales *in vitro* utilizando Ribo-Seq [50]. De esta manera, comprender en detalle el rol de PDCD4 en modelos neuronales, así como evidenciar y describir sus posibles blancos traduccionales en dichos modelos son aspectos de interés para nuestro laboratorio.

Regulación de la traducción en enfermedades neurodegenerativas

El control de la expresión génica mediante la regulación de los niveles traduccionales, independientemente de su modulación por factores proteicos, puede representar un aspecto relevante en el desarrollo de neuropatologías. A modo de ejemplo, algunos de los procesos neuronales donde el control traduccional es de particular importancia son: los procesos de generación de memoria y consolidación por LTP o LDP [51–56], desórdenes genéticos hereditarios que determinan retardo mental como el síndrome de X frágil [57–61], neuropatologías y desórdenes neurodegenerativos como el mal de Parkinson [62,63] y el mal de Alzheimer, en el cual nos enfocaremos en adelante.

El mal de Alzheimer es una enfermedad neurodegenerativa que afecta al cerebro y representa la mayor proporción de los casos de demencia a nivel mundial [64]. Aunque sus causas no son completamente entendidas, salvo casos de inicio temprano con mutaciones específicas [65], la enfermedad está muy bien descrita histopatológicamente. El análisis post mortem de cerebros de pacientes enfermos revela claramente pérdida de masa cerebral y de contactos sinápticos, así como la presencia de placas amiloides y acúmulos de la proteína TAU hiperfosforilada [66,67]. Mientras los acúmulos de TAU hiperfosforilada se observan a nivel intracelular, las placas amiloides se observan principalmente a nivel extracelular y son el resultado de la acumulación del péptido beta amiloide (Aβ), producido por el inapropiado clivaje de la proteína APP [68,69].

A pesar de la gran cantidad de estudios de asociación genética y de expresión génica que han sido realizados en distintos modelos de la enfermedad de Alzheimer, pocos han centrado su atención en la regulación a nivel traduccional. A su vez, recientemente tanto el péptido Aβ como la proteína TAU, los dos factores fundamentales de la enfermedad, han sido vinculados con el proceso de síntesis proteica. Por ejemplo, se ha descrito la regulación de eventos de síntesis proteica local en sinaptosomas obtenidos a partir de cerebros de modelos murinos transgénicos de la enfermedad que sobreexpresan APP [23]. También se ha visto que la

presencia de oligómeros de Aβ inducen la síntesis *de novo* de TAU [70], que TAU es capaz de interaccionar con el ribosoma *in vitro* [71] y que la síntesis de proteínas ribosomales puede verse inhibida en modelos transgénicos que sobreexpresan TAU [72]. Al mismo tiempo, se ha descrito un mecanismo de señalización iniciado por el péptido Aβ que regula la actividad del complejo mTOR [73,74], quien cumple un rol fundamental en el control de la traducción [75].

Considerando toda esta evidencia previa, nos resulta interesante explorar posibles eventos de regulación traduccional en modelos de la enfermedad de Alzheimer extendiendo el uso de metodologías ómicas para el estudio de la traducción a nuevos modelos neuronales con una clara relevancia en salud.

III. HIPÓTESIS DE TRABAJO Y OBJETIVOS

La hipótesis de trabajo en la cual se basa la presente tesis es que los mecanismos de regulación traduccional son importantes para modular procesos celulares en las neuronas. Los mecanismos de regulación traduccional pueden estar asociados a factores proteicos reguladores como PDCD4 y/o pueden estar involucrados en neuropatologías complejas como el mal de Alzheimer.

De esta manera, el principal objetivo de la presente tesis es contribuir a comprender mecanismos y eventos de regulación traduccional en células neuronales utilizando estrategias experimentales y bioinformáticas que permitan observar la traducción a nivel global.

En este contexto, la presente tesis doctoral se encuentra dividida en tres grandes capítulos donde los siguientes objetivos específicos serán abordados y discutidos:

1. Investigar el rol que ejerce PDCD4 en la regulación traduccional y determinar sus ARNm blancos en neuronas obtenidas por diferenciación de células PC12.
2. Optimización de Ribo-Seq en modelos neuronales *in vitro* de células primarias y tejido nervioso animal *in vivo*.
3. Explorar la regulación traduccional en modelos transgénicos de la enfermedad de Alzheimer.

En cada caso, luego de una breve introducción en cada capítulo plantearemos una hipótesis de trabajo específica, dentro del marco de la hipótesis de trabajo aquí planteada, a ser contrastada y evaluada mediante los objetivos específicos arriba mencionados.

IV. CAPÍTULO 1

BÚSQUEDA DE ARNm BLANCOS TRADUCCIONALES DE PDCD4 MEDIANTE RIBO-SEQ EN NEURONAS OBTENIDAS POR DIFERENCIACIÓN DE CÉLULAS PC12

Uno de los primeros desafíos que abordamos en la presente tesis fue culminar los experimentos iniciados durante mi tesis de Maestría relacionados a entender el posible rol de PDCD4 en modelos neuronales, así como la búsqueda de sus blancos traduccionales en dichos modelos. En este sentido, la hipótesis de trabajo que nos planteamos fue que PDCD4 es capaz de regular la traducción de un conjunto de ARNm blancos en modelos celulares neuronales. Para verificar o rechazar esta hipótesis utilizamos la línea celular PC12, capaz de diferenciar a un tipo neuronal bajo exposición a NGF. Durante mi etapa previa de maestría y mediante transfección de vectores lentivirales, generamos una variante capaz de silenciar de manera específica e inducible la expresión de PDCD4. Utilizando este modelo, aplicamos las técnicas de RNA-Seq y Ribo-Seq para estudiar eventos de regulación traduccional influenciados por la presencia/ausencia de PDCD4. En la presente tesis realizamos nuevos experimentos de transfección y secuenciación masiva para aumentar la cantidad de réplicas biológicas y junto con los datos previamente producidos, realizamos el análisis correspondiente para determinar los blancos traduccionales de PDCD4 en el modelo de trabajo tipo neuronal.

De esta manera pudimos estudiar con validez estadística los eventos de regulación traduccional, comparando los niveles de eficiencia traduccional entre ambas condiciones. Así, definimos una lista de ARNm posibles blancos traduccionales de PDCD4 como aquellos genes cuya eficiencia traduccional aumenta con un p-valor asociado <0.05, en ausencia de PDCD4 respecto del control (presencia de PDCD4). Esta lista de 267 ARNm es el primer reporte de blancos traduccionales de PDCD4 en modelos neuronales estudiado mediante aproximaciones ómicas. Anteriormente ha sido publicado el reporte de 62 ARNm blancos de PDCD4, también determinados por Ribo-Seq, en un modelo celular inmortal de células epiteliales [76]. Probablemente por lo alejado que se encuentra este modelo del modelo celular neuronal, no comparten casi ningún ARNm.

A partir de la lista de blancos traduccionales encontrada, realizamos distintos tipos de análisis que revelaron la presencia de una firma génica asociada al crecimiento neurítico o crecimiento axonal, firma que describimos en detalle y reportamos. Realizamos también confirmaciones de algunos de los blancos traduccionales más relevantes encontrados, ya sea por cuantificación relativa de ARNm en fracciones de un gradiente polisomal, o por cuantificación

proteica mediante Western blot. Previamente habíamos observado que el crecimiento neurítico en células PC12 diferenciadas a neuronas se encuentra aumentado en ausencia de PDCD4. Estos resultados y observaciones están en línea con otros resultados de nuestro grupo que también mostraban el mismo control negativo sobre el crecimiento neurítico y axonal en cultivos primarios de neuronas corticales y del ganglio de la raíz dorsal.

De esta manera, gran parte de los resultados obtenidos durante esta etapa, junto con los resultados obtenidos por Andrés Di Paolo durante su tesis de posgrado mencionados anteriormente, formaron parte de una publicación en conjunto en la cual compartimos primer autoría (ver trabajo publicado II a continuación). Los resultados obtenidos correspondientes a este capítulo y no incluidos en la publicación son presentados y discutidos más adelante.

Trabajo publicado II: PDCD4 regulates axonal growth by translational repression of neurite growth-related genes and is modulated during nerve injury responses

Se adjunta a continuación el manuscrito publicado junto con su material suplementario.

Por razones de tamaño y espacio las tablas suplementarias no fueron incluidas. Las mismas pueden encontrarse en el siguiente enlace:

https://rnajournal.cshlp.org/content/26/11/1637/suppl/DC1.

PDCD4 regulates axonal growth by translational repression of neurite growth-related genes and is modulated during nerve injury responses

ANDRÉS DI PAOLO,[1,9] GUILLERMO EASTMAN,[2,9] RAQUEL MESQUITA-RIBEIRO,[3] JOAQUINA FARIAS,[2] ANDREW MACKLIN,[4] THOMAS KISLINGER,[4,5] NANCY COLBURN,[6,10] DAVID MUNROE,[7,10] JOSÉ R. SOTELO SOSA,[1] FEDERICO DAJAS-BAILADOR,[3] and JOSÉ R. SOTELO-SILVEIRA[2,8]

[1]Departamento de Proteínas y Ácidos Nucleicos, Instituto de Investigaciones Biológicas Clemente Estable, Montevideo 11600, Uruguay
[2]Departamento de Genómica, Instituto de Investigaciones Biológicas Clemente Estable, Montevideo 11600, Uruguay
[3]School of Life Sciences, University of Nottingham, Nottingham NG7 2UH, United Kingdom
[4]Princess Margaret Cancer Centre, University Health Network, Toronto M5G 1L7, Canada
[5]University of Toronto, Department of Medical Biophysics, Toronto M5S 1A1, Canada
[6]Former Chief of Laboratory of Cancer Prevention at the National Cancer Institute-NIH at Frederick, Maryland 21702, USA
[7]Former Laboratory of Molecular Technologies, LEIDOS at Frederick National Laboratory for Cancer Research, Frederick, Maryland 21702, USA
[8]Departamento de Biología Celular y Molecular, Facultad de Ciencias UdelaR, Montevideo 11400, Uruguay

ABSTRACT

Programmed cell death 4 (PDCD4) protein is a tumor suppressor that inhibits translation through the mTOR-dependent initiation factor EIF4A, but its functional role and mRNA targets in neurons remain largely unknown. Our work identified that PDCD4 is highly expressed in axons and dendrites of CNS and PNS neurons. Using loss- and gain-of-function experiments in cortical and dorsal root ganglia primary neurons, we demonstrated the capacity of PDCD4 to negatively control axonal growth. To explore PDCD4 transcriptome and translatome targets, we used Ribo-seq and uncovered a list of potential targets with known functions as axon/neurite outgrowth regulators. In addition, we observed that PDCD4 can be locally synthesized in adult axons in vivo, and its levels decrease at the site of peripheral nerve injury and before nerve regeneration. Overall, our findings demonstrate that PDCD4 can act as a new regulator of axonal growth via the selective control of translation, providing a target mechanism for axon regeneration and neuronal plasticity processes in neurons.

Keywords: programmed cell death 4 (PDCD4); axonal growth; axonal regeneration; translation; ribosome profiling

INTRODUCTION

The tumor suppressor programmed cell death 4 (PDCD4) protein was first described in cancer studies and has been shown to regulate protein synthesis by inhibition of EIF4A helicase activity (Yang et al. 2003; Suzuki et al. 2008; Matsuhashi et al. 2019) and via interaction with specific RNA motives present in a particular subset of target mRNAs (Loh et al. 2009; Wedeken et al. 2011; Biyanee et al. 2015). In mitogen stimulated cells, the degradation of PDCD4 is necessary for efficient protein translation, which is a prerequisite for cell growth and proliferation (Dorrello et al. 2006; Schmid et al. 2008). At present, while numerous molecules have been shown to regulate PDCD4, including *p21* (Göke et al. 2004), *Cdk4* (Jansen et al. 2005), and *JNK/c-Jun/AP-1* (Yang et al. 2003, 2006; Bitomsky et al. 2004), there is also a growing list of PDCD4 translational targets, including C-MYB, P53, SIN1, and BDNF (Singh et al. 2011; Wedeken et al. 2011; Wang et al. 2017; Li et al. 2020), together with internal ribosome entry site-regulated apoptosis inhibitors (Liwak et al. 2012). Although misregulation of PDCD4 in a variety of tumors (Zhang et al. 2006; Gao et al. 2007; Mudduluru et al. 2007; Zhen et al. 2016) suggests an important role in cancer development (Zhang et al. 2006; Gao et al. 2007; Mudduluru et al. 2007; Zhen et al. 2016), the full scope of PDCD4 translational targets and its potential role in other growth-dependent cellular

[9]These authors contributed equally to this work.
[10]Deceased.

Corresponding authors: f.dajas-bailador@nottingham.ac.uk, jsotelosilveira@iibce.edu.uy or sotelojos@gmail.com

Article is online at http://www.rnajournal.org/cgi/doi/10.1261/rna.075424.120. Freely available online through the *RNA* Open Access option.

systems has only recently started to be elucidated (Haas et al. 2020). In this regard, the molecular pathways involved in the development of tumor cells share a significant overlap with axonal growth and regeneration processes in the nervous system, particularly in the context of protein synthesis regulation (Chédotal et al. 2005; Heine et al. 2015).

The highly polarized nature that defines the morphology of a neuron makes local protein synthesis in the different cellular compartments (soma, dendrites and axons) an essential need for their development and function, being also important for plasticity and regenerative processes in the adult (Verma et al. 2005; Jiménez-Díaz et al. 2008; Huebner and Strittmatter 2009; Gumy et al. 2010; Park et al. 2010; Jung et al. 2011; Deglincerti and Jaffrey 2012; Kar et al. 2013; Obara and Hunt 2014; Sotelo-Silveira and Holt 2014; Ohtake et al. 2015; Terenzio et al. 2018). The acceptance of local protein translation as a key molecular mechanism in neuronal function has prompted the development of a variety of experimental models and omics approaches to investigate the specific axonal transcriptomes and proteomes (for review, see Farias et al. 2020). In this context, the elucidation of the regulatory pathways that can control the selective translation of axonal mRNAs has become an essential step in the understanding of neuronal development, growth and activity (Swanger and Bassell 2011; Jung et al. 2012). Among the various molecular mechanisms reported so far (Lin and Holt 2008; Holt et al. 2019), the mammalian target of rapamycin (mTOR) complex is described as a master regulator of local axonal translation and an important signaling process in axonal regeneration (Verma et al. 2005; Park et al. 2008; Terenzio et al. 2018), while also being affected in many different tumor types (Murray and Tee 2018). Interestingly, although PDCD4 protein has been described as an important downstream component of the mTOR pathway, it has not been directly associated with axonal processes. So far, the function of PDCD4 in the CNS has been linked to fetal alcohol syndrome, where it regulates general protein synthesis in cortical neurons (Narasimhan et al. 2013; Riar et al. 2014) and depression-like behaviors via BDNF regulation (Li et al. 2020). In spinal cord injury, PDCD4 has been shown to be down-regulated by microRNA-21 (Jiang et al. 2017) reinforcing the view of its potential role in neuronal mechanisms.

Considering the reported overlap in the molecular processes that promote both tumor and axon growth (Chédotal et al. 2005; Duman-Scheel 2009; Frank and Tsai 2009; Heine et al. 2015), we decided to investigate the potential role of PDCD4 in axonal function and regeneration. We hypothesized that as a repressor of translation, PDCD4 could be regulating mRNAs involved in axonal growth, regeneration and/or local protein synthesis and that its expression would be tightly regulated during these processes. Our study demonstrates how the manipulation of PDCD4 levels in central and peripheral nervous system neurons can control axonal growth, suggesting a potentially key role in axon regeneration in vivo. As a way to identify putative mRNAs regulated by PDCD4, we used ribosome profiling (Ribo-seq) to explore the translational effects of PDCD4 at a genome-wide level. We detected more than 250 possible mRNA candidates whose translational efficiency (TE) levels increase in the absence of PDCD4. Among them, we have identified a specific group of genes reported to be relevant in neurite/axonal development and regeneration. Overall, our findings demonstrate that PDCD4 can act as a new regulator of axonal growth via the selective control of translational targets, providing a specific mechanism for axon regeneration and neuronal plasticity processes in neurons.

RESULTS

Localization of PDCD4 in the nervous system

To address the role of PDCD4 in neuronal cells, we first investigated its localization across different neuronal types. As shown in Figure 1A, we could detect PDCD4 protein in the central nervous system (CNS) of adult rats, both in cell bodies and neurites of CA1 hippocampal, Purkinje and cortical neurons. PDCD4 is also present in adult axons of the peripheral nervous system (PNS), as demonstrated following the analysis of its distribution in rat sciatic nerves, where specific axon detection can be more easily assessed. Crucially, this experimental approach allowed us to precisely detect high levels of PDCD4 inside the axoplasmic region of both longitudinal and transversal nerve cryosections (Fig. 1B).

Previous work in cancer cells demonstrated that both the translation and activity of PDCD4 can be regulated via the mTOR-p70S6K pathway (Dorrello et al. 2006), prompting us to investigate the potential link between PDCD4 and its upstream regulator p70S6K. As shown in Figure 1C, both PDCD4 and phosphorylated (active) p70S6K-Thr-389 are present in longitudinal sections of ventral root axons, evidence that the activated mTOR pathway colocalizes with PDCD4 in the axoplasm of peripheral neurons.

Regulation of PDCD4 levels in primary neurons can control axonal growth

Following the demonstration of PDCD4 expression in CNS and PNS neurons, we decided to explore its functional role using neuronal in vitro models. First, we used primary cortical neurons isolated from embryonic mice. These cells can fully differentiate in culture to develop a morphologically intricate and functionally connected neuronal network after 10–12 d in vitro (Cotterill et al. 2016; Banker 2018). Following this period, axonal growth is decreased to allow the synaptic maturation that leads to the establishment of a

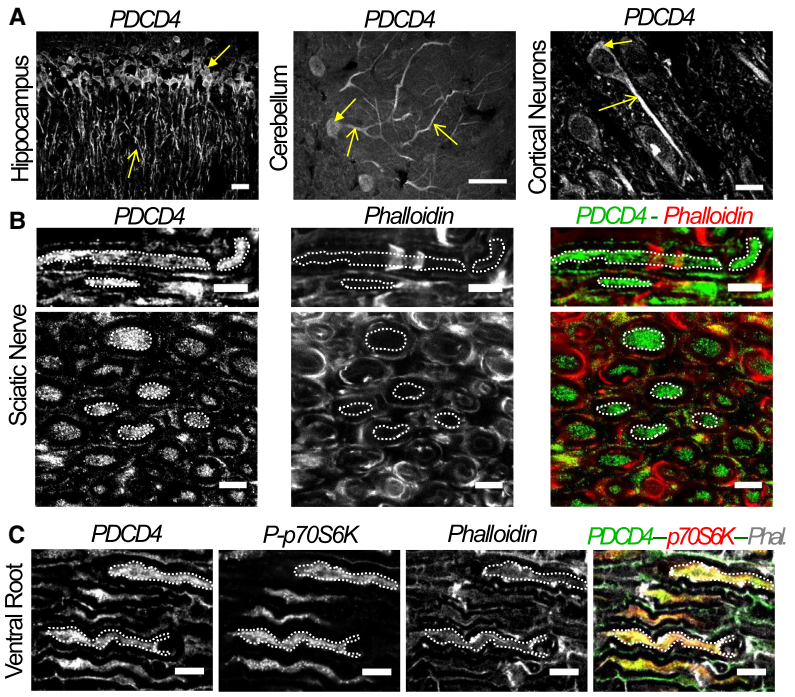

FIGURE 1. PDCD4 is expressed in dendrites and axons of the central and peripheral nervous system. (*A*) Immunohistochemistry assays show the distribution of PDCD4 protein at different types of neurons including CA1 hippocampal neurons, Purkinje of cerebellum and cortical neurons of prefrontal cortex of adult rats. Cell bodies are indicated by filled arrows and axons (or dendrite for Purkinje neurons) by unfilled arrows (scale bar, 20 µm). (*B*) PDCD4 protein is also detected in peripheral axons, like sciatic nerves, by immunohistochemistry. The images *above* correspond to longitudinal sections and the images *below* to transversal sections. Examples of axonal regions are highlighted in white dotted ROIs (scale bar, 10 µm). (*C*) Longitudinal sections of ventral roots. Examples of axonal regions are highlighted with white dotted ROIs. A partial colocalization between PDCD4 and p70-S6K signals is detected (scale bar, 5 µm).

functional network of connected neurons, which is observed after ~2 wk in culture (Chiappalone et al. 2006).

PDCD4 protein was detected in primary cortical neurons throughout their development in culture, with levels significantly increasing in cell body and axons between days 2 and day 5, and a major increase also detected after 12 d in vitro (Fig. 2A). The observation that PDCD4 levels increase in the late stages of neuronal network development and synaptic maturation (day 5–12) supports the hypothesis that increasing levels of PDCD4 could repress axon and/or neurite growth. To test this, we investigated the effect of PDCD4 overexpression on axonal growth following transfection with a PDCD4 plasmid at day 2 (24 h after seeding), with analysis of axonal length carried out 72 h later (day 5 of cell culture). Before the functional evaluation, we confirmed that neurons transfected with PDCD4 plasmid have a significant increase in PDCD4 levels detected by immunocytochemistry (Supplemental Fig. S1A). Increased PDCD4 levels during this period of active axonal growth (days 2–5 in vitro) produced a significant reduction in axonal length (Fig. 2B). To further confirm the dynamic regulation of axonal growth based on PDCD4 levels, we showed that the siRNA-dependent knockdown of PDCD4 produced the opposite effect, with a significant increase in axonal length (Fig. 2C). To assess if this effect was also observed in peripheral neurons, we evaluated axonal growth in dorsal root ganglia (DRG) neurons cultured in compartmentalized microfluidic chambers. Addition of a cell-permeable siRNA probe targeting PDCD4 produced a significant increase in axonal growth (Fig. 2D). Importantly, we confirmed that in both cortical and DRG neurons the addition of PDCD4 siRNA led to a significant decrease in PDCD4 levels detected by immunochemistry (Supplemental Fig. S1B,C), an effect further confirmed by immunoblotting using the neuroblastoma N2a cell line, which has high transfection efficiency (Supplemental Fig. S1D). Overall, these functional studies demonstrate that PDCD4 modulates axonal growth in central and peripheral nervous system neurons.

Ribosome profiling reveals that PDCD4 regulates the translation of genes involved in axon/neurite growth

To explore the capacity of PDCD4 to regulate translation in neurons, we decided to use the ribosome profiling strategy (Ribo-seq) in differentiated PC12 neuron-like cells as a suitable and relevant model for the investigation of neuronal mechanisms (Shao et al. 2016; Zheng et al. 2016). To confirm the experimental validity of this approach, we first demonstrated the expression of PDCD4 in PC12 cells at different time points following NGF-induced neuron differentiation, with levels remaining relatively stable throughout the culture period (Supplemental Fig. S2A). Using a doxycycline inducible shRNA system, we obtained stable cell populations with inducible silencing of PDCD4 expression. In this way, addition of NGF and doxycycline for 72 h allowed us to achieve neuron differentiation of PC12 and silencing of PDCD4 expression (Supplemental Fig. S2B–G).

As a first experimental approach to the use of PC12 neuron-like cells, we analyzed if neurite growth was regulated by the presence or absence of PDCD4. Confirming our previous observations in primary neuron cultures, knockdown of PDCD4 in PC12 cells increased neurite length compared to controls (Fig. 3A,B), allowing us to validate their use in the search for putative PDCD4 translational targets. For this, we isolated polysomal and total RNA from

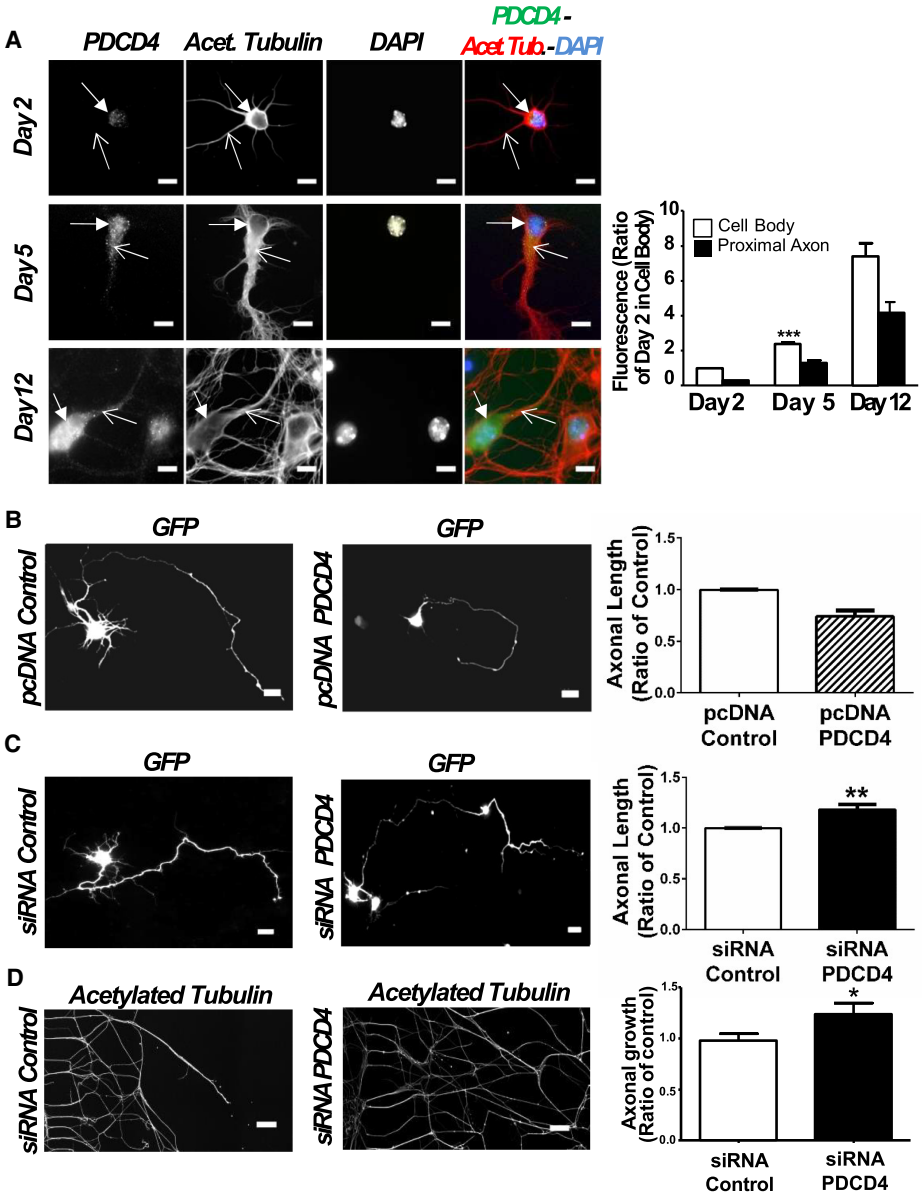

FIGURE 2. PDCD4 axonal levels change during neuron development and modulation of this protein can control axonal growth. (*A*) Immunocytochemistry assays show that PDCD4 levels increase during cortical primary neurons differentiation in vitro (scale bar, 20 µm). Cell bodies were indicated by filled arrows and axons by unfilled arrows. The signal quantification shows that cell bodies and axons have a significant increase in PDCD4 expression for day 5, and a trend to increase for day 12, always compared to day 2 ([***] $P \leq 0.001$, ANOVA test with post-Tukey, error bars: SEM, $n = 3$ independent primary cortical neuron cultures for day 2 and day 5, with three technical replicates for each independent experiment; $n = 2$ for day 12, with two technical replicates for each independent experiment). (*B*) Cotransfected cortical primary neurons with a GFP plasmid and a PDCD4 plasmid, or a GFP plasmid and a pcDNA plasmid (scale bar, 20 µm). Overexpression of PDCD4 in transfected neurons at day 5 induce a decrease in axonal length (25%) compared to control condition ([**] $P \leq 0.01$, paired test, $n = 5$ independent primary cortical neuron cultures, error bars: SEM). (*C*) Same as above but for PDCD4 knockdown using an siRNA for PDCD4 or an siRNA control (scale bar, 20 µm). Down-regulation of PDCD4 induces an increase in axonal length (18%) compared to the control condition ([**] $P \leq 0.01$, paired *t*-test, $n = 6$ independent primary cortical neuron cultures, error bars: SEM). (*D*) Immunocytochemistry assays with acetylated tubulin in peripheral DRG neurons cultured in compartmentalized chambers and transfected with a permeable siRNA for PDCD4, or with a siRNA control (scale bar, 500 µm). Quantification of axonal growth shows similar effect as above: down-regulation of PDCD4 determines an increase (24%) of axonal growth increase (* $P \leq 0.05$, Student's *t*-test, $n = 4$, error bars: SEM). In all cases, the "*n*" corresponds to independent biological replicates.

differentiated PC12 cells in the presence and absence of PDCD4. Samples were analyzed using parallel RNA-seq and Ribo-seq protocols (Supplemental Fig. S3A–C), which allowed us to determine steady-state transcriptome and translatome levels for over 10,000 mRNAs (Supplemental Table S1). Fold changes (shPDCD4/shScrambled) at both

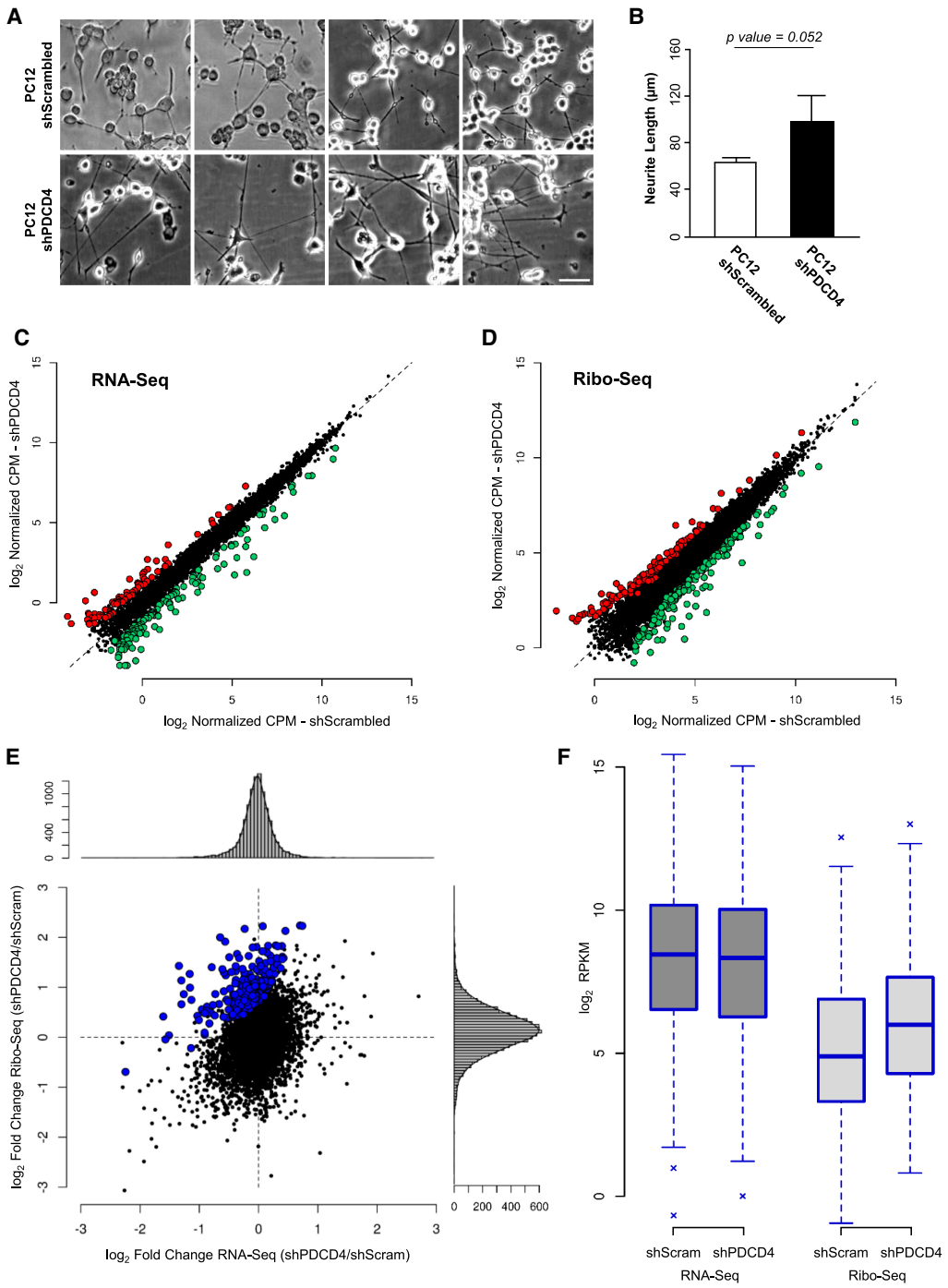

FIGURE 3. Translatome and steady-state transcriptome levels of expression for mRNAs was quantified genome-wide by Ribo-seq and RNA-seq, respectively, in absence (shPDCD4) and presence (shScrambled) of PDCD4 achieved by lentiviral transfection in neuron-like differentiated PC12 cells. (*A*) To explore if PDCD4 modulates neurite outgrowth also in differentiated PC12 cells, we compared neurite length in differentiated PC12 growing in presence and absence of PDCD4. Three independent cultures were contrasted and illustrative fields are shown (scale bar, 50 µm). (*B*) Quantification of neurite length of *A* is shown and an increase of almost 1.6× in absence of PDCD4 is detected, with a marginal trend toward significance ($P = 0.052$, Student's *t*-test, $n = 3$ independent cell cultures with an average of 80 neurites considered by replicate, error bars: SD). (*C*) Scatter plot showing PDCD4 regulation at the level of transcriptome evaluated by RNA-seq. Red and green dots indicate differentially expressed genes, up- and down-regulated, respectively (|fold change| > 2 and $P < 0.05$ estimated by *edgeR*). (*D*) Same as *C* but for PDCD4 regulation at the level of translatome evaluated by Ribo-seq. (*E*) Fold changes (shPDCD4/shScrambled) at transcriptome and translatome levels are contrasted for detected genes. Possible PDCD4 translational targets are those that present a significant increase in translational efficiency ($P <$ 0.05 estimated by *Xtail*), and are indicated in blue (267 mRNAs). Along the scatter plot, *vertical* and *horizontal* histograms show fold change values distribution estimated by Ribo-seq and RNA-seq. (*F*) RPKM gene expression levels for PDCD4 translational targets indicated in blue in *E* are shown for the two compartments (RNA-seq and Ribo-seq) in each condition.

transcriptome and translatome levels were contrasted for detected genes, and according to its previously described role (Matsuhashi et al. 2019), PDCD4-knockdown has an impact on both transcriptome and translatome compartments (Table 1; Fig. 3C,D; Supplemental Fig. S3D–G). To specifically study PDCD4 regulation in protein synthesis, we compared translation efficiency (TE) levels between conditions. TE, which is calculated as the ratio between translatome over transcriptome levels for a particular mRNA, is an informative parameter to discriminate translational regulation events from those exclusively transcriptional, and indicates how efficiently an mRNA is translated (Ingolia et al. 2009). Using the *Xtail* R package (Xiao et al. 2016) to explore TE differences, we detected 267 mRNAs whose TE levels significantly increase following PDCD4 knockdown ($P < 0.05$; Table 1; Fig. 3E,F; Supplemental Fig. S4; Supplemental Table S2), and 100 mRNAs whose TE decreases. The first group, which represents potential PDCD4 targets, displays unaltered steady-state transcriptome levels (88% has |fold change| <1.5-fold), but they increase their levels of translation (86% has fold change >1.5-fold; Fig. 3F). In order to explore if the regulation of translational efficiency was also being observed at the protein level, total protein samples obtained at the same time of the sequencing analysis were quantified by label-free proteomics. Although we observed some specific correlations with Ribo-seq data, we could only detect a small fraction of proteins changing significantly, with the sensitivity of this approach not sufficient to detect global correlations (Supplemental Fig. S5).

To investigate the functional implications of PDCD4 regulation over the 267 putative targets that increase their translational efficiency, protein association analysis was performed using STRING (Jensen et al. 2009). This revealed three to four related and altered protein cores and a network with significantly more interactions than expected (P-value = 0.0163; Supplemental Fig. S6A). The observed related protein cores within PDCD4 putative targets are grouped under *regulation of mitosis* (Moustafa-Kamal et al. 2019), *centromere and kinetochore*; *regulation of transcription and splicing* (Kim et al. 2014; see Fig. 3C; Supplemental Fig. S3D,E); *regulation of mitochondrial activity* (Zhang et al. 2006); and *protein translocation to the endoplasmic reticulum* (Hudson 2008; Wang et al. 2013). Interestingly, when analyzing the list of targets whose translational efficiency decreases in the absence of PDCD4 (100 genes), we found that neither core-related proteins nor protein interactions were significantly altered (P-value = 0.954; Supplemental Fig. S6B). This difference provides a good indication that those putative targets increasing their translation after PDCD4 knockdown represent a defined set of cellular functions, while those down-regulated in our sequencing data are likely emerging as a secondary cell effect and/or experimental noise.

TABLE 1. Number of analyzed and differentially expressed genes ($P < 0.05$) estimated by *edgeR* for transcriptome and translatome, and by *Xtail* for translational efficiency

	Analyzed genes	Up-regulated		Down-regulated	
		FC > 2	FC > 1	FC < −2	FC < −1
Transcriptome	10,946	73	999	134	1039
Translatome	9967	124	269	168	348
Translational efficiency	9931	164	267	95	100

In order to uncover those potential PDCD4 targets with functional links to neurite, axon and/or dendritic growth, we curated the list using in-house software that allowed us to link published articles with gene lists and user-defined terms (Radío S, Sotelo-Silviera JR, and Smircich P, in prep.; https://github.com/sradiouy/IdMiner). We also explored the list of differentially expressed genes separately at the transcriptome or translatome level (fold change >2 and P-value <0.05 estimated by *edgeR*), and the down-regulated genes at TE (100 genes with P-value <0.05 estimated by *Xtail*), searching for genes that might inhibit neurite outgrowth. This comprehensive approach highlighted several experimentally validated axon and/or neurite outgrowth-related genes from the list of potential PDCD4 translational targets. This signature of 36 genes was mainly composed of up-regulated genes at the level of TE in PDCD4 absence (26 genes), but also by genes up-regulated only at the translatome (four genes) or transcriptome levels (three genes), or down-regulated at TE (three genes) whose ascribed function is to inhibit neurite outgrowth. Transcriptome and translatome levels of the 36 genes show a global induction of translation after PDCD4 knockdown, from low-middle to high translational levels (Fig. 4A).

Among the signature of neurite and axon-growth-related genes, we found genes previously reported to directly control neurite outgrowth: *Elavl4*, *Styxl1*, *Bdnf*, *Dmd*, *Lancl2*, *Lif*, and *Nfkb2*. In the case of ELAVL4 (also known as HUD), DMD and LANCL1 proteins, their expression is required for neurite outgrowth in PC12 cells (Mobarak et al. 2000; Acosta et al. 2004; Fukao et al. 2009; Zhang et al. 2009), while the pseudophosphatase MK-STYX (STYXL1) increases both the number of cells with neurite extensions and neurite outgrowth in PC12 (Flowers et al. 2014). Brain-derived neurotrophic factor (BDNF) was shown to increase neurite length in rodent primary neuronal cultures (Iwasaki et al. 1998; Cohen-Cory et al. 2010; Dajas-Bailador et al. 2012), as well as in PC12 cells (Squinto et al. 1991; Iwasaki et al. 1997). On the other hand, the TE of LIF is down-regulated in PDCD4's absence, and it was shown that activating LIF receptor signaling can have a negative impact on neurite extension in PC12 cells (Ng et al. 2003). Particularly interesting is the

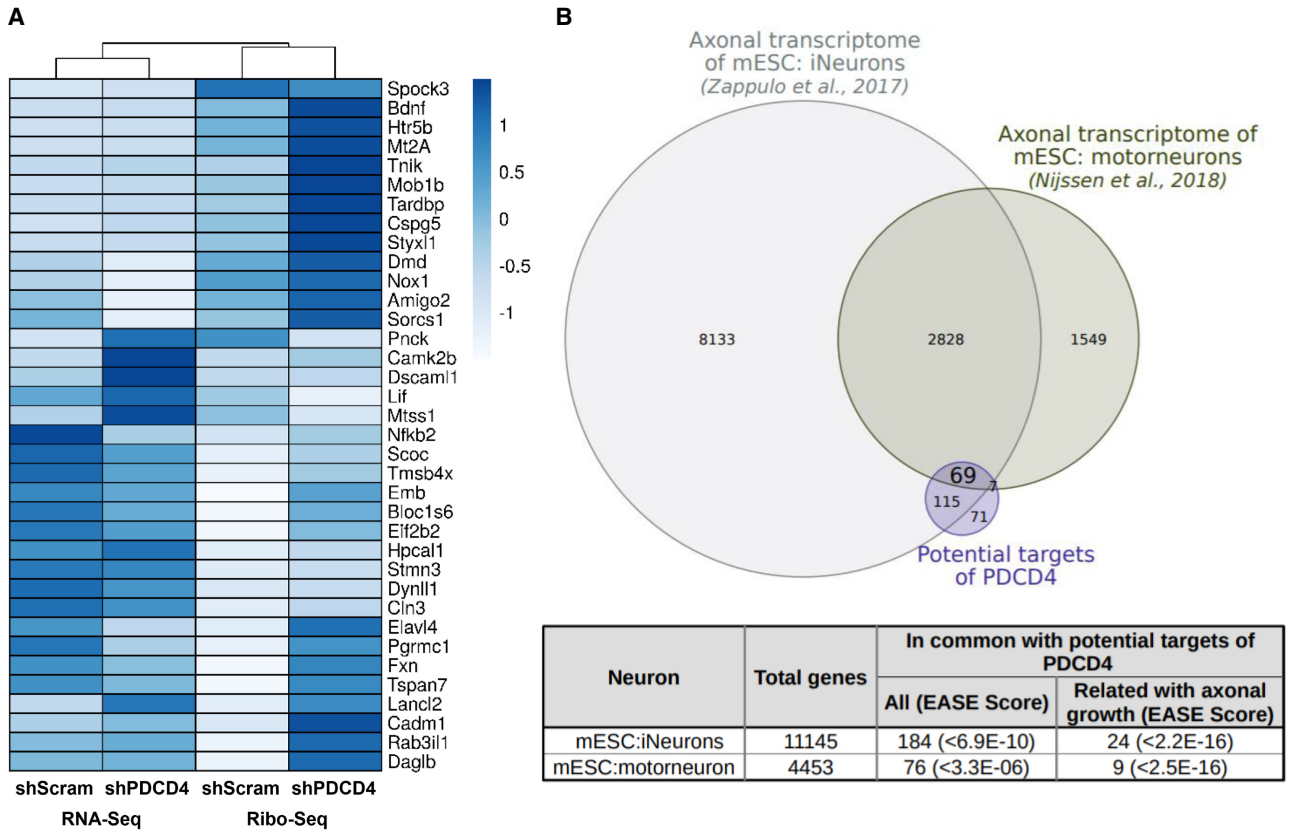

Neuron	Total genes	In common with potential targets of PDCD4	
		All (EASE Score)	Related with axonal growth (EASE Score)
mESC:iNeurons	11145	184 (<6.9E-10)	24 (<2.2E-16)
mESC:motorneuron	4453	76 (<3.3E-06)	9 (<2.5E-16)

FIGURE 4. PDCD4 regulates translation of several neurite growth-related genes evidenced by Ribo-seq and RNA-seq. The putative PDCD4 targets are present in previously described axonal transcriptomes. (*A*) Expression of neurite and axon growth-related genes is represented by a heatmap, where an induced expression at translation level is detected in the absence of PDCD4. (*B*) Venn diagram showing the intersection between the potential PDCD4 targets and axonal transcriptomes derived from mESc (Zappulo et al. 2017; Nijssen et al. 2018). Separate and overlapping expressions between samples are shown. Only transcripts with a level of expression of TPM ≥ 1 were considered. The table shows the type of neuron used in each study, the total genes detected and the number of common genes between potential PDCD4 targets (or potential PDCD4 targets related to axonal growth) and each axonal transcriptome. The EASE Score (a modified Fisher exact *P*-value) is also shown, which indicates gene enrichment.

relationship between the transcription factor complex nuclear factor-kappa-B (NFκB) and neuritogenesis, where activating the NFκB pathway and increasing *Nfkb2* gene expression promotes neuritogenesis in PC12 cells (Manecka et al. 2013). This strong link motivated us to confirm PDCD4 regulation of NFKB2 protein abundance. For this we used a model of cortical neurons in culture, silencing PDCD4 by a new set of lentiviral particles with shRNA against PDCD4, and quantifying protein abundance by western blot. By this, we confirmed by an orthogonal method that NFKB2 total protein levels increase significantly after knockdown of PDCD4 (Supplemental Fig. S7).

In line with the notion that PDCD4 can regulate axon-related mRNA translation in neurons, we found that a significant proportion of the 267 putative translational targets identified in our Ribo-seq analysis are found in two different published axonal transcriptomes from in vitro neuron models (Fig. 4B). On the other hand, those genes for which we observe a decrease in the TE after PDCD4 knockdown are not specifically enriched in axonal transcriptomes, providing further support to our hypothesis that they reflect secondary mechanisms (Supplemental Fig. S8). A significant fraction of PDCD4 mRNA translational targets were also found in the recently described in vivo motor axon transcriptome (Farias et al. 2020) (23 out of 255, in a set of 1008 mRNAs; P-value = 2.8×10^{-04}). These findings support the idea that PDCD4 could also be a player in regulating local axonal responses and plastic processes in vivo.

Sciatic nerve injury in vivo reduces local axonal levels of PDCD4

Our in vitro functional studies and ribosome profiling data support the hypothesis that PDCD4 is a novel regulator of axonal function. For this reason, we decided to test our findings in vivo, using a model of axon regeneration, a cellular process where the regulation of axonal protein

synthesis is important (Verma et al. 2005; Huebner and Strittmatter 2009; Gumy et al. 2010). For this, we performed a full transection of the rat sciatic nerve, using the contralateral nerve as a control for no injury (Fig. 5A). At 18 h post injury, when the nerve is in the active regeneration phase, we analyzed the levels of PDCD4 along the axoplasm. Our analysis demonstrates that uninjured controls show no change in the expression of PDCD4

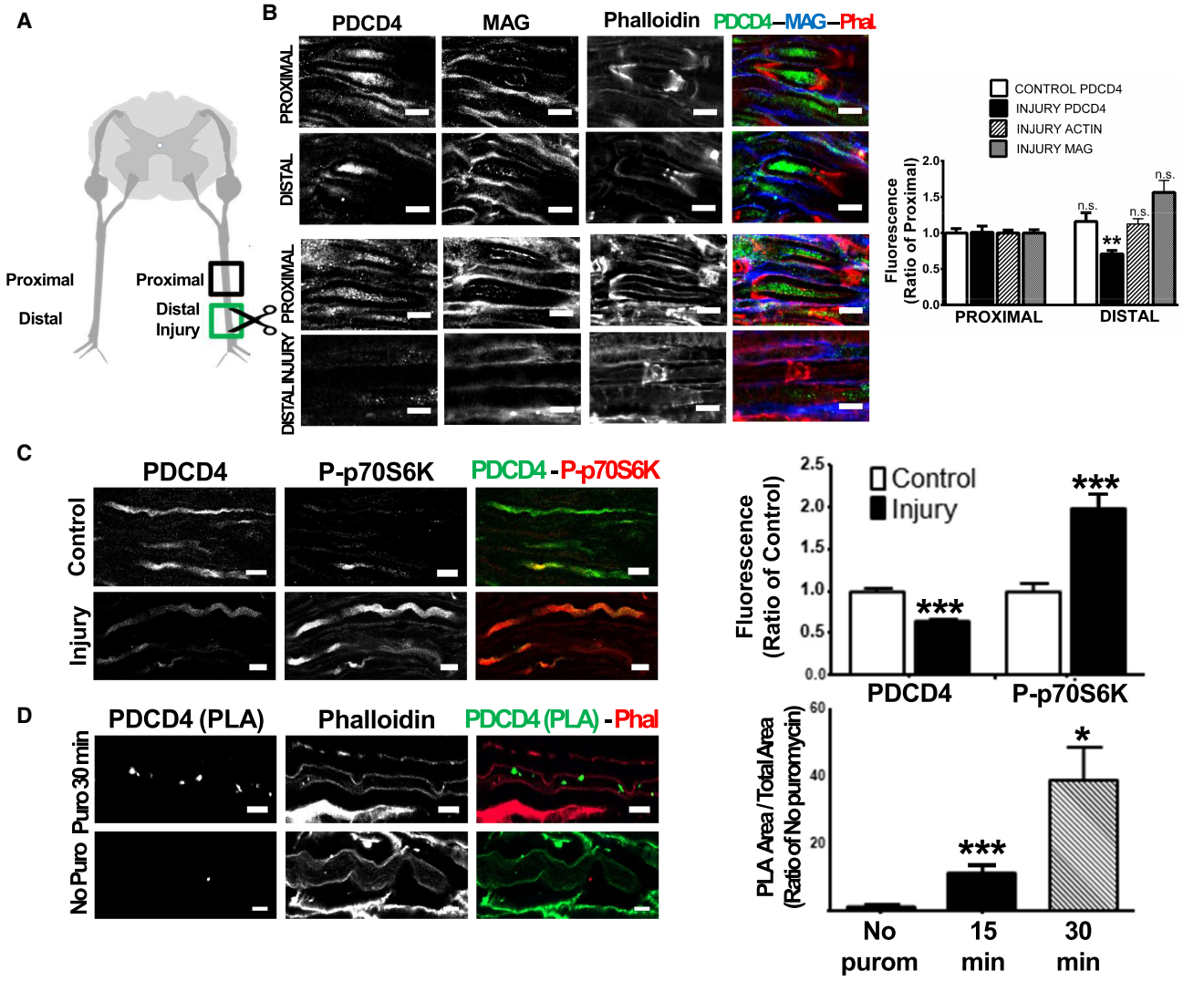

FIGURE 5. Sciatic nerve injury induces a decrease of PDCD4 levels locally in axons next to the injury site and an up-regulation (and activation) of p-p70S6K, a component of mTOR-PDCD4 pathway. PDCD4 could be locally synthetized in peripheral axons as a possible mechanism for protein level regulation. (*A*) A complete transection of the sciatic nerve was performed in adult rats using the contralateral nerve as a control condition. The analyzed regions are labeled as proximal and distal (or distal injury) in reference to cell bodies. (*B*) Eighteen hours post injury, the sciatic nerves were extracted from the animals and the levels of PDCD4 were analyzed by immunohistochemistry (scale bar, 5 µm). Signal quantification shows no differences on PDCD4 levels between regions in the control condition (distal vs. proximal), but in the injury to the sciatic nerves, a significant decrease in PDCD4 levels at the injury region was detected (distal injury vs. proximal). These changes are specific to PDCD4 because other proteins in the axon-like F-Actin (evidenced by phalloidin) and MAG protein did not have differences on expression levels comparing distal injury versus proximal (** $P \leq 0.01$, two-tailed Mann–Whitney test, $n = 3$, error bars: SEM). White dotted ROIs correspond to examples of quantified axonal regions. (*C*) As in *B*, levels of PDCD4 and p70S6K were analyzed by immunohistochemistry comparing injury axons vs control (scale bar, 10 µm). By signal quantification we detect an increase in the phosphorylated form of p70S6K, a direct upstream regulator of PDCD4 expression on the mTOR pathway (*** $P \leq 0.001$, two-tailed Mann–Whitney test, $n = 2$, error bars: SEM). White dotted ROIs correspond to examples of axonal quantified regions. (*D*) Maximum intensity projection images showing Puro-PLA signal for PDCD4 inside the axoplasm at 30 min of puromycin incubation and the associated control condition without puromycin. The green spots inside the axoplasm reveals that PDCD4 is newly synthetized in the axon. The *right* panel shows the signal quantification at two different time points of puromycin incubation compared to the control (*** $P \leq 0.001$ and * $P \leq 0.02$, ANOVA and Mann–Whitney test, $n = 2$, error bars: SEM). White dotted regions define the limits of the axoplasm region. Note that in all the cases, "*n*" are from independent biological replicates.

along the axoplasm of the sciatic nerves (Fig. 5B, confocal images of "Proximal" and "Distal" axonal sections in relation to the cell bodies). However, we observed a significant decrease of ~30% of PDCD4 axonal levels at the site of injury ("distal injury" in diagram) when compared to the proximal region of the same nerve segment (Fig. 5B). Importantly, these changes in PDCD4 levels are not due to an overall loss of protein content at the site of injury, as the levels of actin and MAG do not change when comparing all conditions (Fig. 5B). These findings allowed us to conclude that axonal levels of PDCD4 are dynamically decreased at the site of axonal injury and during the regeneration process.

The potential role of PDCD4 as a translation regulator in axonal growth would require the existence of precise molecular pathways controlling its localized expression. In this regard, degradation of PDCD4 would be able to rapidly promote axon regeneration in the context of nerve injury. Indeed, concomitant to the decrease in PDCD4 levels in injured axons, we found a significant increase in the activated form of p70S6K (phospho-p706SK), which acts as a direct regulator of PDCD4 degradation via the mTOR pathway (Fig. 5C; Dorrello et al. 2006). The tight control of protein levels in the axoplasm is not only dependent on degradation, but also on localized protein translation (Vuppalanchi et al. 2009; Yoon et al. 2009; Sahoo et al. 2018). Indeed, PDCD4 mRNA levels are detected in the axon of peripheral neurons, both in vivo (Farias et al. 2020) and in vitro in our DRG compartmentalized cultures, where qPCR analysis of RNA extracted from the axon compartment showed an increase from day 3 to 12 (day 3 C_t value = 25.5 and day 12 C_t value = 23.6) samples. To test if local translation could control PDCD4 levels in axons, we carried out the Puromycin-Proximity Ligation Assay or Puro-PLA in rat ventral roots in vivo (tom Dieck et al. 2015) to explore local protein synthesis. Consistent with its dynamic role in the control of axon processes, our results indicate that PDCD4 can be locally translated in mature noninjured axons (Fig. 5D). Overall, these results revealed two possible molecular mechanisms for the regulation of PDCD4 levels in mature axons ex vivo, either via degradation and/or local protein synthesis.

DISCUSSION

Our studies demonstrate that PDCD4 is expressed in different neuronal cell types of the CNS and PNS and is distributed in axonal and dendritic compartments, possibly interacting with other components of the mTOR pathway, such as its upstream protein regulator p70S6K (Fig. 1). Since PDCD4 is known to regulate protein synthesis in tumor models and also act as a downstream component of the mTOR pathway, we postulated that it could have a role in molecular processes relevant to axonal function. The possibility that PDCD4 functions as a translation regulator factor in both cancer and neuronal cells agrees with the observation that many of the key cellular hallmarks of cancer encompass molecular processes that are crucial in nervous system development, such as invasive cell growth, cytoskeleton rearrangements, ECM dynamic interactions and survival (Duman-Scheel 2009; Heine et al. 2015).

In mouse primary cortical neurons, we observed that PDCD4 is localized to the cell body and axons, with levels increasing during time in culture (Fig. 2A). This increase in PDCD4 levels correlates with neuronal network maturation and the establishment of synaptic contacts, a period that requires decreased axon growth. It is thus possible that elevated levels of PDCD4 mark the end of active axonal growth and the establishment of a stable cortical network. Further confirmation came from the overexpression of PDCD4, which caused a significant decrease in axonal growth. Importantly, the knockdown of PDCD4 levels caused the opposite effect, with a significant increase in axonal length (Fig. 2C,D). The analysis of axonal growth in primary cortical neurons constituted a useful approach for the investigation of the cellular and molecular mechanisms that control neuronal network development in the CNS. However, the elucidation of those mechanisms that can control axonal growth is also a fundamental area of research in the study of nerve regeneration in PNS (He and Jin 2016). It was thus important to investigate if PDCD4 could have a role in the regulation of axonal growth using an in vitro model of peripheral neurons, such as dissociated DRG primary neurons. Consistent with the high levels of PDCD4 observed in peripheral axons in vivo (Fig. 1B,C), and the functional data from cortical neurons (Fig. 2B,C), siRNA-dependent knockdown of PDCD4 in DRG neurons grown in microfluidic chambers (Taylor and Jeon 2011; Dajas-Bailador et al. 2012) showed a significant increase in axon growth (Fig. 2D). Overall, the functional studies in primary neurons of central and peripheral origin demonstrate a clear mechanistic link between the control of PDCD4 levels and the regulation of axon growth and network development, confirming that PDCD4 can modulate these processes, probably at the level of translation.

In order to explore the molecular signature underlying the link between PDCD4 and the control of neurite/axon growth, we decided to use a genomic approach to elucidate putative PDCD4 translational targets. To do this, we first generated a stable PC12 cell line able to induce PDCD4 knockdown by shRNA (Supplemental Fig. S2), and then confirmed that similar to primary neurons, PDCD4 knockdown caused an increase in the neurite length of differentiated PC12 neuron-like cells (Fig. 3A, B). Despite its described role in selective mRNA translational mechanisms, the investigation of PDCD4 targets has been largely unexplored using genomics approaches, neither in cancer nor in neuronal models. However, very

recent work by Haas and collaborators described PDCD4 targets using transcriptomics and Ribo-seq in a telomerase-immortalized human epithelial cell line (Haas et al. 2020). The implementation of Ribo-seq protocols, which are based on deep sequencing of ribosome-protected mRNA fragments, makes it possible to monitor translation directly, significantly improving the estimation of protein translation levels as compared to the classic RNA-seq approaches (Ingolia et al. 2012; Eastman et al. 2018). Our Ribo-seq data confirmed the key role of PDCD4 in the regulation of translation and provided only the second approximation to the full scope of its cellular targets and the first in a neuronal cell model (Fig. 3C–F). It allowed us to compare the PDCD4-dependent transcriptome and translatome data sets (Fig. 3C,D), identifying 267 mRNAs with a potential role as PDCD4 translational targets (Fig. 3E,F). This set of neuronal-related putative targets significantly increases their translational efficiency in the absence of PDCD4 (*P*-value <0.05 estimated by *Xtail*; Supplemental Table S2). We compared this list with that defined by Haas et al., where 62 mRNAs increase their translation upon PDCD4 silencing. Although 50 of those 62 targets could be detected in our study and show considerable expression levels, only *Cldnd1*, an apoptosis-related gene in epithelial cells (Achari et al. 2015), is common to both studies. This is likely the reflection of differences in cell type, developmental stage and experimental model, and provides a tantalizing perspective on the regulatory potential that can be attributed to PDCD4 and which is likely controlled by the additional recruitment of cell- and stage-specific mechanisms.

In order to further elucidate the regulatory mechanisms at play, samples from the same RNA-seq and Ribo-seq experimental protocols were analyzed by label-free quantitative proteomics (LFQ). However, the number of observed and regulated proteins (~3000 and 141 proteins, respectively) were lower than expected. From 141 differentially expressed proteins (*P*-value <0.05; ANOVA), 87 of them (62%) show the same direction of change seen in the Ribo-seq data (with similarly positive or negative fold changes; Supplemental Fig. S5B). In addition to the lack of sensitivity, it is also likely that protein levels might need to be evaluated at later time points than the Ribo-seq data, but this was beyond the scope of this study. Ultimately, protein levels are also subject to dynamic regulatory processes that control their half-life and degradation, and which might prevent the direct correlation of Ribo-seq data with estimation of proteome levels, particularly for low expression genes, which could be relevant in PDCD4 function (Zubarev 2013; Kumar et al. 2016).

Based on our functional results with primary neurons, we investigated the list of potential PDCD4 targets identified from our Ribo-seq data to uncover a neurite/axon growth gene signature. A list of 36 PDCD4 targets emerged with axon growth and/or neurite outgrowth links (Fig. 4A). Besides the genes associated with neurite outgrowth in PC12 cells described previously, the remaining genes were also described as associated with neurite or axonal growth previously in the literature (Bisogno et al. 2003; Nakanishi et al. 2006; Su et al. 2006; Ghiani et al. 2010; Fiesel et al. 2011; Bali et al. 2013; Kar et al. 2013; Olbrich et al. 2013; Mincheva-Tasheva et al. 2014; Munnamalai et al. 2014; Siddiq et al. 2015; Yu et al. 2016; Parviainen et al. 2017; Tang et al. 2017; Chen et al. 2019). Relevant and interesting examples include genes coding for proteins associated with the cytoskeleton, either actin with *Tmsb4x* (van Kesteren et al. 2006; Yang et al. 2008) or microtubules with *Stmn3* (Riederer et al. 1997; Manna et al. 2007); cell adhesion molecules like *Cadm1* (Nagara et al. 2012), *Amigo2* (Kuja-Panula et al. 2003), *Dscaml1* (Hattori et al. 2008; Zhu et al. 2013; Hutchinson et al. 2014), and *Emb* (Lain et al. 2009), transmembrane proteins associated to signal transduction including *Tspan7* (Bassani and Passafaro 2012); calcium-binding proteins like *Spock3* (Schnepp et al. 2005; Yamamoto et al. 2014), *Hpcal1* (Braunewell et al. 2011; Wang et al. 2014), and *Camk2b* (Fink et al. 2003; Yan et al. 2016), anterograde and retrograde transport and signaling with mRNAs like *Dynll1* (Lin et al. 2015) and *Lancl2*, different kinases like *Tnik* (Kawabe et al. 2010), *Mob1b* (Lin et al. 2011; Song et al. 2018), *Pnck* (Wayman et al. 2004; Uboha et al. 2007), and also synaptic-associated proteins like *Rab3il1* (Villarroel-Campos et al. 2016). Importantly, a significant proportion of PDCD4 putative translational targets identified in our analysis were also found in axonal transcriptomes from in vitro neuron models (Zappulo et al. 2017; Nijssen et al. 2018) and in vivo motor axon transcriptome (Farias et al. 2020) (Fig. 4B), supporting the validity of these processes beyond our experimental models.

Indeed, our own work managed to extend the observation of PDCD4's capacity for regulation of axon growth in primary neurons to an in vivo axon regeneration model, demonstrating that PDCD4 levels decrease following injury and during the regenerative growth phase (Fig. 5A,B). Taking into consideration that PDCD4 levels are high along adult peripheral axons in sciatic nerves (Fig. 1B), we believe a decrease in the levels of this translational repressor would allow the expression of growth-related proteins to aid local axon regeneration. Taken together, our in vitro and in vivo experiments support the idea that the dynamic control of PDCD4 levels in the neurons and axons could act as a new regulatory mechanism of protein synthesis in a specific and growth-oriented manner.

The role proposed for PDCD4 in the regulation of local protein synthesis in neurons would require a tight control of its levels in the axon. In agreement with previous reports (Verma et al. 2005; Terenzio et al. 2018), we found that the active form of p70S6K protein (phosphorylated at Thr 389) was increased twofold at the injury site, when compared to uninjured axons (Fig. 5C). Given that the local activation of

the mTOR pathway in the injured axons increases axonal protein synthesis (Verma et al. 2005; Terenzio et al. 2018), our findings confirm that the increased phosphorylation of p706SK in the axons correlates with a decrease in PDCD4 levels, likely mediated by activation of the proteasome system (Dorrello et al. 2006). In this scenario, the translation repression offered by PDCD4 would be removed, releasing the potential for growth mechanisms.

Local depletion of PDCD4 would be useful to mediate a rapid regeneration response; however, local neosynthesis can be used as an important mechanism to modulate protein synthesis of specific targets in other contexts of neuron development, when axon growth is reduced and synaptic consolidation might be needed. Indeed, PDCD4 levels have been shown to be regulated by miR-21 in cancer models increasing transformation, invasion, and metastasis (Asangani et al. 2008; Matsuhashi et al. 2019). Consistent with this, miR-21 is up-regulated during axonal growth and regeneration in DRG axons (Strickland et al. 2011) and miR-21 and PDCD4 have been analyzed in a model of spinal cord injury, where whole tissue levels of miR-21 increase and PDCD4 decrease after injury (Jiang et al. 2017). To test the potential existence of local protein synthesis as a regulatory mechanism controlling PDCD4 protein levels in the axoplasm, we used proximity ligation assays (PLA) (tom Dieck et al. 2015). Our results suggest that PDCD4 is locally translated in the axoplasm of peripheral neurons (Fig. 5D), supporting previous neurite data of newly synthetized proteomics, where PDCD4 is also detected (Zappulo et al. 2017).

Overall, our study shows the expression of PDCD4 in different types of neurons ex vivo, in vitro and also at different development stages in both mouse and rat experimental models. These results demonstrate a role of PDCD4 in processes where the dynamic regulation of protein synthesis is of crucial importance, such as axonal growth, in both development and regeneration. We report the first Riboseq data set for PDCD4 in a neuronal model, defining 267 mRNAs that could be regulated by PDCD4 at the translational level, with a significant number of these being related to neuronal plasticity and axonal growth processes. The potential relevance of this regulatory capacity for PDCD4 is further suggested by its regulation by local protein synthesis and/or degradation in peripheral axons. Taken together, our findings uncover a new role for PDCD4 in protein synthesis regulation at neuronal and specifically axon levels. This represents new evidence of the interesting correlation between cancer and neuronal pathways, especially the ones related to axonal growth and regeneration during injury. Further studies should elucidate the functional implications of those specific mRNAs regulated by PDCD4 in neurons, and particularly those acting locally in axons, a process that could provide novel functional insights in both plasticity and regenerative processes.

MATERIALS AND METHODS

Animals and injury procedures

Sprague-Dawley male adult rats (6–9 mo old) were used for ex vivo experiments. The maintenance was made in accordance with international agreements at IIBCE bioterium in Montevideo, Uruguay. Sciatic nerve transection was performed as in Canclini and collaborators (Canclini et al. 2014). All the experimental procedures were made according to the Uruguayan ethical national committee (CNEA) with approved project code "005/01/2014."

Cell cultures

Rats (Sprague-Dawley) and mice (C57/BL6) used for primary neuron cultures were housed at the Animal Unit in the School of Life Sciences (University of Nottingham). They were bred and sacrificed according to the UK Animal (Scientific Procedures) Act 1986. Primary cortical neuron cultures were obtained from C57/BL6 E16 mice brains as previously described (Lucci et al. 2020). Primary DRG cultures were obtained from E18 rat embryos. PC12 cell lines from ATCC (ATCC CRL-1721) were grown in collagen I (ThermoFisher, Cat# A1048301) coated plastic surfaces at 8 $\mu g/cm^2$. Complete medium was made of RPMI (ThermoFisher, Cat# 31800022), 10% of horse serum (ThermoFisher, Cat# 26050088), 5% of fetal bovine serum (Capricorn Scientific, Cat# FBS-11A), and antibiotics (Sigma-Aldrich, Cat# A5955). The cells were cultured following commercial instructions and neuronal differentiation was achieved by removing growth factors and antibiotics and exposing cells to 100 ng/mL of NGF 2.5S (ThermoFisher, Cat# 13257019) for at least 72 h. Neuroblastoma (Neuro2a) cell lines were a kind gift from the Robert Layfield laboratory, University of Nottingham, UK. For more details about cell cultures, please see Supplemental Materials and Methods.

siRNA and plasmid transfections

Primary cortical neurons and Neuro2a cells were both transfected 24 h after neuron seeding (day 2 of culture). For siRNA experiments we used 25 nM of siGENOME Mouse Pdcd4 SMARTpool 5 nmol (Cat# M-044032-01-0005) or siGENOME Non-Targeting siRNA Control Pool No.1, 5 nmol (Cat# D-001206-13-05), both from GE Healthcare Dharmacon—Horizon Solutions. Transfection protocols followed manufacturer's instructions using Lipofectamine 2000 (Invitrogen, ThermoFisher). Plasmid transfections were performed with 2 µg of PDCD4-pcDNA 3.1 (zeromycin), kindly gifted by Yang Hsin-Sheng, using an empty plasmid as control. Cortical neurons were cotransfected with 1 µg pmax-GFP Green-cat (ThermoFisher). In the specific case of primary DRG neuron cultures, the cell permeable Accell SMART POOL Pdcd4 siRNA 5 nmol (Cat# E-097927-00-0005) or Accell Non-Targeting Pool 5 nmol (Cat# D-001910-10-05), both from GE Healthcare Dharmacon—Horizon Solutions, were incubated at 1 µM final concentration in the cell body side of compartmentalized chambers after DRGs develop neurites. The PC12 cell line was transfected using commercial lentiviral particles from Dharmacon GE, with an inducible shRNA against PDCD4 (SMARTchoice Inducible Rat PDCD4 PGK–turboGFP shRNA, 100 µL, 10^7 TU/mL; Material# VSR6432-223515627), or shScrambled control

(SMARTchoice Inducible Non-targeting Control PGK/TurboGFP, 50 µL, 10^7 TU/mL; Material# VSC6580). After transfection, cells were grown in complete medium for 24 h and selected with 5 µg/mL of puromycin (P7255, Sigma-Aldrich) for 3–5 d. Cells were then cultured in complete medium to obtain stable cell lines able to induce silencing of PDCD4 or express a scrambled shRNA control.

Immunohistochemistry and immunocytochemistry

For tissue sections, rats were intracardially perfused with 3% sodium citrate (S4641-500, Sigma-Aldrich) and 4% PFA (158127, Sigma-Aldrich) in Phosphate Buffer Saline (PBS) buffer pH 7.4 (137 mM NaCl, 2.7 mM KCl, 8 mM Na_2HPO_4, and 2 mM KH2PO4). Following standard cryoprotection and 0.5% triton X-100 (13444259, ThermoFisher) permeabilization, 20 µm cryosections were made. Incubation with primary and secondary antibodies was performed in a blocking buffer with 5% NGS (MERCK, NS02L) overnight at 4°C. The PHEM buffer (60 mM PIPES, 25 mM HEPES, 10 mM EGTA, 2 mM $MgCl_2$) was used for washes. For primary neurons and cell lines, cells were rinsed with PBS buffer and fixed with 4% PFA, 5 mM $CaCl_2$ and 4% sucrose in PBS buffer for 30 min (RT), permeabilized in 0.2% Triton + 10 mM glycine in PBS for 20 min (RT) and incubated with antibodies overnight. Cells were mounted using Vectashield with DAPI (H-1200-10, VectorLabs) or Pro-Long Gold Antifade (P36930, ThermoFisher) mountant reagents. For a list of antibodies and probes used, please see Supplemental Material.

Puro-PLA protocol

Ventral roots were extracted from adult rats and incubated in neurobasal media with puromycin at 300 µM. Then a fixation with 4% PFA for 1 h was performed and cryosections were made as described above. The PLA protocol was carried out according to the manufacturer's instructions of DuoLink, Sigma using the following reagents: Duolink In Situ PLA Probe Anti-Rabbit PLUS (Cat#DUO92002-30RXN), Duolink In Situ PLA Probe Anti-Mouse MINUS (Cat#DUO92004-30RXN), Duolink In Situ Detection Reagents FarRed (DUO92013-30RXN).

Image acquisition and quantification analysis

Neocortex, cerebellum, sciatic nerves, and PC12 cell images were taken using an LSM confocal OLYMPUS FV300 with a 60× oil, NA 1.42 objective. For primary cultures, we used an inverted fluorescent microscope ZEISS axiovert 200 M coupled to a CCD camera (Photometrics CoolSnap MYO). For axonal length images, a 10× air NA 0.3 or 20× air NA 0.8 were used, while immunofluorescence quantification was done with a 63× oil NA 1.3. For PLA experiments on ventral roots, an LSM confocal ZEISS 800 was used with a 63× oil, NA 1.4. The stacks were always taken at an ideal µm number between each *z* plane.

For image quantification, the Fiji (*Just Image J*) tools (Schindelin et al. 2012) and the Neuron_Growth plugin software developed by Fanti and collaborators at the Universidad Nacional Autónoma de México (http://www.ifc.unam.mx/ffm/conditions.html) were used. For full details of quantification methods, see Supplemental Methods.

Ribosome profiling

Cells were treated with 100 mg/µL of cycloheximide (01810, Sigma-Aldrich) for 1 h at 37°C in the hood to stop translation before collection of RNA on ice. A transcriptome sample was separated to use as total RNA control and submitted to RNA extraction using mirVana Isolation Kit (ThermoFisher, Cat# AM1560) and RNA-seq protocol. At the same time, a proteome sample was separated and submitted to label-free quantitative proteomics using an LC-MS/MS Orbitrap Fusion. For translatome samples, cells were lysed and a polysomal pellet was obtained by ultracentrifugation in sucrose cushion, resuspended and digested with Benzonase (Sigma-Aldrich, Cat# E1014). Ribosomal footprints were isolated running a denaturalized 15% PAGE 7 M urea, cutting the proper band identified by length (~30 nt) and extracting RNA from gel slice. Ribosomal footprints quality and quantity was checked using 2100 Agilent Bioanalyzer Small RNA Kit and submitted to small RNA-seq protocol. Two biological replicates per condition (shPDCD4 and shScrambled) and per compartment (transcriptome, translatome and proteome) were obtained.

Sequencing and bioinformatic analysis

All transcriptome and translatome samples were sequenced in BGI Tech Solutions. Transcriptome samples were sequenced using RNA-Seq Quantification Library (Normal Library: 2–10 µg) protocol, with poly(A)$^+$ selection and 20 million paired-end (2 × 100 bp) reads obtained. Translatome samples were submitted to Small RNA Library (Low-Input Library: 0.2–1 µg) protocol and 40 million single-end reads were obtained. Sequence data is available at the NCBI Sequence Read Archive (SRA; https:// trace.ncbi.nlm.nih.gov/Traces/sra/) under BioProject ID PRJNA6 11824.

Sequences were mapped using *bowtie2* (Langmead and Salzberg 2012) versus curated mRNAs described in the mouse genome (available at NCBI ftp site). Read counts were estimated by *featureCounts* (Liao et al. 2014) and differential gene expression analysis between transcriptomes or translatomes was done using *edgeR* (Robinson et al. 2010). Normalized counts were exported and translational efficiency was calculated and contrasted between conditions (shPDCD4 vs. shScrambled) using *Xtail* R package (Xiao et al. 2016). Gene lists analysis was performed using the online free tool *STRING* (Jensen et al. 2009) and in-house software (Radío S, Sotelo-Silviera JR, and Smircich P, in prep.; https://github.com/sradiouy/IdMiner).

For comparison between potential PDCD4 translational targets and axonal transcriptomes, we used published axonal RNA-seq data sets (Zappulo et al. 2017; Nijssen et al. 2018). Downloaded FASTQ files were mapped to the *Mus musculus* genome (GRCm38) with HISAT2 (Kim et al. 2015). StringTie (Pertea et al. 2015, 2016) was used to assemble and quantify the transcripts. For subsequent analysis, low expression genes were removed (TPM < 1). For the comparison, mouse orthologs of the potential PDCD4 translational targets were used, since all the axonal transcriptomes data sets come from murine models. The Venn diagram was performed with the VennDiagram package of R (Chen and Boutros 2011). The EASE Score (a modified Fisher exact

P-value) was used to test if axonal transcriptomes were enriched in potential PDCD4 translational targets, and specifically those related with axonal growth. Extended protocols and details are available in SI Appendix.

SUPPLEMENTAL MATERIAL

Supplemental material is available for this article.

ACKNOWLEDGMENTS

We thank the School of Life Sciences Imaging (SLIM) facility in the University of Nottingham and the IIBCE Confocal and Sequencing Facility. We would like to acknowledge the following institutions for the financial support received: Agencia Nacional de Investigación e Innovación (ANII) for funding projects codes: INI_X_2011_1_3852, POS_NAC_2012_1_8584, POS_NAC_2013_1_11165, POS_NAC_2016_1_129865, POS_NAC_2016_1_129959; Comisión Sectorial de Investigación Científica (CSIC) for funding projects codes: CSIC Inciación 2013 #197 and #370; Programa de Desarrollo de las Ciencias Básicas (PEDECIBA); Wellcome Trust (Seed Award UNS56079 to F.D.-B. and R.M.-R.); the International Union of Biochemistry and Molecular Biology (IUBMB) Wood-Whelan Fellowships grants of 2017, the 2018 American Society for Biochemistry and Molecular Biology (ASBMB)-PROLAB fellowships, and the Science and Innovation Fund from the Foreign and Commonwealth Office-ANII Grant code UK_ID_2015_1_3.

Author contributions: J.R.S-S. conceived the project. J.R.S-S. and D.M. conceptualized the project. J.R.S-S. and F.D-B. designed and supervised the research. A.DP. performed the experiments for Figures 1, 2, 5 and Supplemental Figure S1. G.E. performed the experiments and data curation for Figures 3, 4 and Supplemental Figures S2–S7. R.M-R. and J.F. performed experiments. A.M., T.K., and N.C. contributed new reagents and resources. A.DP. and G.E. analyzed data, and A.DP., G.E., F.D.-B., and J.R.S.-S. wrote the paper.

Received March 22, 2020; accepted July 20, 2020.

REFERENCES

Achari C, Winslow S, Larsson C. 2015. Down regulation of CLDND1 induces apoptosis in breast cancer cells. *PLoS ONE* **10:** e0130300. doi:10.1371/journal.pone.0130300

Acosta R, Montañez C, Fuentes-Mera L, Gonzalez E, Gómez P, Quintero-Mora L, Mornet D, Alvarez-Salas LM, Cisneros B. 2004. Dystrophin Dp71 is required for neurite outgrowth in PC12 cells. *Exp Cell Res* **296:** 265–275. doi:10.1016/j.yexcr.2004.01.015

Asangani IA, Rasheed SAK, Nikolova DA, Leupold JH, Colburn NH, Post S, Allgayer H. 2008. MicroRNA-21 (miR-21) post-transcriptionally downregulates tumor suppressor Pdcd4 and stimulates invasion, intravasation and metastasis in colorectal cancer. *Oncogene* **27:** 2128–2136. doi:10.1038/sj.onc.1210856

Bali N, Arimoto JM, Morgan TE, Finch CE. 2013. Progesterone antagonism of neurite outgrowth depends on microglial activation via Pgrmc1/S2R. *Endocrinology* **154:** 2468–2480. doi:10.1210/en.2012-2109

Banker G. 2018. The development of neuronal polarity: a retrospective view. *J Neurosci* **38:** 1867–1873. doi:10.1523/JNEUROSCI.1372-16.2018

Bassani S, Passafaro M. 2012. TSPAN7: a new player in excitatory synapse maturation and function. *Bioarchitecture* **2:** 95–97. doi:10.4161/bioa.20829

Bisogno T, Howell F, Williams G, Minassi A, Cascio MG, Ligresti A, Matias I, Schiano-Moriello A, Paul P, Williams E-J, et al. 2003. Cloning of the first sn1-DAG lipases points to the spatial and temporal regulation of endocannabinoid signaling in the brain. *J Cell Biol* **163:** 463–468. doi:10.1083/jcb.200305129

Bitomsky N, Böhm M, Klempnauer K-H. 2004. Transformation suppressor protein *Pdcd4* interferes with JNK-mediated phosphorylation of c-Jun and recruitment of the coactivator p300 by c-Jun. *Oncogene* **23:** 7484–7493. doi:10.1038/sj.onc.1208064

Biyanee A, Ohnheiser J, Singh P, Klempnauer K-H. 2015. A novel mechanism for the control of translation of specific mRNAs by tumor suppressor protein *Pdcd4*: inhibition of translation elongation. *Oncogene* **34:** 1384–1392. doi:10.1038/onc.2014.83

Braunewell KH, Dwary AD, Richter F, Trappe K, Zhao C, Giegling I, Schönrath K, Rujescu D. 2011. Association of *VSNL1* with schizophrenia, frontal cortical function, and biological significance for its gene product as a modulator of cAMP levels and neuronal morphology. *Transl Psychiatry* **1:** e22. doi:10.1038/tp.2011.20

Canclini L, Wallrabe H, Di Paolo A, Kun A, Calliari A, Sotelo-Silveira JR, Sotelo JR. 2014. Association of Myosin Va and Schwann cells-derived RNA in mammal myelinated axons, analyzed by immunocytochemistry and confocal FRET microscopy. *Methods* **66:** 153–161. doi:10.1016/j.ymeth.2013.06.007

Chédotal A, Kerjan G, Moreau-Fauvarque C. 2005. The brain within the tumor: new roles for axon guidance molecules in cancers. *Cell Death Differ* **12:** 1044–1056. doi:10.1038/sj.cdd.4401707

Chen H, Boutros PC. 2011. VennDiagram: a package for the generation of highly-customizable Venn and Euler diagrams in R. *BMC Bioinformatics* **12:** 35. doi:10.1186/1471-2105-12-35

Chen P, Xu L, Zhang J, Cai X, Yang Y, Yu J, Qiu J, Ge J, Yu K, Zhuang J. 2019. Up-regulation of SorCS1, an important sorting receptor, in the retina of a form-deprivation rat model. *Cell Mol Neurobiol* **40:** 395–405. doi:10.1007/s10571-019-00740-1

Chiappalone M, Bove M, Vato A, Tedesco M, Martinoia S. 2006. Dissociated cortical networks show spontaneously correlated activity patterns during in vitro development. *Brain Res* **1093:** 41–53. doi:10.1016/j.brainres.2006.03.049

Cohen-Cory S, Kidane AH, Shirkey NJ, Marshak S. 2010. Brain-derived neurotrophic factor and the development of structural neuronal connectivity. *Dev Neurobiol* **70:** 271. doi:10.1002/dneu.20774

Cotterill E, Hall D, Wallace K, Mundy WR, Eglen SJ, Shafer TJ. 2016. Characterization of early cortical neural network development in multiwell microelectrode array plates. *J Biomol Screen* **21:** 510–519. doi:10.1177/1087057116640520

Dajas-Bailador F, Bonev B, Garcez P, Stanley P, Guillemot F, Papalopulu N. 2012. microRNA-9 regulates axon extension and branching by targeting Map1b in mouse cortical neurons. *Nat Neurosci* **15:** 697–699. doi:10.1038/nn.3082

Deglincerti A, Jaffrey SR. 2012. Insights into the roles of local translation from the axonal transcriptome. *Open Biol* **2:** 120079. doi:10.1098/rsob.120079

Dorrello NV, Peschiaroli A, Guardavaccaro D, Colburn NH, Sherman NE, Pagano M. 2006. S6K1- and βTRCP-mediated degradation of PDCD4 promotes protein translation and cell growth. *Science* **314:** 467–471. doi:10.1126/science.1130276

Duman-Scheel M. 2009. Netrin and DCC: axon guidance regulators at the intersection of nervous system development and cancer. *Curr Drug Targets* **10:** 602–610. doi:10.2174/138945009788680428

Eastman G, Smircich P, Sotelo-Silveira JR. 2018. Following ribosome footprints to understand translation at a genome wide level. *Comput Struct Biotechnol J* **16:** 167–176. doi:10.1016/j.csbj.2018.04.001

Farias J, Holt CE, Sotelo JR, Sotelo-Silveira JR. 2020. Axon micro-dissection and transcriptome profiling reveals the in vivo RNA content of fully differentiated myelinated motor axons. *RNA* **26:** 595–612. doi:10.1261/rna.073700.119

Fiesel FC, Schurr C, Weber SS, Kahle PJ. 2011. TDP-43 knockdown impairs neurite outgrowth dependent on its target histone deacetylase 6. *Mol Neurodegener* **6:** 64. doi:10.1186/1750-1326-6-64

Fink CC, Bayer K-U, Myers JW, Ferrell JE Jr, Schulman H, Meyer T. 2003. Selective regulation of neurite extension and synapse formation by the β but not the α isoform of CaMKII. *Neuron* **39:** 283–297. doi:10.1016/S0896-6273(03)00428-8

Flowers BM, Rusnak LE, Wong KE, Banks DA, Munyikwa MR, McFarland AG, Hinton SD. 2014. The pseudophosphatase MK-STYX induces neurite-like outgrowths in PC12 cells. *PLoS ONE* **9:** e114535. doi:10.1371/journal.pone.0114535

Frank CL, Tsai L-H. 2009. Alternative functions of core cell cycle regulators in neuronal migration, neuronal maturation, and synaptic plasticity. *Neuron* **62:** 312–326. doi:10.1016/j.neuron.2009.03.029

Fukao A, Sasano Y, Imataka H, Inoue K, Sakamoto H, Sonenberg N, Thoma C, Fujiwara T. 2009. The ELAV protein HuD stimulates cap-dependent translation in a Poly(A)- and eIF4A-dependent manner. *Mol Cell* **36:** 1007–1017. doi:10.1016/j.molcel.2009.11.013

Gao F, Zhang P, Zhou C, Li J, Wang Q, Zhu F, Ma C, Sun W, Zhang L. 2007. Frequent loss of PDCD4 expression in human glioma: possible role in the tumorigenesis of glioma. *Oncol Rep* **17:** 123–128. doi:10.3892/or.17.1.123

Ghiani CA, Starcevic M, Rodriguez-Fernandez IA, Nazarian R, Cheli VT, Chan LN, Malvar JS, de Vellis J, Sabatti C, Dell'Angelica EC. 2010. The dysbindin-containing complex (BLOC-1) in brain: developmental regulation, interaction with SNARE proteins and role in neurite outgrowth. *Mol Psychiatry* **15:** 115. 204–215. doi:10.1038/mp.2009.152

Göke R, Barth P, Schmidt A, Samans B, Lankat-Buttgereit B. 2004. Programmed cell death protein 4 suppresses CDK1/cdc2 via induction of $p21^{Waf1/Cip1}$. *Am J Physiol Cell Physiol* **287:** C1541–C1546. doi:10.1152/ajpcell.00025.2004

Gumy LF, Tan CL, Fawcett JW. 2010. The role of local protein synthesis and degradation in axon regeneration. *Exp Neurol* **223:** 28–37. doi:10.1016/j.expneurol.2009.06.004

Haas A, Nilges BS, Leidel SA, Klempnauer K-H. 2020. PDCD4 controls the G1/S-phase transition in a telomerase-immortalized epithelial cell line and affects the expression level and translation of multiple mRNAs. *Sci Rep* **10:** 2758. doi:10.1038/s41598-020-59678-w

Hattori D, Millard SS, Wojtowicz WM, Zipursky SL. 2008. Dscam-mediated cell recognition regulates neural circuit formation. *Annu Rev Cell Dev Biol* **24:** 597–620. doi:10.1146/annurev.cellbio.24.110707.175250

He Z, Jin Y. 2016. Intrinsic control of axon regeneration. *Neuron* **90:** 437–451. doi:10.1016/j.neuron.2016.04.022

Heine P, Ehrlicher A, Käs J. 2015. Neuronal and metastatic cancer cells: unlike brothers. *Biochim Biophys Acta* **1853:** 3126–3131. doi:10.1016/j.bbamcr.2015.06.011

Holt CE, Martin KC, Schuman EM. 2019. Local translation in neurons: visualization and function. *Nat Struct Mol Biol* **26:** 557–566. doi:10.1038/s41594-019-0263-5

Hudson BJ. 2008. *Loss of PDCD4 results in insulin resistance through ER stress.* University of Pennsylvania. https://repository.upenn.edu/dissertations/AAI3347091

Huebner EA, Strittmatter SM. 2009. Axon regeneration in the peripheral and central nervous systems. *Results Probl Cell Differ* **48:** 339–351. doi:10.1007/400_2009_19

Hutchinson KM, Vonhoff F, Duch C. 2014. Dscam1 is required for normal dendrite growth and branching but not for dendritic spacing in *Drosophila* motoneurons. *J Neurosci* **34:** 1924–1931. doi:10.1523/JNEUROSCI.3448-13.2014

Ingolia NT, Ghaemmaghami S, Newman JRS, Weissman JS. 2009. Genome-wide analysis in vivo of translation with nucleotide resolution using ribosome profiling. *Science* **324:** 218–223. doi:10.1126/science.1168978

Ingolia NT, Brar GA, Rouskin S, McGeachy AM, Weissman JS. 2012. The ribosome profiling strategy for monitoring translation in vivo by deep sequencing of ribosome-protected mRNA fragments. *Nat Protoc* **7:** 1534–1550. doi:10.1038/nprot.2012.086

Iwasaki Y, Ishikawa M, Okada N, Koizumi S. 1997. Induction of a distinct morphology and signal transduction in TrkB/PC12 cells by nerve growth factor and brain-derived neurotrophic factor. *J Neurochem* **68:** 927–934. doi:10.1046/j.1471-4159.1997.68030927.x

Iwasaki K, Isaacs KR, Jacobowitz DM. 1998. Brain-derived neurotrophic factor stimulates neurite outgrowth in a calretinin-enriched neuronal culture system. *Int J Dev Neurosci* **16:** 135–145. doi:10.1016/S0736-5748(98)00011-2

Jansen AP, Camalier CE, Colburn NH. 2005. Epidermal expression of the translation inhibitor programmed cell death 4 suppresses tumorigenesis. *Cancer Res* **65:** 6034–6041. doi:10.1158/0008-5472.CAN-04-2119

Jensen LJ, Kuhn M, Stark M, Chaffron S, Creevey C, Muller J, Doerks T, Julien P, Roth A, Simonovic M, et al. 2009. STRING 8—a global view on proteins and their functional interactions in 630 organisms. *Nucleic Acids Res* **37:** D412–D416. doi:10.1093/nar/gkn760

Jiang Y, Zhao S, Ding Y, Nong L, Li H, Gao G, Zhou D, Xu N. 2017. MicroRNA–21 promotes neurite outgrowth by regulating PDCD4 in a rat model of spinal cord injury. *Mol Med Rep* **16:** 2522–2528. doi:10.3892/mmr.2017.6862

Jiménez-Díaz L, Géranton SM, Passmore GM, Leith JL, Fisher AS, Berliocchi L, Sivasubramaniam AK, Sheasby A, Lumb BM, Hunt SP. 2008. Local translation in primary afferent fibers regulates nociception. *PLoS ONE* **3:** e1961. doi:10.1371/journal.pone.0001961

Jung H, O'Hare CM, Holt CE. 2011. Translational regulation in growth cones. *Curr Opin Genet Dev* **21:** 458–464. doi:10.1016/j.gde.2011.04.004

Jung H, Yoon BC, Holt CE. 2012. Axonal mRNA localization and local protein synthesis in nervous system assembly, maintenance and repair. *Nat Rev Neurosci* **13:** 308–324. doi:10.1038/nrn3210

Kar AN, MacGibeny MA, Gervasi NM, Gioio AE, Kaplan BB. 2013. Intra-axonal synthesis of eukaryotic translation initiation factors regulates local protein synthesis and axon growth in rat sympathetic neurons. *J Neurosci* **33:** 7165–7174. doi:10.1523/JNEUROSCI.2040-12.2013

Kawabe H, Neeb A, Dimova K, Young SM, Takeda M, Katsurabayashi S, Mitkovski M, Malakhova OA, Zhang D-E, Umikawa M, et al. 2010. Regulation of Rap2A by the ubiquitin ligase Nedd4-1 controls neurite development. *Neuron* **65:** 358–372. doi:10.1016/j.neuron.2010.01.007

Kim J, Park RY, Chen J-K, Kim J, Jeong S, Ohn T. 2014. Splicing factor SRSF3 represses the translation of programmed cell death 4 mRNA by associating with the 5′-UTR region. *Cell Death Differ* **21:** 481–490. doi:10.1038/cdd.2013.171

Kim D, Langmead B, Salzberg SL. 2015. HISAT: a fast spliced aligner with low memory requirements. *Nat Methods* **12:** 357–360. doi:10.1038/nmeth.3317

Kuja-Panula J, Kiiltomäki M, Yamashiro T, Rouhiainen A, Rauvala H. 2003. AMIGO, a transmembrane protein implicated in axon tract development, defines a novel protein family with leucine-rich repeats. *J Cell Biol* **160:** 963–973. doi:10.1083/jcb.200209074

Kumar D, Bansal G, Narang A, Basak T, Abbas T, Dash D. 2016. Integrating transcriptome and proteome profiling: strategies and applications. *Proteomics* **16:** 2533–2544. doi:10.1002/pmic.201600140

Lain E, Carnejac S, Escher P, Wilson MC, Lømo T, Gajendran N, Brenner HR. 2009. A novel role for embigin to promote sprouting of motor nerve terminals at the neuromuscular junction. *J Biol Chem* **284:** 8930–8939. doi:10.1074/jbc.M809491200

Langmead B, Salzberg SL. 2012. Fast gapped-read alignment with Bowtie 2. *Nat Methods* **9:** 357–359. doi:10.1038/nmeth.1923

Li Y, Jia Y, Wang D, Zhuang X, Li Y, Guo C, Chu H, Zhu F, Wang J, Wang X, et al. 2020. Programmed cell death 4 as an endogenous suppressor of BDNF translation is involved in stress-induced depression. *Mol Psychiatry* doi:10.1038/s41380-020-0692-x

Liao Y, Smyth GK, Shi W. 2014. featureCounts: an efficient general purpose program for assigning sequence reads to genomic features. *Bioinformatics* **30:** 923–930. doi:10.1093/bioinformatics/btt656

Lin AC, Holt CE. 2008. Function and regulation of local axonal translation. *Curr Opin Neurobiol* **18:** 60–68. doi:10.1016/j.conb.2008.05.004

Lin C-H, Hsieh M, Fan S-S. 2011. The promotion of neurite formation in Neuro2A cells by mouse Mob2 protein. *FEBS Lett* **585:** 523–530. doi:10.1016/j.febslet.2011.01.003

Lin T, Pan P-Y, Lai Y-T, Chiang K-W, Hsieh H-L, Wu Y-P, Ke J-M, Lee M-C, Liao S-S, Shih H-T, et al. 2015. Spindle-F is the central mediator of Ik2 kinase-dependent dendrite pruning in *Drosophila* sensory neurons. *PLoS Genet* **11:** e1005642. doi:10.1371/journal.pgen.1005642

Liwak U, Thakor N, Jordan LE, Roy R, Lewis SM, Pardo OE, Seckl M, Holcik M. 2012. Tumor suppressor PDCD4 represses internal ribosome entry site-mediated translation of antiapoptotic proteins and is regulated by S6 kinase 2. *Mol Cell Biol* **32:** 1818–1829. doi:10.1128/MCB.06317-11

Loh PG, Yang H-S, Walsh MA, Wang Q, Wang X, Cheng Z, Liu D, Song H. 2009. Structural basis for translational inhibition by the tumour suppressor Pdcd4. *EMBO J* **28:** 274–285. doi:10.1038/emboj.2008.278

Lucci C, Mesquita-Ribeiro R, Rathbone A, Dajas-Bailador F. 2020. Spatiotemporal regulation of GSK3β levels by miRNA-26a controls axon development in cortical neurons. *Development* **147:** dev180232. doi:10.1242/dev.180232

Manecka D-L, Mahmood SF, Grumolato L, Lihrmann I, Anouar Y. 2013. Pituitary adenylate cyclase-activating polypeptide (PACAP) promotes both survival and neuritogenesis in PC12 cells through activation of nuclear factor κB (NF-κB) pathway: involvement of extracellular signal-regulated kinase (ERK), calcium, and c-REL. *J Biol Chem* **288:** 14936–14948. doi:10.1074/jbc.M112.434597

Manna T, Grenningloh G, Miller HP, Wilson L. 2007. Stathmin family protein SCG10 differentially regulates the plus and minus end dynamics of microtubules at steady state in vitro: implications for its role in neurite outgrowth. *Biochemistry* **46:** 3543–3552. doi:10.1021/bi061819d

Matsuhashi S, Manirujjaman M, Hamajima H, Ozaki I. 2019. Control mechanisms of the tumor suppressor PDCD4: expression and functions. *Int J Mol Sci* **20:** 2304. doi:10.3390/ijms20092304

Mincheva-Tasheva S, Obis E, Tamarit J, Ros J. 2014. Apoptotic cell death and altered calcium homeostasis caused by frataxin depletion in dorsal root ganglia neurons can be prevented by BH4 domain of Bcl-x_L protein. *Hum Mol Genet* **23:** 1829–1841. doi:10.1093/hmg/ddt576

Mobarak CD, Anderson KD, Morin M, Beckel-Mitchener A, Rogers SL, Furneaux H, King P, Perrone-Bizzozero NI. 2000. The RNA-binding protein HuD is required for GAP-43 mRNA stability, GAP-43 gene expression, and PKC-dependent neurite outgrowth in PC12 cells. *Mol Biol Cell* **11:** 3191–3203. doi:10.1091/mbc.11.9.3191

Moustafa-Kamal M, Kucharski T, El Assad W, Gandin V, Abas Y, Nagar B, Pelletier J, Topisirovic I, Teodoro JG. 2019. The mTORC1/S6K/PDCD4/eIF4A axis determines outcome of mitosis. *bioRxiv* 794545. doi:10.1101/794545v1.abstract

Mudduluru G, Medved F, Grobholz R, Jost C, Gruber A, Leupold JH, Post S, Jansen A, Colburn NH, Allgayer H. 2007. Loss of programmed cell death 4 expression marks adenoma-carcinoma transition, correlates inversely with phosphorylated protein kinase B, and is an independent prognostic factor in resected colorectal cancer. *Cancer* **110:** 1697–1707. doi:10.1002/cncr.22983

Munnamalai V, Weaver CJ, Weisheit CE, Venkatraman P, Agim ZS, Quinn MT, Suter DM. 2014. Bidirectional interactions between NOX2-type NADPH oxidase and the F-actin cytoskeleton in neuronal growth cones. *J Neurochem* **130:** 526–540. doi:10.1111/jnc.12734

Murray JT, Tee AR. 2018. Mechanistic target of rapamycin (mTOR) in the cancer setting. *Cancers (Basel)* **10:** 168. doi:10.3390/cancers10060168

Nagara Y, Hagiyama M, Hatano N, Futai E, Suo S, Takaoka Y, Murakami Y, Ito A, Ishiura S. 2012. Tumor suppressor cell adhesion molecule 1 (CADM1) is cleaved by a disintegrin and metalloprotease 10 (ADAM10) and subsequently cleaved by γ-secretase complex. *Biochem Biophys Res Commun* **417:** 462–467. doi:10.1016/j.bbrc.2011.11.140

Nakanishi K, Aono S, Hirano K, Kuroda Y, Ida M, Tokita Y, Matsui F, Oohira A. 2006. Identification of neurite outgrowth-promoting domains of neuroglycan C, a brain-specific chondroitin sulfate proteoglycan, and involvement of phosphatidylinositol 3-kinase and protein kinase C signaling pathways in neuritogenesis. *J Biol Chem* **281:** 24970–24978. doi:10.1074/jbc.M601498200

Narasimhan M, Rathinam M, Riar A, Patel D, Mummidi S, Yang H-S, Colburn NH, Henderson GI, Mahimainathan L. 2013. Programmed cell death 4 (PDCD4): a novel player in ethanol-mediated suppression of protein translation in primary cortical neurons and developing cerebral cortex. *Alcohol Clin Exp Res* **37:** 96–109. doi:10.1111/j.1530-0277.2012.01850.x

Ng YP, He W, Ip NY. 2003. Leukemia inhibitory factor receptor signaling negatively modulates nerve growth factor-induced neurite outgrowth in PC12 cells and sympathetic neurons. *J Biol Chem* **278:** 38731–38739. doi:10.1074/jbc.M304623200

Nijssen J, Aguila J, Hoogstraaten R, Kee N, Hedlund E. 2018. Axon-seq decodes the motor axon transcriptome and its modulation in response to ALS. *Stem Cell Rep* **11:** 1565–1578. doi:10.1016/j.stemcr.2018.11.005

Obara I, Hunt SP. 2014. Axonal protein synthesis and the regulation of primary afferent function. *Dev Neurobiol* **74:** 269–278. doi:10.1002/dneu.22133

Ohtake Y, Hayat U, Li S. 2015. PTEN inhibition and axon regeneration and neural repair. *Neural Regeneration Res* **10:** 1363–1368. doi:10.4103/1673-5374.165496

Olbrich L, Wessel L, Balakrishnan-Renuka A, Böing M, Brand-Saberi B, Theiss C. 2013. Rapid impact of progesterone on the neuronal growth cone. *Endocrinology* **154:** 3784–3795. doi:10.1210/en.2013-1175

Park KK, Liu K, Hu Y, Smith PD, Wang C, Cai B, Xu B, Connolly L, Kramvis I, Sahin M, et al. 2008. Promoting axon regeneration in the adult CNS by modulation of the PTEN/mTOR pathway. *Science* **322:** 963–966. doi:10.1126/science.1161566

Park KK, Liu K, Hu Y, Kanter JL, He Z. 2010. PTEN/mTOR and axon regeneration. *Exp Neurol* **223:** 45–50. doi:10.1016/j.expneurol.2009.12.032

Parviainen L, Dihanich S, Anderson GW, Wong AM, Brooks HR, Abeti R, Rezaie P, Lalli G, Pope S, Heales SJ, et al. 2017. Glial cells are functionally impaired in juvenile neuronal ceroid lipofuscinosis and detrimental to neurons. *Acta Neuropathol Commun* **5:** 74. doi:10.1186/s40478-017-0476-y

Pertea M, Pertea GM, Antonescu CM, Chang T-C, Mendell JT, Salzberg SL. 2015. StringTie enables improved reconstruction of a transcriptome from RNA-seq reads. *Nat Biotechnol* **33:** 290–295. doi:10.1038/nbt.3122

Pertea M, Kim D, Pertea GM, Leek JT, Salzberg SL. 2016. Transcript-level expression analysis of RNA-seq experiments with HISAT, StringTie and Ballgown. *Nat Protoc* **11:** 1650–1667. doi:10.1038/nprot.2016.095

Riar AK, Narasimhan M, Rathinam ML, Vedpathak D, Mummidi S, Henderson GI, Mahimainathan L. 2014. Ethanol-induced transcriptional activation of programmed cell death 4 (Pdcd4) is mediated by GSK-3β signaling in rat cortical neuroblasts. *PLoS ONE* **9:** e98080. doi:10.1371/journal.pone.0098080

Riederer BM, Pellier V, Antonsson B, Di Paolo G, Stimpson SA, Lütjens R, Catsicas S, Grenningloh G. 1997. Regulation of microtubule dynamics by the neuronal growth-associated protein SCG10. *Proc Natl Acad Sci* **94:** 741–745. doi:10.1073/pnas.94.2.741

Robinson MD, McCarthy DJ, Smyth GK. 2010. edgeR: a Bioconductor package for differential expression analysis of digital gene expression data. *Bioinformatics* **26:** 139–140. doi:10.1093/bioinformatics/btp616

Sahoo PK, Smith DS, Perrone-Bizzozero N, Twiss JL. 2018. Axonal mRNA transport and translation at a glance. *J Cell Sci* **131:** jcs196808. doi:10.1242/jcs.196808

Schindelin J, Arganda-Carreras I, Frise E, Kaynig V, Longair M, Pietzsch T, Preibisch S, Rueden C, Saalfeld S, Schmid B, et al. 2012. Fiji: an open-source platform for biological-image analysis. *Nat Methods* **9:** 676–682. doi:10.1038/nmeth.2019

Schmid T, Jansen AP, Baker AR, Hegamyer G, Hagan JP, Colburn NH. 2008. Translation inhibitor Pdcd4 is targeted for degradation during tumor promotion. *Cancer Res* **68:** 1254–1260. doi:10.1158/0008-5472.CAN-07-1719

Schnepp A, Komp Lindgren P, Hülsmann H, Kröger S, Paulsson M, Hartmann U. 2005. Mouse testican-2. Expression, glycosylation, and effects on neurite outgrowth. *J Biol Chem* **280:** 11274–11280. doi:10.1074/jbc.M414276200

Shao J, Cao J, Wang J, Ren X, Su S, Li M, Li Z, Zhao Q, Zang W. 2016. MicroRNA-30b regulates expression of the sodium channel Nav1.7 in nerve injury-induced neuropathic pain in the rat. *Mol Pain* **12:** 1744806916671523. doi:10.1177/1744806916671523

Siddiq MM, Hannila SS, Carmel JB, Bryson JB, Hou J, Nikulina E, Willis MR, Mellado W, Richman EL, Hilaire M, et al. 2015. Metallothionein-I/II promotes axonal regeneration in the central nervous system. *J Biol Chem* **290:** 16343–16356. doi:10.1074/jbc.M114.630574

Singh P, Wedeken L, Waters LC, Carr MD, Klempnauer K-H. 2011. Pdcd4 directly binds the coding region of c-*myb* mRNA and suppresses its translation. *Oncogene* **30:** 4864–4873. doi:10.1038/onc.2011.202

Song Z, Han X, Zou H, Zhang B, Ding Y, Xu X, Zeng J, Liu J, Gong A. 2018. PTEN-GSK3β-MOB1 axis controls neurite outgrowth in vitro and in vivo. *Cell Mol Life Sci* **75:** 4445–4464. doi:10.1007/s00018-018-2890-0

Sotelo-Silveira JR, Holt CE. 2014. Introduction to the special issue on local protein synthesis in axons. *Dev Neurobiol* **74:** 207–209. doi:10.1002/dneu.22163

Squinto SP, Stitt TN, Aldrich TH, Davis S, Bianco SM, Radziejewski C, Glass DJ, Masiakowski P, Furth ME, Valenzuela DM. 1991. *trk*B encodes a functional receptor for brain-derived neurotrophic factor and neurotrophin-3 but not nerve growth factor. *Cell* **65:** 885–893. doi:10.1016/0092-8674(91)90395-F

Strickland IT, Richards L, Holmes FE, Wynick D, Uney JB, Wong L-F. 2011. Axotomy-induced miR-21 promotes axon growth in adult dorsal root ganglion neurons. *PLoS ONE* **6:** e23423. doi:10.1371/journal.pone.0023423

Su C-W, Tharin S, Jin Y, Wightman B, Spector M, Meili D, Tsung N, Rhiner C, Bourikas D, Stoeckli E, et al. 2006. The short coiled-coil domain-containing protein UNC-69 cooperates with UNC-76 to regulate axonal outgrowth and normal presynaptic organization in *Caenorhabditis elegans*. *J Biol* **5:** 9. doi:10.1186/jbiol39

Suzuki C, Garces RG, Edmonds KA, Hiller S, Hyberts SG, Marintchev A, Wagner G. 2008. PDCD4 inhibits translation initiation by binding to eIF4A using both its MA3 domains. *Proc Natl Acad Sci* **105:** 3274–3279. doi:10.1073/pnas.0712235105

Swanger SA, Bassell GJ. 2011. Making and breaking synapses through local mRNA regulation. *Curr Opin Genet Dev* **21:** 414–421. doi:10.1016/j.gde.2011.04.002

Tang G-B, Zeng Y-Q, Liu P-P, Mi T-W, Zhang S-F, Dai S-K, Tang Q-Y, Yang L, Xu Y-J, Yan H-L, et al. 2017. The histone H3K27 demethylase UTX regulates synaptic plasticity and cognitive behaviors in mice. *Front Mol Neurosci* **10:** 267. doi:10.3389/fnmol.2017.00267

Taylor AM, Jeon NL. 2011. Microfluidic and compartmentalized platforms for neurobiological research. *Crit Rev Biomed Eng* **39:** 185–200. doi:10.1615/CritRevBiomedEng.v39.i3.20

Terenzio M, Koley S, Samra N, Rishal I, Zhao Q, Sahoo PK, Urisman A, Marvaldi L, Oses-Prieto JA, Forester C, et al. 2018. Locally translated mTOR controls axonal local translation in nerve injury. *Science* **359:** 1416–1421. doi:10.1126/science.aan1053

tom Dieck S, Kochen L, Hanus C, Heumüller M, Bartnik I, Nassim-Assir B, Merk K, Mosler T, Garg S, Bunse S, et al. 2015. Direct visualization of newly synthesized target proteins in situ. *Nat Methods* **12:** 411–414. doi:10.1038/nmeth.3319

Uboha NV, Flajolet M, Nairn AC, Picciotto MR. 2007. A calcium- and calmodulin-dependent kinase Iα/microtubule affinity regulating kinase 2 signaling cascade mediates calcium-dependent neurite outgrowth. *J Neurosci* **27:** 4413–4423. doi:10.1523/JNEUROSCI.0725-07.2007

van Kesteren RE, Carter C, Dissel HMG, van Minnen J, Gouwenberg Y, Syed NI, Spencer GE, Smit AB. 2006. Local synthesis of actin-binding protein β-thymosin regulates neurite outgrowth. *J Neurosci* **26:** 152–157. doi:10.1523/JNEUROSCI.4164-05.2006

Verma P, Chierzi S, Codd AM, Campbell DS, Meyer RL, Holt CE, Fawcett JW. 2005. Axonal protein synthesis and degradation are necessary for efficient growth cone regeneration. *J Neurosci* **25:** 331–342. doi:10.1523/JNEUROSCI.3073-04.2005

Villarroel-Campos D, Bronfman FC, Gonzalez-Billault C. 2016. Rab GTPase signaling in neurite outgrowth and axon specification. *Cytoskeleton* **73:** 498–507. doi:10.1002/cm.21303

Vuppalanchi D, Willis DE, Twiss JL. 2009. Regulation of mRNA transport and translation in axons. *Results Probl Cell Differ* **48:** 193–224. doi:10.1007/400_2009_16

Wang Q, Dong Z, Liu X, Song X, Song Q, Shang Q, Jiang Y, Guo C, Zhang L. 2013. Programmed cell death-4 deficiency prevents diet-induced obesity, adipose tissue inflammation, and insulin resistance. *Diabetes* **62:** 4132–4143. doi:10.2337/db13-0097

Wang W, Zhong Q, Teng L, Bhatnagar N, Sharma B, Zhang X, Luther W, Haynes LP, Burgoyne RD, Vidal M, et al. 2014. Mutations that disrupt PHOXB interaction with the neuronal calcium sensor HPCAL1 impede cellular differentiation in neuroblastoma. *Oncogene* **33:** 3316–3324. doi:10.1038/onc.2013.290

Wang Q, Zhu J, Wang Y-W, Dai Y, Wang Y-L, Wang C, Liu J, Baker A, Colburn NH, Yang H-S. 2017. Tumor suppressor Pdcd4 attenuates Sin1 translation to inhibit invasion in colon carcinoma. *Oncogene* **36:** 6225–6234. doi:10.1038/onc.2017.228

Wayman GA, Kaech S, Grant WF, Davare M, Impey S, Tokumitsu H, Nozaki N, Banker G, Soderling TR. 2004. Regulation of axonal extension and growth cone motility by calmodulin-dependent protein kinase I. *J Neurosci* **24:** 3786–3794. doi:10.1523/JNEUROSCI.3294-03.2004

Wedeken L, Singh P, Klempnauer K-H. 2011. Tumor suppressor protein Pdcd4 inhibits translation of p53 mRNA. *J Biol Chem* **286:** 42855–42862. doi:10.1074/jbc.M111.269456

Xiao Z, Zou Q, Liu Y, Yang X. 2016. Genome-wide assessment of differential translations with ribosome profiling data. *Nat Commun* **7:** 11194. doi:10.1038/ncomms11194

Yamamoto A, Uchiyama K, Nara T, Nishimura N, Hayasaka M, Hanaoka K, Yamamoto T. 2014. Structural abnormalities of corpus callosum and cortical axonal tracts accompanied by decreased anxiety-like behavior and lowered sociability in spock3- mutant mice. *Dev Neurosci* **36:** 381–395. doi:10.1159/000363101

Yan X, Liu J, Ye Z, Huang J, He F, Xiao W, Hu X, Luo Z. 2016. CaMKII-mediated CREB phosphorylation is involved in $Ca2^{+}$-induced BDNF mRNA transcription and neurite outgrowth promoted by electrical stimulation. *PLoS ONE* **11:** e0162784. doi:10.1371/journal.pone.0162784

Yang H-S, Jansen AP, Komar AA, Zheng X, Merrick WC, Costes S, Lockett SJ, Sonenberg N, Colburn NH. 2003. The transformation suppressor Pdcd4 is a novel eukaryotic translation initiation factor 4A binding protein that inhibits translation. *Mol Cell Biol* **23:** 26–37. doi:10.1128/MCB.23.1.26-37.2003

Yang H-S, Matthews CP, Clair T, Wang Q, Baker AR, Li C-CH, Tan T-H, Colburn NH. 2006. Tumorigenesis suppressor Pdcd4 down-regulates mitogen-activated protein kinase kinase kinase kinase 1 expression to suppress colon carcinoma cell invasion. *Mol Cell Biol* **26:** 1297–1306. doi:10.1128/MCB.26.4.1297-1306.2006

Yang H, Cheng X, Yao Q, Li J, Ju G. 2008. The promotive effects of thymosin β4 on neuronal survival and neurite outgrowth by upregulating L1 expression. *Neurochem Res* **33:** 2269–2280. doi:10.1007/s11064-008-9712-y

Yoon BC, Zivraj KH, Holt CE. 2009. Local translation and mRNA trafficking in axon pathfinding. *Results Probl Cell Differ* **48:** 269–288. doi:10.1007/400_2009_5

Yu J, Lin S, Wang M, Liang L, Zou Z, Zhou X, Wang M, Chen P, Wang Y. 2016. Metastasis suppressor 1 regulates neurite outgrowth in primary neuron cultures. *Neuroscience* **333:** 123–131. doi:10.1016/j.neuroscience.2016.07.002

Zappulo A, van den Bruck D, Mattioli C C, Franke V, Imami K, McShane E, Moreno-Estelles M, Calviello L, Filipchyk A, Peguero-Sanchez E, et al. 2017. RNA localization is a key determinant of neurite-enriched proteome. *Nat Commun* **8:** 583. doi:10.1038/s41467-017-00690-6

Zhang H, Ozaki I, Mizuta T, Hamajima H, Yasutake T, Eguchi Y, Ideguchi H, Yamamoto K, Matsuhashi S. 2006. Involvement of programmed cell death 4 in transforming growth factor-β1-induced apoptosis in human hepatocellular carcinoma. *Oncogene* **25:** 6101–6112. doi:10.1038/sj.onc.1209634

Zhang W, Wang L, Liu Y, Xu J, Zhu G, Cang H, Li X, Bartlam M, Hensley K, Li G, et al. 2009. Structure of human lanthionine synthetase C-like protein 1 and its interaction with Eps8 and glutathione. *Genes Dev* **23:** 1387–1392. doi:10.1101/gad.1789209

Zhen Y, Li D, Li W, Yao W, Wu A, Huang J, Gu H, Huang Y, Wang Y, Wu J, et al. 2016. Reduced PDCD4 expression promotes cell growth through PI3K/Akt signaling in non-small cell lung cancer. *Oncol Res* **23:** 61–68. doi:10.3727/096504015X14478843952861

Zheng W, Chong C-M, Wang H, Zhou X, Zhang L, Wang R, Meng Q, Lazarovici P, Fang J. 2016. Artemisinin conferred ERK mediated neuroprotection to PC12 cells and cortical neurons exposed to sodium nitroprusside-induced oxidative insult. *Free Radic Biol Med* **97:** 158–167. doi:10.1016/j.freeradbiomed.2016.05.023

Zhu K, Chen X, Liu J, Ye H, Zhu L, Wu JY. 2013. AMPK interacts with DSCAM and plays an important role in netrin-1 induced neurite outgrowth. *Protein Cell* **4:** 155–161. doi:10.1007/s13238-012-2126-2

Zubarev RA. 2013. The challenge of the proteome dynamic range and its implications for in-depth proteomics. *Proteomics* **13:** 723–726. doi:10.1002/pmic.201200451

PDCD4 regulates axonal growth by translational repression of neurite growth-related genes and is modulated during nerve injury responses

Andrés Di Paolo, Guillermo Eastman, Raquel Mesquita-Ribeiro, et al.

RNA 2020 26: 1637-1653 originally published online August 3, 2020
Access the most recent version at doi:10.1261/rna.075424.120

Supplementary Information

PDCD4 regulates axonal growth by translational repression of neurite growth-related genes and is modulated during nerve injury responses

Andrés Di Paolo, Guillermo Eastman, Raquel Mesquita-Ribeiro, Joaquina Farias, Andrew Macklin, Thomas Kislinger, Nancy Colburn, David Munroe, José Sotelo Sosa, Federico Dajas-Bailador, José Roberto Sotelo-Silveira.

This file contains:

Supplementary Materials and Methods

Animals and injury procedures

Sprague Dawley male adult rats (6-9 months old) were used for ex vivo experiments. The maintenance was made in accordance with international agreements at IIBCE bioterium in Montevideo, Uruguay. Animals were anesthetized with ketamine and xylazine mix (100 mg/kg, 10 mg/kg) by intraperitoneal injection. Afterwards the animals were intracardially perfused using paraformaldehyde.

- Sciatic nerve transection

Adult Sprague-Dawley rats were anesthetized with 50 mg/kg pentobarbital. An incision was made at mid-thigh and the sciatic nerve was transected, which was then closed with cyanoacrylate glue. After 18 h recovery, rats were euthanized by decapitation and a 2-cm sciatic nerve segment proximal to the transection was removed. Equivalent contralateral uninjured segments were used as controls. Afterwards we labelled the proximal region using a strand and quickly fixed with PFA 4% for 1 hour at RT. Immunohistochemistry protocols were carried out as described for *in vivo* tissues. All the experimental procedures were made according to the Uruguayan ethical national committee (CNEA) with approved project code “005/01/2014”.

Cell Cultures

Rats (Sprague-Dawley) and mice (C57/BL6) used for primary neuron cultures were housed at the Animal Unit in the School of Life Sciences (University of Nottingham). They were bred and sacrificed according to the UK Animal (Scientific Procedures) Act 1986.

- Primary cortical neurons culture

Primary cortical neuron cultures were obtained from C57/BL6 E16 mice brains as previously described (Lucci et al. 2020). Brain cortices were dissected, and the meninges separated under a dissection microscope. The tissue was further incubated in Hanks Balanced Salt Solution (HBSS, Ca^{2+} and Mg^{2+}-free; Gibco) with 1 mg/ml trypsin and 5 mg/ml DNAse I (Sigma-Aldrich) at 37°C for 30’. Following the addition of 0.05% (v/v) soybean trypsin inhibitor (Sigma-Aldrich), the tissue was mechanically dissociated in Neurobasal media (Invitrogen) supplemented with 1X GlutaMax and 2% B-27 (Gibco). Dissociated neurons were resuspended in supplemented Neurobasal media ($10x10^6$ cells/mL).

- Primary DRG neurons culture

Primary DRGs cultures were obtained from E18 rat embryos. Briefly, approximately 200 DRGs ganglions were extracted from 11-15 embryos per experiment in L15 cold media, trypsinized in Ca^{2+}-Mg^{2+} PBS 0.025% trypsin for 10 minutes at 37°C, 5% CO_2 and incubated with 0.1% collagenase type I (filtered 0.2 µm) for 20 min, 37°C, 5% CO_2. Pellet is resuspended and dissociated in DMEM *complete* media (2% B27, 2 mM glutamate, 1% PE, 50 ng/mL NGF, 50 ng/µL GDNF, 4 µM APH). Cells were centrifuged at 1000 g for 5 minutes, and the pellet resuspended in complete media before seeding into compartmentalized microfluidic chambers (Xona Microfluidics, Xona SND 150) pre-coated with laminin 20 µg/mL for 1 hour, 37°C. Then 10 µL of dissociated DRGs were seeded into the designated channel (approximately 30 DRGs in each).

- PC12 cell line culture and lentiviral transfection

PC12 cells from ATCC were grown in RPMI 1640 medium (Gibco) supplemented with 10% horse serum, 5% of fetal bovine serum and antibiotics (penicillin and streptomycin), at 37°C with 5% CO_2. Plastic surfaces were coated with 8 µg/cm^2 collagen I from rat tail. Neuronal differentiation was achieved by removing growth factors and antibiotics and exposing cells to 100 ng/mL of NGF 2.5S for at least 72 h. To achieve PDCD4 silencing, commercial lentiviral viral particles from Dharmacon GE, with an inducible shRNA against PDCD4, were used. After transfection, cells were grown in complete medium for 24 hrs and selected with 5 µg/mL of puromycin for 3-5 days. Cells were then cultured in complete medium to obtain stable cell lines able to induce silencing of PDCD4 or express a scrambled shRNA control.

- Neuroblastoma (Neuro2a) Cell line culture

Neuro2a cells were a kind gift from Robert Layfield lab, University of Nottingham, UK. Cells were maintained in DMEM, 10% FCS, 1% PS and seeded on 12-well plates at 1.5x10^5 cells/well.

siRNA and plasmid transfections

In the primary cortical neuron and Neuro2a cell line, transfections were performed 24 hours after neuron seeding (day 2 of cell culture) using Lipofectamine 2000 (Invitrogen) as suggested by manufacturer's instructions. 25 nM of siGENOME Mouse Pdcd4 SMARTpool 5 nmol (catalog number M-044032-01-0005) and siGENOME Non-Targeting siRNA Control Pool N°1 5 nmol (catalog number D-001206-13-05) both from GE Healthcare Dharmacon-Horyzon Solutions, using Lipofectamine 2000 (Invitrogen, Thermo Scientific), following the manufacturer's instructions. For plasmid transfections the PDCD4-pcDNA 3.1 (zero) was kindly gifted by Yang Hsin-Sheng, with empty plasmid used as a control. Both plasmids were applied at 2 µg final concentration and added 24 hours after neuron seeding (day 2 of cell culture). To identify transfected cortical neurons the siRNA and PDCD4 plasmids were co-transfected with pmax-GFP Green-cat (ThermoScientific) 1 µg of final concentration and cells were fixed 72 hours after transfection (day 5 of cell culture). In the specific case of primary DRG neuron cultures, the cell permeable Accell SMARTPOOL Pdcd4 siRNA 5 nmol (catalog number E-097927-00-0005) or Accell Non Targeting Pool 5 nmol (catalog number D-001910-10-05) both from Healthcare Dharmacon - Horyzon Solutions were incubated at 1 µM final concentration in the cell body side of compartmentalized chambers after DRGs develop neurites. 96 hours later neurons were fixed.

Semi-quantitative Real Time PCR

PDCD4 quantification in PC12 cells was performed by semi-quantitative real time PCR and ΔΔCt method (Livak and Schmittgen 2001). For this, RNA was isolated using Trizol (Invitrogen, Cat#15596026) or mirVana isolation kit (ThermoFisher, Cat# AM1560). Genomic DNA was removed by DNAse treatment (Invitrogen, Cat#AM2222) and RNA was re-isolated by the same method. cDNA was produced by retrotranscription by SuperScript II (Invitrogen, Cat#18064014) or III (Invitrogen, Cat#18080044) reverse transcriptase and quantified with SYBR Green Master Mix (Applied Biosystems, Cat#A25742) in Corbett Rotor-Gene 6000 instrument with the following PCR conditions: 10 minutes at 95°C, 40 cycles of: 15 seconds at 95°C, 15 seconds at 58°C and 45 seconds at 60°C; and 72°C to 90°C melting. In all cases, three independent biological replicates were used to evaluate significant differences by Student's test using RPL29 gene as housekeeping (Zhou et al. 2010).

For primary DRGs cultures, E18 rat embryos were cultured at two channel compartmentalized microfluidic chambers as described in the previous section. Axonal RNA was obtained as described previously (Garcez et al. 2016). To obtain cDNA, 50 ng of RNA were retrotranscribed by Superscript III reverse transcriptase (ThermoFisher, Cat#18080093) according to manufacturer instructions. The qPCR was performed using PowerUp SYBR Green (Applied Biosystems) in an Applied Biosystems Step One Plus thermocycler, using cycling parameters recommended by Applied Biosystems (mRNA). Data was acquired with Applied Biosystems SDS2.3 software. As above, RPL-29 gene was used as housekeeping gene (Zhou et al. 2010).

Primers sequences were obtained from literature: PDCD4 forward: 5'-TGAGCACGGAGATACGAACGA-3' and PDCD4 reverse: 5'-GCTAAGGACACTGCCAACACG-3' from (Liu et al. 2010), RPL29 forward: 5'-CAAGTCCAAGAACCACACCAC-3' and RPL29 reverse: 5'-GCAAAGCGCATGTTCCTCAG-3' from (Parker et al. 2013).

Immunohistochemistry and immunocytochemistry

- Tissue sections

For brain, cerebellum and sciatic nerve tissue, rats were intracardially perfused with 3% sodium citrate and then 4% PFA in PBS buffer. Tissue extraction was done after two hours of perfusion, and a final fixation step was performed overnight (ON), 4°C for brain and cerebellum and 1 hour at RT for sciatic nerves. 3x10 minutes washes in PBS and cryo-protection steps with successive incubations in 15 and

30% sucrose ON, 4°C for one and two days respectively were performed. Cryosections of 20 µm were collected on glass slides pre-treated with Poly-L-Lysine 0.1% in mQ water. Permeabilization with 0.5% Triton in the PHEM buffer for 20 minutes at RT, 3x5 washes in PHEM buffer and blocking in 3% BSA, 1% glycine for 30 minutes at RT were developed. Incubation with the primary and secondary antibodies was performed in a blocking buffer with 5% NGS, ON at 4°C with 3x10 minutes washes in buffer PHEM between and after incubation.

- Primary neurons and cell lines

For cortical, DRG neurons, PC12 and Neuro2a cell lines, the media was removed, and cells rinsed with PBS and fixed with 4% PFA with 5 mM $CaCl_2$ and 4% sucrose in PBS buffer for 30 minutes (RT). Cells were permeabilized in 0.2% Triton + 10 mM glycine in PBS for 20 minutes at RT. Incubation with the primary antibody was made in 3% BSA ON at 4°C, while incubation with secondary antibodies was made in the same buffer for 2 hours at RT. Cells were mounted using Vectashield with DAPI or Pro-Long Antifade reagent.

List of antibodies and probes

Rabbit polyclonal PDCD4 antibody (dilution 1:200) Abcam (ab51495); Mouse monoclonal MAG antibody (dilution 1:1500) Millipore (Cat#MAB1567); Mouse monoclonal antibody Phospho-p70 S6 Kinase (Thr389) (1A5) (dilution 1:400) CellSignaling (#9206); Mouse Monoclonal Anti-Acetylated Tubulin antibody (dilution (1:1000) Sigma - Aldrich (Cat#T7451); Alexa Fluor 555 Phalloidin (dilution 1:150) Invitrogen-ThermoFisher (Cat#A34055); Alexa Fluor 647 Phalloidin (dilution 1:150) Invitrogen-ThermoFisher (Cat#A22287); Goat anti-Mouse IgG, (H+L) HRP conjugate antibody Millipore (Cat# AP308P); Swine anti-rabbit IgG HRP antibody Dako (Cat# P0217); Goat anti-Mouse IgG (H+L) Cross-Adsorbed Secondary Antibody Alexa Fluor 488 (dilution 1:1000) ThermoFisher (Cat# A-11001); Goat anti-Mouse IgG (H+L) Secondary Antibody, Alexa Fluor 555 conjugate (dilution 1:1000) ThermoFisher (Cat# A-21422); Goat Anti-Mouse IgG (H+L) Antibody Alexa Fluor 633 Conjugated (dilution: 1:1000) ThermoFisher (Cat# A-21052); DAPI (dilution 1:2000) ThermoFisher (Cat#D1306).

Puro-PLA protocol

A total of 2 independent experiments were made. Ventral roots were extracted from adult rats and incubated in neurobasal media with puromycin at 300 µM final concentration for 15 and 30 minutes or without puromycin as a control condition. Then a fixation with 4% PFA for 1 hour was performed and cryosections were made as described above.

The PLA protocol was carried-out according to the manufacturer's instructions of DuoLink, Sigma using the following reagents: Duolink® In Situ PLA® Probe Anti-Rabbit PLUS dilution 1/5 (Cat#DUO92002-30RXN), Duolink® In Situ PLA® Probe Anti-Mouse MINUS dilution 1/5 (Cat#DUO92004-30RXN), Duolink® In Situ Detection Reagents FarRed (DUO92013-30RXN).

Protein extraction and western blot protocol for Neuro2a cell line

A total of 3 independent experiments were performed. Cells were scraped 72 h after transfection, lysed with 150 µL of RIPA (50 mM Tris-HCl, pH 8.0, with 150 mM sodium chloride, 1.0% Igepal CA-630 (NP-40), 0.5% sodium deoxycholate and 0.1% sodium dodecyl sulphate), centrifuged for 20 min at 12,000g and supernatants collected and run on a 12% SDS-PAGE gel. Proteins were separated by standard electrophoresis protocol. For blocking step 5% milk in TBST (TBS buffer with Tween-20 0.1%) was used for 1 hour at RT. The primary antibodies were incubated ON, 4°C and a chemiluminescence protocol was performed using HRP secondary antibodies. The enzyme substrate was the Supersignal West femto-maximum sensitivity substrate revealed and was incubated for 1 minute and then washed with blocking buffer. Western blot bands were detected with a Las 3000 mini from FUJIFILM using the accumulated signal method.

Image acquisition

Neo-cortex, cerebellum, sciatic nerves and PC12 cells images were taken on the LSM confocal OLYMPUS FV300 using a 60X oil, NA 1.42 objective. The software for controlling the microscope and taking the images was the Fluoview version 5.0c.

For primary cultures, an inverted fluorescent microscope ZEISS axiovert 200M coupled to a CCD camera (Photometrics CoolSnap MYO) was used. For axon length images, a 10X air NA 0.3 or 20X air NA 0.8 were used, while quantification of immunofluorescence used a 63X oil NA 1.3. The micromanager software version 1.4 was employed to acquire the images and control the microscope.

For PLA experiments on ventral roots an LSM confocal ZEISS 800 was used. A 63x oil, NA 1.4 premium objective adapted for AiryScan was used for image acquisition. The stacks were always taken at ideal

µm number between each z plane. The software for controlling the microscope and taking the images was the ZEN Blue version 2.3.

Image quantification and analysis

In all image quantification analysis, we kept the same PMT (below 700 V) and/or time exposures of the camera in order to compare control and experimental conditions. We also kept the same PMT (below 700 V) and same laser intensities for each experiment between conditions, with all the images from each experimental group taken on the same day.

- Quantification of fluorescence

Quantification of expression levels from immunofluorescence signals at different regions of interest (ROIs) was made with Fiji (Just ImageJ) software (Schindelin et al. 2012). Following the selection of ROIs, the Raw_Integrated_Density was calculated and divided by the size of the selected area. For each condition an average of these values was calculated and normalized against its control. The value for the controls was defined as 1. For the selection of ROIs in cortical and DRG neurons the acetylated tubulin was used to define subcellular compartments. For quantitative analysis in cortical neurons a total of 292 cell bodies and 129 axons were quantified from three independent experiments (unless as indicated for day 12) In experiments with sciatic nerve ventral roots axoplasms, MAG, phalloidin and light-chain neurofilament 68 KDa were used as counter-stains.

- Quantification of axonal length of cortical neurons

Images were taken from at least four independent preparations. GFP-positive neurons were assessed with axons defined as a neurite that was longer than 80 µm and at least three times the length of other processes, measured from the cell body to the distal extent of the central region of the growth cone. Selected axon projections were measured using ImageJ, and the data expressed as percentage of the respective controls. For determination of axon versus branch, the axon was defined as the process that remained parallel to the axon segment proximal to the branch point. Branches were defined as processes extending at orthogonal angles to the axon. Total length of axon branches was not included in the measurement. The average length of axons in control groups was ± 341 µm (mean ± 14.92). The average for each experimental condition (siRNA PDCD4 or plasmid PDCD4) was normalized against its control. A total number of ~400 cortical axons were measured per condition for the PDCD4 overexpression analysis and ~600 axons per condition for the PDCD4 silencing analysis. The n number was defined as separate experiments from independent neuronal preparations for all conditions.

- Quantification of axonal length of DRG neurons

A stitched image of the entire axonal channel of the microfluidic chambers stained for axons (acetylated tubulin) was obtained using micromanager software and the stitching plugin of Fiji software for each axonal microfluidic compartment. A total of 4 independent experiments with siRNA control chambers and 3 with siRNA of Pdcd4 were used (in total 9 siRNA Control and 7 siRNA PDCD4 chambers were used). Image analysis for neuron growth was processed using the Neuron_Growth plugin software developed by Fanti & collaborators at the Universidad Nacional Autónoma de México (http://www.ifc.unam.mx/ffm/conditions.html). The same software settings were used for all images and the percentage of the area covered by the axons was quantified. Average values were calculated for the siRNA control chambers and for the siRNA PDCD4 chambers and normalized to the internal control.

- Quantification of neurite length of differentiated PC12 cells

Images were taken from five independent preparations. For quantifying neurite length of differentiated PC12 cells in the presence and absence of PDCD4, three independent cell cultures were growth for each condition. After 72 h of shRNA induction, cells were exposed to NGF for 72 h to achieve neuron-like differentiation. The free line tool of ImageJ was used to mark neurites in several optic fields for each culture and length was quantified. An average of 80 neurites were quantified per replicate. Neurite length was contrasted in the two conditions comparing 3 vs 3 averages per replicate

- Puro-PLA Pdcd4 spots quantifications

Fiji (just ImageJ) software was used to quantify PLA signal. After selection of axoplasm regions (counterstained with phalloidin and/or light-chain-neurofilament) from Z-stack images a z project with maximum intensity projection algorithm was used to obtain a single image with all the PLA spots for each stack. Then a threshold was defined to detect each spot as black and the rest as white. Then the “analyze particles” algorithm was used with the size between 0.20-10 in all cases. The “masks display exclude clear” algorithm was used to count and see the mask on each spot and to control if the protocol was adequately working for each image. The experiment without puromycin was used as a control condition and the count of PLA/area were defined as “1”. Following this, the PLA counts for 15 minutes and 30 minutes exposure to puromycin were normalized to the control.

- Western Blot quantification

Images were obtained with the same exposure settings. Fiji (Just ImageJ) gel quantification software was used selecting ROIs equal to the biggest protein band for each image. Each band was quantified and then divided by the one corresponding to actin (control band) for each line. The values corresponding to siRNA PDCD4 were expressed as a percent of the siRNA control.

Ribosome Profiling

After 72 h of 100 ng/mL NGF 2.5S and 500 ng/mL doxycycline exposure, to achieve neuronal differentiation and shRNA expression, $80x10^6$ cells per condition were used to isolate total RNA and polysomes, in two biological replicates per condition. For this, cells were treated with 100 mg/µL of cycloheximide (CHX) for 1 hour at 37°C in the hood to stop translation before collection of RNA on ice. A Transcriptome sample was separated to use as total RNA control and submitted to RNA extraction using mirVana isolation kit (ThermoFisher, Cat# AM1560) and RNA-Seq protocol. At the same time, a proteome sample was separated and submitted to label-free quantitative proteomics using an Orbitrap Fusion. For translatome samples, cells were lysed and post mitochondrial supernatant was loaded in a 12%-33.5% sucrose cushion and ultracentrifugated in SW40Ti rotor at 35,000 RPM for 2:45 hrs at 4°C. Polysomal pellet was resuspended and digested with 200 U of Benzonase for 10 minutes at RT. Digestion was stopped with mirVana Lysis Buffer to continue with RNA isolation. Ribosomal footprints were isolated running a denaturalized 15% PAGE 7M urea, cutting the proper band identified by length (~30nt) and extracting RNA from gel slice. Ribosomal footprints (Translatome sample) are then concentrated by precipitation and quality and quantity checked using 2100 Agilent Bioanalyzer Small RNA Kit.

Sequencing and bioinformatic analysis

All transcriptome and translatome samples were sequenced in BGI Tech Solutions. Transcriptome samples were submitted to RNA-Seq Quantification Library (Normal Library: 2-10 µg) protocol, using poly(A)+ selection and 20 millions of paired-end (2x100 bp) reads were obtained. Translatome samples were submitted to Small RNA Library (Low-Input Library: 0.2-1 µg) protocol and 40 millions of single-end reads were obtained.

Fastq files obtained were analyzed using servers available in the Genomics Department at IIBCE. Sequences were mapped using bowtie2 (Langmead and Salzberg 2012) versus curated mRNAs described in the mouse genome (available at NCBI ftp site). For translatome samples, sequences were first mapped against *Rattus norvegicus* rRNA genes to remove contamination. Reads counts were estimated by featureCounts (Liao et al. 2014) and differential gene expression analysis between transcriptomes or translatomes was done using edgeR (Robinson et al. 2010). Normalized counts were exported and translational efficiency was calculated and contrasted between conditions (shPDCD4 vs shScrambled) using Xtail R package (Xiao et al. 2016). Gene lists analysis were performed using on-line free tools like STRING (Jensen et al. 2009) and an in-house software (manuscript in preparation; https://github.com/sradiouy/IdMiner).

Protein samples were submitted to label-free quantitative proteomics using an LC-MS/MS Orbitrap Fusion instrument. Protein intensity values (LFQ/iBAQ) were averaged and statistical differences were reported using ANOVA.

General statistical analysis

All data groups shown are expressed as the mean ± SEM and the probability distribution of the data set was analyzed before further statistical analysis. Normality tests were made for all the data sets. With normal data, a two tailed t-student test was performed or paired t test for plasmid and siRNA axonal length quantifications. If the data sets don't pass the normality tests, a Mann Whitney test was used. In all cases p values less or equal to 0.05 were considered as significant. Each “n” was defined as an independent experiment from a separate culture preparation. The following general code was used: (*): p value <0.05; (**): p value <0.01; (***): p value <0.001.

Supplementary Figures Legends.

Figure S1. (A) Fluorescent image of cortical neurons overexpressing PDCD4: GFP and PDCD4 expression is shown in cortical neurons transfected with a PDCD4 cDNA plasmid or with a pcDNA control plasmid. In both cases, a GFP co-transfected plasmid was used as a positive evidence of transfection. White arrows indicate the transfected neurons (scale bar 20 µm). The right panel shows quantification of PDCD4 levels, detecting an increase of 2.3 fold compared to the control condition (p value (***) ≤0.001, two tailed Mann Whitney test, n=3 with 3 technical replicates, error bars: SEM). **(B)** Same as (A) but for cortical neurons were PDCD4 was knockdown using a mix of 4 siRNA sequences against PDCD4 (Dharmacon siRNA SMARTPOOL) or a mix of 4 scrambled siRNA sequences as control. Again a GFP co-transfected plasmid was used, and the white arrows show the transfected neurons (scale bar 20 µm). The right panel shows quantification of PDCD4 levels, detecting a decrease of 0.66 fold compared to the control (p value (**) ≤0.01, two tailed Mann Whitney test, n=3 with 3 technical replicates, error bars: SEM). **(C)** Fluorescent image of DRG neurons were PDCD4 was knockdown using 4 cell permeable siRNA sequences against PDCD4 (Dharmacon Accell siRNA SMARTPOOL) or a mix of 4 Accell scrambled siRNA sequences as control. Tubulin and PDCD4 expression is shown (scale bar 20 µm). The right panel shows quantification of PDCD4 levels detecting a decrease of 0.65 fold compared to the control (p value (*) ≤0.02, two tailed Mann Whitney test, n=3 with 3 technical replicates, error bars: SEM). **(D)** To test if the siRNA probes or plasmids have an effect on total PDCD4 protein levels, we transfect N2A cell line, as a high transfection efficiency model. PDCD4 expression is shown by western blot as the upper bands, while lower bands correspond to actin as a loading control. The right panel shows relative quantification of PDCD4 Western Blots bands (p value (***) ≤0.001 and p value (*) ≤0.02, two tailed Mann Whitney test, n=3 with 2 technical replicates, error bars: SEM).

Figure S2. PDCD4 expression silenced by inducible shRNA in the PC12 cell line. Inducible PDCD4 silencing in PC12 cells was achieved by lentiviral transfection and confirmed by semi-quantitative RealTime PCR and immunofluorescence. **(A)** PDCD4 expression was followed at different time points of NGF-induced neuron differentiation in wt PC12 cells using immunofluorescence. **(B)** Neuron-like phenotype achieved in PC12 cells after 72 h of NGF exposure, evidenced by phase contrast microscopy. **(C)** PDCD4 expression evaluated by immunofluorescence was analyzed in PC12-shScrambled and PC12-shPDCD4 cells after NGF exposure alone or with shRNA expression induction by doxycycline (DOX). Illustrative images are shown. **(D)** PDCD4 signal quantification shows a high decrease in PDCD4 only in PC12-shPDCD4 exposed to NGF+DOX (p value (**) <0.01, One-way ANOVA with post-hoc Tukey test; n=2 with almost 150 cells analyzed per replicate). **(E)** PDCD4 silencing was also confirmed by semi-quantitative RealTime PCR (p value (***) <0.001, Student's t test, n=3, error bars: SD). **(F)** GFP expression was also monitored by immunofluorescence as an indication of shRNA expression induction by DOX. Illustrative images are shown. **(G)** Quantification of GFP signal shows insignificant levels in absence of DOX while considering levels when is present. Differences were statistically significant (p value (**) <0.01, one-way ANOVA with post-hoc Tukey test, n=2 with almost 150 cells analyzed per replicate). In A-C and F scale bars means 20 µm.

Figure S3. RNA-Seq and Ribo-Seq data were analyzed individually by edgeR. **(A)** Ribosomal footprints periodicity was explored comparing 5'-end read mapping distribution among the three codon nucleotides. Each dot represents a fraction of reads in each position for each sample (transcriptome RNA-Seq derived and translatome Ribo-Seq derived). For translatome samples the first position in the codon tends to be enriched but for transcriptome samples distribution tends to be uniform. **(B)** Mapping distribution among mRNA features was studied comparing 5'UTR, CDS and 3'-UTR expression and comparing between transcriptomes and translatomes. In the first, the three regions are expressed while for translatome samples CDS is preferentially expressed over UTRs regions. **(C)** Inter-replicate Pearson correlation value is shown for transcriptome and translatome samples, in the two conditions (shScrambled and shPDCD4). **(D)** and **(E)** Volcano and MA plot, respectively, for transcriptome compartment (RNA-Seq). **(F)** and **(G)**, same as (D) and (E) but for translatome compartment (Ribo-Seq). In D-G red and green dots indicate differentially expressed genes, up- and down-regulated, respectively (|fold change| >2 and p value <0.05).

Figure S4. Heatmap of potential PDCD4 targets. RNA-Seq and Ribo-Seq expression levels in PDCD4 presence and absence (shScrambled and shPDCD4, respectively) is shown for the 267 putative PDCD4 mRNA targets.

Figure S5. Quantification and comparison of protein abundance in PDCD4 presence and absence (shScrambled and shPDCD4, respectively) by label-free quantitative proteomics. **(A)** Scatter plot comparing protein abundance (LFQ/iBAQ values) in shScrambled and shPDCD4 conditions. Red and green dots indicate differentially expressed proteins, up- and down-regulated respectively (p value <0.05 estimated by ANOVA). PDCD4 is indicated in the scatter where the knock-down could be also evidenced. **(B)** Correlation between fold change values estimated by proteomics and Ribo-Seq for 87 differentially expressed proteins at the proteome that also show the same direction of change in the Ribo-Seq data.

Figure S6. Functional protein association network by STRING for PDCD4 putative translational targets defined by translational efficiency criteria **(A)** and for the opposite direction genes **(B)**. In (A) the 4 functional-related clusters discussed in the text are indicated: Cluster 1 in blue, highlighting genes associated to mitosis and cell cycle; Cluster 2 in red, highlighting genes associated to the nucleus; Cluster 3 correspond to mitochondrial activity and Cluster 4 in yellow, highlighting genes associated to protein export. Disconnected nodes are hidden in (A) but shown in (B) for illustrative reasons.

Figure S7. Lentiviral shPDCD4 on cortical neurons cultured *in vitro* upregulates total levels of NFKB2 measured by Western Blot. **(A)** Cortical neurons were transfected with increasing amounts of lentiviral particles (+ and ++) containing shPDCD4 sequences, or with vehicle (no lentiviral particles). Western blot bands for PDCD4, NFKB2 and TUBB3 as non-target control are shown in each case. **(B)** Relative quantitation of PDCD4 and NFKB2 levels in each condition is shown. While levels of PDCD4 descend down to three-fold with increasing lentiviral particles, NFKB2 levels increase more than two fold.

Figure S8. Comparison of down-regulated mRNAs targets after PDCD4 knockdown with previously reported axonal transcriptomes. **(A)** Venn diagram showing the intersection between TE down-regulated mRNAs by PDCD4 and axonal transcriptomes described in Figure 4B. Separate and overlapping expressions between samples are shown. Only transcripts with a level of expression of TPM ≥ 1 were considered. **(B)** The table shows the type of neuron used in each study, the total genes detected and the number of common genes between potential PDCD4 targets (or potential PDCD4 targets related to axonal growth) and each axonal transcriptome. The EASE Score (a modified Fisher Exact *p-value*) is also shown, which indicates gene-enrichment.

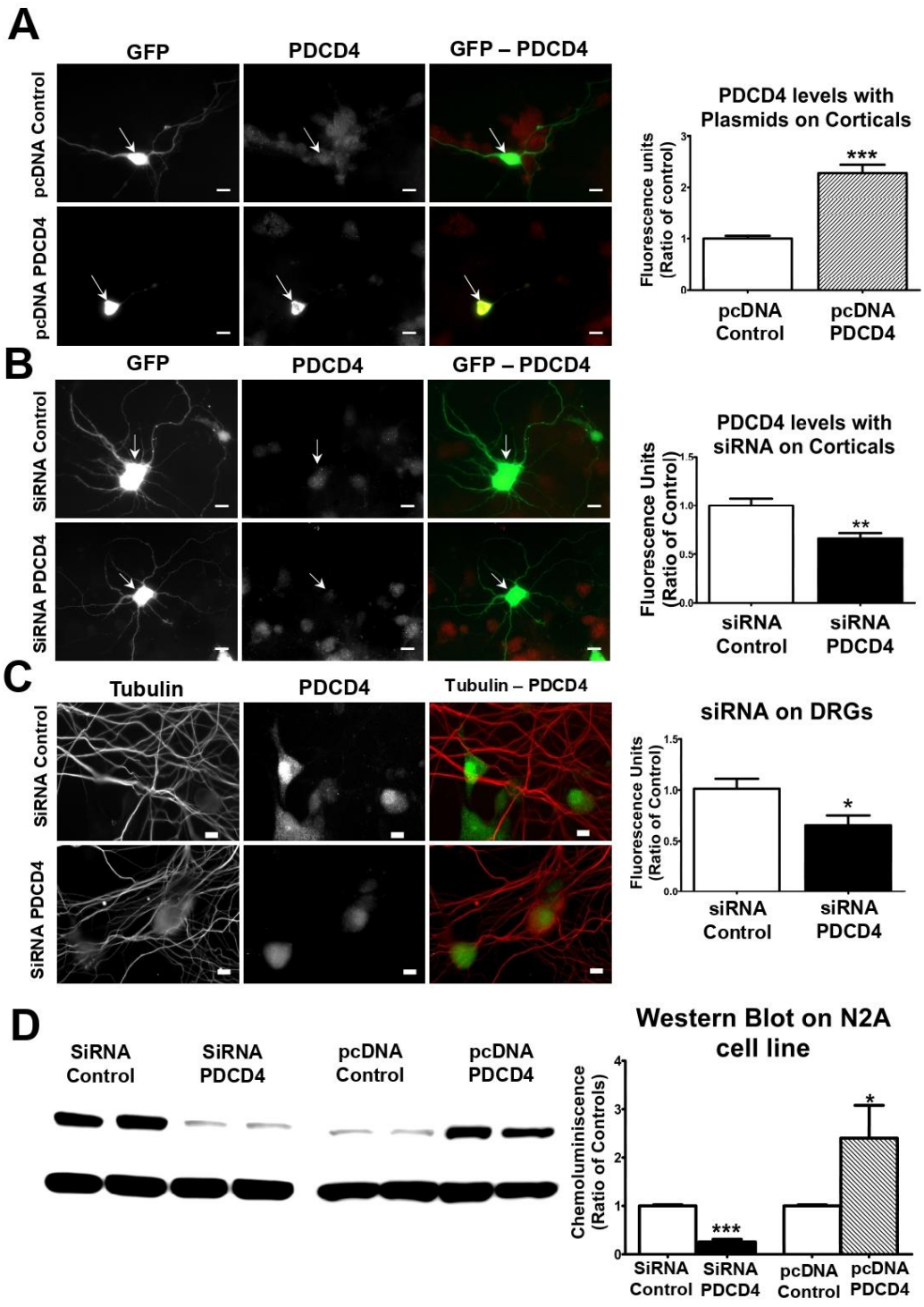
A
GFP
PDCD4
GFP – PDCD4
pcDNA Control
pcDNA PDCD4
PDCD4 levels with Plasmids on Corticals
Fluorescence units (Ratio of control)
***
pcDNA Control
pcDNA PDCD4
B
GFP
PDCD4
GFP – PDCD4
SiRNA Control
SiRNA PDCD4
PDCD4 levels with siRNA on Corticals
Fluorescence Units (Ratio of Control)
**
siRNA Control
siRNA PDCD4
C
Tubulin
PDCD4
Tubulin – PDCD4
SiRNA Control
SiRNA PDCD4
siRNA on DRGs
Fluorescence Units (Ratio of Control)
*
siRNA Control
siRNA PDCD4
D
SiRNA Control
SiRNA PDCD4
pcDNA Control
pcDNA PDCD4
Western Blot on N2A cell line
Chemoluminiscence (Ratio of Controls)
***
*
SiRNA Control
SiRNA PDCD4
pcDNA Control
pcDNA PDCD4

Figure S1

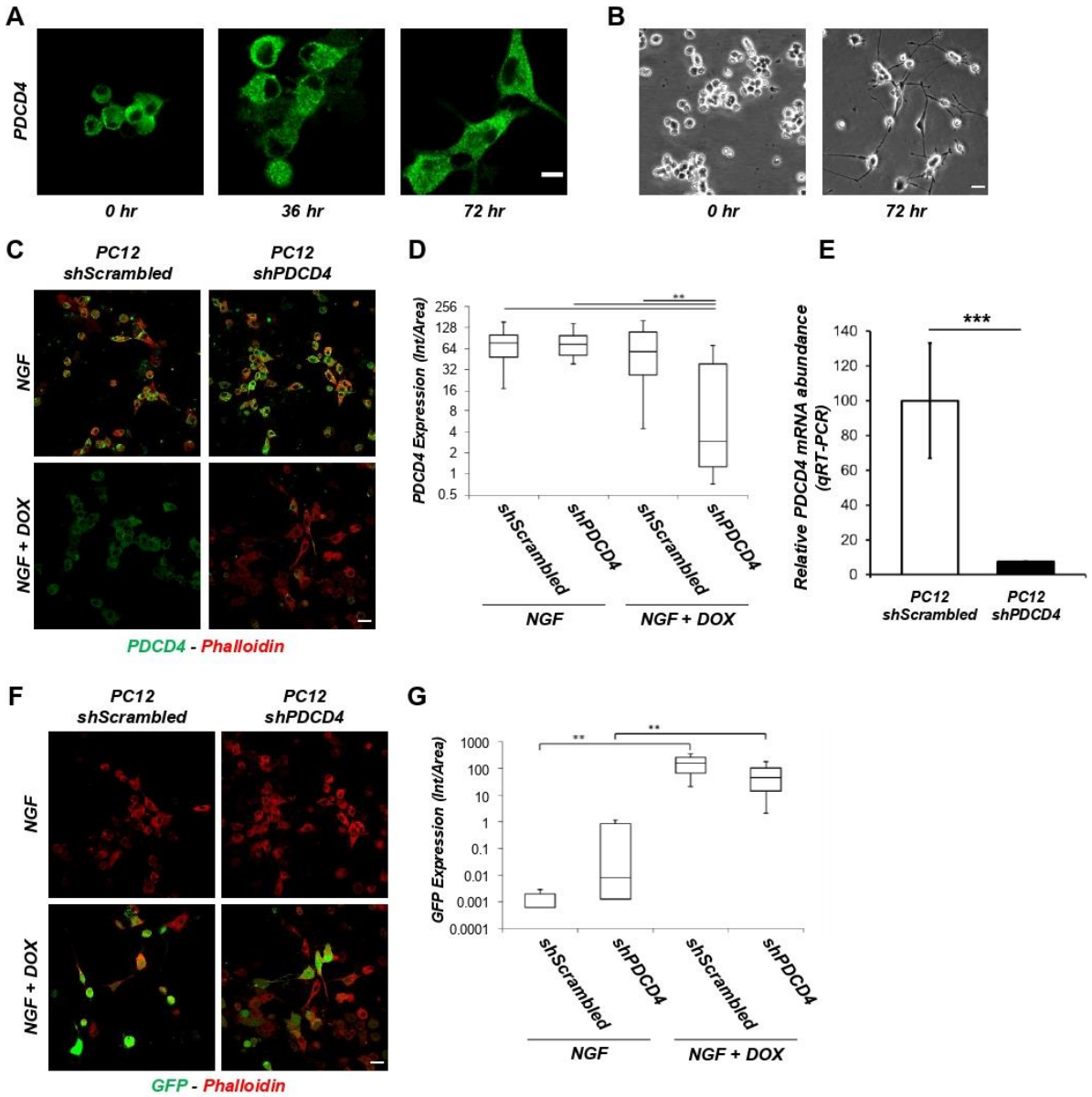
A
PDCD4
0 hr
36 hr
72 hr
B
0 hr
72 hr
C
PC12 shScrambled
PC12 shPDCD4
NGF
NGF + DOX
PDCD4 - Phalloidin
D
PDCD4 Expression (Int/Area)
256
128
64
32
16
8
4
2
1
0.5
**
shScrambled
shPDCD4
shScrambled
shPDCD4
NGF
NGF + DOX
E
Relative PDCD4 mRNA abundance (qRT-PCR)
140
120
100
80
60
40
20
0
***
PC12 shScrambled
PC12 shPDCD4
F
PC12 shScrambled
PC12 shPDCD4
NGF
NGF + DOX
GFP - Phalloidin
G
GFP Expression (Int/Area)
1000
100
10
1
0.1
0.01
0.001
0.0001
**
**
shScrambled
shPDCD4
shScrambled
shPDCD4
NGF
NGF + DOX

Figure S2.

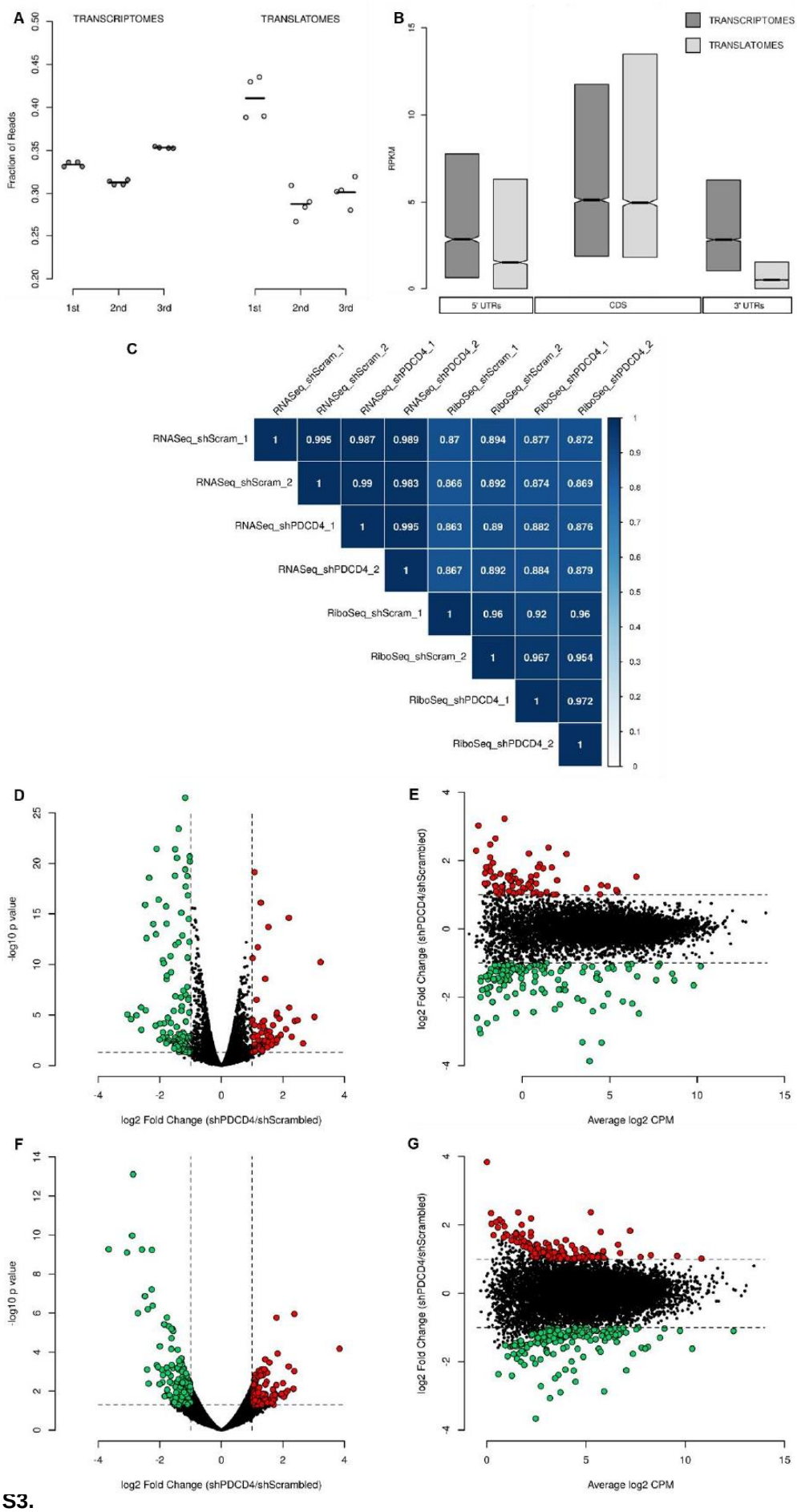
A
TRANSCRIPTOMES
TRANSLATOMES
Fraction of Reads
1st
2nd
3rd
B
TRANSCRIPTOMES
TRANSLATOMES
RPKM
5' UTRs
CDS
3' UTRs
C
RNASeq_shScram_1
RNASeq_shScram_2
RNASeq_shPDCD4_1
RNASeq_shPDCD4_2
RiboSeq_shScram_1
RiboSeq_shScram_2
RiboSeq_shPDCD4_1
RiboSeq_shPDCD4_2
1 0.995 0.987 0.989 0.87 0.894 0.877 0.872
1 0.99 0.983 0.866 0.892 0.874 0.869
1 0.995 0.863 0.89 0.882 0.876
1 0.867 0.892 0.884 0.879
1 0.96 0.92 0.96
1 0.967 0.954
1 0.972
1
D
-log10 p value
log2 Fold Change (shPDCD4/shScrambled)
E
log2 Fold Change (shPDCD4/shScrambled)
Average log2 CPM
F
-log10 p value
log2 Fold Change (shPDCD4/shScrambled)
G
log2 Fold Change (shPDCD4/shScrambled)
Average log2 CPM

Figure S3.

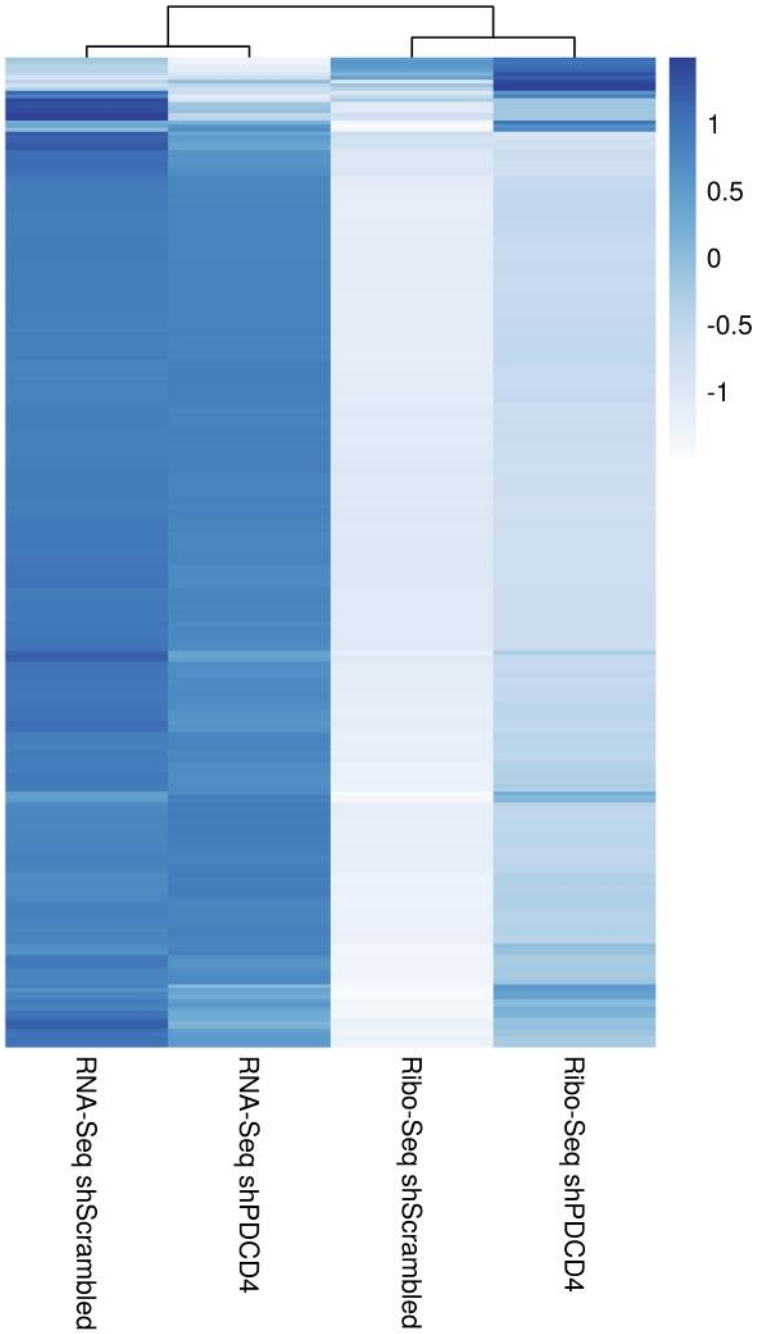
1
0.5
0
-0.5
-1
RNA-Seq shScrambled
RNA-Seq shPDCD4
Ribo-Seq shScrambled
Ribo-Seq shPDCD4

Figure S4.

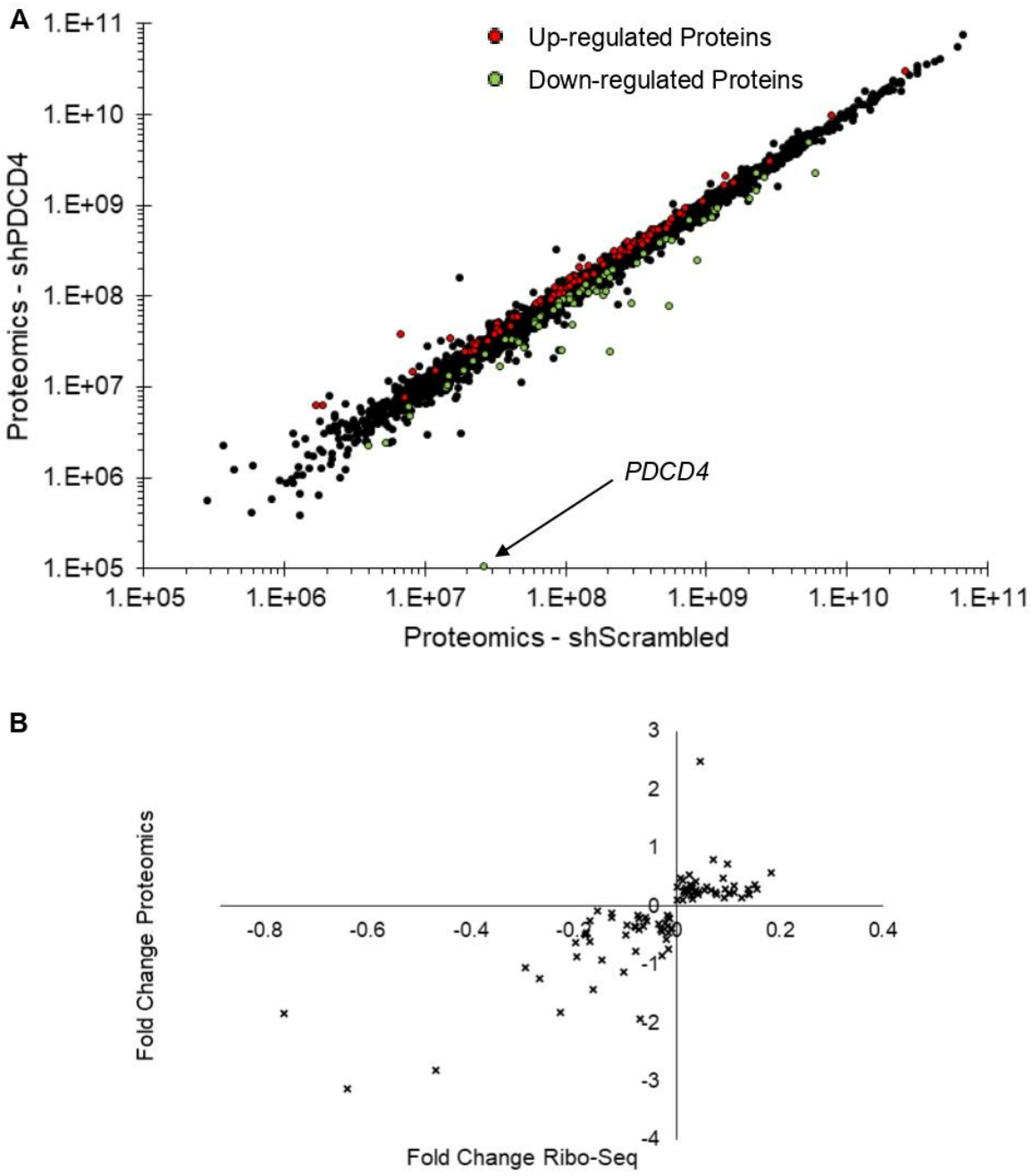
A
Up-regulated Proteins
Down-regulated Proteins
Proteomics - shPDCD4
Proteomics - shScrambled
PDCD4
1.E+11
1.E+10
1.E+09
1.E+08
1.E+07
1.E+06
1.E+05
B
Fold Change Proteomics
Fold Change Ribo-Seq
3
2
1
0
-1
-2
-3
-4
-0.8
-0.6
-0.4
0.2
0.4

Figure S5.

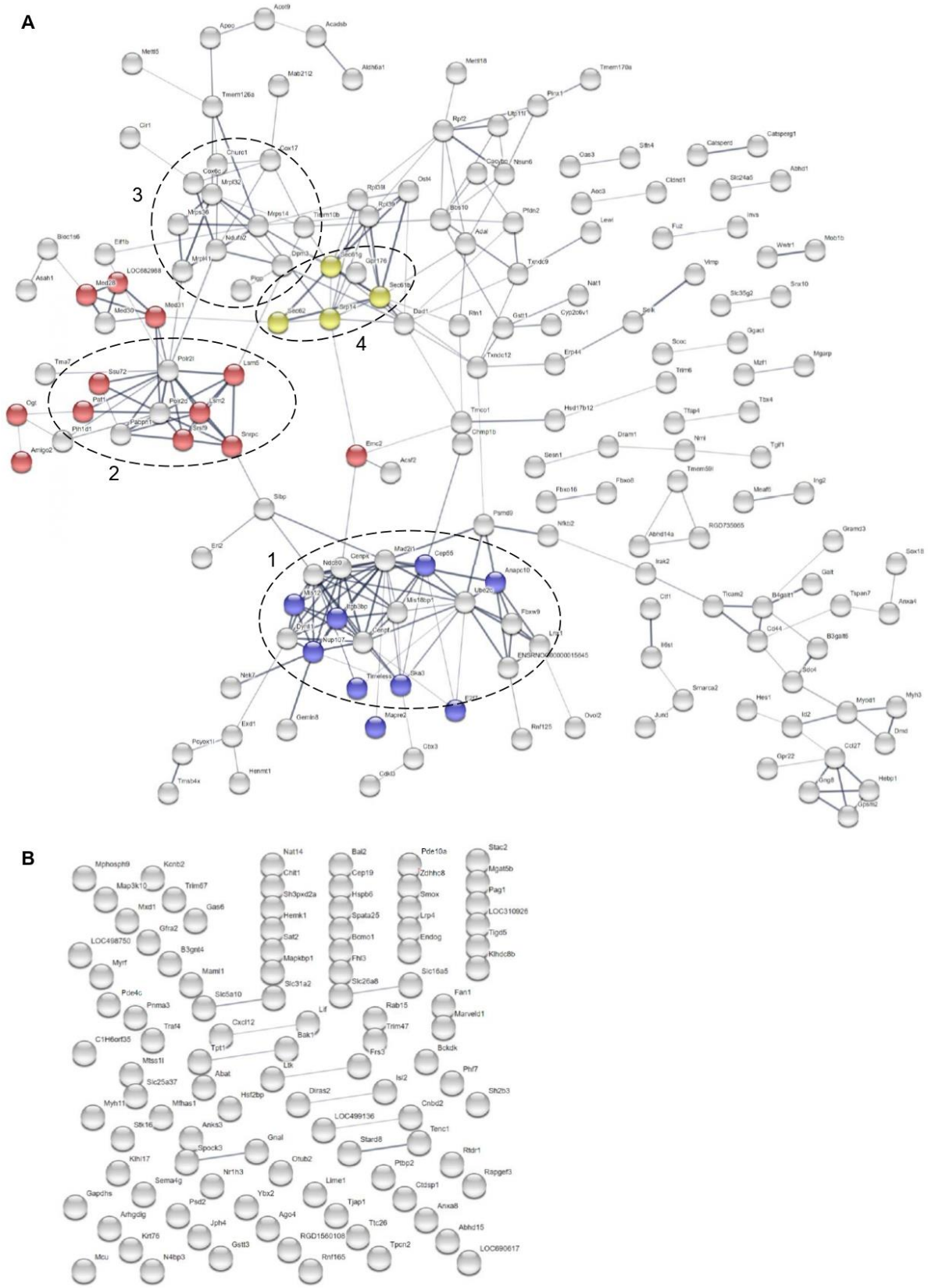

Figure S6.

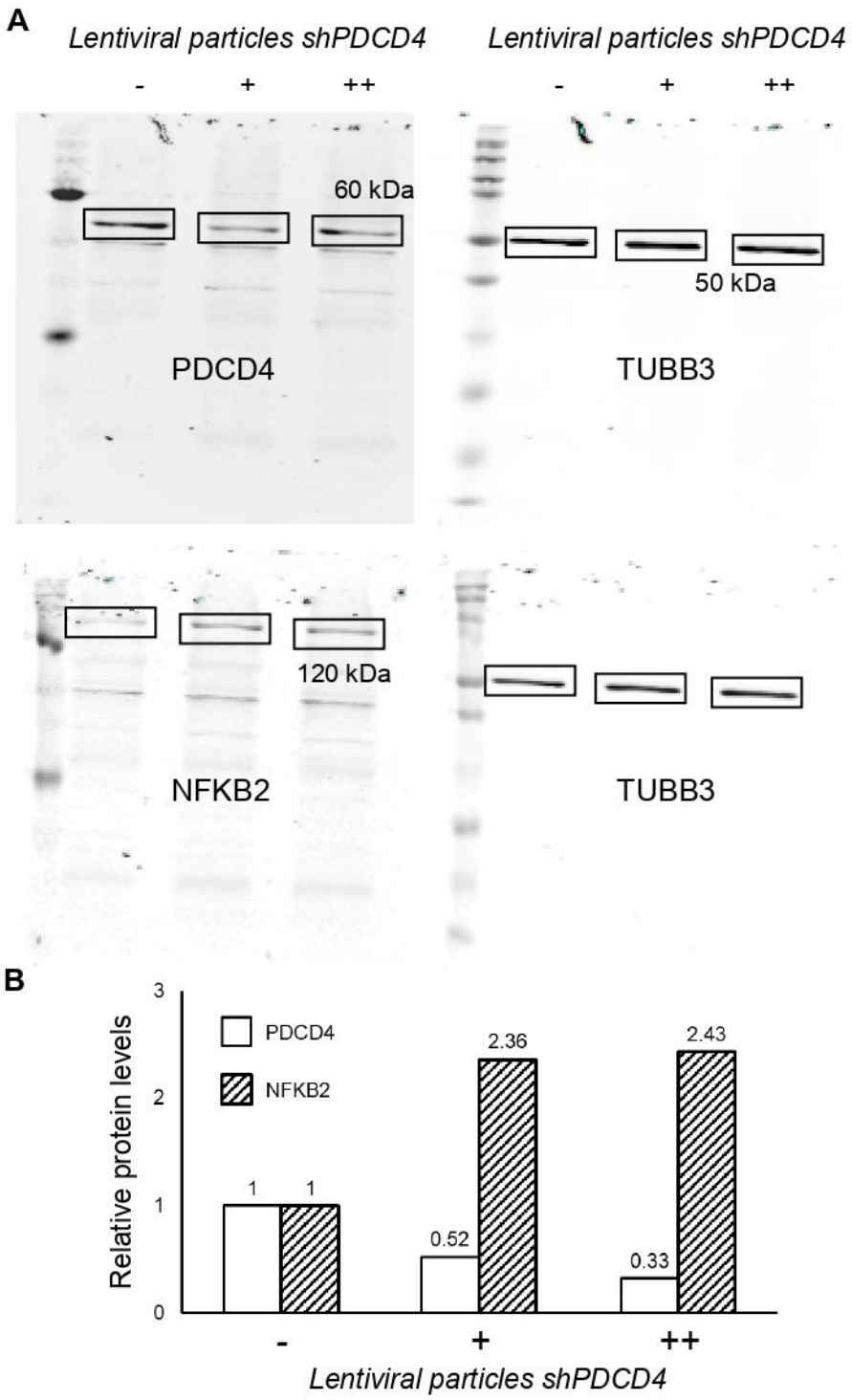
A
Lentiviral particles shPDCD4
- + ++
60 kDa
PDCD4
Lentiviral particles shPDCD4
- + ++
50 kDa
TUBB3
120 kDa
NFKB2
TUBB3
B
Relative protein levels
PDCD4
NFKB2
1 1
0.52
2.36
0.33
2.43
0 1 2 3
- + ++
Lentiviral particles shPDCD4

Figure S7.

A

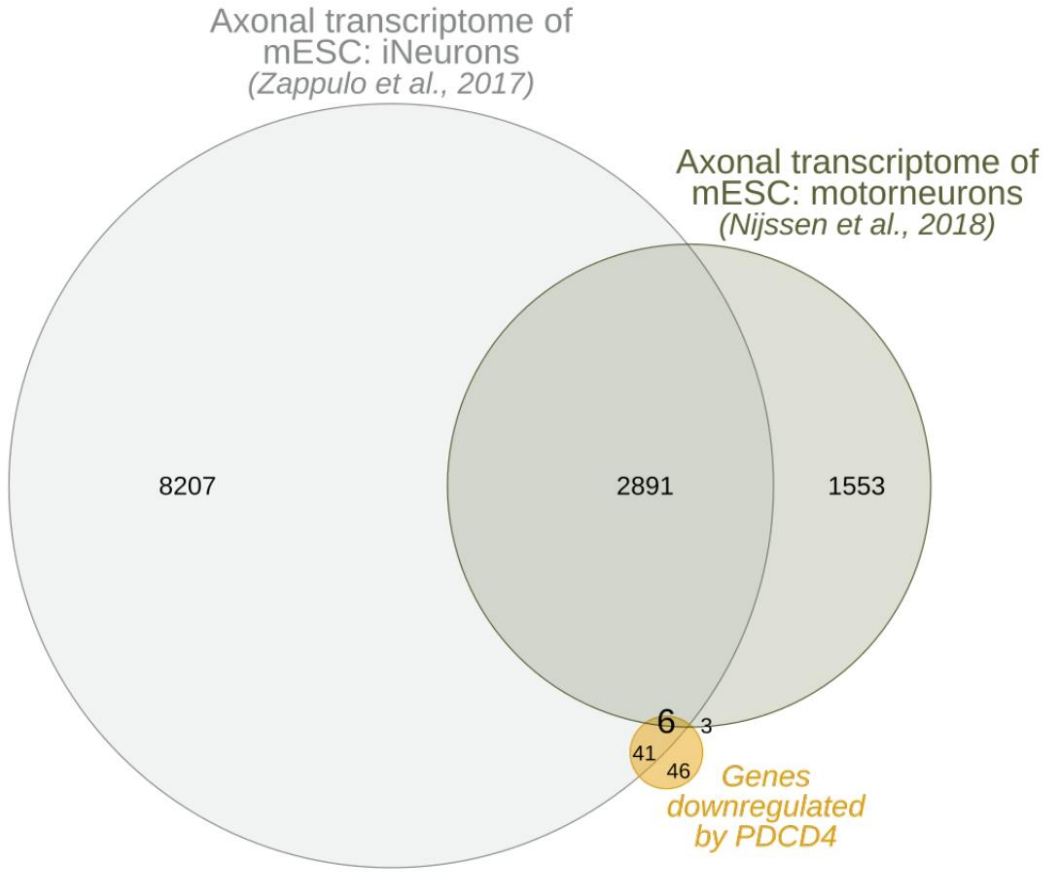

B

Neuron	Total genes	In common with genes downregulated by PDCD4	Reference
		All (EASE Score)	
mESC:iNerons	11145	47 (0.2263)	Zappulo *et al., 2017*
mESC:motorneuron	4453	9 (0.1118)	Nijssen *et al., 2018*

Figure S8.

Supplementary Tables Legends.

Table S1. Total number of reads sequenced and mapped in both transcriptome and translatome samples.

Table S2. Average RPKM expression values, $\log_2$ fold change in translational efficiency and p values for putative PDCD4 targets.

SI References

Garcez PP, Guillemot F, Dajas-Bailador F. 2016. Study of miRNA Function in the Developing Axons of Mouse Cortical Neurons: Use of Compartmentalized Microfluidic Chambers and In Utero Electroporation. *MicroRNA Technologies* 59–71. http://dx.doi.org/10.1007/7657_2016_12.

Jensen LJ, Kuhn M, Stark M, Chaffron S, Creevey C, Muller J, Doerks T, Julien P, Roth A, Simonovic M, et al. 2009. STRING 8--a global view on proteins and their functional interactions in 630 organisms. *Nucleic Acids Res* **37**: D412–6.

Langmead B, Salzberg SL. 2012. Fast gapped-read alignment with Bowtie 2. *Nat Methods* **9**: 357–359.

Liao Y, Smyth GK, Shi W. 2014. featureCounts: an efficient general purpose program for assigning sequence reads to genomic features. *Bioinformatics* **30**: 923–930.

Liu X, Cheng Y, Yang J, Krall TJ, Huo Y, Zhang C. 2010. An essential role of PDCD4 in vascular smooth muscle cell apoptosis and proliferation: implications for vascular disease. *Am J Physiol Cell Physiol* **298**: C1481–8.

Livak KJ, Schmittgen TD. 2001. Analysis of Relative Gene Expression Data Using Real-Time Quantitative PCR and the 2−ΔΔCT Method. *Methods* **25**: 402–408. http://dx.doi.org/10.1006/meth.2001.1262.

Lucci C, Mesquita-Ribeiro R, Rathbone A, Dajas-Bailador F. 2020. Spatiotemporal regulation of GSK3β levels by miRNA-26a controls axon development in cortical neurons. *Development* **147**. http://dx.doi.org/10.1242/dev.180232.

Parker SS, Mandell EK, Hapak SM, Maskaykina IY, Kusne Y, Kim J-Y, Moy JK, St John PA, Wilson JM, Gothard KM, et al. 2013. Competing molecular interactions of aPKC isoforms regulate neuronal polarity. *Proc Natl Acad Sci U S A* **110**: 14450–14455.

Robinson MD, McCarthy DJ, Smyth GK. 2010. edgeR: a Bioconductor package for differential expression analysis of digital gene expression data. *Bioinformatics* **26**: 139–140.

Schindelin J, Arganda-Carreras I, Frise E, Kaynig V, Longair M, Pietzsch T, Preibisch S, Rueden C, Saalfeld S, Schmid B, et al. 2012. Fiji: an open-source platform for biological-image analysis. *Nat Methods* **9**: 676–682.

Xiao Z, Zou Q, Liu Y, Yang X. 2016. Genome-wide assessment of differential translations with ribosome profiling data. *Nat Commun* **7**: 11194.

Zhou L, Lim Q-E, Wan G, Too H-P. 2010. Normalization with genes encoding ribosomal proteins but not GAPDH provides an accurate quantification of gene expressions in neuronal differentiation of PC12 cells. *BMC Genomics* **11**: 75. http://dx.doi.org/10.1186/1471-2164-11-75.

Regulación traduccional de PDCD4 sobre el ARNm de Nfkb2

En la publicación anterior se presenta como ejemplo de regulación traduccional ejercida por PDCD4 el caso de *Nfkb2*. Como se describe en la publicación, considerando el particular rol que cumple dicho gen en el crecimiento neurítico se procedió a verificar el control negativo que ejerce PDCD4 sobre la expresión traduccional del ARNm de *Nfkb2*. De esta manera, se mostró mediante Western blot que silenciar la expresión de PDCD4 en cultivos de neuronas corticales aumenta significativamente la abundancia proteica de NFKB2, respecto del control (ver Figura Suplementaria 7 de Di Paolo & Eastman *et. al* RNA 2020). Con el objetivo de complementar la evidencia a favor de dicha regulación, nos propusimos también cuantificar la abundancia del ARNm de *Nfkb2* en distintas fracciones de un gradiente polisomal en presencia y ausencia de PDCD4. Efectivamente pudimos confirmar que en ausencia de PDCD4, la cantidad de ARNm de *Nfkb2* aumenta en las fracciones polisomales respecto del control en presencia de PDCD4, como se describe a continuación.

Materiales y Métodos

- Cuantificación de la abundancia de ARNm en distintas fracciones polisomales

El mismo protocolo que el descrito para Ribo-Seq en el trabajo publicado II fue utilizado para producir perfiles polisomales a partir de células PC12 diferenciadas a neuronas en presencia y ausencia de PDCD4. En este caso, el sobrenadante postmitocondrial fue cargado en gradientes lineales de sacarosa de 10% a 50% y ultracentrifugado en un rotor SW40Ti a 35.000 RPM por 2 horas a 4°C. Como control se utilizó 25 mM de EDTA para desensamblar los polisomas. El perfil polisomal fue visualizado mediante un detector UV en línea (Cole-Parmer) y se colectaron distintas fracciones. El ARN se purificó mediante Trizol (Invitrogen) y se generó ADN copia mediante retrotranscripción (SuperScript II y III, Invitrogen). La cuantificación relativa de los genes se realizó mediante el kit *SYBR Green Master Mix* (Invitrogen) en el equipo *BioRad CFX96 Touch™ Real-Time PCR Detection System*. Las secuencias de los cebadores utilizados fue diseñada con la herramienta *Primer-BLAST* del NCBI y se muestran a continuación: NFKB2 forward: 5'-AGCATTGTACGGCTACGCTT-3', NFKB2 reverse: 5'-GGAGACTTGCTGTCGTGGAT-3'.

Resultados

- El ARNm de *Nfkb2* aumenta su abundancia en las fracciones polisomales tras silenciar PDCD4.

Con el objetivo de visualizar mediante técnicas ortogonales el aumento en los niveles traduccionales de blancos relevantes de PDCD4, nos propusimos colectar distintas fracciones de un gradiente polisomal y evaluar la cantidad relativa de ARNm en cada fracción, en presencia y ausencia de PDCD4. De esta manera, preparamos perfiles polisomales que registramos en línea mediante cuantificación de absorbancia a λ=254 nm. Los picos correspondientes tanto a las subunidades 40S y 60S del ribosoma, así como el ribosoma completo, y la región polisomal fueron evidenciados mediante el tratamiento de la muestra con 25 mM de EDTA, lo cual desensambla los ribosomas (ver Figura IV.1 A). Seleccionamos entonces tres distintas regiones del gradiente que se corresponden a fracciones libres de polisomas, con polisomas livianos o con polisomas pesados. La abundancia relativa de los ARNm de *Pdcd4* y *Nfkb2*, blanco traduccional de PDCD4 y regulador clave del crecimiento neurítico en células PC12, fue evaluada mediante RT-PCR en tiempo real. Los resultados muestran que para *Pdcd4* se observa una disminución en la cantidad de ARNm que ingresa en las fracciones polisomales, como es de esperarse, tras el silenciamiento. Por su parte, para *Nfkb2*, observamos que en la condición sin PDCD4 la cantidad de ARNm aumenta en las fracciones polisomales, en especial en la fracción de polisomas livianos (ver Figura IV.1 B).

Discusión

En este primer capítulo nos propusimos como objetivo determinar el rol de PDCD4 en modelos neuronales y explorar su posibles ARNm blancos traduccionales. Para esto utilizamos la línea celular PC12, capaz de diferenciar a un tipo neuronal tras exposición a NGF, y utilizando vectores lentivirales producimos un modelo capaz de silenciar de manera inducible la expresión de PDCD4, así como su respectivo control. Resultados obtenidos en simultáneo en nuestro laboratorio, e incluidos en el trabajo publicado II presentado antes, mostraban que PDCD4 podía regular el crecimiento axonal en neuronas corticales primarias y del ganglio de la raíz dorsal. Por esta razón, primero exploramos si en nuestro modelo celular tipo neuronal se observaba el mismo efecto sobre el crecimiento de neuritas. Efectivamente demostramos que el silenciamiento de PDCD4 determina que las células PC12 diferenciadas presenten neuritas más largas (en promedio 1,6 veces más largas; p valor = 0.052; ver trabajo publicado II).

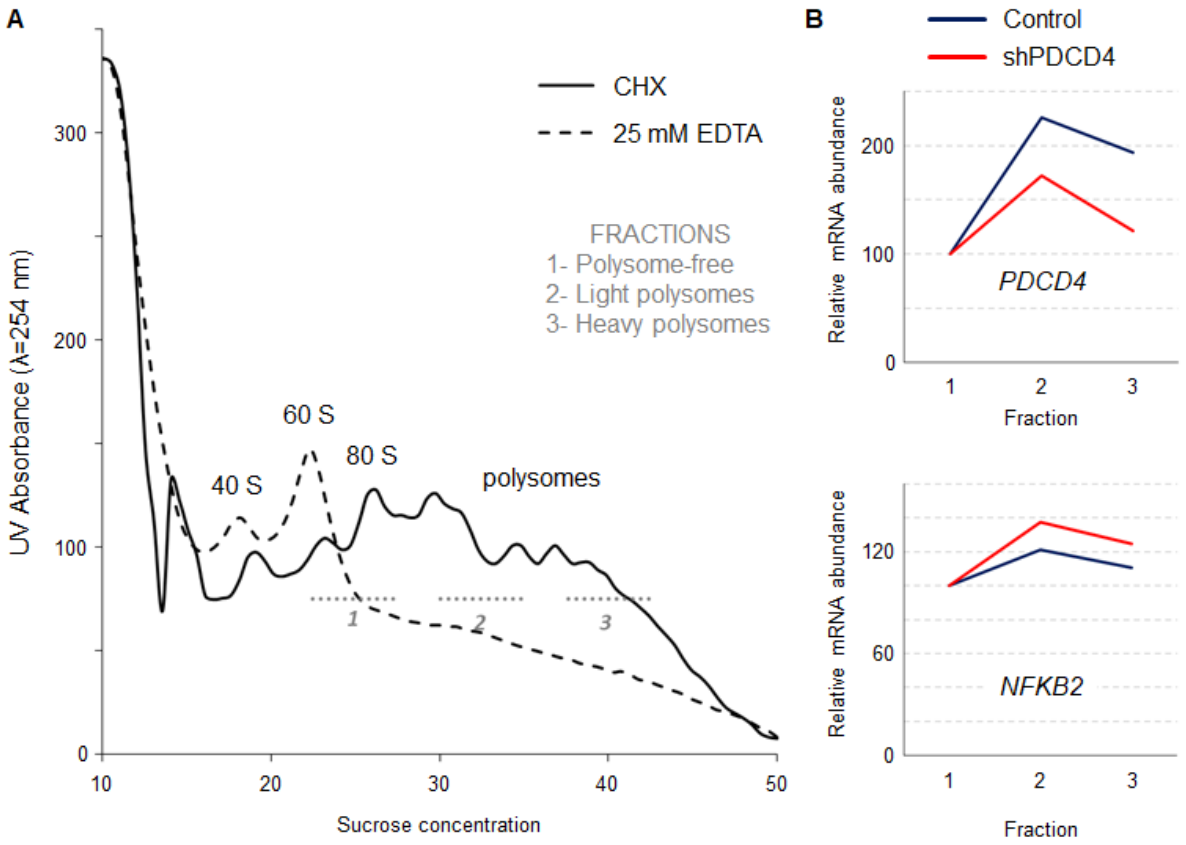

Figura IV.1. Cuantificación de *Pdcd4* y *Nfkb2* en distintas fracciones de un gradiente polisomal en presencia y ausencia de PDCD4. (**A**) Se muestra un perfil polisomal obtenido a partir de células PC12. La cantidad de ARN representada por el valor de absorbancia a 254 nm es graficado versus la posición en el gradiente de sacarosa de 10% a 50%. El gráfico en negro muestra la condición tratada con cicloheximida (CHX) que detiene la traducción, mientras que el gráfico punteado muestra la condición tratada con 25 mM de EDTA que desensambla los polisomas. Los picos correspondientes a las subunidades 40S, 60S, el ribosoma (80S) y la fracción polisomal son indicados. Además se muestra el rango en el cual se colectaron las 3 fracciones analizadas correspondientes a (1) fracción libre de polisomas, (2) fracción de polisomas livianos y (3) fracción de polisomas pesados. (**B**) Se muestra la cuantificación relativa de ARNm para *Pdcd4* (arriba) y *Nfkb2* (abajo) por RT-PCR para las tres fracciones colectadas. En azul se muestra la condición Control (o shScrambled) y en rojo la condición con PDCD4 silenciado (shPDCD4).

Con el objetivo de conocer las funciones posiblemente reguladas por PDCD4 y describir los posibles blancos traduccionales de dicho factor en modelos neuronales, aplicamos la técnica de Ribo-Seq en el modelo celular neuronal descrito anteriormente. De esta manera definimos una lista de 267 ARNm posibles blancos traduccionales de PDCD4 cuya eficiencia de expresión traduccional aumenta de manera significativa en ausencia de PDCD4.

Considerando que el efecto observado sobre el crecimiento neurítico o axonal era conservado en distintos modelos neuronales *in vitro*, exploramos la lista de blancos traduccionales de PDCD4 en búsqueda de una firma génica asociada al crecimiento neurítico o axonal. De esta

manera, describimos un grupo de 36 genes cuya eficiencia traduccional se ve aumentada en ausencia de PDCD4 y cuyas funciones biológicas descritas están directamente asociadas al crecimiento neurítico o axonal. Un ejemplo relevante es el gen de *Nfkb2* que describimos como blanco traduccional de PDCD4 y que se ha demostrado promueve la neuritogénesis en PC12 diferenciadas [77]. Pudimos confirmar de manera ortogonal la regulación ejercida por PDCD4 en dicho gen tras evaluar la abundancia proteica de NFKB2 en presencia y ausencia de PDCD4 en un modelo de neuronas corticales *in vitro* (ver trabajo publicado II). Resultados similares se obtuvieron al evaluar las cantidades relativas del ARNm de dicho gen en distintas fracciones polisomales en presencia y ausencia de PDCD4 (ver Figura IV.1). En este caso observamos que la cantidad relativa del ARNm de *Nfkb2* aumenta en las fracciones correspondientes a los polisomas luego de silenciar PDCD4, lo cual confirmaría también su denominación como blanco traduccional de PDCD4.

V. CAPÍTULO 2

OPTIMIZACIÓN Y APLICACIÓN DE LA TÉCNICA DE RIBO-SEQ EN MODELOS NEURONALES *IN VITRO* E *IN VIVO*

Durante mi tesis de Maestría trabajamos en la puesta a punto y realización de la técnica Ribo-Seq utilizando líneas celulares [50]. De esa manera fue que logramos aplicarla con éxito utilizando la línea celular PC12 que es capaz de diferenciar a un modelo tipo neuronal, como se mencionó anteriormente. Sin embargo, nos planteamos como un primer objetivo de este capítulo evaluar la aplicación de Ribo-Seq en distintos modelos neuronales, como cultivos de neuronas embrionarias o tejidos nerviosos provenientes de animales. Conociendo las ventajas y limitaciones que cada modelo neuronal posee, disponer de la técnica en un conjunto variado de sustratos nos aportaría un valor adicional.

Como fuera mencionado en la Introducción (ver Trabajo publicado I), el protocolo de Ribo-Seq puede ser dividido en tres pasos principales: i) obtención de una muestra representativa del estado traduccional celular; ii) ensayo de digestión de dicha muestra con ARNasas y recuperación de las huellas ribosomales y iii) secuenciación masiva de dichos fragmentos y posteriores análisis *in silico*. Respecto del primer punto, el protocolo que nuestro grupo de trabajo ha desarrollado y aplicado previamente [78–80] implica la recuperación de la fracción polisomal activa mediante ultracentrifugación del sobrenadante postmitocondrial en colchones de sacarosa [81]. Este representa ser un paso crítico debido al generalmente bajo rendimiento en la recuperación de ARN tras la ultracentrifugación, lo cual implica disponer de una gran cantidad de material de partida. Lamentablemente, esto no es posible es todos los modelos biológicos, en particular en modelos neuronales donde el número de células con las que se trabaja suele ser bajo en comparación a las que podemos obtener de cultivos de líneas celulares. En la literatura algunas alternativas han sido descritas para sobrellevar este problema. Por un lado, un trabajo liderado por Hornstein del grupo de Peter Sims [82] describe un protocolo para producir librerías de huellas ribosomales para secuenciación masiva sin pasos de ligación, lo cual reduce la complejidad del protocolo y permite obtener resultados a partir de cantidades muy pequeñas de huellas ribosomales (>1 ng). Este protocolo se base en producir las librerías de ADN en una sola reacción donde se utiliza una retrotranscriptasa con actividad de cambio de hebra (del inglés, *template switching*) utilizada comúnmente en protocolos de construcción de librerías de *low-input* ARN para secuenciación de célula única (*single cell* RNA-Seq). Por otro lado, el grupo de Chekulaeva, utilizando modelos neuronales y contrastando diferencias entre el soma y las neuritas [83], realizó el ensayo de digestión

directamente sobre el sobrenadante postmitocondrial, sin posterior recuperación de la fracción monosomal, y comparó los resultados con el protocolo clásico donde sí se recupera dicha fracción luego del paso de digestión. En este caso, los autores compararon diversos parámetros entre ambos protocolos, como el largo de las huellas ribosomales obtenidas, su distribución de mapeo sobre las distintas regiones del ARNm, su periodicidad, entre otros. Los resultados no muestran diferencias significativas entre ambos protocolos por lo cual los autores eliminaron el paso de recuperación de la fracción monosomal, también realizado mediante ultracentrifugación y que por lo tanto requiere de una gran cantidad de material de partida.

Contemplando estos antecedentes y con el objetivo de aplicar el protocolo de Ribo-Seq en distintos modelos neuronales *in vitro* e *in vivo*, transformamos los desafíos de cada modelo en particular en objetivos específicos a optimizar. Por ejemplo, en el caso de los cultivos de neuronas *in vitro*, donde la cantidad de células obtenidas es bajo, nos propusimos trabajar en la optimización del protocolo suprimiendo el paso de ultracentrifugación. En líneas generales, el protocolo se reduce a obtener un sobrenadante postmitocondrial sobre el cual se realiza el ensayo de digestión y se procede luego a la directa separación y recuperación de huellas ribosomales mediante PAGE. Por otro lado, en el caso del uso de muestras de tejido nervioso, como pueden ser distintas secciones de cerebro, la limitante de la cantidad de células puede ser solucionada aumentando la cantidad de tejido. De esta manera, en este caso el principal desafío fue poner a punto la rápida obtención del sobrenadante postmitocondrial asegurando la total lisis de las células y la integridad de los polisomas. En suma, brevemente, en cada caso se ajustaron la cantidad inicial de material a utilizar, los protocolos de lisis celular y obtención de polisomas, así como el posterior ensayo de protección con ARNasa.

Por otro lado, en segundo lugar en este capítulo, nos planteamos realizar un ensayo comparativo utilizando dos ARNasas distintas, por un lado la enzima Benzonasa con la cual solemos trabajar en nuestro laboratorio, y por el otro lado la enzima RNAsa I, ampliamente utilizada en los trabajos que siguen la descripción del protocolo original [84].

Benzonasa es el nombre comercial que recibe la enzima extracelular secretada por la bacteria *Serratia marcescens*, por lo que también se la conoce como endonucleasa *Serratia* [85,86]. Esta enzima es un dímero de dos subunidades de 245 aminoácidos y 30 kDa, con dos puentes de disulfuro esenciales [86]. Muestra un patrón de digestión no específico y es capaz de degradar tanto ARN, como ADN, ya sean simple o doble cadena, lineares o circulares. Por el otro lado, la enzima RNAsa I, que se obtiene de *Escherichia coli* [87,88], tiene un tamaño de 27 kDa y digiere de manera no específica solamente ARN, con una marcada preferencia por ARN simple cadena respecto de ARN doble cadena. A pesar de no degradar ADN, se ha

observado que la enzima tiene capacidad de unirse al mismo. Más allá de estas diferencias, en el contexto del protocolo de Ribo-Seq importa destacar que la enzima Benzonasa, la que utilizamos en nuestros protocolos, produce fragmentos de ARN cuyos extremos 5' se encuentran fosforilados y 3' desfosforilados, listos para la ligación de adaptadores y los siguientes pasos del protocolo de producción de librerías de secuenciación. En cambio, los fragmentos producidos por la RNAsa I tienen fosforilado el extremo 3' por lo que es necesaria la desfosforilación de los mismos antes de ligar adaptadores [84]. Esto introduce, al menos, una ronda extra de precipitación, concentración y resuspensión del ARN que, además de posiblemente introducir algún tipo de sesgo asociado a la reacción enzimática de desfosforilación, disminuye la cantidad final recuperada por los rendimientos inherentes de los protocolos de precipitación y concentración.

En este sentido, la hipótesis de trabajo planteada es que ambas enzimas producen huellas ribosomales con características distintas, pero determinan niveles de expresión traduccional comparables en un mismo modelo celular. Así, nos propusimos como objetivos producir y secuenciar huellas ribosomales a partir de células HEK293 en condiciones basales, utilizando las enzimas Benzonasa y RNAsa I por separado. Luego nos planteamos comparar las características de las huellas ribosomales producidas en cada caso y también contrastar los traductomas y los niveles de expresión traduccional definidos por cada enzima. Trabajos similares en la literatura han estudiado el uso de distintas enzimas para la preparación de huellas ribosomales, aunque sin incluir la enzima Benzonasa [89].

A modo de resumen, en el presente capítulo logramos poner a punto el uso de la técnica de Ribo-Seq en desafiantes sustratos biológicos como cultivos primarios de neuronas (bajo número de células) y tejido nervioso animal (complejos protocolos de lisis). En ambos casos, las huellas ribosomales obtenidas y/o secuenciadas cumplieron todos los controles de calidad esperados. En segundo lugar, también obtuvimos y comparamos huellas ribosomales producidas a partir de dos ARNasas distintas, Benzonasa y RNAsa I. La cuantificación de los niveles de expresión génica traduccional definidos por cada enzima resultaron comparables a pesar de las diferencias observadas en las características de las huellas ribosomales, como su tamaño, patrón de mapeo y periodicidad.

Materiales y Métodos

- Cultivo *in vitro* de neuronas corticales embrionarias

Los cultivos de neuronas corticales fueron obtenidos de embriones en gestación en el día 17-18 siguiendo los protocolos utilizados en el laboratorio del Dr. George Bloom [68]. Brevemente, el cerebro de los embriones es removido y colocado en un ambiente estéril en presencia de buffer HBSS donde se obtiene el tejido cortical. El tejido es digerido con tripsina 0,25% a 37°C por 40 minutos, luego la reacción es inactivada con suero fetal bovino y las células son lavadas 3 veces con buffer HBSS. Se realiza un tratamiento con ADNasa y luego se disocian las células mecánicamente con pipetas Pasteur. Las células son plaqueadas a una tasa de 60.000 células por cm^2 en medio neurobasal libre de suero y suplementado con B27, L-glutamina, glucosa, antibióticos y 5% de suero fetal bovino. El medio de plaqueo es removido luego de 3 horas y reemplazado por un medio idéntico sin suero fetal bovino. Se realizan cambios de medio parciales (50%) cada 3-4 días hasta alcanzar los 10-12 días de crecimiento *in vitro*. En todos los casos las neuronas crecen en superficies pretratadas con 10 µg/cm^2 de poli-D-lisina *overnight* a 4°C (ver Nota 1 en Anexo).

- Procesamiento de corteza cerebral de ratones adultos para obtener el sobrenadante postmitocondrial

Los ratones fueron crecidos, alimentados y reproducidos en el bioterio de la Universidad de Virginia (EE.UU.) siguiendo los protocolos establecidos en su propia reglamentación. Para el disecado de la corteza cerebral los ratones fueron sacrificados por dislocación cervical previamente anestesiados en cámara de CO_2. Rápidamente se procede a cortar la cabeza del ratón, abrir el cráneo y obtener el cerebro entero que se coloca en una placa de plástico fría con PBS y 100 µg/mL CHX (ver Nota 2 en Anexo). Utilizando bisturís y pinzas primero se remueven el bulbo olfatorio y el cerebelo. Luego se divide el cerebro con un corte sagital en sus dos hemisferios y se remueve el tejido blanco (hipocampo y otras estructuras subcorticales) de manera de obtener solamente la corteza. Por último el tejido final es pesado, triturado con bisturís y se termina de homogeneizar utilizando un homogenizador de vidrio y buffer de lisis (5 mM Tris pH 7,5; 2,5 mM $MgCl_2$; 1,5 mM KCl; 0,5% Tritón X-100; 0,5% deoxicolato de sodio; 2 mM DTT y 100 µg/mL CHX) en relación 10% (m/v). El lisado es agitado en vortex por 5 segundos y reposado 5 minutos en hielo. Los restos celulares, núcleos y mitocondrias son eliminados mediante dos centrifugaciones consecutivas de 1 y 10 minutos, a máxima velocidad y 4°C, recuperando el sobrenadante.

- Cultivo de células HEK293

Los cultivos de células HEK293 se realizaron sobre placas de plástico utilizando medio DMEM suplementado con 10% de suero de ternero (Cosmic, GE Healthcare Life Sciences) y antibióticos, en estufas a 37°C con atmósferas húmedas y 5% de CO_2.

- Ribo-Seq

Tanto la fracción polisomal enriquecida como el sobrenadante postmitocondrial fueron utilizados para los ensayos de Ribo-Seq. La obtención de los sobrenadantes postmitocondriales a partir de los cultivos celulares *in vitro*, tanto para neuronas corticales embrionarias como para células HEK293, se realizó de la siguiente manera: los cultivos celulares son pretratados por 1 hora a 37°C con 100 µg/mL CHX e inmediatamente después son colocados en hielo. Se remueve el medio y los cultivos son lavados de dos a tres veces con PBS frío en presencia de 100 µg/mL CHX. Luego del último lavado se remueve el líquido y las células son despegadas por acción mecánica mediante raspado. Mediante centrifugación a 2000 RPM y 4°C por 10 minutos las células son concentradas y luego resuspendidas en buffer de lisis (5 mM Tris pH 7,5; 2,5 mM $MgCl_2$; 1,5 mM KCl; 0,5% Tritón X-100; 0,5% deoxicolato de sodio; 2 mM DTT y 100 µg/mL CHX) intercalando agitaciones de 5 segundos en vortex. Por último se centrifuga a máxima velocidad y 4°C por 2 minutos para obtener el sobrenadante postmitocondrial.

Las fracciones polisomales se obtuvieron mediante ultracentrifugación del sobrenadante postmitocondrial en colchones de sacarosa de 12% y 33,5% en buffer polisomal (20 mM HEPES pH 7,5; 5 mM $MgCl_2$; 100 mM KCl y 100 µg/mL CHX) utilizando un rotor SW41Ti a 36,000 RPM y 4°C por 2 horas. El pellet polisomal obtenido es resuspendido en el mismo buffer polisomal.

Los ensayos de protección con ARNasa se realizaron con distintas cantidades de la enzima Benzonasa (Sigma) según correspondiere (los detalles en este paso de optimización se discuten más adelante). En todos los casos, la digestión se realizó por 10 minutos a temperatura ambiente y se interrumpió mediante el agregado de buffer de lisis del kit *mirVana* (Invitrogen) para la posterior extracción de ARN con el mismo kit. El ARN obtenido fue precipitado y concentrado con etanol 80% y acetato de sodio 3 M pH 5,2 para maximizar la recuperación de fragmentos pequeños. En este caso y en todos los protocolos siguientes de precipitación de ARN se utilizó una sustancia co-precipitante inerte, como el GlycoBlue (Invitrogen), a los efectos de visualizar el pellet. Las digestiones fueron separadas utilizando geles comerciales de poliacrilamida al 15% en presencia de Urea 7 M (Novex, Thermofischer) en buffer TBE durante 65 minutos a 200 V. Un marcador de peso molecular de ADN de rango

ultra bajo (Invitrogen) y oligos de ARN de 26 y 34 nucleótidos (nt) de largo fueron utilizados para reconocer las bandas correspondientes a las huellas ribosomales. Los geles fueron revelados con GelRed (Biotium) y visualizados en cuarto oscuro bajo radiación UV donde se cortan las bandas correspondientes a las huellas ribosomales. El ARN se extrajo del gel *overnight* en agitación suave y en presencia de buffer de extracción (300 mM acetato de sodio pH 5,2; 1 mM EDTA y 0,25% (m/v) de SDS). Luego el ARN es precipitado con isopropanol y resuspendido en agua DEPC listo para control de calidad y envío a secuenciación.

En los experimentos donde se utilizó enzima RNAsa I (Invitrogen) para ensayos de digestión se introdujeron las variantes que se describen a continuación. La digestión con RNAsa I se realizó por 45 minutos a temperatura ambiente con agitación suave, utilizando 300 unidades de enzima según el protocolo descrito [84]. Luego, se continuó con el mismo protocolo descrito anteriormente para la extracción de ARN, separación por electroforesis y recuperación del ARN correspondiente a las huellas ribosomales. Para la fosforilación de los extremos 5' de las huellas ribosomales producidas con la enzima RNAsa I se utilizaron 10 unidades de T4 quinasa (New England BioLabs) a 37°C por 30 minutos. La reacción se inactiva a 65°C por 20 minutos y luego el ARN se precipita y concentra con etanol 80% para sus posteriores usos (control de calidad y/o secuenciación masiva).

El control de calidad de las muestras de huellas ribosomales fue realizado en la plataforma *2100 Agilent Bioanalyzer* utilizando kits y chips para ARN pequeños (*small RNA*; Agilent). La secuenciación masiva de las muestras se realizó utilizando servicios comerciales extranjeros como *BGI Tech Solutions* - Hong-Kong. Para la secuenciación de huellas ribosomales se utilizó el protocolo de *small RNA library* obteniendo al menos 80 millones de lecturas *single-end* de 50 nt de largo.

- Análisis de datos

Los archivos de secuenciación fueron procesados en los servidores del Departamento de Genómica. Para el análisis se utilizaron tanto software comerciales, como *CLC Genomics Workbench*, como software libre. Brevemente la calidad de los archivos de secuenciación fue evaluada mediante *FastQC* [90] y en caso de ser necesario las secuencias fueron trimeadas por calidad utilizando *sickle* [91]. Para los mapeos se utilizó tanto *bowtie1* [92] como *bowtie2* [93] y las versiones disponibles más actualizadas de los genomas de referencia de ratón (*Mus musculus*, versión mm10, 2011/12 - GRCm38) y humano (*Homo sapiens*, versión hg38, GRCh38) descargadas del sitio web ftp del NCBI (ftp://ftp.ncbi.nlm.nih.gov/refseq/). Las tablas de conteo fueron producidas con *featureCounts* [94] y los análisis de expresión génica diferencial fueron realizados con el paquete de R *edgeR* [95,96]. Los análisis de ontología

génica fueron realizados con herramientas web libres como *g:GOST* de *g:Profiler* [97] y *STRING* [98].

Se utilizaron scripts de elaboración propia en lenguaje *python*, así como *samtools* [99], *bedtools* [100] y herramientas de bash para algunos análisis específicos, como el estudio de la periodicidad de huellas ribosomales, la distribución de mapeos en regiones codificantes y no codificantes, y la preferencia de sitio de corte de las enzimas. Diversos paquetes de R fueron utilizados para la creación de gráficos y representación visual de datos.

Resultados

- Optimización del número de células y la cantidad de enzima a utilizar en ensayos de digestión sobre el sobrenadante postmitocondrial

Considerando que una de las principales desventajas del protocolo de Ribo-Seq es la gran cantidad de material de partida necesario, ya sean células creciendo *in vitro* o tejido, nos propusimos en una primera instancia optimizar el protocolo para evitar el paso de purificación de polisomas y realizar el ensayo de protección con ARNasa directamente sobre el sobrenadante postmitocondrial, como ya ha sido descrito en trabajos previos [83]. Esta variante, nos permitiría trabajar con muestras más delicadas de las cuales no sea factible recoger las grandes cantidades de material de partida necesarias en la versión estándar del protocolo, un ejemplo claro son los cultivos de neuronas embrionarias.

En una primera instancia utilizamos cultivos de células HEK293 de manera de evaluar el rango óptimo de número de células necesaria para producir y recuperar huellas ribosomales en cantidad y calidad adecuadas para su posterior secuenciación. También trabajamos en ajustar la cantidad de enzima ARNasa a utilizar, considerando que en contraparte al ensayo clásico donde la digestión se realiza sobre un pellet polisomal, en este caso tenemos una muestra más compleja, que de hecho probablemente incluya restos de ADN que son también digeridos por la enzima Benzonasa.

Como se muestra en la figura V.1 se utilizaron cantidades decrecientes de células para obtener distintos sobrenadantes postmitocondriales. Estos sobrenadantes fueron digeridos con cantidades adecuadas de Benzonasa según cálculos derivados de protocolos anteriores ($\geq$250 U por cada 400 µg de ARN estimados por Nanodrop en el sobrenadante). El ARN de cada digestión es purificado, obteniéndose cantidades decrecientes acordes, y luego dichas digestiones fueron separadas mediante PAGE al 15% en condiciones desnaturalizantes. Las bandas correspondientes a las huellas ribosomales fueron cortadas y el ARN recuperado fue

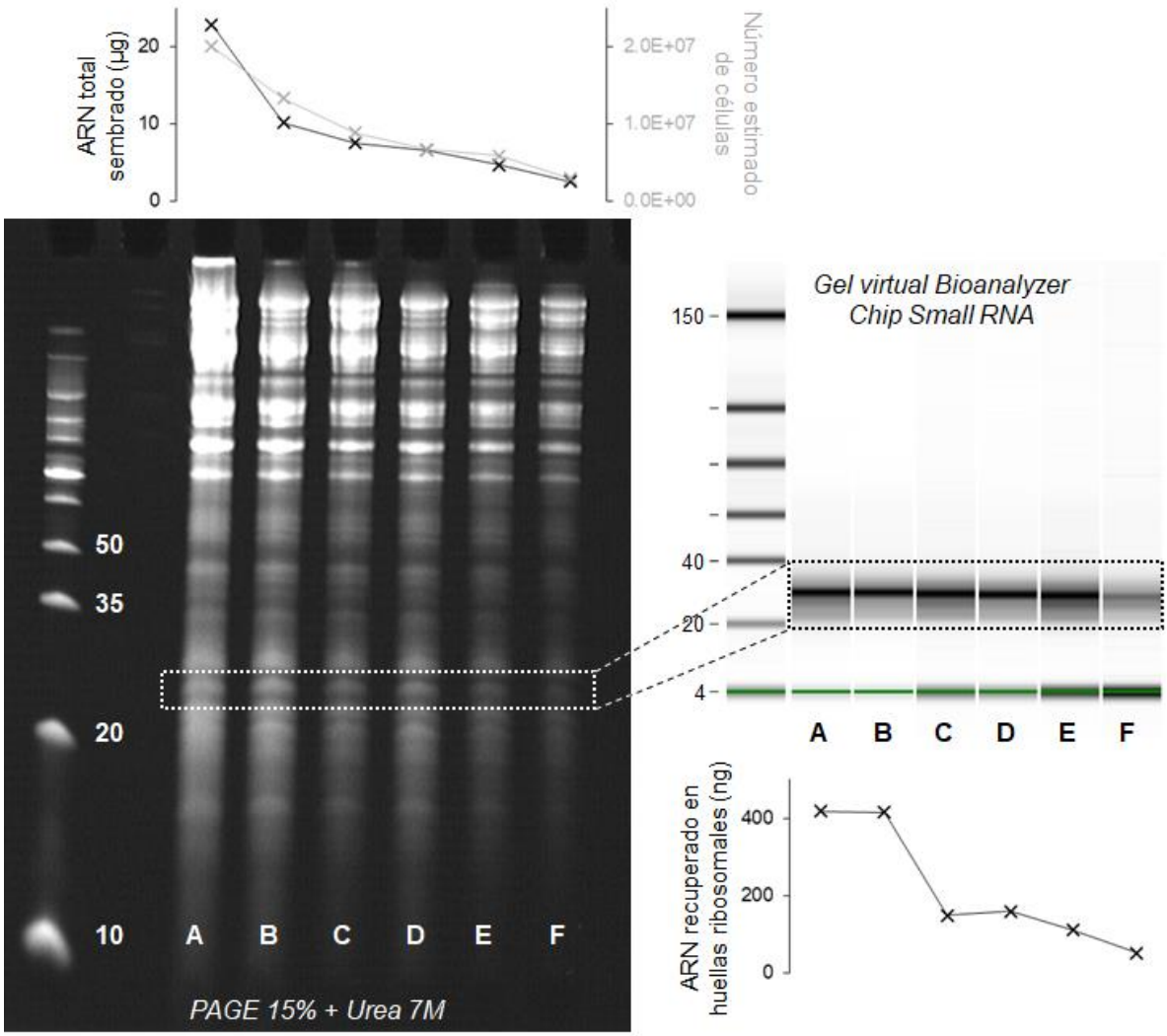

Figura V.1. Optimización de la cantidad de células a utilizar para producir huellas ribosomales a partir del sobrenadante postmitocondrial. En el panel izquierdo de la figura se muestra un gel de poliacrilamida al 15% en condiciones desnaturalizantes por la presencia de urea 7 M. En el carril de más a la izquierda se muestra un marcador de peso molecular de ADN y se indica el tamaño de algunas bandas. Luego se muestra el perfil de las digestiones (A-F) realizadas a partir de cantidades decrecientes de células y por lo tanto cantidades decrecientes de ARN total sembrado (ver gráfico superior). En el rectángulo punteado blanco se muestra la región correspondiente a las huellas ribosomales que fue cortada y utilizada para recuperar el ARN. El ARN recuperado es evaluado en electroforesis capilar en el instrumento *Bioanalyzer* utilizando chips de *small RNA*. La reconstrucción virtual del gel se muestra en el panel derecho y abajo se puede observar la cuantificación de ARN recuperado en cada una de las fracciones correspondientes a las huellas ribosomales.

---

observado por electroforesis capilar en un chip de *Bioanalyzer* que permitió evaluar el tamaño y la cantidad del mismo. Los resultados indican que existe una saturación en la recuperación de ARN correspondiente a las huellas ribosomales cuando partimos de grandes cantidades de células. El rendimiento relativo máximo se obtiene para el caso donde separamos en el gel de poliacrilamida una digestión que contiene 10 µg de ARN (muestra B), como esperábamos

según la literatura [84]. De todas maneras, a partir de todas las muestras se logró recuperar ARN correspondiente a las huellas ribosomales en cantidades suficientes para lograr producir librerías de secuenciación. La muestra con menor cantidad inicial (muestra F) representaba aproximadamente menos de 3 millones de células, que implicaron 2,5 µg de ARN sembrados en el gel de poliacrilamida. De la banda correspondiente a las huellas ribosomales se obtuvieron apenas más de 50 ng de ARN, lo cual a pesar de ser una cantidad baja, es suficiente para construir librerías de secuenciación con protocolos de *low input*.

Con el objetivo de evaluar la cantidad apropiada de enzima para realizar el ensayo de digestión sobre el sobrenadante postmitocondrial, procedimos a realizar un ensayo de digestión sobre muestras equivalentes con distintas cantidades de enzima. De esta manera, se utilizaron nuevamente cultivos de células HEK293 en alto grado de confluencia para obtener el sobrenadante postmitocondrial. Dicho sobrenadante fue digerido con cuatro cantidades distintas de Benzonasa: 0; 2,5; 25 y 250 unidades. Los valores utilizados responden a la experiencia previa y los cálculos realizados del experimento anterior, los cuales indicaban que debíamos utilizar para este experimento puntual en el orden de 20 unidades. La figura V.2 muestra los resultados obtenidos. En primera instancia se pueden observar claras diferencias entre las distintas muestras respecto del perfil de bandas que se aprecian en el gel de poliacrilamida (ver Figura V.2 A). Mientras la muestra no digerida prácticamente que no logra ingresar al gel y apenas se separan y observan unas bandas de tamaños grandes (aproximadamente >100 nt), probablemente correspondientes a ARN ribosomales pequeños y de transferencia, las distintas digestiones muestran patrones similares a grandes rasgos. De todas maneras, se pueden observar diferencias entre los perfiles de las distintas digestiones en cuanto a presencia y ausencia de bandas o intensidad de las mismas, como era de esperar. Las muestras también fueron separadas por electroforesis capilar utilizando chips de *small RNA* en el instrumento *Bioanalyzer*. En este caso podemos observar con mayor detalle las diferencias entre las muestras observando los electroferogramas generados (ver Figura V.2 B). En particular, si nos enfocamos en la región entre 20 y 40 nucleótidos correspondiente a las huellas ribosomales podemos observar diferencias mayores entre las distintas muestras. A pesar de que la digestión con 250 unidades de Benzonasa es la que muestra mayor cantidad de ARN en la región centrada en los 30 nucleótidos, debido a que presenta el electroferograma con mayor intensidad, no se observa un pico definido en dicha zona, solamente uno de menor tamaño (~25 nt). Algo similar se observa para la digestión con 2,5 unidades de enzima, con la desventaja de que además es la que presenta menos cantidad de ARN por mostrar valores más bajos de fluorescencia. En cambio, la muestra digerida con 25 unidades de enzima presenta un claro pico del tamaño esperado para las huellas ribosomales (30 nt) y con buenos valores de fluorescencia. Las

bandas correspondientes a las huellas ribosomales fueron cortadas del gel, se recuperó el ARN y se separó por electroforesis capilar en *Bioanalyzer* para evaluar la distribución de tamaños y cantidad de las huellas. De esta manera pudimos confirmar que los fragmentos de ARN presentes en la banda obtenida en la digestión con 25 unidades de enzima tenían el tamaño esperado (tamaño promedio de 28 nt) y se recuperaban en cantidad adecuada para proceder con la generación de librerías de secuenciación (~300 ng en este caso).

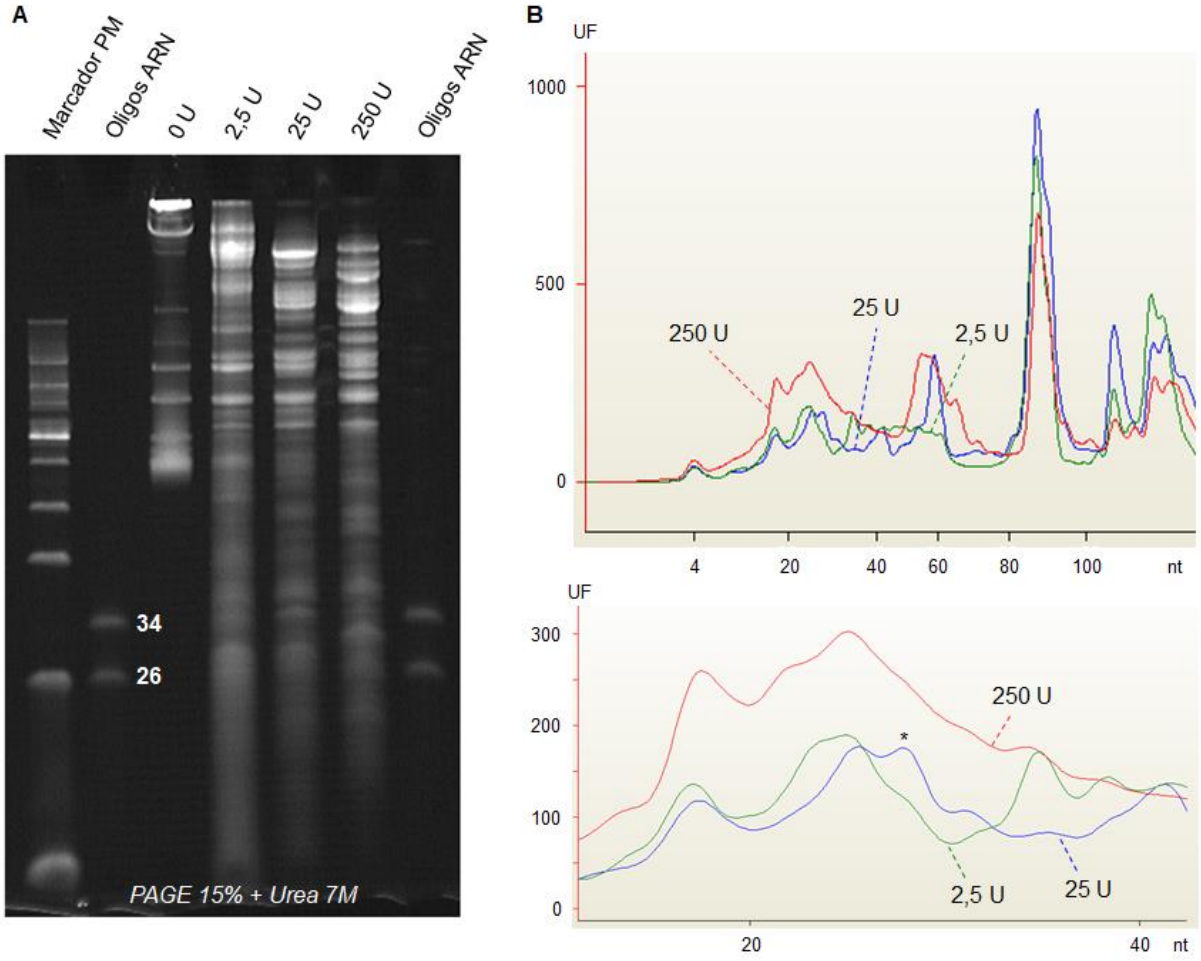

Figura V.2. Optimización de la cantidad de enzima a utilizar para producir huellas ribosomales a partir del sobrenadante postmitocondrial. (**A**) Se muestra un gel de poliacrilamida al 15% en condiciones desnaturalizantes por la presencia de urea 7 M donde se separaron digestiones de sobrenadantes postmitocondriales con distintas cantidades de enzima. Además de utilizar un marcador de peso molecular de ADN se corrieron dos oligos de ARN de 26 y 34 nt de largo para tener una indicación más precisa de la banda correspondiente a las huellas ribosomales. En el gel se muestran 4 tratamientos distintos: sin digerir (0 unidades) y digestiones con 2,5; 25 y 250 unidades de Benzonasa. (**B**) Las muestras también fueron separadas por electroforesis capilar en *Bioanalyzer* utilizando chips de *small RNA* y se muestran los perfiles de electroferogramas para las tres digestiones: en verde la digestión con 2,5 U; en azul con 25 U y en rojo con 250 U. En el panel inferior se muestran los electroferogramas ampliados para la región correspondiente a las huellas ribosomales, con el mismo código de colores. Con un asterisco (*) se indica el pico correspondiente a las huellas ribosomales de 28 nucleótidos.

Vale mencionar que para este experimento trabajamos en el rango inferior del experimento anterior, considerando que la cantidad de neuronas *in vitro* a disponer se encuentra en dicho rango (entre 3 y 5 millones de células en una placa de petri de 10 cm). En este caso nuevamente pudimos obtener fragmentos de ARN correspondientes a huellas ribosomales de tamaño y cantidad esperados utilizando 25 unidades de Benzonasa.

- Ensayo de Ribo-Seq sobre cultivos *in vitro* de neuronas corticales primarias

Una vez ajustados los detalles del protocolo de Ribo-Seq para trabajar con un bajo número de células, procedimos a aplicar esta estrategia en cultivos *in vitro* de neuronas corticales embrionarias. Como primera aproximación, en este caso utilizamos dos genotipos distintos: neuronas derivadas de embriones de ratones *wild-type* C57/BL6 (wt) o de ratones *tau-knockout* (tauKO; [101]). Se obtuvieron aproximadamente 4 millones de células para cada genotipo y se crecieron por entre 10-11 días *in vitro* (ver Figura V.3 A). Vale mencionar que estos cultivos no se componen exclusivamente de células neuronales, sino que también están presentes células no neuronales, como células gliales, aunque en menor medida. De todas maneras, para simplificar la nomenclatura, los llamaremos cultivos de neuronas de aquí en adelante. Una vez alcanzado el grado de diferenciación neuronal esperado, se obtuvieron los sobrenadantes postmitocondriales y se realizaron los ensayos de digestión con la cantidad adecuada de Benzonasa (ver más arriba). En este caso se logró recuperar cerca 230 ng de ARN de las bandas correspondientes a las huellas ribosomales cuyo tamaño estimado por Bioanalyzer fue de entre 25 y 34 nucleótidos (ver Figura V.3 B y C).

La secuenciación masiva de los fragmentos de ARN derivados de las huellas ribosomales arrojó 92 y 141 millones de lecturas para las neuronas wt y tauKO, respectivamente. A pesar de que, como era de esperar, gran parte de dichas lecturas derivan de fragmentos de ARN ribosomal (ARNr) contaminante (84% y 78% respectivamente), se pudo obtener una gran cantidad de lecturas mapeando sobre el transcriptoma de referencia (7,5 y 14,8 millones de lecturas respectivamente). A su vez, una alta proporción de esas lecturas mapearon sobre ARNm resultando en un total de 4 y 8,4 millones de lecturas mapeadas sobre transcriptos codificantes.

En este caso realizamos una serie de análisis globales para evaluar la performance de la técnica aplicada a este modelo biológico. En primer lugar evaluamos la cantidad de genes detectados, o genes por encima de un mínimo de expresión, utilizando distintos umbrales entre 1 y 100 CPM (conteos por millón; ver Figura V.4 A). Por ejemplo, utilizando un umbral de 5 CPM que podríamos considerar adecuado, logramos detectar 11.274 y 11.589 en los genotipos wt y tauKO, respectivamente. Dichos genes muestran valores de expresión que se

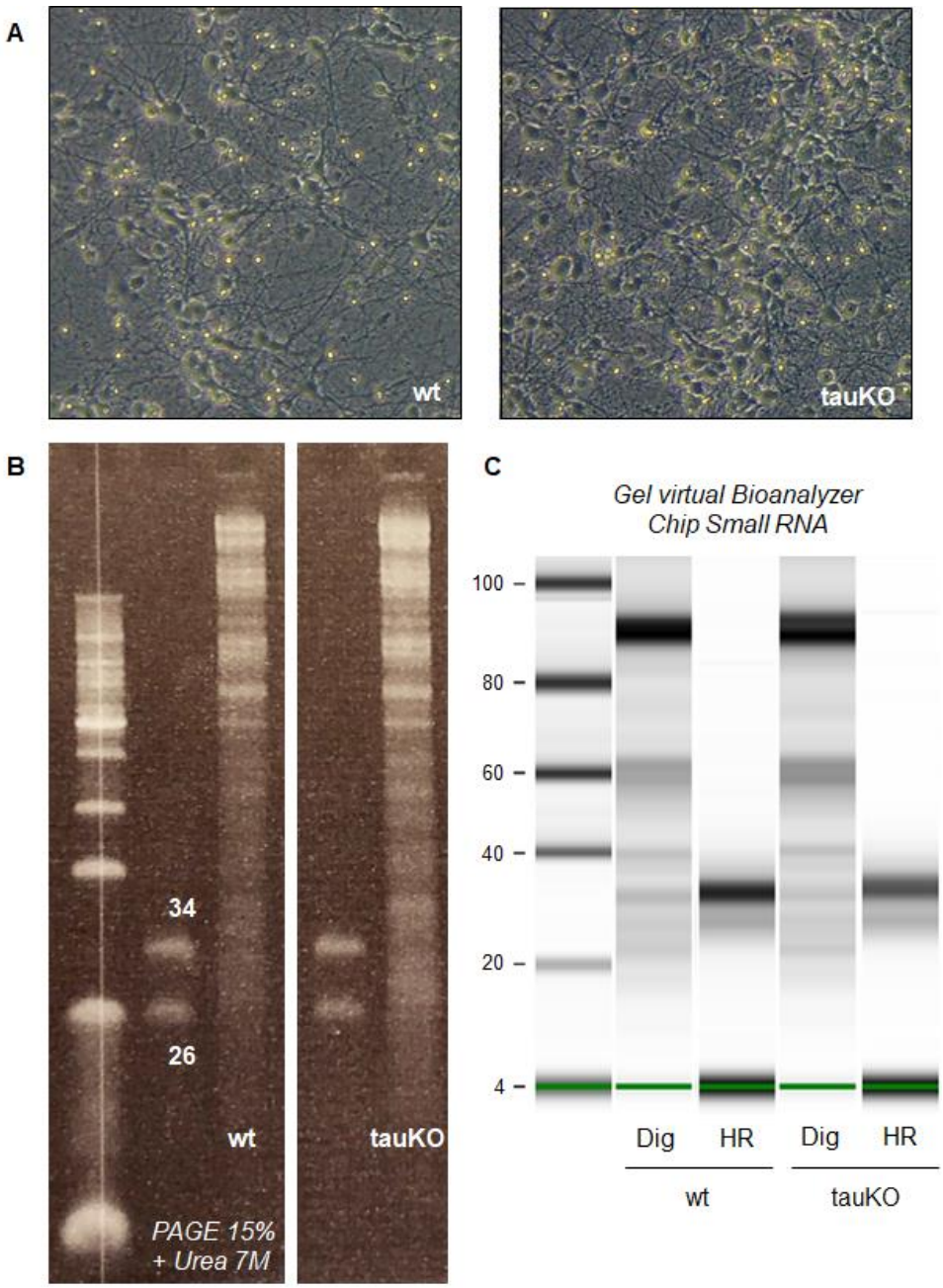

Figura V.3. Producción de huellas ribosomales a partir de cultivos *in vitro* de neuronas corticales primarias. (**A**) Imágenes ilustrativas de microscopía de contraste de fases tomadas a 10X mostrando los cultivos *in vitro* de neuronas corticales derivadas de embriones de ratones *wild-type* (wt; izquierda) y *tau-knockout* (tauKO, derecha). (**B**) Se muestra el gel de poliacrilamida al 15% con urea donde se separan las digestiones de los sobrenadantes postmitocondriales obtenidos. Se utilizaron oligos de ARN de 26 y 34 nt para reconocer las bandas correspondientes a las huellas ribosomales que fueron cortadas del gel. (**C**) Se muestra una reconstrucción digital del gel de electroforesis capilar obtenido en *Bioanalyzer* utilizando chips de *small RNA*. Además de las digestiones (Dig) puede observarse el perfil del ARN recuperado de las bandas del gel correspondientes a las huellas ribosomales (HR).

---

distribuyen de la manera esperada y similar entre ambos genotipos (ver Figura V.4 B). Luego evaluamos la distribución de la región de mapeo de las huellas ribosomales sobre los ARNm

comparando las regiones traducidas (CDS) versus las no traducidas (5'- y 3'-UTR). En este caso observamos que, tanto para las huellas obtenidas del genotipo wt como tauKO, existe una preferencia de mapeo sobre la región codificante (>60%). La región 5'-UTR casi no se ve representada y la 3'-UTR si presenta mapeo de huellas ribosomales (ver Figura V.4 C). Estas asimetrías no son resultado de diferencias en el tamaño de cada región estudiada, ya que es de esperarse que regiones más largas presenten más lecturas. Esto no ocurre en este caso ya que como se observa en la Figura V.4 D la distribución de tamaños de los CDS y 3'-UTR estudiados es muy similar.

Por último, evaluamos otro parámetro característico de las huellas ribosomales como es la periodicidad. Debido a que el ribosoma se mueve de codón en codón, suele observarse una patrón de mapeo de las huellas ribosomales que refleja este movimiento. Si nos enfocamos en genes de alta expresión y con cobertura homogénea, logramos ver como uno de los tres nucleótidos del codón se ve favorecido en el mapeo de los extremos 5' de las huellas ribosomales [102]. En este caso, observamos dicha periodicidad en el subset de genes y huellas ribosomales analizado (ver Figura V.4 E y F). De manera similar a lo que observamos comúnmente cuando utilizamos Benzonasa, las huellas ribosomales muestran un claro patrón de periodicidad cuando tienen un tamaño de 39 nt, ó cuando se alejan 3 nt (36 y 42 nt, por ejemplo, ver más adelante).

En líneas generales podemos afirmar que el protocolo de producción y secuenciación masiva de huellas ribosomales a partir de cultivos *in vitro* de neuronas corticales primarias funcionó de manera óptima. Pudimos detectar niveles de expresión traduccional para una gran cantidad de genes (>10.000), sobre los cuales las huellas ribosomales mapearon preferentemente en las regiones codificantes y mostrando el patrón de periodicidad que las caracteriza. En este caso utilizamos neuronas corticales derivadas de dos genotipos distintos de ratones (wt y tauKO). De todas maneras todos los análisis globales realizados no arrojaron diferencias sustanciales con base en el genotipo utilizado.

- Puesta a punto del protocolo de obtención de huellas ribosomales a partir de corteza cerebral de ratón

Considerando otra alternativa posible de modelos neuronales a utilizar nos propusimos trabajar con secciones de cerebro de ratón. Como primera aproximación nos centramos específicamente en la corteza cerebral por tratarse de una de las regiones con mayor cantidad de células y mayor proporción de células neuronales [103]. De esta manera, trabajamos utilizando distintos protocolos de lisis evaluando la recuperación de la fracción polisomal mediante ultracentrifugación en colchones de sacarosa, en presencia y ausencia de EDTA,

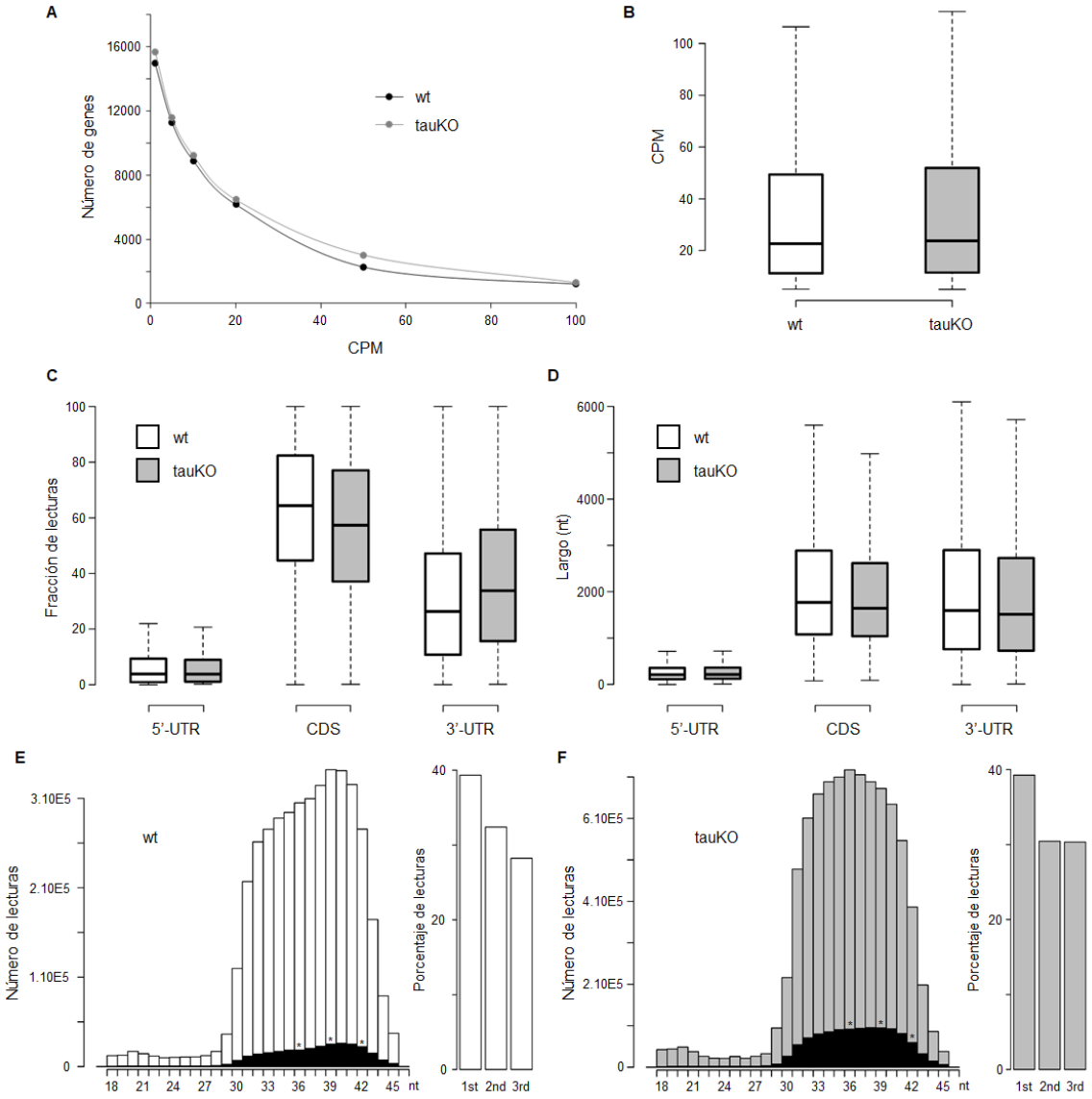

Figura V.4. Análisis globales de la secuenciación masiva de huellas ribosomales obtenidas a partir de cultivos *in vitro* de neuronas corticales primarias. (**A**) El gráfico muestra el número de genes detectado para cada uno de los genotipos utilizados (wt, *wild-type* y tauKO, *tau-knockout*) utilizando distintos valores de conteos por millón (CPM) como mínimo exigido. (**B**) Se muestra la distribución de los valores de expresión génica mediante boxplots, para ambos genotipos, utilizando aquellos genes con >5 CPM (11.274 y 11.589 genes en los genotipos wt y tauKO, respectivamente). (**C**) Se muestra la distribución de las regiones donde mapean las lecturas sobre el ARNm (5'-UTR, CDS y 3'-UTR) para ambos genotipos. (**D**) Como control de las distribuciones que se muestran en (C), se grafica la distribución de los tamaños de las regiones utilizadas. (**E**) Se muestra, mediante histogramas, la distribución de tamaño de las huellas ribosomales mapeadas en el genotipo wt y del subset utilizado para el cálculo de periodicidad (en negro). Los tamaños indicados con asteriscos (*) fueron utilizados para el cálculo de la periodicidad cuyo resultado se muestra a la derecha, donde se indica el porcentaje de lecturas que caen en cada uno de los tres nucleótidos del codón. (**F**) Idem (E) pero para el genotipo tauKO.

---

como agente que desensambla los polisomas. Por ejemplo, esperamos que la cantidad de ARN presente en el pellet polisomal disminuya cuando corremos la muestra en presencia de EDTA.

Una vez que logramos obtener pellet polisomales con suficiente cantidad de ARN, procedemos a realizar los ensayos de digestión y separar las muestras en PAGE 15% con urea 7 M. Luego cortamos las bandas correspondientes a las huellas ribosomales y recuperamos el ARN de manera de evaluar el rendimiento final, la cantidad de ARN obtenido y los tamaños de huellas recuperadas.

En la figura V.5 se muestra el resultado del protocolo final optimizado a partir del cual logramos obtener huellas ribosomales a partir de corteza cerebral en cantidad, calidad y tamaño adecuado para la posterior generación de librerías de secuenciación. Se muestra el gel desnaturalizante de poliacrilamida al 15% donde puede verse el perfil de bandas generado, así como el control sin digerir. Se muestra también la reconstrucción virtual del gel generada por el *Bioanalyzer* resultado de la electroforesis capilar en chip de *small RNA*. En este caso también se observa específicamente la muestra de ARN correspondiente a las huellas ribosomales extraídas de la banda cortada del gel. Por último se muestran los perfiles de electroferogramas de la digestión y las huellas ribosomales superpuestos. Puede observarse como la muestra correspondiente a las huellas ribosomales está enriquecida en fragmentos de 28 y 31 nt de largo como es de esperarse. En este caso se obtuvieron aproximadamente 300 ng de ARN lo cual es suficiente para proceder a los protocolos de secuenciación. Este mismo protocolo, aquí optimizado y puesto a punto, será utilizado en el capítulo 3 (ver más adelante).

- Comparativa entre huellas ribosomales producidas con Benzonasa y RNAsa I

Con el objetivo de buscar similitudes y diferencias en los resultados obtenidos a partir de diferentes protocolos, donde se utilizan distintas enzimas para la producción de huellas ribosomales, nos propusimos comparar los resultados obtenidos a partir de digestiones realizadas con Benzonasa y RNAsa I. Nuestro grupo ha trabajado desde un principio con la enzima Benzonasa debido a que es capaz de generar fragmentos de ARN con los extremos 5’ fosforilados y 3’ desfosforilados (ejemplos en [78–80]). Esto representa una clara ventaja desde el punto de vista del protocolo pues permite la ligación directa de adaptadores de secuenciación, sin necesidad de pasos intermedios de fosforilación, precipitación y recuperación, que podrían introducir sesgos o disminuir los rendimientos [104,105]. Por el otro lado, la enzima RNAsa I es la utilizada en el protocolo original y la más utilizada, en general, en los trabajos donde se utiliza la técnica de Ribo-Seq [84]. Sin embargo, esta enzima si deja

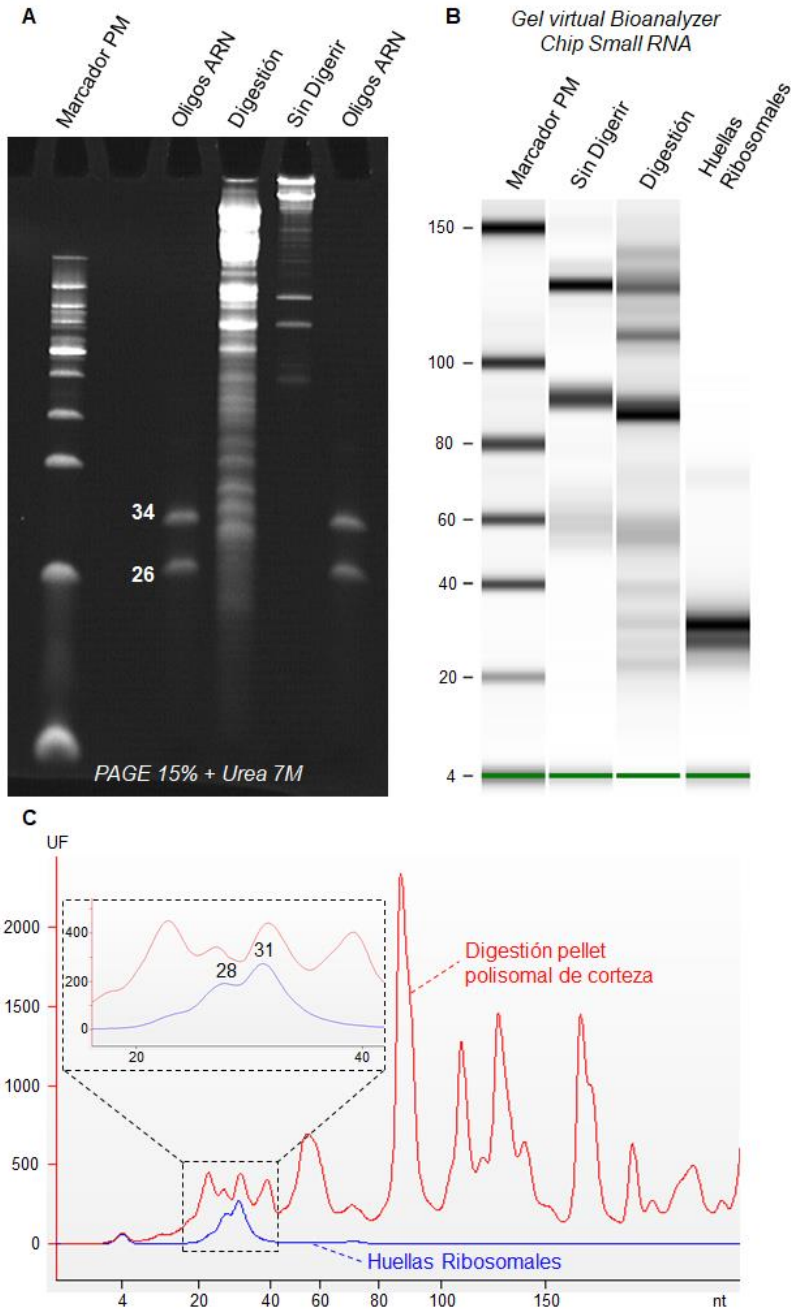

Figura V.5. Purificación de huellas ribosomales a partir de corteza de ratón. (**A**) Se muestra el gel de poliacrilamida 15% con urea 7 M donde se sembró la digestión del pellet polisomal y el control correspondiente sin digerir. Los oligos de ARN de 26 y 34 nt fueron utilizados para reconocer las bandas de las huellas ribosomales. (**B**) Se muestra la reconstrucción virtual del gel corrido en *Bioanalyzer* utilizando chip de *small RNA*. Nuevamente se muestra el control sin digerir, la muestra digerida y la fracción de ARN correspondientes a las huellas ribosomales recuperada del gel. (**C**) Se muestran los electroferogramas obtenidos del *Bioanalyzer* superpuestos para la digestión del pellet polisomal de corteza en rojo y las huellas ribosomales recuperadas en azul. La zona correspondiente a las huellas ribosomales se muestra ampliada y se pueden apreciar los picos en 28 y 31 nt correspondientes a las huellas ribosomales.

---

los extremos 3’ fosforilados por lo cual es necesario un paso de desfosforilación previo a la construcción de librerías de secuenciación.

Para realizar dicha comparación obtuvimos distintos pellet polisomales a partir de células HEK293 en cultivo y realizamos en paralelo y en duplicado digestiones con Benzonasa y RNAsa I sobre muestras equivalentes. Purificamos el ARN de cada digestión y separamos las mismas mediante corrida electroforética. Luego obtuvimos las huellas ribosomales a partir de las bandas correspondientes y en el caso de las huellas ribosomales derivadas de la digestión con la enzima RNAsa I, procedimos a fosforilar los extremos 5’ y desfosforilar los extremos 3’. En último lugar el ARN es precipitado, recuperado y concentrado nuevamente (ver Figura V.6).

Los perfiles de digestiones obtenidos con las dos enzimas muestran algunas diferencias que son particularmente claras en las regiones de tamaños mayores a las huellas ribosomales (ver Figura V.7 A y B). Específicamente en la región correspondiente a las huellas ribosomales también se pueden apreciar diferencias. Por ejemplo, el electroferograma observado en la región correspondiente a las huellas ribosomales muestra que las digestiones con Benzonasa producen un pico cercano a 28 nt y dos hombros de menor absorbancia a 26 y 31 nt. Por su parte, el perfil de digestión producido por la RNAsa I en estas condiciones muestra un pico principal a 31 nt y un hombro a la altura de 28 nt (ver Figura V.7 B). Luego de purificadas y concentradas, y para el caso de las huellas producidas con RNAsa I también desfosforiladas, las huellas ribosomales muestran pequeñas diferencias de tamaños (ver Figura V.7 C). De todas maneras, en ambos casos se obtuvieron cantidades suficientes para la construcción de librerías de secuenciación: 768 y 636 ng de ARN para las huellas producidas con Benzonasa y 370 y 350 ng de ARN para las producidas con RNAsa I. Se puede observar aquí que al comparar la cantidad de huellas ribosomales producidas con RNAsa I recuperadas del gel y la cantidad final obtenida luego de desfosforilar, precipitar y concentrar, observamos una pérdida cercana al 50%, como mencionábamos anteriormente.

La secuenciación masiva de las huellas ribosomales, en duplicados biológicos, producidas con Benzonasa y RNAsa I generó en promedio más de 120 millones de lecturas simples. De éstas, cerca del 85% correspondían a fragmentos de ARNr mientras que cerca de 10 millones mapearon sobre ARNm (ver Tabla V.1). El análisis de componentes principales (PCA) muestra como las dos réplicas de cada condición, que a continuación llamaremos directamente Benzonasa y RNAsa I, se separan claramente según la primera componente que explica casi el 87% de la variación observada (ver Figura V.8 A). También se observa cómo ambas réplicas de cada condición muestran altos niveles de correlación, con valores de correlación de Pearson superiores a 0,98 (ver Figura V.8 B). Como una primera aproximación,

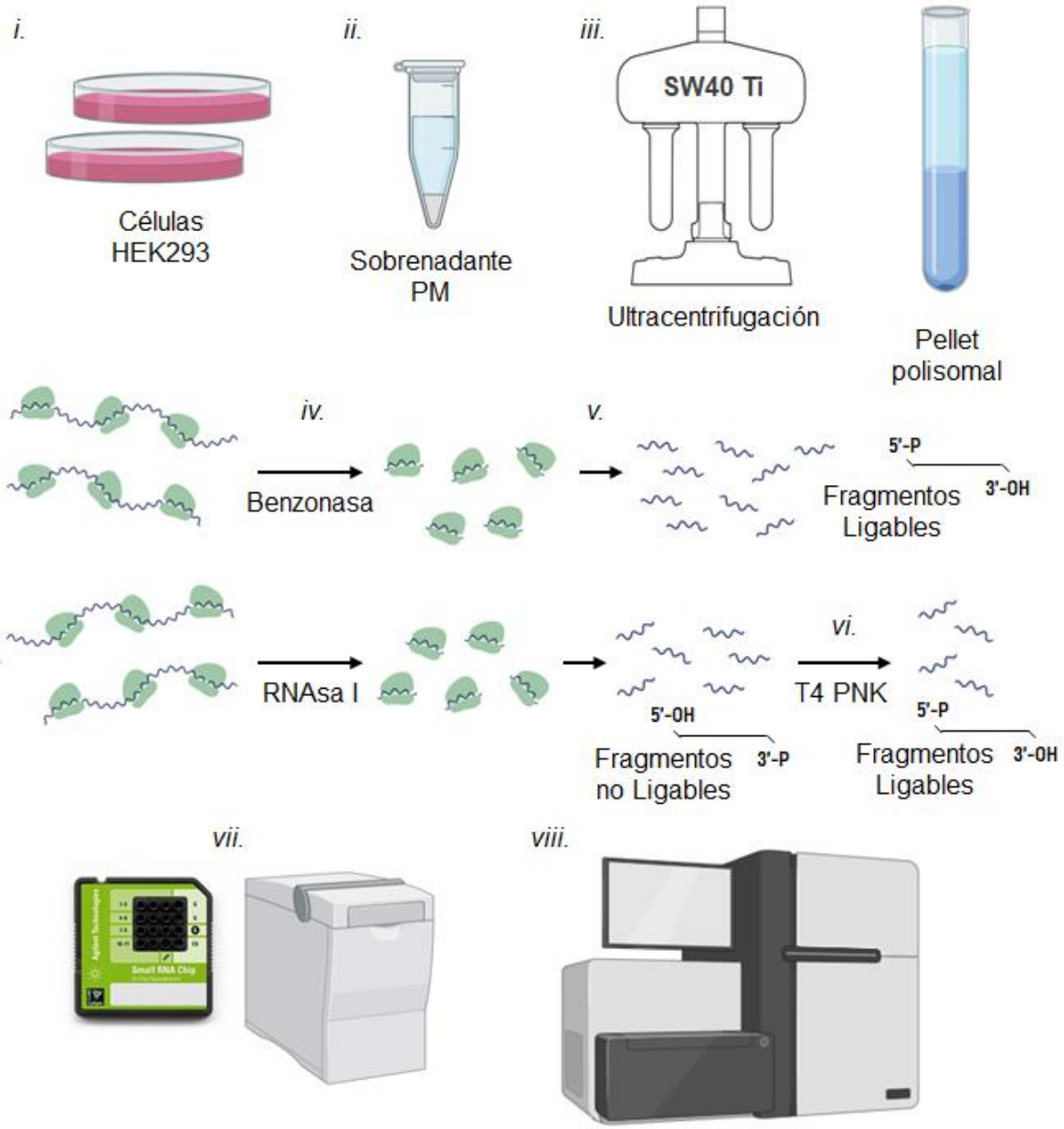

Figura V.6. Estrategia experimental para la producción y comparación de huellas ribosomales utilizando Benzonasa y RNAsa I. Se muestra un esquema del protocolo realizado para la obtención y secuenciación de huellas ribosomales generadas con Benzonasa y RNAsa I. Se cultivan células HEK293 en confluencia (i) y se lisan para obtener el sobrenadante postmitocondrial (PM; ii). Dicho sobrenadante es ultracentrifugado en colchones de sacarosa para obtener un pellet polisomal (iii). Cantidades equivalentes del pellet polisomal son digeridas en paralelo con ambas enzimas (iv) y las huellas ribosomales son recuperadas (v). Las huellas ribosomales producidas con la enzima Benzonasa presentan un extremo 5' fosforilado y un extremo 3' desfosforilado, por lo que son fragmentos ligables. Por su parte, las huellas producidas con RNAsa I son fragmentos no ligables por lo que requieren un paso adicional de fosforilación de extremos 5' mediante acción de la T4 quinasa (T4 PNK; vi). Por último los fragmentos son evaluados en calidad y cantidad mediante chips de *small RNA* en *Bioanalyzer* (vii) y posteriormente secuenciados de manera masiva (viii).

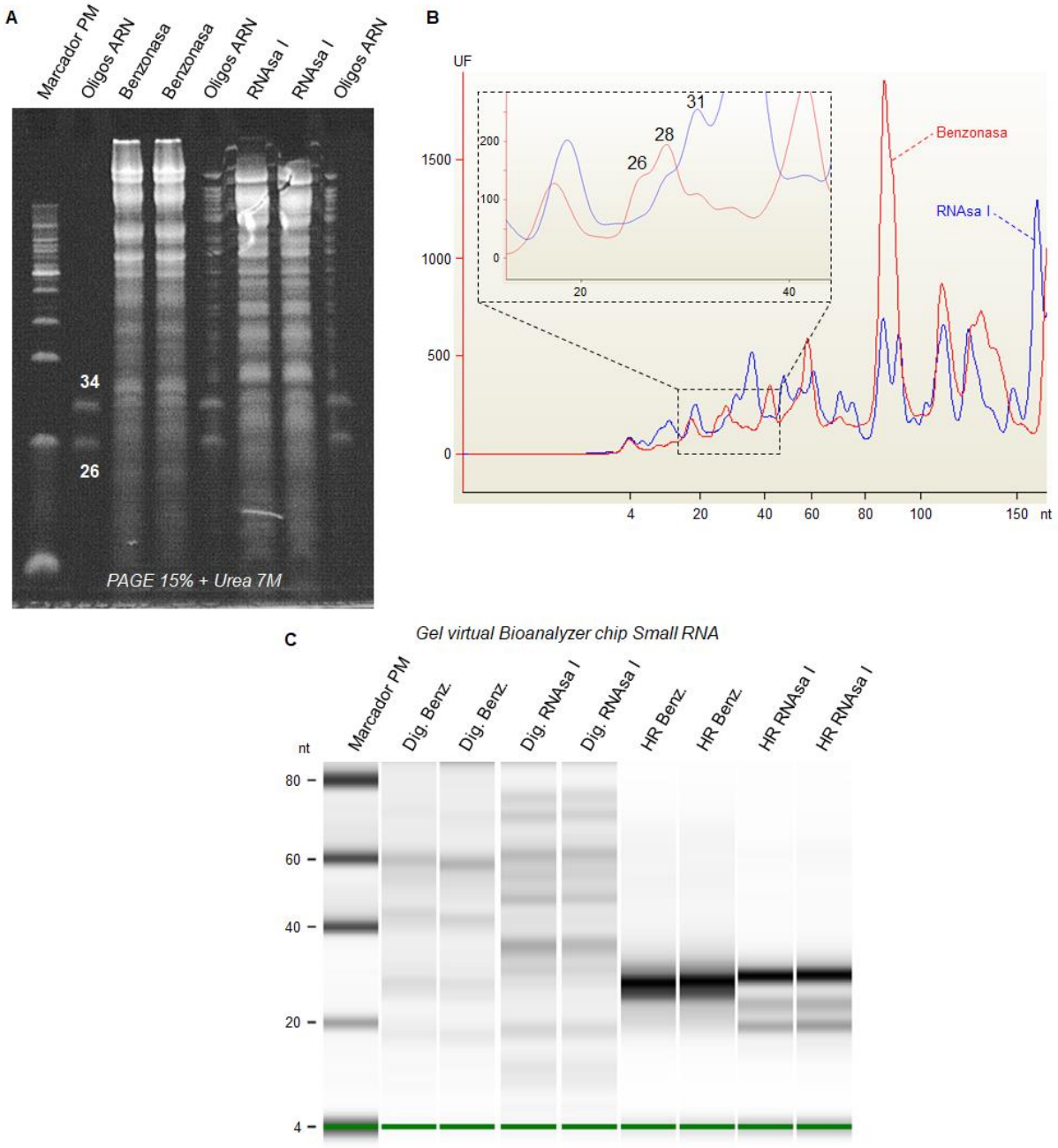

Figura V.7. Purificación de huellas ribosomales utilizando Benzonasa y RNAsa I. (**A**) Se muestra la corrida en PAGE 15% con urea 7 M de las digestiones de pellet polisomales utilizando Benzonasa y RNAsa I, en duplicados. Los oligos de ARN se utilizaron para identificar y cortar las bandas correspondientes a las huellas ribosomales. (**B**) Las digestiones también fueron evaluadas por electroforesis capilar en chip de *small RNA* en *Bioanalyzer*. Se muestra el electroferograma observado para las dos enzimas: en rojo Benzonasa y en azul RNAsa I. Se muestra también ampliada la zona correspondiente a las huellas ribosomales. (**C**) Se observa la representación virtual del gel producida por el *Bioanalyzer*. Se pueden observar las distintas digestiones (Dig) obtenidas de las dos enzimas (Benz y RNAsa I), así como las bandas específicas de las huellas ribosomales (HR) obtenidas en último lugar.

Tabla V.1. Estadísticos de secuenciación y mapeo de huellas ribosomales obtenidas a partir de Benzonasa y RNAsa I. La tabla muestra el número total de lecturas obtenidas, el porcentaje de las mismas que corresponde a contaminación por ARNr, la cantidad de lecturas mapeadas sobre el transcriptoma de referencia y específicamente sobre los ARNm.

Enzima	#	Total de lecturas	% de ARNr	Lecturas mapeadas	Lecturas mapeadas sobre ARNm	% sobre ARNm
Benzonasa	1	122.906.986	81,8%	16.673.224	14.720.802	88,3%
	2	95.768.276	84,2%	9.438.694	8.106.113	85,9%
RNAsa I	1	123.579.208	87,7%	8.549.450	7.310.863	85,5%
	2	153.015.842	88,7%	10.700.276	9.222.608	86,2%

comparamos la equivalencia de ambas enzimas para producir huellas ribosomales de los mismos genes. Luego de filtrar según distintos valores de expresión, para evitar usar genes con pocas lecturas cercanos al ruido, intersectamos las listas de genes detectados en cada caso. De esta manera, por ejemplo, utilizando un filtro de genes con valores de expresión mayores a 1 CPM, detectamos 15.631 genes con la enzima Benzonasa y 14.998 con la RNAsa I, de los cuales 14.549 eran compartidos (el 93% y 97% respectivamente). De manera similar, si filtramos según un valor de expresión mayor a 5 CPM se observan resultados similares: 11.431 genes detectados con la Benzonasa y 11.084 con la RNAsa I habiendo 10.501 en común, el 92% y 95% respectivamente (ver Figura V.8 C). Además de compartir un alto porcentaje de los genes detectados entre las dos condiciones, se puede observar una buena correlación global entre los niveles de expresión cuantificados con cada enzima, como se muestra en el *scatter plot* de la Figura V.8 D.

En primer lugar, nos planteamos estudiar si los niveles de expresión traduccional definidos por cada enzima eran comparables o si existían grandes grupos de genes detectados con una enzima pero ausentes con la otra. Así, nos propusimos evaluar posibles diferencias o sesgos en los genes detectados por una enzima y no por la otra. De esta manera, considerando que los valores de expresión génica calculados para cada enzima mostraban distribuciones globales similares (ver Figura V.9 A), decidimos aplicar tres criterios para definir los grupos de genes asociados a cada enzima. En cada grupo, se espera representar genes

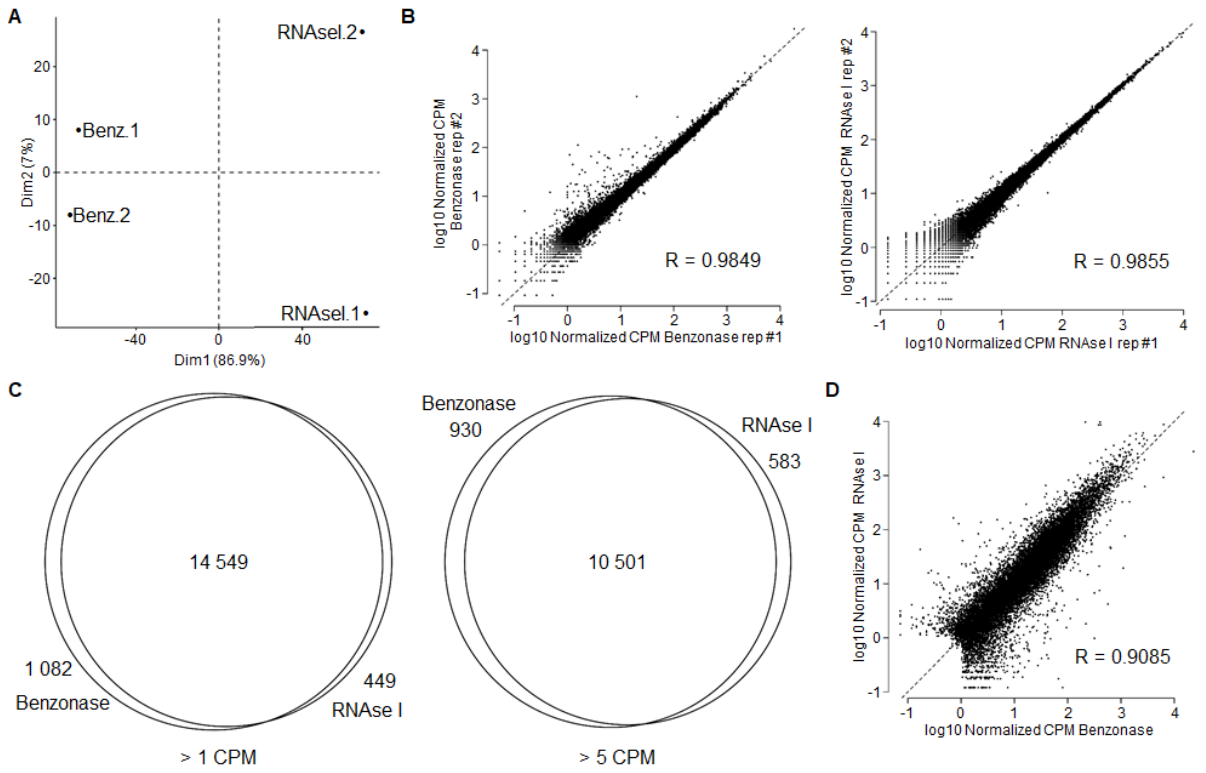

Figura V.8. Comparación global de los niveles de expresión génica obtenidos a partir de las dos enzimas. (**A**) Se muestra un PCA de las 4 muestras donde se observa claramente la separación de las dos condiciones según la primera componente que explica el 86,9% de la variación. (**B**) Se muestra la correlación entre los valores de expresión génica calculados para cada réplica (n=2) según la enzima utilizada mediante sendos *scatter plots* (Benzonasa izquierda y RNAsa I derecha). Se indica también el valor de correlación de Pearson. (**C**) Los genes son filtrados según su nivel de expresión (>1 CPM, izquierda y >5 CPM, derecha) y las listas de genes son comparadas entre las dos enzimas. Se muestran los diagramas de Venn de dichas comparaciones. (**D**) Los valores promedio de expresión génica estimados según el uso de la Benzonasa y la RNAsa I son comparados en el *scatter plot* que se muestra. El valor de correlación de Pearson también es indicado.

---

apenas detectados con una enzima pero muy bien expresados con la otra, o genes que varían demasiado sus niveles de expresión entre las dos condiciones. Para esto, definimos tres criterios de filtrado que denominamos, según su lógica, de la siguiente manera: filtro por cuartiles, por expresión o por ranking. El filtro por cuartiles detecta aquellos genes que se encuentran en el primer cuartil de la distribución para una condición, pero su valor está por encima de la mediana en la segunda condición. El filtro por expresión devuelve aquellos genes con las diferencias de expresión más altas entre las dos condiciones. En este caso nos quedamos con el top50. En tercer lugar, el filtro por ranking selecciona aquellos genes que, luego de ordenarlos por niveles de expresión, cambian su posición en el ranking entre las dos condiciones más de 5000 puestos. Utilizando estos tres criterios filtramos 58, 50 y 136 genes respectivamente, cuya expresión y/o presencia se ve favorecida con la enzima Benzonasa.

Por su parte, para la enzima RNAsa I, filtramos 39, 50 y 117 genes, respectivamente para los tres criterios. Los valores de expresión de cada subgrupo así como la lógica de cada filtro puede observarse en la Figura V.9 B. De todas maneras, los filtros no son excluyentes y existe cierto solapamiento entre los distintos criterios. En el caso de la Benzonasa el número de genes únicos total fue de 188 y para la RNAsa I de 170 (ver Figura V.9 C). En un primer lugar nos interesaba conocer si este grupo de genes representaba alguna función biológica o proceso en particular, por lo que realizamos análisis de ontología. Los resultados mostraron por un lado que los 188 genes de detección sesgada con la Benzonasa no representaban funciones ontológicas sobrerrepresentadas, solamente detectamos enriquecidas vías KEGG asociadas al espliceosoma y al transporte de ARN (ver Figura V.9 D y Figura Suplementaria XI.1). Por el otro lado, los 170 genes asociados a la RNAsa I si mostraron sobrerrepresentadas categorías ontológicas principalmente relacionadas al ribosoma, unión al ARN, plegamiento de proteínas y traducción (ver Tabla Suplementaria XI.1). En este caso las vías KEGG enriquecidas fueron el ribosoma, el procesamiento de proteínas en el retículo endoplásmico y el espliceosoma (ver Figura V.9 D y Figura Suplementaria XI.2). De todas maneras llamó nuestra atención la baja proporción de genes codificantes en las listas analizadas. Por ejemplo, el porcentaje de genes codificantes en ambas listas fue de 41,5% y 58,2% para Benzonasa y RNAsa I respectivamente. Por esta razón exploramos la identidad de los genes no codificantes en cada set de datos y encontramos una importante presencia de ARN pequeños, en particular especies *small nuclear* y *small nucleolar* (ver Figura V.9 E).

En paralelo aplicamos paquetes de análisis de expresión génica diferencial para reconocer genes cuyos valores de expresión estimados por las dos enzimas sean estadísticamente diferentes y así complementar el análisis anterior en búsqueda de genes asociados a cada enzima. Vale aclarar en este aspecto, que el concepto de expresión génica diferencial en este caso no está asociado al clásico estudio de dos condiciones biológicas distintas, sino a la comparación entre los niveles de expresión génica cuantificados mediante una y otra enzima en la misma condición biológica. En este caso, la comparativa entre las dos réplicas de cada condición pudo identificar una gran cantidad de genes expresados diferencialmente según el criterio de tasa de cambio mayor a 2 y p-valor ajustado (FDR) menor a 0,05. De todas maneras, observamos que una gran proporción de dichos genes indicados como diferenciales corresponden a genes de baja expresión (<10 CPM en ambas condiciones): 1283 de los 2412 genes sobrerrepresentados con la enzima Benzonasa (47%) y 604 de los 1947 sobrerrepresentados con la enzima RNAsa I (31%; ver Figura V.10 A). Por dicha razón, eliminamos estos genes de baja expresión de las listas de genes diferenciales. A nivel global,

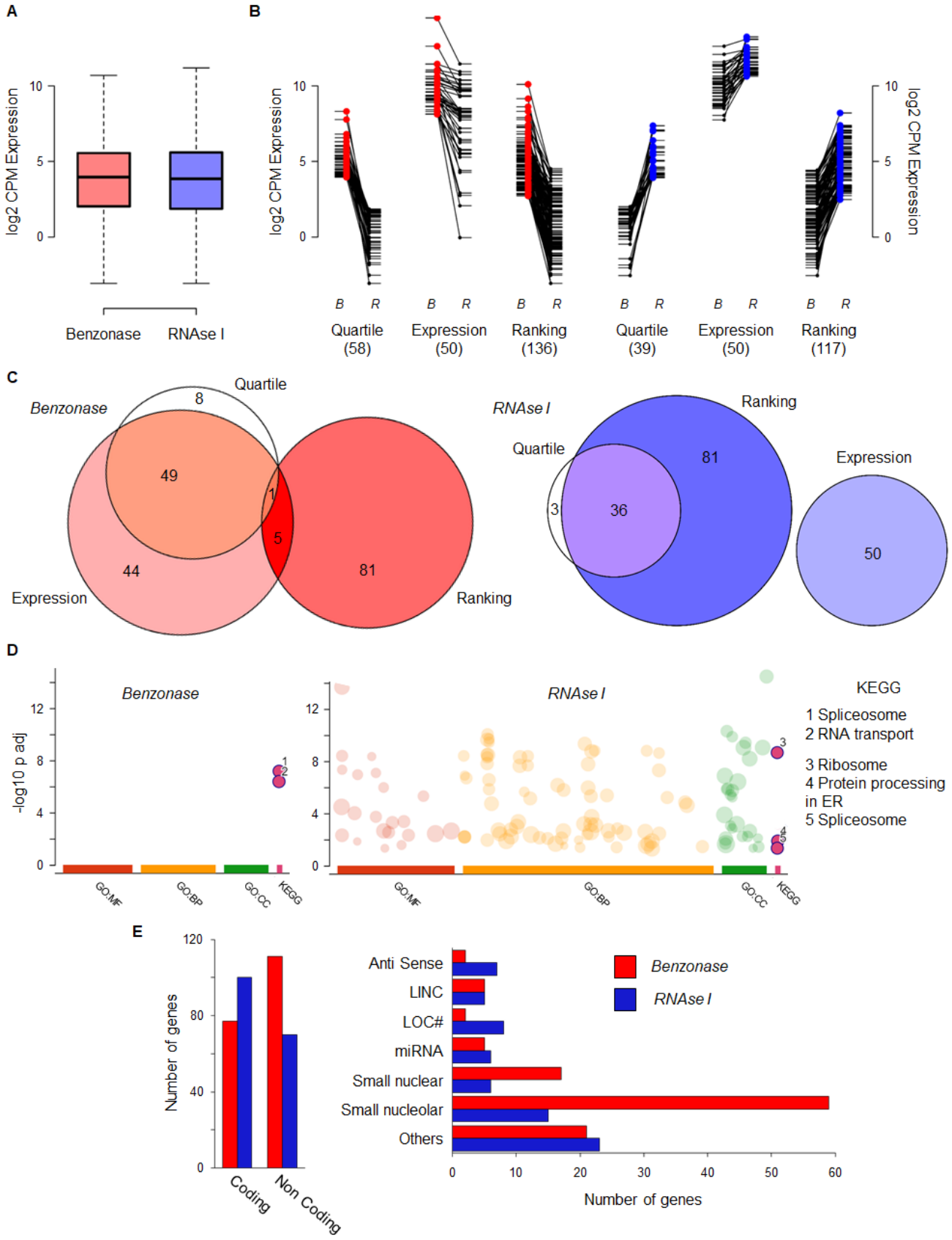

Figura V.9. Identificación de genes asociados con cada enzima y análisis funcional de los mismos. (**A**) Se muestra la distribución global de los valores de expresión (CPM) determinados para cada enzima mediante *boxplots*. (**B**) Se muestran los niveles de expresión de los genes seleccionados por cada criterio de filtrado (*Quartile*, *Expression* y *Ranking*; se

(la leyenda continúa en la siguiente hoja)

indica el número de genes en cada caso). En rojo se representan los genes asociados a la Benzonasa y en azul a la RNAsa I. (**C**) Mediante diagramas de Venn se muestran las coincidencias entre cada una de las tres listas de genes producidas por cada criterio de filtrado. A la izquierda, en rojo, para los asociados a la Benzonasa y a la derecha, en azul, para la RNAsa I. (**D**) Se muestran los resultados del análisis de ontología génica realizados con la herramienta g:GOSt del g:Profiler. A la izquierda para los genes asociados a la Benzonasa y a la derecha para los asociados a la RNAsa I. En los dos casos se muestran las categorías de función molecular (GO:MF), procesos biológicos (GO:BP), compartimento celular (GO:CC) y vías KEGG (KEGG). Las vías KEGG señaladas numéricamente son indicadas a la derecha. (**E**) A la izquierda se muestra el número de genes codificantes y no codificantes asociados a cada enzima. A la derecha se muestran en detalle los genes no codificantes agrupados según distintas categorías, para las dos enzimas. En ambos casos, en rojo se muestran los genes asociados a la Benzonasa y en azul a la RNAsa I.

---

se observa el aumento de expresión de los genes diferenciales en cada condición (ver Figura V.10 B y C). Si comparamos las listas de genes asociados a cada enzima discutidas anteriormente observamos que una gran proporción de los genes se encuentran expresados diferencialmente: 74% de los asociados a la Benzonasa y 83% de los asociados a la RNAsa I (ver Figura V.10 D). El análisis de ontología de la lista de genes diferenciales arrojó varias funciones enriquecidas de manera significativa, como era de esperar considerando la gran cantidad de genes analizados (ver Figura V.10 E y F). Principalmente, en los genes sobrerrepresentados con la enzima Benzonasa se reconocen procesos metabólicos generales y funciones asociadas a la transcripción, mientras que en los genes sobrerrepresentados con la enzima RNAsa I se destacan el ribosoma y la cadena de transporte de electrones de la mitocondria.

De esta manera, con base en los resultados anteriores (ver Figuras V.8, V.9 y V.10) podemos afirmar que a pesar de existir grupos de genes cuya detección parece verse asociada al uso de una u otra enzima en particular, y encontrar eventos de expresión génica diferencial, los compartimentos traduccionales definidos por ambas enzimas presentan estimaciones de expresión génica comparables.

A continuación, y al igual que para el análisis de las huellas ribosomales producidas a partir de los cultivos *in vitro* de neuronas corticales primarias, en este caso también analizamos características globales de las huellas ribosomales producidas con cada enzima, por ejemplo su distribución entre las regiones codificantes y no codificantes de los ARNm, su periodicidad y preferencia de corte, así como también los perfiles de mapeo producidos en cada caso. En primer lugar, la distribución de mapeo sobre las regiones del ARNm mostró los resultados esperados (ver Figura V.11 A). Para ambas enzimas, las huellas mapean de manera preferencial sobre las regiones correspondientes a los CDS respecto de las regiones no traducidas. La distribución para las huellas generadas con Benzonasa muestra un perfil similar

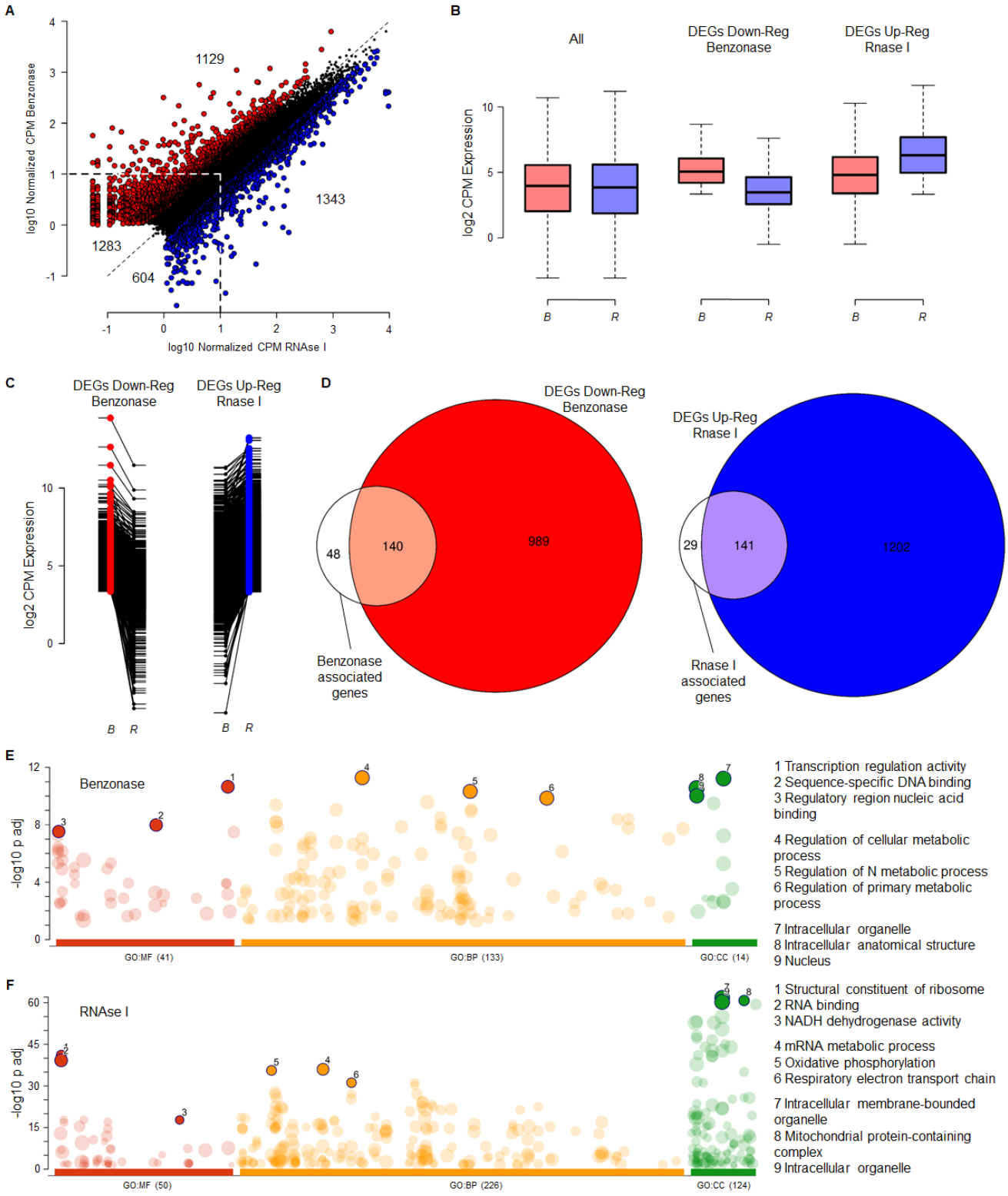

Figura V.10. Análisis de expresión génica diferencial entre los traductomas producidos con Benzonasa y RNAsa I. (**A**) *Scatter plot* comparando los niveles de expresión determinados para cada enzima. En colores se indican los genes expresados diferencialmente: en rojo los sobrerrepresentados con la Benzonasa y en azul con la RNAsa I. Se muestra el corte en el valor de expresión de 10 CPM por debajo del cual se descartan esos genes por ser de baja expresión. (**B**) La distribución de los valores de expresión de todos los genes, los sobrerrepresentados con la Benzonasa y los sobrerrepresentados con la RNAsa I se muestran mediante boxplots. En rojo los valores de expresión para la condición

(la leyenda continúa en la siguiente hoja)

Benzonasa y en azul para la RNAsa I. (**C**) Se muestran los cambios en los niveles de expresión para los genes diferenciales asociados a cada enzima. En rojo para la Benzonasa y en azul para la RNAsa I. (**D**) Los genes comunes entre los asociadas a cada enzima definidos por los tres criterios definidos anteriormente y los genes expresados diferencialmente se muestran mediante diagramas de Venn para cada enzima. (**E**) Se muestran los resultados del análisis de ontología génica realizados con la herramienta g:GOSt del g:Profiler para los genes sobrerrepresentados con la Benzonasa. Se muestran las categorías de función molecular (GO:MF), procesos biológicos (GO:BP) y compartimento celular (GO:CC). En cada caso, las tres categorías más significativas son indicadas numéricamente e indicadas a la derecha. (**F**) Idem a (E) para los genes sobrerrepresentados con la enzima RNAsa I.

---

al obtenido para las neuronas *in vitro* (ver Figura V.4 C). De todas maneras se aprecian claras diferencias al comparar las distribuciones entre las dos enzimas. Las huellas producidas con RNAsa I muestran mapeos con un claro sesgo al CDS (93-94%) y casi no vemos representadas a las regiones no traducidas, aunque el 5'-UTR se ve un poco más representado que el 3'-UTR (3,2% y 0,6%, respectivamente; ver Figura V.11 A). Por su parte, las huellas producidas con Benzonasa mapean con un patrón global distinto. Se distribuyen de manera mayoritaria sobre la región codificante (70%), aunque la región correspondiente al 3'-UTR se ve más representada (20%) que en las huellas derivadas de la RNAsa I, mientras que el 5'-UTR parece verse igual de representado (4%). Al igual que mencionamos anteriormente, estas asimetrías en las distribuciones entre regiones codificantes y no codificantes no se deben a diferencias en el tamaño de las regiones analizadas (ver Figura V.11 B).

Inspirados en el trabajo de TP. Miettinen & M. Bjorklund (NAR, 2015) y en los resultados e hipótesis que los autores elaboran, nos propusimos analizar un poco más en detalle posibles razones que fundamenten la presencia de huellas ribosomales en el 3'-UTR, como se describen en el caso de la Benzonasa. Pudimos observar que, tal como muestran los anteriores autores, las huellas ribosomales presentes en el 3'-UTR tienen un tamaño distinto al observado para las huellas que mapean en el 5'-UTR o CDS. La diferencia se observa tanto en el caso de la Benzonasa, pero también para la RNAsa I aunque el porcentaje de lecturas mapeadas en esta región sea muy bajo (ver Figura V.12). De hecho, a pesar de presentar claras diferencias de tamaño en las huellas que mapean sobre el 5'-UTR y CDS (ver también más adelante), las huellas que mapean sobre el 3'-UTR parecen tener una distribución de tamaños similar con las dos enzimas, centradas en 35 nt de largo. En el trabajo anterior, una de las posibles razones que los autores elaboran para fundamentar la observación de huellas ribosomales en el 3'-UTR que encuentran con otra ARNasa (nucleasa micrococal), pero no

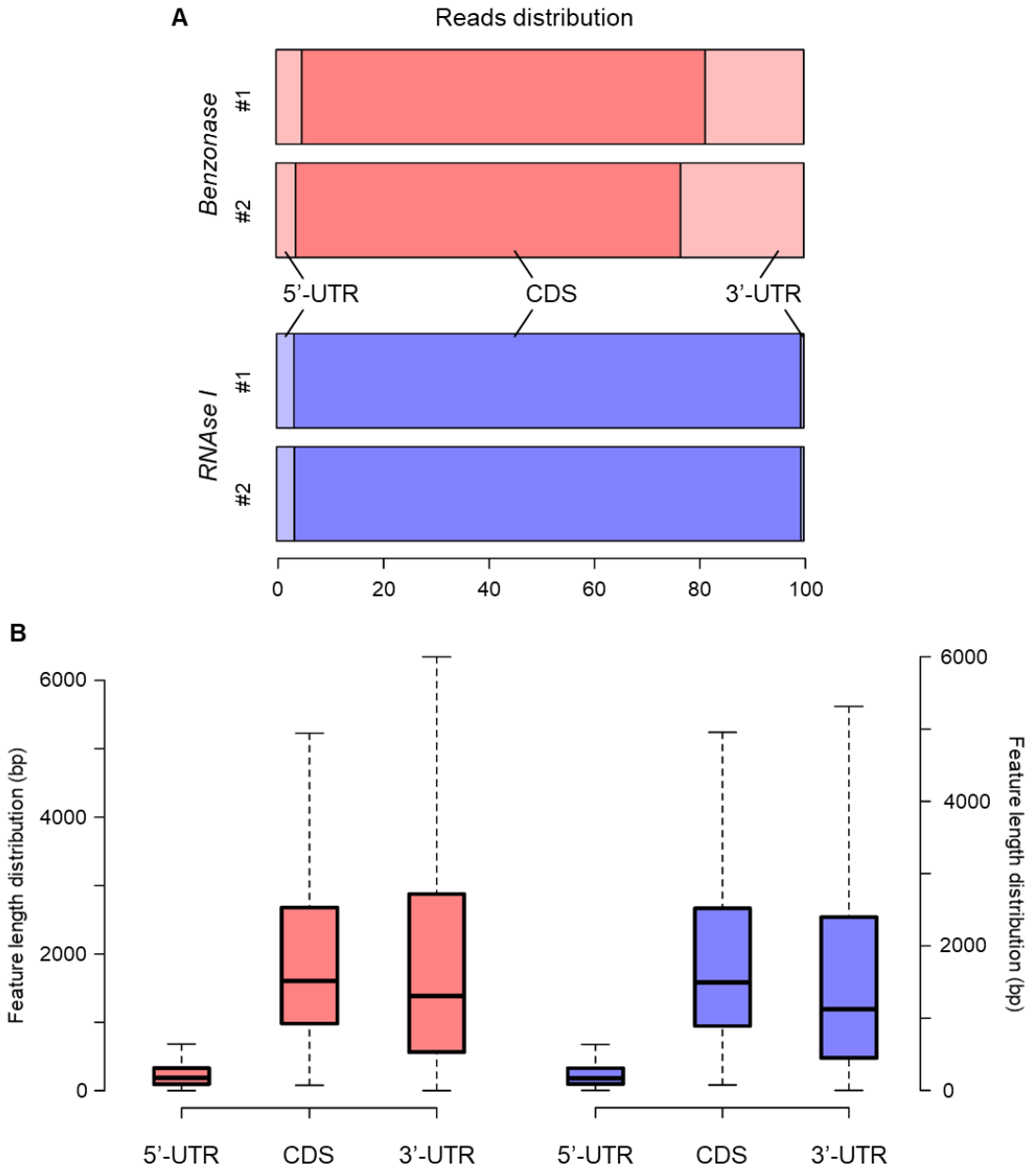

Figura V.11. Análisis de la distribución de las regiones de mapeo de las huellas ribosomales obtenidas con las dos enzimas. (**A**) Se muestra la distribución de las regiones donde mapean las lecturas en el ARNm (5'-UTR, CDS y 3'-UTR) para las dos réplicas de cada enzima (arriba y en rojo, Benzonasa; abajo y en azul, RNAsa I). (**B**) Como control de las distribuciones que se muestran en (A), se grafica la distribución de los tamaños de las regiones utilizadas. Puede observarse que el hecho de que se favorezcan los mapeos de las huellas ribosomales sobre la región traducida (CDS) no se debe a que éstas tengan un largo mayor y preponderante sobre las regiones no traducidas (5' y 3'-UTRs).

---

con RNAsa I, es la diferencia en la agresividad de la digestión por cada enzima. Entre otros, un argumento para fundamentar esto es que la RNAsa I produce fragmentos de ARNr derivados del 18S y 28S, presentes en las subunidades menor y mayor del ribosoma, respectivamente. En nuestro caso, efectivamente observamos fragmentos derivados de

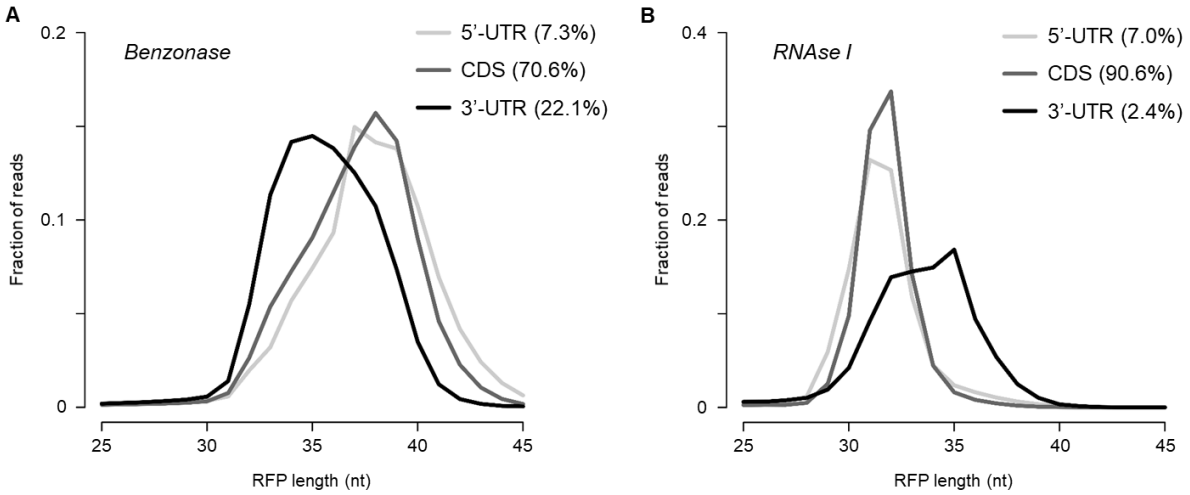

Figura V.12. Análisis de la distribución de los largos de las huellas ribosomales producidas con ambas enzimas en función de su región de mapeo. (**A**) Se muestra la distribución de largos para las huellas mapeadas sobre el 5'-UTR, CDS y 3'-UTR, indicando el porcentaje de huellas analizadas en cada región, para la Benzonasa. (**B**) Ídem (A), pero para las huellas ribosomales producidas con RNAsa I.

---

ambas especies de ARNr para la RNAsa I, mientras que en el caso de la Benzonasa solo observamos fragmentos del ARNr 28S (subunidad mayor; ver Figura V.13). Estas diferencias podrían indicar que la digestión con RNAsa I es más agresiva que la digestión con Benzonasa.

Considerando que los ribosomas en el 3'-UTR ya no son traduccionales y, en base a las diferencias de tamaños de las huellas, podrían adquirir otra conformación distinta a la de los ribosomas traduccionalmente activos que encontramos en el CDS, una hipótesis válida a plantear es que la digestión con la RNAsa I es más agresiva y logra romper por completo dichos ribosomas en el 3'-UTR, mientras que la Benzonasa no, y por eso la diferencia entre presencia y ausencia de huellas ribosomales en dicha región.

Retomando los análisis clásicos que mencionábamos para las huellas ribosomales, en segundo lugar, el estudio de la periodicidad de las huellas ribosomales también reveló diferencias entre las huellas producidas con una u otra enzima (ver Figura V.14). Por un lado, para las huellas ribosomales producidas con la enzima Benzonasa se obtuvo un patrón de tamaños y de periodicidad similar al obtenido para las neuronas *in vitro* y al observado en trabajos previos (ver [78,80] y capítulo 3), con niveles de periodicidad en el entorno de 40% para huellas de tamaños de 39 nt ± 3 nt (ver Figura V.14 A y B). Por el otro lado, las huellas ribosomales producidas con RNAsa I mostraron una distribución de tamaños distinta, centrada en 31-32 nt, y con mayores niveles de periodicidad (~60%) para las huellas de 31 nt, casi que sin verse representado el segundo nucleótido del codón (ver Figura V.14 C y D). Estos perfiles

de tamaños y periodicidad se asemejan a lo que se describe en la literatura en los trabajos que utilizaron RNAsa I para producir huellas ribosomales (ejemplo en [29]).

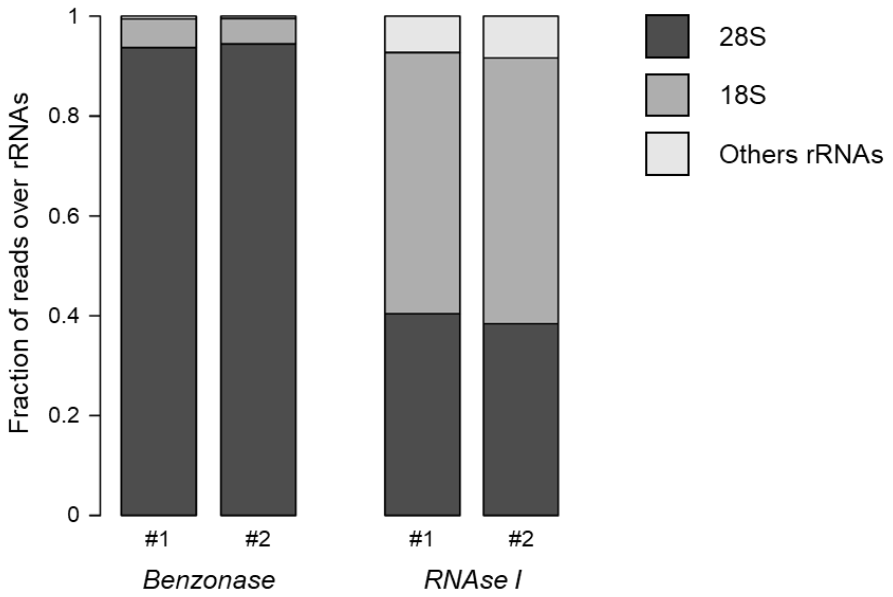

Figura V.13. Distribución de fragmentos de ARNr producidos por ambas enzimas entre las distintas especies de ARNr. Se muestra la fracción de huellas ribosomales derivadas de ARNr entre las distintas especies de ARNr, principalmente ARNr 18S (presente en la subunidad menor del ribosoma) y 28S (presente en la subunidad mayor), para las dos réplicas de cada enzima.

En tercer lugar analizamos si se observaba una preferencia en el sitio de corte de las dos enzimas evaluando la composición nucleotídica de los extremos de las lecturas. Pudimos observar que, como se esperaba, tanto para la Benzonasa como para la RNAsa I no se aprecian grandes sesgos o preferencias de corte (ver Figura V.15). Tanto en los primeros tres nucleótidos de las huellas ribosomales, como en los últimos tres, la distribución de nucleótidos es bastante uniforme.

En cuarto lugar, nos propusimos comparar perfiles de mapeos sobre algunos genes, en busca de coincidencias o diferencias. Para esto, seleccionamos genes de alta expresión comunes en todos los set de datos (ver Tabla Suplementaria XI.2), como ha sido realizado anteriormente para este tipo de análisis [89]. Así, elegimos 5 genes, todos codificantes para proteínas y con ARNm de un largo considerable (1285 a 3512 nt), y presentes en el top30 de genes más expresados en cada set de datos (al menos >20.000 lecturas mapeadas en cada muestra). A grandes rasgos, no se puede observar un patrón de mapeo conservado entre las dos enzimas (ver Figura V.16). La Benzonasa parece favorecer picos sobre el codón de inicio, que no se observan en los perfiles obtenidos con RNAsa I, y se observa mayor presencia de lecturas en las regiones 3'-UTR en los mapeos producidos con Benzonasa (ver Figura V.16),

como anticipamos anteriormente (ver Figura V.11).

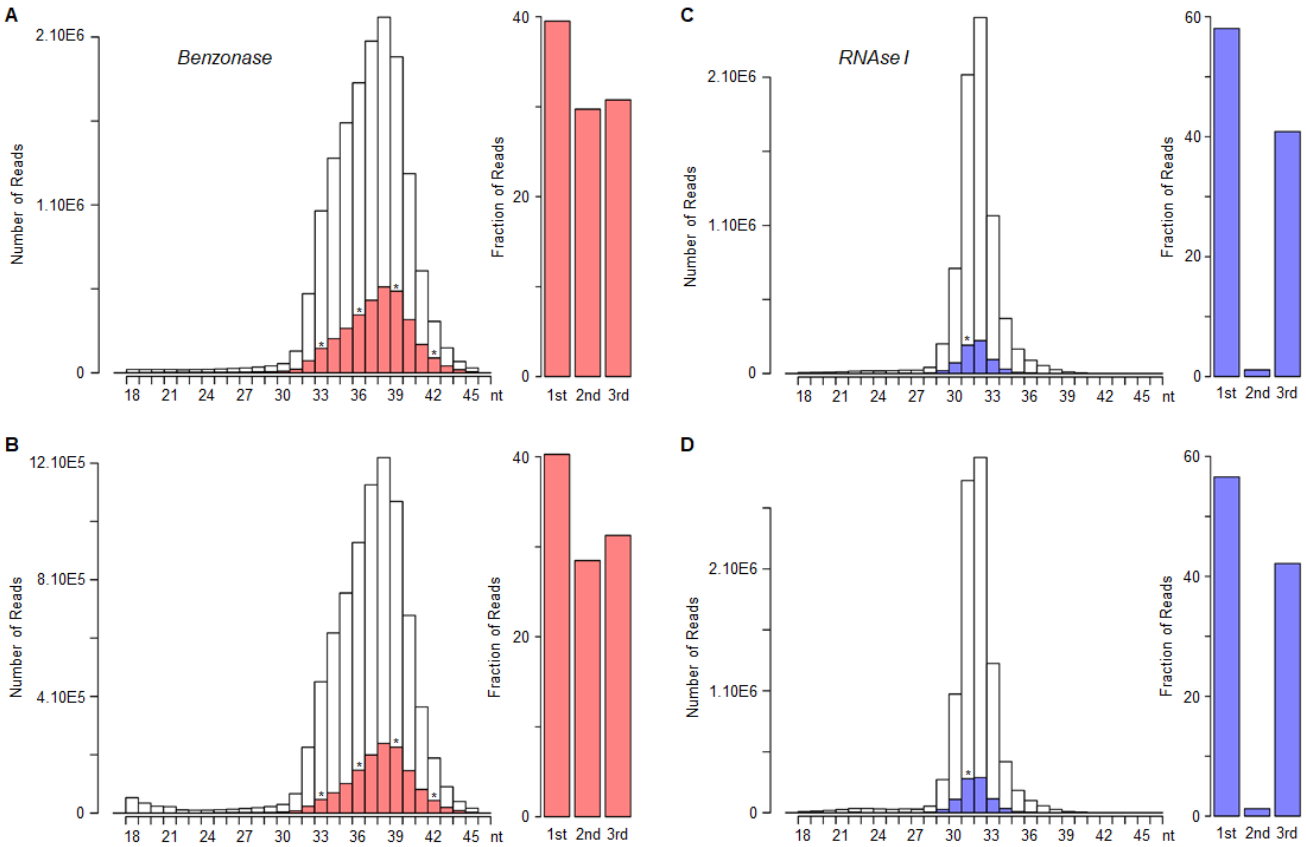

Figura V.14. Estudio de la periodicidad de huellas ribosomales obtenidas con ambas enzimas. (**A**) y (**B**) Se muestra, mediante histogramas, la distribución de tamaño de las huellas ribosomales obtenidas con Benzonasa para ambas réplicas. En rojo se muestra la distribución de tamaños del subset de huellas utilizado para el cálculo de periodicidad. Los tamaños indicados con asteriscos (*) son los que muestran el mayor grado de periodicidad, cuyo resultado se muestra a la derecha, donde se indica el porcentaje de lecturas que caen en cada uno de los tres nucleótidos del codón. (**C**) y (**D**) Idem a (A) y (B) pero para las dos réplicas obtenidas utilizando la enzima RNAsa I.

En último lugar, nos propusimos evaluar y comparar la población de fragmentos derivados de ARNr producidos por las dos enzimas. Como se mencionó anteriormente (ver Tabla V.1), en este experimento obtuvimos un promedio de 83% y 88% de contaminación por ARNr en las lecturas derivadas de las huellas ribosomales producidas con Benzonasa y RNAsa I, respectivamente. Esto representa 90 y 122 millones de lecturas, en promedio, respectivamente. Aquí observamos que tanto la distribución de estas lecturas entre las distintas especies de ARNr, como la abundancia de las mismas varía sustancialmente en función de la enzima utilizada en la digestión. Por ejemplo, 6 fragmentos derivados del ARNr 28S abarcan de manera casi equitativa el 93% del total de secuencias contaminantes cuando utilizamos Benzonasa. En cambio, cuando utilizamos RNAsa I son 7 los fragmentos y derivan,

5 del ARNr 28S y 2 del ARNr 18S (ver Figura V.17 y Tabla V.2), como anticipamos anteriormente (ver Figura V.13).

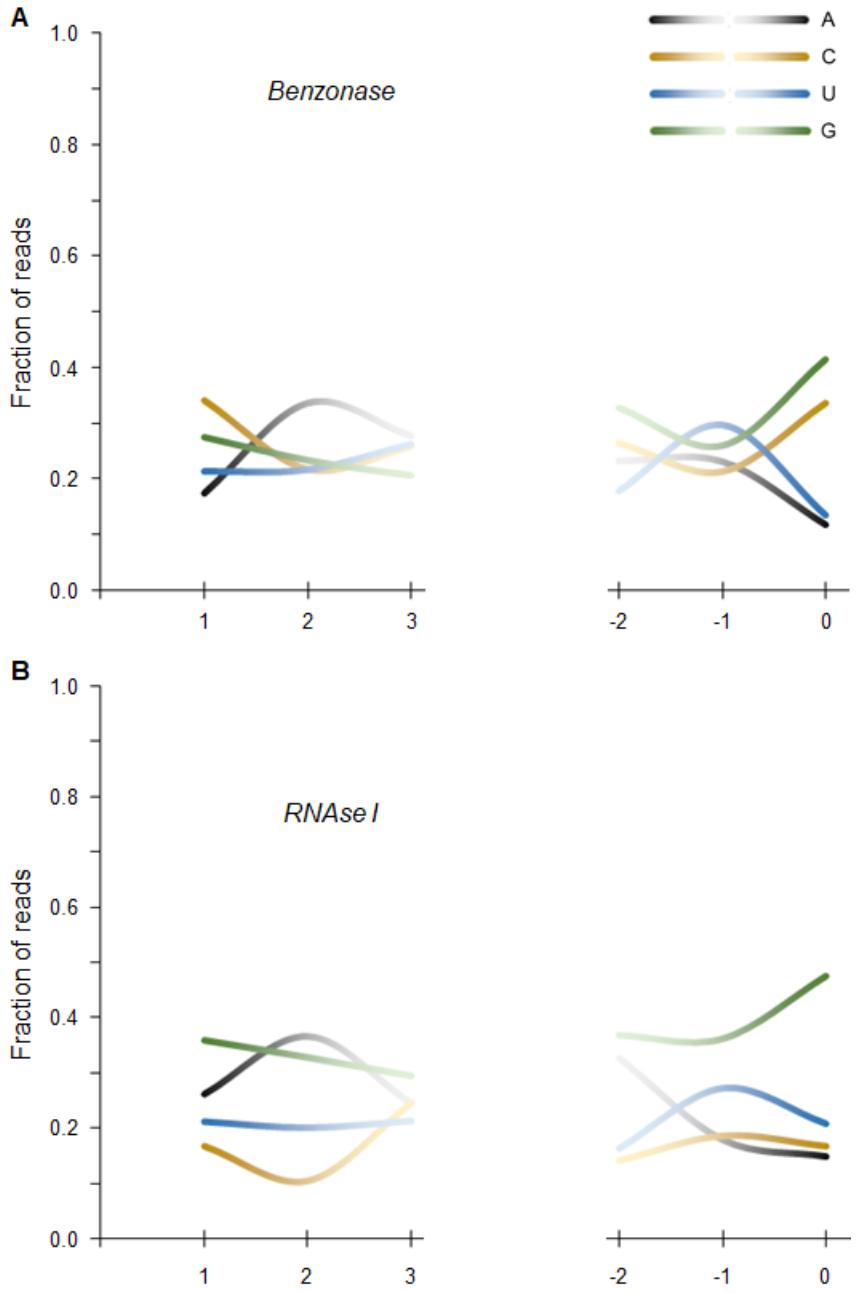

Figura V.15. Análisis de la preferencia de corte de Benzonasa y RNAsa I. Se muestra la distribución de los nucleótidos en las tres primeras y las tres últimas posiciones de las huellas ribosomales producidas con Benzonasa (**A**) y RNAsa I (**B**).

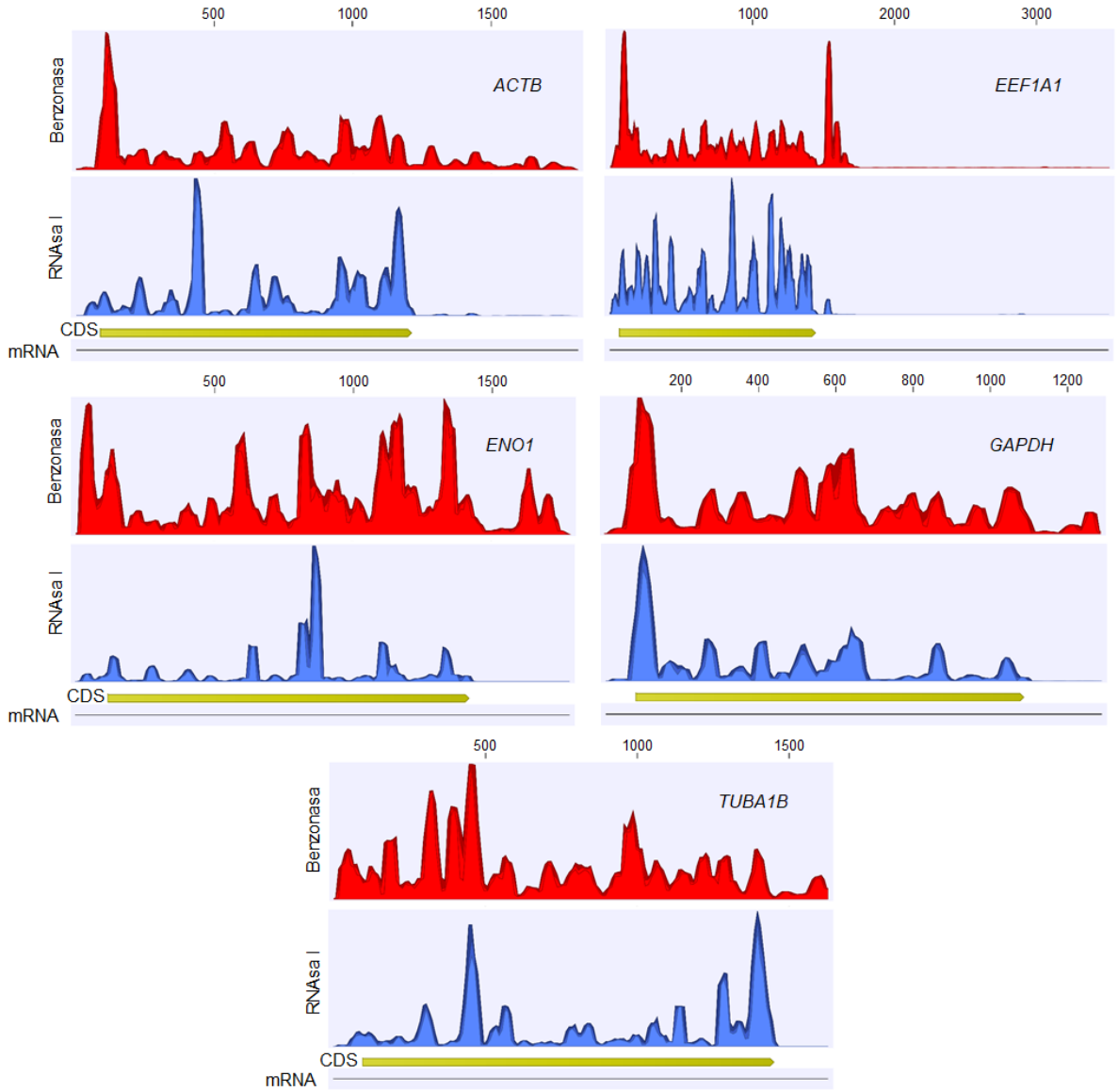

Figura V.16. Comparación de los patrones de mapeo sobre distintos ARNm de alta expresión entre ambas enzimas. Se muestran los perfiles de mapeo de huellas ribosomales producidas con Benzonasa (arriba, rojo) y RNAsa I (abajo, azul) para 5 distintos ARNm de alta expresión: *ACTB*, *EEF1A1*, *ENO1*, *GAPDH* y *TUBA1B*. En todos los casos se representa el ARNm maduro y se indica la región codificante (CDS).

En la Figura V.17 se puede observar el perfil de mapeo sobre los ARNr mencionados donde solo se observan picos puntuales que corresponden a los fragmentos derivados de la digestión del ribosoma y que concentran la gran mayoría de las secuencias. También podemos observar que los perfiles de mapeos obtenidos sobre las mismas especies de ARNr con Benzonasa y RNAsa I muestran distintos patrones de picos (ver Figura V.17 A). Tanto las secuencias como el tamaño de estos picos pueden encontrarse en la Tabla V.2. Puede apreciarse aquí también que no se comparte ninguno de los picos entre las dos enzimas. Del total de las 7 secuencias

contaminantes que aquí describimos en el ensayo con RNAsa I, encontramos 5 de ellas descritas como parte de oligos biotinilados para la sustracción de contaminación de ARNr según el protocolo original donde se utiliza esta misma enzima [84].

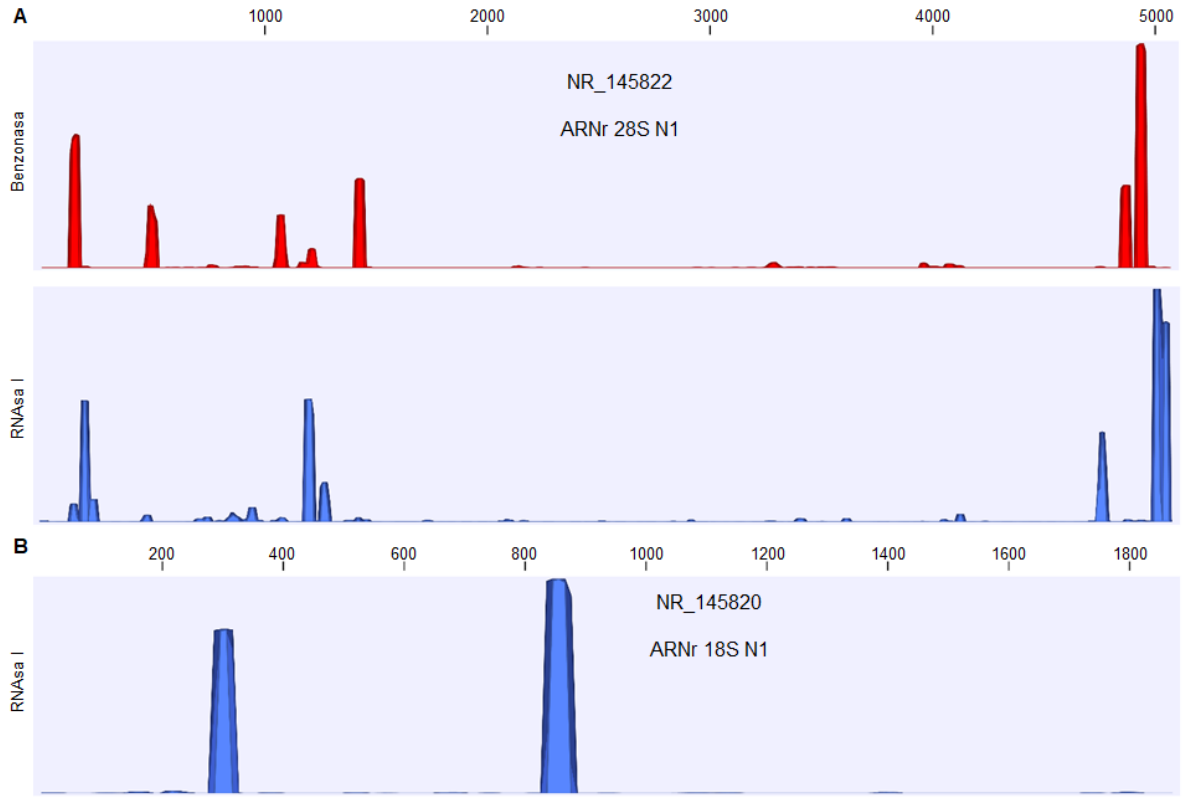

Figura V.17. Perfiles de mapeo sobre ARNr 28S y 18S con Benzonasa y RNAsa I. (**A**) Se muestran los perfiles de mapeo para un transcrito de ARNr 28S a modo de ejemplo (NR_145822), obtenidos a partir de la digestión con Benzonasa (arriba, rojo) y RNAsa I (abajo, azul). (**B**) Similar a (A) solo que se muestra el mapeo sobre un ARNr 18S (NR_145820) obtenido con RNAsa I. En cada caso se muestra, en la parte superior, una escala de tamaño del transcrito.

Tabla V.2. Secuencias y tamaños de los fragmentos de ARNr responsables de la contaminación producida con cada enzima.

RNAsa I	
Picos en ARNr 28S	Tamaño
5′-TCGTGGGGGGCCCAAGTCCTTCTGATCGAGGCC-3′	33
5′-CAGTGCGCCCCGGGCGGGTCGCGCCGTCGGGCCCGGGGG-3′	39
5′-AGCGCCGCGGAGCCTCGGTTGGCCTCGGATAGCCGGTCCCCCG-3′	43
5′-CTGGGTCGGGGTTTCGTACGTAGCAGAGCAGCTCC-3′	35
5′-TCGCTGCGATCTATTGAAAGTCAGCCCTCGACACAA-3′	36
Picos en ARNr 18S	
5′-CTTTGGTGACTCTAGATAACCTCGGGCCGATCGCAC-3′	36
5′-GCCGCCTGGATACCGCAGCTAGGAATAATGGAATAG-3′	36
Benzonasa	
Picos en ARNr 28S	
5′-CCGCGGCGGGGCGCGGGACATGTGGCGTACGGAAGACC-3′	38
5′-GGATTCAACCCGGCGGCGGGTCCGGCCGTGTCGGCGGCCCGGCGGATCTTTCCC-3′	54
5′-CGGCGTCTCCTCGTGGGGGGGCCGGGCCACCCCTCCCACGGCGCGAC-3′	47
5′-CGCGCTCGCCGGCCGAGGTGGGATCCCGAGGCCTCTCCAG-3′	40
5′-CGCGCGCCGGGACCGGGGTCCGGTGCGGAGTGCCCTTCGTCCTG-3′	44
5′-CCCTCGCCCGTCACGCACCGCACGTTCGTGGGGAACCTGG-3′	40

Discusión

En el presente capítulo nos propusimos como principales objetivos poner a punto el uso de la técnica de Ribo-Seq en distintos modelos neuronales, así como comparar de manera global los traductomas definidos por huellas ribosomales producidas con Benzonasa o con RNAsa I.

En primer lugar, respondiendo al desafío de aplicar la técnica utilizando una baja cantidad de células como es el caso de las cantidades que se obtienen de cultivos neuronales primarios, trabajamos en la optimización de la obtención de huellas ribosomales realizando el ensayo de digestión directamente sobre el sobrenadante postmitocondrial, suprimiendo la previa purificación de pellet polisomal, como fuera realizado por Zappulo *et. al* [83]. De esta manera, utilizando cantidades decrecientes de células hasta niveles comparables a los que obtenemos en cultivos *in vitro* de neuronas corticales embrionarias, realizamos ensayos de digestión sobre el sobrenadante postmitocondrial (ver Figura V.1). En todos los casos logramos obtener huellas ribosomales en cantidades suficientes para producir librerías de secuenciación: al menos >50 ng de ARN. También evaluamos distintas cantidades de enzima al momento de realizar las digestiones debido a que se trata de una muestra distinta a la utilizada en el protocolo habitual. Así, definimos el rango óptimo de uso de la enzima Benzonasa de manera tal que produzca huellas ribosomales de los tamaños adecuados (28 a 31 nt; ver Figura V.2). En este contexto, producimos y secuenciamos huellas ribosomales a partir de cultivos *in vitro* de neuronas corticales primarias derivadas de embriones de ratones wt y tauKO, como una primera aproximación (ver Figura V.3). Vale mencionar, como aclaramos anteriormente, que en este caso los cultivos contienen otros tipos celulares accesorios, como células gliales, entre otros, por lo que las huellas ribosomales no derivan exclusivamente de células neuronales. Los análisis primarios y globales realizados sobre los traductomas secuenciados revelaron resultados alentadores (ver Figura V.4). Se pudo obtener una gran cantidad de lecturas mapeando sobre ARNm de manera tal que se pudieron estimar niveles de expresión génica traduccional para más de 10.000 genes por encima del ruido (ver Figura V.4 A y B). Las huellas ribosomales obtenidas mapean de manera preferencial sobre las regiones codificantes de los ARNm y muestran además el patrón esperado de periodicidad (ver Figura V.4 C-F). Un resultado que llamó nuestra atención fue el tamaño observado de las lecturas correspondientes a las huellas ribosomales, que se ubicó entre 30 y 40 nt (ver Figura V.4 E y F). A pesar de que el tamaño indicado por el *Bioanalyzer* era el adecuado (entre 25 y 34 nt; ver Figura V.3 C) atribuimos esta diferencia a que posiblemente las bandas recortadas hayan correspondido a tamaños levemente mayores y que la estimación por *Bioanalyzer* no haya sido 100% precisa, como hemos observado en casos previos similares. De todas maneras, vale destacar que las lecturas producidas muestran todas las características esperadas para

las huellas ribosomales, como mencionamos anteriormente, asimetría de mapeo en regiones codificantes y no codificantes y periodicidad de mapeo (ver Figura V.4 C-F).

En segundo lugar y utilizando otro modelo neuronal, como es el tejido nervioso derivado de animales, nos propusimos optimizar el protocolo de Ribo-Seq para su realización a partir de la corteza cerebral de ratones. De esta manera trabajamos principalmente en los pasos de obtención del tejido, lisado celular y obtención del sobrenadante postmitocondrial, y purificación del pellet polisomal. Una vez ajustados estos pasos previos logramos obtener y purificar huellas ribosomales del tamaño y calidad esperada y en cantidad suficiente para su secuenciación masiva (28 a 31 nt y 300 ng de ARN, respectivamente; ver Figura V.5). En el siguiente capítulo se describe cómo utilizamos este protocolo para su aplicación en modelos murinos transgénicos de la enfermedad de Alzheimer.

Por último nos propusimos estudiar y comparar los protocolos de producción de huellas ribosomales con Benzonasa, la enzima que utilizamos habitualmente en los protocolos del laboratorio, y RNAsa I, la enzima utilizada en el protocolo descrito originalmente por Ingolia y colaboradores [84]. Para esto utilizamos células HEK293 a partir de las cuales obtuvimos pellet polisomales y ante muestras equivalentes realizamos, en duplicados, digestiones con cada una de las enzimas. Las huellas producidas con la RNAsa I fueron fosforiladas en el extremo 5’ y desfosforiladas en el 3’, como mencionábamos anteriormente, previo al envío a los servicios de secuenciación masiva (ver Figura V.6). Los perfiles de bandas de las digestiones obtenidas con cada enzima, así como las bandas específicas correspondientes a las huellas ribosomales recuperadas ya mostraban algunas diferencias entre las dos enzimas (ver Figura V.7). Los fragmentos de ARN correspondientes a las huellas ribosomales fueron secuenciados de manera masiva y se obtuvieron en promedio más de 120 millones de lecturas por muestra. Los porcentajes de contaminación por fragmentos derivados de ARNr fueron los esperados, aunque levemente más altos en las muestras correspondientes a la RNAsa I (88% vs 83%). Los niveles de mapeo sobre el transcriptoma de referencia fueron muy buenos, con un alto porcentaje de las lecturas asignadas a ARNm (ver Tabla V.1).

El análisis de los datos producidos reveló que las muestras se separan de manera esperada en un análisis de componentes principales y que las réplicas realizadas de cada enzima correlacionan muy bien (ver Figura V.8 A y B). Utilizando distintos umbrales de filtrado de genes de baja expresión observamos un gran porcentaje de genes compartidos entre ambas enzimas (ver Figura V.8 C). También, a nivel global se observan buenos niveles de correlación entre las estimaciones de expresión génica traduccional derivadas a partir de las dos enzimas (ver Figura V.8 D), como ha sido documentado para otras enzimas [89].

En primer lugar nos interesamos en explorar diferencias y similitudes respecto del traductoma definido por cada enzima, tanto en la identidad de los genes detectados como en sus niveles de expresión. Para esto, buscamos genes particulares asociados a cada enzima, es decir, genes cuya detección sea exclusiva mediante el uso de una enzima en particular, o cuyos niveles de expresión sean claramente superiores en una condición respecto de la otra. De esta manera diseñamos una estrategia en base a tres criterios de selección que denominamos: filtrado por cuartiles, por expresión y por ranking. Cada criterio, como mencionamos anteriormente, intenta seleccionar genes cuya detección esté asociada a una enzima en particular o cuyos niveles de expresión varíen sustancialmente entre las dos enzimas. Así, más allá de cierto grado de coincidencia entre los tres criterios, pudimos seleccionar un total de 188 y 170 genes asociados a la Benzonasa y RNAsa I, respectivamente (ver Figura V.9 A-C). El análisis funcional de estas listas de genes reveló resultados interesantes. Por un lado, la lista asociada a la Benzonasa no muestra funciones ontológicas sobrerrepresentadas, solamente vías KEGG asociadas al espliceosoma y al transporte de ARN. Por el otro lado, la lista asociada a la RNAsa I muestra un claro enriquecimiento de funciones ontológicas y vías KEGG asociadas al ribosoma, procesamiento de proteínas en el retículo endoplásmico y espliceosoma (ver Figura V.9 D, Figuras Suplementarias XI.1 y XI.2 y Tabla Suplementaria XI.1). A su vez, observamos una importante componente de genes no codificantes presentes en las listas: 111 de 188 para la Benzonasa y 70 de 170 para la RNAsa I son genes no codificantes. Por esto también analizamos las distintas clases de genes no codificantes presentes en cada lista de genes (ver Figura V.9 E), donde parecen predominar ARN del tipo *small nuclear* y *small nucleolar*.

Como una aproximación similar pero diferente también realizamos análisis de expresión génica diferencial entre los traductomas obtenidos con las dos enzimas (ver Figura V.10). De todas maneras, consideramos que la búsqueda de genes diferenciales representa una estrategia diferente que no necesariamente se complementa o sustituye a la estrategia discutida anteriormente. Entendemos que la comparación entre las huellas ribosomales producidas por las dos enzimas no debe reducirse a cálculos de expresión génica diferencial, sino que debe contemplar otro tipo de enfoque. Los análisis de expresión diferencial no necesariamente solo abarcan los escenarios de cambios en la expresión génica que quisimos representar mediante los criterios de filtrado anteriores, sino que también muchos otros casos donde los genes son detectados en ambas condiciones pero a niveles de expresión distintos. De hecho, las listas de genes expresados diferencialmente son mucho más extensas que la cantidad de genes definidos como asociados a cada enzima y también abarcan a una gran cantidad de éstos (ver Figura V.10 D). En este caso, el análisis ontológico de los genes diferenciales mostró altos niveles de enriquecimiento en diversas funciones biológicas (ver

Figura V.10 E y F), donde se destacan proteínas de unión a ADN y ARN, así como el ribosoma y la mitocondria.

A modo de resumen, más allá de poder definir un grupo de genes particularmente sesgados al uso de una u otra enzima y observar eventos de expresión génica diferencial entre los niveles estimados por las dos enzimas, los resultados funcionales muestran que no hay grandes diferencias entre los traductomas definidos tanto por Benzonasa como por RNAsa I.

A continuación comparamos características propias de las huellas ribosomales definidas por cada enzima, como ya realizamos anteriormente para otro set de datos, evaluando el mapeo preferencial en las regiones codificantes de los ARNm, la periodicidad de las huellas y la preferencia de corte. En primer lugar, más allá de que observamos claramente la preferencia en el mapeo de las huellas ribosomales por las regiones codificantes para ambas enzimas (ver Figura V.11), se pueden apreciar diferencias entre las distribuciones de mapeo de cada enzima. Por un lado, las huellas ribosomales producidas con RNAsa I muestran una clara preferencia por el CDS respecto de los 5'- y 3'-UTR (94% versus 3,2% y 0,6%; respectivamente). Por el otro lado, las huellas derivadas de la digestión con Benzonasa se distribuyen de la siguiente manera: 70% en el CDS, 20% en el 3'-UTR y 4% en el 5'-UTR. La presencia de huellas ribosomales en el 3'-UTR ya ha sido descrita y evidenciada por otros autores (ver ejemplos en: JG. Dunn et al. Elife 2013; MA. Skabkin et al. Molecular Cell 2013; TP. Miettinen & M. Bjorklund NAR 2015; S. Archer et al. Nature 2016; DJ. Young et al. Molecular Cell 2018), en particular al utilizar enzimas alternativas a la RNAsa I. En nuestro caso, pudimos observar que las huellas ribosomales presentes en el 3'-UTR presentaban un tamaño distinto al de las huellas derivadas del 5'-UTR o CDS (ver Figura V.12), lo cual sugiere una conformación y/o composición del ribosoma distinta una vez finaliza la traducción. Además, considerando que la digestión con RNAsa I es más agresiva, pues produce fragmentos de ARNr derivados de las dos subunidades del ribosoma (ver Figura V.13), se plantea la hipótesis de que la RNAsa I logra romper los ribosomas en el 3'-UTR y por eso no se evidencian huellas ribosomales en esta región. Por su parte, la Benzonasa cuya digestión es menos agresiva (solo produce fragmentos de ARNr derivados de la subunidad mayor), conserva la integridad de los ribosomas en el 3'-UTR y por lo tanto se recuperan huellas ribosomales en esta región, como se ha visto para otras enzimas como la nucleasa micrococal.

En segundo lugar, al evaluar la periodicidad de las huellas ribosomales detectamos en primer instancia claras diferencias en el tamaño de las huellas ribosomales mapeadas en cada caso (ver Figura V.14). Las huellas producidas con Benzonasa resultaron en promedio más grandes y de mayor rango que las producidas con RNAsa I (33 a 40 nt versus 31-32 nt,

respectivamente). Los porcentajes de periodicidad también mostraron diferencias. Mientras que en el caso de la Benzonasa observamos porcentajes similares a los encontrados previamente con esta enzima, cercanos al 40% [78,80] (ver también capítulo 3), para la RNAsa I la distribución entre los tres nucleótidos del codón fue distinta, viéndose más favorecido el primer nucleótido (<60%) y casi que sin verse representada la posición #2. Estos patrones se parecen a los reportados previamente en estudios donde utilizaron la misma enzima [29,106]. En tercer lugar, verificamos como se mencionaba anteriormente, que ambas enzimas son inespecíficas y que ninguna presenta un sesgo en el sitio de corte, ya que ningún nucleótido en particular se ve favorecido en los extremos de las huellas ribosomales generadas con cada enzima (ver Figura V.15). De hecho, para la RNAsa I se observa una mayor presencia de nucleótidos de guanina en la última posición de las huellas ribosomales, como ha sido documentado previamente [89].

Con el objetivo de buscar diferencias entre las dos enzimas, también exploramos los perfiles de mapeo generados con ambas enzimas en distintos genes de alta expresión (ver Figura V.16 y Tabla Suplementaria XI.2). De la misma manera como ha sido descrito, aquí decidimos utilizar genes con un tamaño adecuado y con un mínimo de cobertura y mapeos para minimizar sesgos [89,107]. En primera instancia vale mencionar que los perfiles de cobertura de las distintas réplicas biológicas son sumamente parecidos, casi idénticos. De todas maneras, se observan grandes diferencias en los perfiles generados por las dos enzimas, con apenas unos pocos picos de mapeos compartidos. Este resultado es similar a lo que ha sido observado cuando se compararon otras ARNasas con la RNAsa I [89]. En nuestro caso, los perfiles derivados de la Benzonasa presentan picos mayores en la zona del codón de inicio así como se observan mapeos en la región 3'-UTR, como comentábamos antes. Diferencias en los perfiles de mapeo sobre un mismo gen no solo han sido descritas para enzimas distintas, sino que se ha observado diferencias utilizando la misma enzima, en el mismo organismo, pero en distintos trabajos con protocolos ligeramente distintos [89].

Considerando este resultado, junto con los anteriores, es claro que existen diferencias entre el uso de una enzima o lo otra. Además del tamaño de las lecturas, su patrón de periodicidad y distribución de mapeos en las distintas regiones del ARNm, parecen existir pequeñas diferencias en la identidad de los genes que cada enzima detecta. Éstas diferencias podrían atribuirse a pequeños sesgos en los sitios de corte de cada enzimas, a diferencias en el tamaño molecular, o a diferencias en la afinidad por el ARN simple cadena, que como se mencionó al principio, son propiedades que difieren entre ambas enzimas. De todas maneras, no parecen existir grandes grupos o funciones biológicas particularmente sobrerrepresentadas o subrepresentadas en el uso de cada enzima. Aún así se observan afectados muchos genes no codificantes, como ARN pequeños, que pueden estar presentes

en la fracción polisomal, y que por lo general no son el centro de los análisis del tipo traductómicos. Un ejemplo que puede ilustrar que las diferencias encontradas no son necesariamente importantes desde el punto de vista biológico es la presencia de distintas variantes del gen de la actina en los genes asociados a cada enzima. La beta actina aparece enriquecida en los genes asociados a la Benzonasa, seleccionada por el filtro de cambio en el nivel de expresión. Por el otro lado, la alfa 1 y gamma 1 actinas aparecen en las listas de genes asociados a la RNAsa I, seleccionadas por el filtro de cambio en el ranking de expresión y cambio en el nivel de expresión, respectivamente. De todas maneras, si sumamos los niveles de expresión de las 3 variantes obtenemos niveles comparables: 5.550 CPM con Benzonasa y 5.880 CPM con RNAsa I. Esto podría indicar que pueden existir sesgos en la producción de huellas ribosomales en este gen en particular, donde se favorece una variante génica por encima de las otras con un enzima en particular. También, podría ocurrir que una gran proporción de las huellas ribosomales producidas deriven de regiones conservadas de este grupo de genes y al momento de mapear se distribuyan en las distintas variantes de manera diferencial aunque efectivamente tengan el mismo origen.

Por último, uno de los aspectos claves a considerar en el diseño y puesta a punto de la metodología de Ribo-Seq es la presencia no deseada de fragmentos derivados de ARNr. Estos fragmentos, que se producen en la digestión de los polisomas con la enzima, suelen representar un alto porcentaje de la población de ARN, alrededor del 80% y hasta el 95%, y por lo tanto consumen un grado equivalente de los recursos de secuenciación masiva. Por esto, como último punto nos propusimos evaluar los fragmentos correspondientes a ARNr producidos en este experimento así como comparar los resultados obtenidos por las dos enzimas. Como mencionamos antes, los porcentajes de contaminación por ARNr son similares para los enzimas, aunque levemente superiores con la RNAsa I (88% vs 83%; ver Tabla V.1). Para esta enzima se definieron 7 fragmentos contaminantes procedentes de ARNr 28S y 18S, mientras que para la Benzonasa se identificaron 6 fragmentos, todos derivados de ARNr 28S (ver Tabla V.2 y Figura V.17). Los perfiles de mapeo sobre estos genes ribosomales son distintos para cada enzima y en cada caso se reconocen picos particulares donde se ven representadas las secuencias más abundantes generadas (ver Figura V.17). Las secuencias representadas en cada pico, las cuales como decíamos no se comparten entre las enzimas, representan información valiosa para la construcción de oligos biotinilados u otra alternativa experimental, que nos permita sustraer estas especies claramente abundantes (ver Tabla V.2). De hecho en la descripción del protocolo original que utiliza RNAsa I están disponibles las secuencias de un total de 14 oligos biotinilados para la sustracción de ARNr [84], de los cuales 5 están presentes entre las 7 secuencias que aquí observamos. Sin dudas que conocer esta información es de gran utilidad ya que permite

diseñar estrategias de sustracción de ARNr específicas para el uso de la Benzonasa, que como observamos en este caso, genera fragmentos completamente distintos a los producidos y descritos para la RNAsa I.

En suma, se pueden identificar diferencias tanto a nivel de las huellas ribosomales producidas por cada enzima como de los traductomas cuantificados a partir del mapeo de dichas huellas. En cierto nivel, estas diferencias son esperadas respecto a lo que se ha visto en trabajos previos, donde se compararon otras ARNasas con la RNAsa I [89]. De todas maneras, esta es la primera vez que se realiza una comparación del estilo con la enzima Benzonasa. Es interesante discutir acerca de las posibles razones biológicas que explican las diferencias tanto en las características de las huellas ribosomales producidas como en los niveles de expresión traduccional estimados a partir de ellas. Respecto a lo primero, parece ser claro que las diferencias en tamaños se explican por diferencias en la actividad de las enzimas, sus mecanismos de acción y tamaño. Mencionamos anteriormente que los sustratos de la Benzonasa son más variados que los de la RNAsa I. Además, la Benzonasa es una enzima de mayor tamaño lo cual seguramente dificulte su acceso a las regiones más cercanas al ribosoma. En cambio, la RNAsa I de menor tamaño podría digerir más fácilmente las regiones del mensajero cercanas al ribosoma, produciendo huellas ribosomales más pequeñas como las que aquí, y en otros estudios, se observan [29,106]. Quizás diferencias en los mecanismos de acción, procesividad y tamaños de las enzimas determinen que sean más o menos agresivas con el ribosoma. Comprometer la integridad del ribosoma puede afectar no solo el tamaño de la huella sino también su presencia o ausencia, justificando por ejemplo por que se observan más huellas ribosomales producidas con Benzonasa mapeando en las regiones 3'-UTRs. Sin dudas que son hipótesis que resultan interesantes de explorar en un futuro. Respecto a las diferencias en las estimaciones de expresión de los compartimentos traduccionales, nuevamente las razones anteriores parecen estar involucradas. La capacidad de cada enzima de digerir polisomas con gran o poca cantidad de ribosomas, con complejas o simples estructuras secundarias de ARN, con varios o pocos factores proteicos unidos al mismo, son sin duda factores que pueden explicar porque varían los niveles estimados de expresión entre las dos enzimas. Nuevamente, estas diferencias, junto con las diferencias en los patrones de mapeo sobre ARNm individuales han sido previamente documentadas en la literatura comparando otras ARNasas como S7, T1 y A [89]. En nuestro caso, la comparativa global de niveles de expresión fue lo suficientemente buena, con un valor de correlación de Pearson de 0,91. De todas maneras, se pudieron identificar varios genes como expresados diferencialmente. Además, un análisis detallado nos permitió, mediante tres criterios de selección, identificar genes que estuvieran particularmente asociados a una enzima. Así, identificamos menos de 200 genes que tienden a verse favorecidos con una enzima respecto

a la otra. Sin embargo, muchos de estos genes correspondían a genes no codificantes, posiblemente presentes por arrastre en el pellet polisomal, asociados a ribonucleopartículas o al propio ribosoma. Un ejemplo claro parecen ser los ARN del tipo *small nucleolar*, muy abundantes dentro de los genes no codificantes asociados a cada enzima, en especial la Benzonasa. Dado que las dos enzimas presentan actividades catalíticas distintas, se espera que digieran el ribosoma de manera distinta. Este tipo en particular de ARN, se ha visto que regulan modificaciones en el ARNr así como la propia biogénesis del ribosoma [108]. Para finalizar, vale destacar que las diferencias que aquí observamos entre Benzonasa y RNAsa I pueden darnos la seguridad de que el utilizar Benzonasa para la digestión polisomal no introduce mayores sesgos de relevancia biológica, siempre y cuando utilicemos la misma enzima para las distintas condiciones biológicas a estudiar.

VI. CAPÍTULO 3

TRADUCTÓMICA DE MODELOS MURINOS TRANSGÉNICOS DEL MAL DE ALZHEIMER

En la literatura los estudios de expresión génica mediante aproximaciones ómicas, o más recientemente tecnologías de célula única (*single cell* RNA-Seq), son muy abundantes para modelos animales o celulares del mal de Alzheimer e incluso para muestras humanas de pacientes enfermos. De todas maneras, el centro de la atención ha sido principalmente el control a nivel transcripcional, evaluando la expresión génica midiendo la abundancia de ARNm mediante RNA-Seq. Sin embargo, algunas evidencias recientes indican la existencia de eventos de regulación traduccional importantes en modelos de la enfermedad [23,72]. En dichos eventos, la participación de las dos moléculas centrales en el desarrollo de la patología, Aβ y TAU, ha sido documentada [70–74]. Por esta razón, en el presente capítulo nos planteamos evaluar la siguiente hipótesis de trabajo: existen eventos de regulación traduccional en modelos animales transgénicos de la enfermedad de Alzheimer que son fundamentales para el desarrollo de esta patología neurodegenerativa. En este contexto, definimos como principal objetivo estudiar los eventos de regulación traduccional, mediante aproximaciones ómicas, en la corteza cerebral de modelos animales de la enfermedad, y conocer los principales genes y funciones biológicas reguladas.

De esta manera, utilizando modelos murinos transgénicos que simulan el desarrollo de la enfermedad, aplicamos la metodología de Ribo-Seq en la corteza cerebral de ratones machos adultos de edad joven, preferentemente asintomáticos. Hasta donde conocemos, este es el primer estudio de este tipo que se realiza en modelos animales o celulares de Alzheimer, ya que aproximaciones similares (Ribo-Tag y polysome-seq) han sido aplicadas específicamente a la microglia (ver SS. Kang et al. J Exp Med 2018 y Z. Haimon et al. Nat Immunol 2018). Recientemente han sido publicados trabajos similares, dos en donde se aplicó Ribo-Seq en distintas regiones del cerebro de ratones modelo del síndrome de X frágil [61,109], y el otro en donde también se aplicó la técnica de Ribo-Seq en un modelo celular de Parkinson [62].

Los dos modelos animales utilizados, del tipo amiloides (CVN: *App* SwDI; *Nos2*$^{-/-}$ y Tg2576: *App* Sw; ver Manuscrito I), mostraron eventos de regulación tanto a nivel transcriptómico, como traductómico. En particular, los ratones CVN mostraron una mayor cantidad de genes regulados a nivel de la traducción que el modelo Tg2576. Específicamente en ratones CVN, los genes diferenciales en ambos niveles revelan la regulación positiva de una firma génica microglial particular que responde a la acumulación de Aβ en las primeras etapas. El análisis ontológico de las listas de genes regulados muestra una regulación negativa de varios

procesos de neurodegeneración, mientras que se favorecen procesos de tipo neuroprotectores como el aumento de células neuronales y gliales y transmisiones sinápticas, entre otros. En general, la identidad de los genes regulados en ambos niveles revelan una compleja firma molecular que implica “los dos lados de la moneda”: por un lado encontramos genes asociados a funciones neuroprotectoras o beneficiosas, como reducir los altos niveles de Aβ, pero en el otro lado tenemos genes con funciones neurotóxicas relacionados a la producción de Aβ o a la pérdida de funciones neuronales.

Este trabajo podría, probablemente, dilucidar nuevas vías comunes como posibles marcadores tempranos de la enfermedad de Alzheimer y así permitirnos comprender mejor los procesos moleculares aberrantes que podrían impulsar la neurodegeneración. A su vez, el análisis de los datos revela eventos de regulación de la expresión génica que ocurren a nivel traduccional, lo cual no ha sido considerado hasta el momento y permite entonces explorar nuevos mecanismos de control y vías de señalización desreguladas.

Los resultados obtenidos, junto con una introducción al trabajo, materiales y métodos y la discusión de los mismos, se presentan a continuación en formato de manuscrito.

Manuscrito I: Tandem transcriptional and translational analysis of gene expression in mouse models of Alzheimer's disease

Se adjunta a continuación.

Tandem transcriptional and translational analysis of gene expression in mouse models of Alzheimer's disease

Guillermo Eastman[a], Elizabeth R. Sharlow[b], John S. Lazo[b,c], George S. Bloom[d,e,f] * and José R. Sotelo-Silveira[a,f] *

[a]*Departamento de Genómica, Instituto de Investigaciones Biológicas Clemente Estable, Ministerio de Educación y Cultura, Montevideo, Uruguay*

[b]*Department of Pharmacology, University of Virginia, Charlottesville, VA, USA*

[c]*Department of Chemistry, University of Virginia, Charlottesville, VA, USA*

[d]*Department of Biology, University of Virginia, Charlottesville, VA, USA*

[e]*Department of Cell Biology, University of Virginia, Charlottesville, VA, USA*

[f]*Department of Neuroscience, University of Virginia, Charlottesville, VA, USA*

[g]*Sección Biología Celular, Facultad de Ciencias, Universidad de la República, Montevideo, Uruguay*

* Correspondence to:

José R. Sotelo-Silveira, Departamento de Genómica, Instituto de Investigaciones Biológicas Clemente Estable, Av. Italia 3318, 11600, Montevideo, Uruguay. Tel.: +598 2487 1616 (173); E-mail: jsotelosilveira@iibce.edu.uy or sotelojos@gmail.com

George S. Bloom, Department of Biology, University of Virginia, PO Box 400328, Charlottesville, VA 22904-4328, USA. Tel.: +1 434 243 3543; E-mail: gsb4g@virginia.edu

Running title: *Comparative RNA-Seq and Ribo-Seq of AD Mouse Models*

ABSTRACT (250 words)

Alzheimer's disease (AD) is the most common cause of dementia worldwide, but efforts to prevent or delay symptom onset, or reduce the rate at which symptoms progress have so far been unsuccessful. This devastating disorder has a well characterized neuropathology that consists of extracellular plaques made predominantly from amyloid-beta (Aβ) peptides and intraneuronal neurofibrillary tangles formed mainly by the neuron-specific microtubule-associated protein, tau. Not surprisingly, most efforts to develop therapeutics for AD have focused on reducing the burden of toxic forms of Aβ or tau in brain, but without much regard for the normal cellular signaling networks they may compromise or the pathogenic signaling they may provoke. With this background in mind, we compared gene expression profiles in cerebral cortex of two AD model mouse strains and wild type (WT) mice of the same strain background at 6 months of age by tandem transcriptome and translatome analysis. The transgenic strains were CVN (APP_{SwDI};$NOS2^{-/-}$) and Tg2576 (APP_{Sw}), and RNA-Seq and Ribo-Seq were performed from identical starting pools of isolated bulk RNA for transcriptomic and translatomic analysis, respectively. Compared to the WT strains, the AD model mice had similar levels of transcription regulation, but differences at the level of translation regulation. Besides cognitive performance are almost unaffected in the two transgenic mice, both show decreased neurodegenerative-related processes and an increased neuroprotective response, particularly the CVN model. A specific microglial signature associated with early stages of Aβ accumulation is displayed up-regulated at both transcriptome and translatome level in the CVN mice. Although the two mice do not share large lists of regulated genes, they show common regulated pathways related to APP metabolism associated with neurotoxicity and neuroprotective functions. This work represents the first genome-wide study of translation regulation using the brain cortex of transgenic mice models of AD and provides evidence of a tight and early translational regulation of gene expression controlling the balance of neuroprotection and neurodegeneration processes in the brain.

Keywords (4-10)***:*** Ribo-Seq; RNA-Seq; Tg2576 mice; CVN mice; Neurodegeneration; APP metabolism.

INTRODUCTION

Alzheimer's disease (AD) is a progressive brain neurodegenerative disorder considered the main cause of dementia worldwide. For example, in the USA it's considered to be the most expensive disease, responding only marginally and briefly to currently available drugs. At the histopathological level, AD has a well characterized hallmark that consists of extracellular accumulation of amyloid-beta (Aβ) plaques, intracellular accumulation of hyperphosphorylated tau protein and neuron loss [1].

The complete understanding of the molecular mechanisms underlying AD is paramount for the development of novel therapies able to modify the biology of the disease and efficiently fight the increase of AD with age in our ever-increasing life expectancy. In particular, regulation of mRNA translation has been described and previously associated with other neurological diseases, mainly in cellular models [2–5]. In the case of AD, revealing results have been recently published linking Aβ and tau with translation [6–11]. For example, it has been shown that local protein synthesis is deregulated in brain synaptosomes in a transgenic mice model of AD APP-related [6]. Also, it has been demonstrated that Aβ oligomers induce *de novo* protein synthesis of tau [8] and ATF4 [11], that tau is able to interact with the ribosome *in vitro* [9] and decrease the synthesis of ribosomal proteins in tau-related transgenic mice models [7]. At the same time, an interesting relation between Aβ and mTOR complex has been described [12,13]. Considering the fully described role of mTOR in controlling translation [14] and the previously described evidence, result of interest to explore translation regulation events at a genome-wide level in AD models.

While powerful genomics tools to study transcriptional regulation are becoming more frequently applied to AD research (see examples in [15–18]), focus on translation has been almost unexplored. Here we use ribosome profiling (Ribo-Seq; [19–21]) as a genomic screening technique to recognize mRNA translation regulation events in the brain cortex of transgenic mice models of AD (CVN and Tg2576) at young ages, when learning and memory in the mice is almost unaffected. In particular in the CVN model, neither cognitive nor histopathological changes are noticed by the age used. Briefly, we produced and sequenced ribosome footprints that reveal the exact position of an active ribosome at the mRNA. Quantification analysis allows us to have an estimation of translational levels at a genome-wide level and to compare translational efficiency [20] between transgenic mice and wild type (WT) genotypes. Uncovered translational regulated genes at these asymptomatic

stages reveals a complex signature that implicates genes associated to protective/beneficial functions for example involved in the reduction of high levels of Aβ, but on the other side we have genes related to Aβ biosynthesis or neurotoxicity. In addition, the data obtained can be of use to the community as a source for further data mining in the search for early AD markers.

MATERIALS AND METHODS

Mice

Three 6 month old mice from each of the following genotypes were used: CVN (APP_{SwDI}/$NOS2^{-/-}$) [22], Tg2576 (APP_{Sw}) [23]) and their respective WT controls (C57/BL6 and B6;SJL, respectively; see Table 1). Animals were maintained, bred and euthanized in compliance with all policies of the Animal Care and Use Committee of the University of Virginia.

Transcriptomic and Ribosome Profiling of brain cortex

Cortices (~250 mg each) were dissected from freshly removed brains in cold PBS containing of 100 µg/ml cycloheximide (CHX; Sigma-Aldrich, catalog # 01810). The tissue was then cut into smaller pieces with a sterile scalpel and Dounce homogenized on ice in lysis buffer (5 mM Tris pH 7.5, 2.5 mM $MgCl_2$, 1.5 mM KCl, 0.5% Triton X-100, 0.5% sodium deoxycholate, 2 mM DTT (1,4-dithiothreitol) and 100 µg/ml CHX), using 1 mL of lysis buffer per 100 mg of tissue. At this point, a transcriptome sample was separated and total RNA was isolated using a *mirVana Total RNA Isolation Kit* according to the product's recommended protocol (Invitrogen, catalog # AM1560). Ribo-Seq was performed as previously described [24,25]. Briefly, the sample was centrifuged twice at 4°C and full speed (~17,000g), for 1 and 10 minutes consecutively, to remove large cellular debris, nuclei, and mitochondria. The post-mitochondrial supernatant (~1.6 mL; OD_{260}= 5-10 AU) was carefully loaded onto a 12-33.5% (w/v) sucrose cushion prepared in polysome buffer (20 mM HEPES pH 7.5, 5 mM $MgCl_2$, 100 mM KCl, 100 µg/ml CHX) and centrifuged for 2 hours, at 36,000 rpm in a Beckman SW41Ti rotor at 4°C. The polysome-enriched pellet was resuspended in polysome buffer and digested with 180-200 units of Benzonase nuclease (Millipore, catalog # E1014) for 10 minutes at room temperature to produce the ribosome footprints and remove

the RNA that was not protected by ribosomes. Digestion was stopped by addition of 3 volumes of *mirVana Lysis Buffer* and the RNA was isolated and then concentrated by overnight precipitation with 80% ethanol to maximize small RNA recovery. The concentrated, ribosome-protected mRNA, ribosome footprints (10-15 µg per sample) was then size fractionated by electrophoresis using 15% polyacrylamide-urea gels (ThermoFisher Scientific, catalog # EC68852BOX), run at 200 volts in TBE (89 mM Tris-borate, pH 8.3, 2 mM EDTA) for 65 minutes. Gels were stained using GelRed (Biotium, catalog # 41003) and circular agitation for 10 minutes in the dark. The ribosome footprint bands were identified using 26-mer and 34-mer RNA oligonucleotides [24] and excised in a dark room under UV light exposure. RNA recovery from gel slices was done overnight at room temperature by gentle mixing, e.g. on a Nutator [24]. Size, quality and quantity of both transcriptome and translatome samples were evaluated in a Agilent 2100 Bioanalyzer using Nano and Small RNA kits (Agilent Technologies, catalog #s 5067-1511 and 5067-1548, respectively).

Sequencing

All transcriptome and translatome samples were sequenced at BGI Tech Solutions (Hong Kong). Transcriptome samples were sequenced using an RNA-Seq quantification library protocol with ribosomal RNA (rRNA) removal library preparation, yielding at least 20 million paired-end (2x100 bp) reads. Translatome samples (ribosome footprints) were processed by small RNA library protocol, yielding at least 80 million single-end (50 bp) reads. Raw sequence data are available at the NCBI Sequence Read Archive (SRA; https://trace.ncbi.nlm.nih.gov/Traces/sra/) under BioProject ID PRJNA677972.

Data Analysis

Quality control of sequence files was performed using *FastQC* [26] and then mapped against the *Mus musculus* genome (mm10/GRCm38 version) using *bowtie2* [27]. Read counts over mRNAs or genes were estimated by *featureCounts* [28], and differential gene expression analysis of transcriptomes or translatomes was done separately using *edgeR* [29] comparing each strain with their respective wild type. Normalized counts were exported, and translational efficiency was calculated and contrasted between mice strain and WT using the *Xtail* R package [30]. For both transcriptomes and translatomes, differentially expressed genes (DEGs) were defined by a p-adjusted value (FDR) <0.05 and a fold change

of >1 or >1.5, as indicated accordingly in each case. Functional interpretation and ontology enrichment analysis of DEGs lists were performed using *IPA* (QIAGEN Inc.) [31], online tools as *STRING* [32] and *g:Profiler* [33], and in-house software (manuscript in preparation; https://github.com/sradiouy/IdMiner). AmiGO2 database [34] was used to retrieve genes related to APP, Aβ and tau metabolism. Plots were generated using R, by general or specific packages as *pheatmap* (https://CRAN.R-project.org/package=pheatmap) and *GOplot* [35].

RESULTS

General features of the CVN and Tg2576 transcriptome and translatome data

Two transgenic mice models of AD at six months of age and their respective WT controls (Table 1, Figure 1A) were used to explore transcriptional and translational gene expression regulation in the brain cortex using RNA-Seq and Ribo-Seq, respectively (Figure 1B). More than 20 million of paired-end reads were obtained for transcriptomes and an average of 120 million reads for translatomes (Table S1), derived from total RNA and isolated ribosome footprints (Figure S1), respectively. For transcriptome samples 88% of the reads aligned over the reference genome, of those, 90% mapped in gene regions and 77% in mRNA regions (Table S1A). On the other hand, for translatome samples we were able to map more than 10 million reads over mRNAs regions (Table S1B). In this case, ribosomal RNA depletion was avoided to minimize protocol biases.

Expression levels (CPM, counts per million) were estimated for more than 14 thousand different mRNAs in each sample above low/noise signal (Figure S2). Inter-replicates correlation indicates high similarity between either transcriptome or translatome samples, but lower correlations were obtained between RNA-Seq and Ribo-Seq data as expected, hereafter named transcriptional and translational compartments (Figure S3). In the same line, quality control comparisons between transcriptome and translatome samples reveals the expected difference at the level of triplet periodicity and read distribution among mRNA features (Figures S4 and S5). In addition, principal component analysis (PCA) shows a clear separation between genotypes for both compartments (Figure S6).

Differential gene expression regulation

We used *edgeR* R package [29] to detect differential gene expression regulation comparing each transgenic mice with their respective WT controls. For the CVN transgenic model we found 469 differentially expressed genes (DEGs; p-adjusted value <0.05) at the transcriptome level and 1165 at the translatome level. Of those, 240 and 377 were changing at >1.5 fold in each level (Table 2 and Figure 2). For the Tg2576 model, we found 343 DEGs at the transcriptome level and 135 at the translatome level. In this case, 140 and 94 respectively, change at >1.5 fold in each level (Table 2 and Figure 3).

In order to specifically identify translational regulation events and disentangle transcriptome from translatome regulation we estimated and compared translational efficiency as the ratio between translatome and transcriptome levels. For this we used the *Xtail* R package [30] and found 797 genes regulated in the CVN model, of which 144 were changing at >1.5 fold (Table 2 and Figure 2). On the other hand, 87 genes were statistically regulated at translational efficiency levels and 50 of them were changing at >1.5 fold in the Tg2576 model (Table 2 and Figure 3).

Global distribution of DEGs expression values, the relationship between fold change and p-adjusted values and association between transcriptome and translatome fold changes are shown for both models in Figures 2, 3, S7 and S8. As expected, DEGs are distributed along all expression levels (Figure 2A and D, 3A and D) and the relationship between fold change and p-adjusted values shows the classic Volcano plots for both transcriptome and translational efficiency levels (Figure 2B and E, 3B and E). When fold change at the translatome level is plotted against transcriptome fold change, a clear correlation is evidenced (Figure 2C and 3C). For example, in the CVN model, 106 out of the 160 DEGs at fold change >1.5 at the transcriptome level are also DEGs at the same cutoff at the translatome level (Figure S9A). The same correlation is evidenced for the transcriptional down-regulated genes: 32 out of 80 are also down-regulated at the translational level (Figure S9B). This correlation, also observed in the Tg2576 model (Figure S9C and D), indicates the expected association between transcriptome and translatome samples. Regulated genes at the level of translational efficiency, although less in number than those regulated at the transcriptome level, show a different pattern of regulation (Figure 2F and 3F). In general, regulation at translational efficiency implies genes with minimal changes at transcriptome levels (fold changes values close to one), while increasing or decreasing

translatome levels. This pattern is also observed in Figure 4 where an expression heatmap of DEGs is shown (see below).

Expression levels of DEGs at the transcriptome level show classical patterns of regulation (Figure 4A and C) but at the translational efficiency level, different scenarios could explain the observed regulation. For example, similar expression levels at the transcriptome but an increase/decrease at the translatome implies translational efficiency regulation. In the same way, increasing transcriptome levels while reducing translatomes also leads to changes in translational efficiency. All these scenarios can be observed in Figures 4B and D. Heatmaps of regulated genes exclusively at the translational level are described in Figures S7D and S8D for each transgenic model.

Functional analysis of regulated genes

In order to explore enriched biological functions up- or down-regulated we used *IPA* (QIAGEN Inc.) [31]. As a group of genes we used DEGs changing at >1-fold to analyze a larger gene list and obtain more robust biological signatures. As illustrated in Figure 5, the CVN model shows a clear functional response at the transcriptome, translatome and translational efficiency levels (Figure 5A, S10 and Table S2). For this model, down-regulated biological functions are clearly related to neurodegeneration process (neurodegeneration, degeneration of neurons, nerves and neuro system, release of L-glutamic acid, among others). Regarding up-regulated functions, we observed a neuroprotective response of the microglia cells probably to the early accumulation of Aβ and also other neuron-related processes with protective functions, such as quantity of neurons, growth of neurites, synaptic transmission, etc. However, we found evidence that activation of neurodegenerative-related processes are occurring, especially at the transcriptome level, as the categories of axonal growth were decreased and neuronal cell death processes were increased (Table S2). Also, at the translational efficiency level, we found a marginal (low z-score) decreased category corresponding to long-term potentiation (LTP) (Figure 5A). For the Tg2576 mice model, the functional response was barely informative since only few categories were found as enriched (Figure 5B and Table S2). At the transcriptome level only three categories were found as increased, all of them related to neuroprotective functions. Also, at the translatome level only one category was found decreased, but with a low z-score, and no results were found when analyzing translational efficiency DEGs.

We then performed an upstream analysis to infer modulated genes by the observed regulation of their targets. Here, we were able to reveal genes as inhibited or activated at the three levels studied, that are not discovered among the DEGs. For the CVN model, most of the upstream genes found are closely related to AD pathology and could be interpreted as regulated in a protective direction, to avoid Aβ accumulation and response against neurodegeneration (Figure 6). For example, inhibited upstream inferred genes include: *Psen1*, *Psen2*, *Apoe*, *B4galnt1*, *St8sia1* and *Ctcf* from the transcriptome level; *Ssb* from the translatome level and *Adora2a* from the translational efficiency level (Figure 6A, C and E). In all these genes, an inhibited activity could be interpreted as neuroprotective as is clear for *Psen1*, *Psen1* and *Apoe*, but also for *B4galnt1* and *St8sia1*, two ganglioside synthase which increase APP cleavage and affect memory [36,37]. CTCF, a transcription factor that could act as activator or repressor, and is also an insulator protein that defines chromatin domains, is able to up-regulate APP expression [38]. Also *Ctcf* knockout in mice hippocampus increase cytokines expression and activates microglia [39]. In the case of ADORA2A, an adenosine receptor, it has been observed that pharmacological inhibition or downregulation of these receptors can restore LTP and revert memory deficits [40,41]. On the other hand, upstream genes indicated as activated seems to represent both protective and degenerative fashions (Figure 6B, D and F). Genes as *Tcf7l2* and *Csf1*, inferred as activated from the transcriptome level, have probably a protective function: TCF7L2 may be involved in improving neurogenesis and compensate neuron loss [42] and CSF1 has been associated to microglia activation, prevention of cognitive loss and reduction of Aβ accumulation [43,44]. *Ptf1a* and *Ifng* genes, defined as upstream activated gene from the translational level study, may also act as protective. PTF1A can induce neuronal stem cell generation that can improve cognitive dysfunction [45]. Interferon gamma can activate microglia to suppress Aβ deposition and can induce neurogenesis improving cognition [46–48]. In addition, other genes as *Tnf* may be activated in a degenerative fashion: TNF is a proinflammatory cytokine that exacerbates both Aβ and tau pathologies *in vivo* and TNF inhibitors might slow down cognitive decline [49]. However, the roles of cytokines as IFN-γ and TNF-α could be controversial in AD [50]. The upstream activated genes identified from the translational efficiency DEGs were *Ptf1a* (see above) and *Prkcg*, both probably protective. The protein kinase C gamma, PRKCG, is able to stimulate the APP processing by α-secretase to produce soluble fragments of APP and reduce Aβ accumulation [51]. On the other hand, as

anticipated by the uninformative functional enrichment analysis for the Tg2576 mice, we did not observe any upstream regulated gene for this model.

Regulated genes in the CVN model reveals an specific microglia signature responding to Aβ

To complement the functional analysis we used an in-house developed tool named *IdMiner* (manuscript in preparation; https://github.com/sradiouy/IdMiner) to fully interpret represented functions in DEGs lists. This software is a text-mining tool that captures previously reported associations between gene lists and user-defined terms using the PubMed database. We found that among up-regulated genes in the CVN model at both transcriptome and translatome levels there was a clear signature of disease-associated microglia (DAM). This signature includes genes as *Trem2, Tyrobp, Tlr2, Cd68, Gpr84, Gpnmb, Itgax, Itgb2, Lpl, Clec7a, Cst7* and *Ccl6* [17,18,52–55]. All these genes encode for transmembrane proteins that were described to be highly expressed in a microglia subpopulation that specifically respond against neurodegeneration. The overexpression of these markers orchestrate DAM to localize Aβ deposition and favors its clearance [17,52]. This signature is part of the immune system process, a statistically overrepresented function among up-regulated genes networks at the transcriptome and translatome level (Figures S11 and S12).

Other up-regulated genes at both levels include genes expressed either in non-neuronal or neuronal cells, as previously reported. For example *Gfap* and *Serpin3* genes were found to be overexpressed in astrocytes in AD conditions [56–59]. Solute carrier family members and hippocalcin-like proteins are also up-regulated in accordance with their possible neuroprotective described functions in AD context [60,61]. We also found up-regulation of *Mid1* gene expression, a member of the Mid1 complex which binds to and accelerates *App* mRNA translation through mTOR pathway [62]. The tyrosine kinase *Fgr* was also up-regulated at both levels. This kinase is able to bind tau but its interaction is not well described [63]. However, the *Fgr* paralog *Fyn* is able to phosphorylate tau causing neurotoxicity [64], so we hypothesize that *Fgr* could also be involved in post-translational modifications of tau.

The analysis of the list of up-regulated genes specifically at the translatome level reveals more interesting cases. For example, we found the histocompatibility 2 class II antigen A gene, *H2-Ab1*, that is also described as a marker for DAM [52,53]. Also, complement components 4a and 4b were up-regulated as previously described in response

to Aβ plaques increase [59]. The *Csf3r* gene was also up-regulated at the translatome level as expected since it was found highly expressed in early stages of AD [65]. Deficiency in its ligand, G-CSF, has a deep impact in hippocampal structure and function leading to disruption in memory formation and impaired behavioral performance [66]. Concordantly, G-CSF administration functions as a neurotrophic factor and induces astrocytes and microglia activation [67,68], so probably, increasing G-CSF receptor CSF3R is a response mechanism to mitigate neurodegeneration.

When studying the list of up-regulated genes particularly at translational efficiency level, although having a small number of genes we found several interesting cases from which we highlight *Serpina3g, Frmd4a, Rras2, Nav2, Adam12, Pparg, Mid1, Ldlrad3* and *Cd44*. Here we found some genes associated with protective/beneficial functions, for example trying to reduce the high levels of Aβ production: *Frmd4a*, *Pparg* and *Rras2* [69–72], but also other genes (*Adam12*, *Mid1* and *Ldlrad3*) related to Aβ production or neurotoxicity [62,73,74].

Regarding down-regulated genes, we also found genes related to Aβ accumulation. Complement defense 59a, *Cd59a*, was down-regulated at the transcriptome level as is expected in response to Aβ and could explain neuronal vulnerability and loss [75,76]. Calbindin 2 or Calretinin (*Calb2*) positive interneurons are specifically decreased as early targets of Aβ accumulation in the hippocampus [77] and here its expression was down-regulated at the transcriptome and translatome levels. *Pin4* was also down-regulated at both levels in accordance with the decrease observed for Pin1, a paralog gene, which plays a role in the accumulation of Aβ [78–80]. Other down-regulated genes, probably due to the neuropathological context, were *Rplp0* and *Igf2* [7,81], while genes like *Slc17a8* and Tenascin-C were probably down-regulated in order to ameliorate pathology [82].

Tg2576 model shows differentially expressed genes associated to APP metabolism

The same analysis performed above was applied for the study of DEGs list in the Tg2576 mice model. Although the number of DEGs in this model is almost half compared to the CVN mice model, interesting genes arise from the analysis. For example, the Toll like receptor 6 gene (*Tlr6*) was up-regulated at both the transcriptome and translatome levels. This receptor is able to dimerize with TLR4 and interact with CD36 to bind Aβ and activate microglia promoting neurodegeneration [83]. Calpain 11 was also up-regulated at the transcriptome level, as expected since calpains are hyperactivated in AD [84,85]. *Cdk5rap1*,

an inhibitor of *Cdk5*, was also up-regulated and could have a protective effect since *Cdk5* activation causes hyperphosphorylation of APP and tau leading to plaques and tangles [86–88]. Also, CDK5 has been described as a mediator of Aβ-induced neuronal cell cycle reentry that leads to neurodegeneration [89].

At the translatome level, other interesting up-regulated genes were found. Apolipoprotein D, which has displayed a neuroprotective effect [90] and is induced in hippocampal cells in response to Aβ [91], increases its translational levels. Another gene with a neuroprotective function up-regulated at the translatome level was Metallothionein 3 which is expressed by the astrocytes to uptake Aβ [92]. However, its role is still controversial with opposite findings *in vitro* and *in vivo*, and over the different models used. For example, a study using the Tg2576 mice model shows that this gene could have opposite effects depending on gender, brain region and age [93]. Genes up-regulated exclusively at the level of translational efficiency were related to Aβ production and disease. For example *Serf2*, a positive regulator of amyloid protein aggregation [94,95], and *Hras2*, described as an AD biomarker, is stimulated by Aβ and produces a reduction in LTP [70].

Regarding down-regulated genes at transcriptome level, several cases confirm what was expected from previous reports. For example, *Klk6*, a peptidase that cleaves APP was found to be down-regulated in the cortex of human postmortem samples of AD patients compared to controls [96,97]. The somatostatin receptor 5 was also down-regulated at both transcriptome and translatome levels, consistently with the decreased levels found for these receptors in the cortex of AD patients [98,99]. The *Fabp5* gene was found to be down-regulated at the translational efficiency level as expected since a FABP5 deficiency was associated with increased vulnerability to cognitive deficits in mice with APP pathology [100,101].

Common regulated genes in both transgenic mice models

In order to explore commonalities shared by both models, we compared DEGs obtained in each comparison using a fold change cutoff of 1 to handle larger numbers (Table 2). Although common genes represent less than 10% in all pairs of lists compared some interesting cases were observed. For example, when comparing up-regulated genes at the transcriptome level between the CVN (282 genes) and the Tg2576 mice models (195 genes) we found 25 shared genes. Of those, 19 are classified as predicted genes. Exhaustive analysis reveals that those genes are mainly protein coding genes encoding for Zinc finger

proteins, Alpha-takusan like proteins, and also a long non-coding RNA (*Gm26650*). Alpha-takusan proteins are a large family that regulates synaptic activity and have been reported that can mitigate Aβ-induced synaptic loss [102,103]. Among common and annotated genes we found *Lrrc37a*, a leucine-rich repeat containing gene that encodes a plasma membrane protein involved in intracellular vesicle trafficking [104] and *Osmr*, the Oncostatin M Receptor. *Lrrc37a* was previously associated with AD because it presents significant SNPs genome-wide associations in APOE-affected individuals and it is located in a locus adjacent to *Mapt* [105]. On the other hand, it has been reported that Oncostatin M has a neuroprotective effect against Aβ toxicity [106].

When exploring the list of up-regulated genes at the translational level shared in both transgenic models several interesting cases were noticed. In this particular case, due to the small number of translational up-regulated genes in the Tg2576 model (66 genes, Table 2), we only found 6 genes in common. However, among them we found the *Lrrc37a* gene and a predicted gene (*Gm3173*) annotated as an alpha-takusan-like protein (see above). Other interesting genes found were *Gfap* and hemoglobins alpha 1 and 2. Glial fibrillary acidic protein (GFAP) is an intermediate filament protein and a glial marker highly expressed in the reactive astrocytes who surround Aβ plaques [56,107]. Regarding hemoglobin alpha 1 and 2 (*Hba-a1* and *Hba-a2*) it has been observed that neurons can express these proteins [108] and that hemoglobin can bind Aβ and co-localize with plaques [109,110].

Among common down-regulated genes we found a total of 13 genes, 8 down-regulated at the transcriptome level and 5 at the translational level. Here we highlight *Tmem59l* (Transmembrane Protein 59 Like), an important paralog of *Tmem59*, down-regulated at the transcriptome level. TMEM59 has been identified as a novel modulator of APP shedding, controlling APP post-translational modification, APP cellular traffic and cleavage [111]. More recently, it has been reported that TMEM59 interacts with TREM2 (see above and discussion) and that TMEM59 homeostasis is regulated by TREM2 in order to control microglia activity [112]. Common genes down-regulated at the translatome level include ribosomal proteins and a ribosome biogenesis factor (Rpl5, Rpl32 and Wbscr22), the fatty acid binding protein 5 (FABP5) discussed before and an adaptor related protein complex 4 (AP4S1). It has been observed that the adaptor protein 4 interacts with APP and that the disruption of this interaction stimulates APP cleavage and Aβ production [113].

Finally, we also observed biological functions shared between the two APP-related mice models. For example, it is interesting to note that several genes affected in each model

are associated with APP and Aβ metabolism, either with neuroprotective or neurotoxic functions (Figure 7).

DISCUSSION

We used RNA-Seq and Ribo-Seq to explore transcriptional and translational gene expression regulation, respectively, in the brain of two transgenic mice models of AD. The study of translation regulation using Ribo-Seq in animal's brain tissue is not so extended (see examples in [114–117]), and as far as we know, this work represents the first approach in AD models. The selected transgenic mice models used are both amyloid models since the two of them have a transgenic insertion of the APP gene with specific mutations that increase levels of Aβ and amyloid plaques (Table 1). Mice were sacrificed at 6 months old, as a relative adult age and preferentially asymptomatic: the CVN mice are completely asymptomatic at this age, showing no phenotypic alteration reported. On the other hand, the Tg2576 mice exhibit cognitive deficits before 6 months of age, but interestingly develop Aβ plaques later, around 12 months of age (Figure 1A).

The isolated total RNA and ribosome footprints obtained from the brain cortex (Figure S1) yield more than 20 and 120 millions of paired-end and single-end reads, respectively (Table S1). We decided to specifically use the brain cortex in order to be focused on a region highly degenerated and pathologically compromised over disease progression in humans, but also in animal models. As anticipated, around 80% of the ribosome footprints samples were rRNA fragments derived from the RNAse digestion. Having this in mind, we decided to proceed with a deep sequencing in order to obtain a considerable amount of non-rRNA reads. By doing so, we were able to get more than 10 million of ribosome footprints mapping over mRNAs in each sample (Table S1), avoiding adding extra steps handling the footprints in an effort to reduce variability and biases. In this scenario, we defined expression levels for more than 14 thousands genes in each transgenic mice. As expected, almost all detected genes at both transcriptome and translatome levels were in common (Figure S2). By studying mapping features and read periodicity we could properly separate transcriptome-derived from translatome-derived reads (Figures S4 and S5). Translatome-derived reads are more prone to map over coding regions than transcriptome-derived reads that also are found in untranslated regions as 5'- and 3'-UTRs. Also, translatome-derived reads show the

classical three nucleotide mapping pattern periodicity not detected in transcriptome-derived reads, mounting evidence of a solid transcription and translation dataset.

Differential gene expression analysis was performed over transcriptome and translatome samples separately, comparing transgenic mice versus WT, to explore deregulated genes in each model. However, considering that differences at the translatome level could be explained by regulation at the transcriptome level, we estimated translational efficiency as the ratio between translatome and transcriptome levels to specifically identify translational regulation events [19] (Figures 2 and 3). Despite the fact we have used different animals as replicates, which compromise a considerable level of biological variation, samples clustered as expected as evidenced by PCA (Figure S6). Also, we were able to define lists of genes with a significant statistical difference between genotypes at the level of p-adjusted value <0.05 (Table 2). Expression levels of DEGs also separates samples as expected and shows the different levels of regulation observed, especially when analyzing translational efficiency regulation (Figure 4). As a control comparison, we also explored differential gene expression between WT animals. Although identifying DEGs, there is not a considerable overlap with previously defined DEGs and enriched biological functions observed were either not related to the results previously discussed or absent (Figures S13 and S14).

The functional analysis of regulated genes involves different approaches and techniques. In the first place, we used standard gene ontology and functional enrichment tools, as *IPA* and *STRING*. These approaches revealed interesting results indicating a clear signature of decreased neurodegenerative-related process and increased neuroprotective-related functions, particularly for the CVN strain (Figures 5 and 6). In second place, we complement the analysis with an in-house developed tool (https://github.com/sradiouy/IdMiner) to deeply explore DEGs lists in order to find relevant associations between genes and biological functions related to pathology. By using this approach we detected several genes associated either with the neurodegenerative and neurotoxicity phenotype or with protective and beneficial functions (see below).

We identified a clear DAM gene signature in the CVN transgenic model mainly composed of transmembrane proteins up-regulated at both transcriptome and translatome levels, identified at a first place as members of an immune system process response (Figure S11 and S12). The main functions of this DAM population, characterized by the presence of these genes, is to localize Aβ plaques and proceed to its clearance and it has been

described before in other transgenic mice models of AD at the same age or at older ages [17,18,52,53]. It is interesting to point out that this is the first time this signature is described in the CVN transgenic model and that also is the first time it is seen activated at translatome levels since previous studies were focused only on transcriptome quantifications. Also it is noteworthy that this DAM population is present in a complete asymptomatic and early stage of the mice phenotype, since this model is supposed to describe Aβ deposits and cognitive impairment at 12 months old. Among the genes present in this signature we found several interesting cases, for example *Trem2* and *Tyrobp* genes both were up-regulated (transcriptome level: fold change = 2.12 and 1.66, p-adjusted = 1.18E-15 and 6.22E-4, respectively; translatome level: fold change = 1.90 and 1.72, p-adjusted = 4.25E-8 and 1.39E-4, respectively). The TREM2/TYROBP complex expressed in microglial is necessary to prevent Aβ accumulation and diffusion [17,118–120]. TREM2/TYROBP-dependent cell activation seems to be beneficial [121], while *Trem2* deficiency impairs cellular metabolism and promotes increased autophagy in microglia in an AD mouse model [122]. Concordantly, we found several members of the TYROBP AD-related pathway [54,123] either regulated at the transcriptome, translatome or both levels in the CVN mice (Figure S15). Regarding TREM2, transgenic overexpression of the human version of this gene modified the morphological and functional responses of microglia, which resulted in amelioration of the pathology and memory deficits in an AD mouse model [124]. Interestingly, it has been reported that TREM2 interacts with TREM59 and modulates microglia activation [112]. Here we found *Trem59l* as a down-regulated gene at the transcriptional level present in both transgenic mice models (CVN: fold change = -1.89 and p-adjusted = 3.56E-28; Tg2576: fold change = -1.29 and p-adjusted = 0.01). Considering the upregulated genes at the translational level, two different sets of genes are observed. One set associated with protective functions like reducing Aβ production, and others related to the high levels of Aβ and neurotoxicity. A similar interpretation is made from the lists of down-regulated genes.

Regarding the Tg2576 transgenic model, although it presents behavior alterations at young ages, Aβ plaques are not described at 6 months old (Figure 1). However, we found a group of genes regulated at transcriptome and/or translatome levels that have been reported to be altered in response to the presence of Aβ. Also, as observed in the CVN model, we found genes associated with neuroprotective functions and others with a neurodegenerative phenotype related to APP metabolism.

We also explored common DEGs at transcriptome or translatome levels in both transgenic mice models. In spite of each transgenic mice has a different genetic background (Table 1), they show a complete different pattern of phenotypic alterations (Figure 1A) and each model shows different regulation levels (Table 2), it is interesting that they share regulated genes at the transcriptome and translatome levels. These genes, evidenced at early stages of the disease, have described functions that could be associated with AD pathology, for instance: alpha-takusan proteins, *Lrrc37a*, *Osmr*, *Gfap*, hemoglobins alpha 1 and 2, *Tmem59l* and *Fabp5*. Despite no Aβ plaques are described in the mice's brains at this age, most of the genes are implicated in APP metabolism in a neuroprotective fashion that responds to Aβ accumulation. This set of common regulated genes, and the set of genes described before, represents interesting and challenging cases to further explore in order to better understand the transcriptional and translational control of gene expression that is occurring in AD pathology.

Recent advances in genomic views of translation have been essential to widen our current concepts about the dynamic properties of protein translation as a process, and increase the relevance that regulation of translation has on particular sets of mRNAs, thereby later impacting the overall view of proteostasis. Besides pointing to novel transcriptional regulation events in AD disease models, here we uncover that translation is important in regulating key AD related genes at early asymptomatic stages of the disease models that may impact in the slow and accumulative process that initiates AD. Several of the dysregulated pathways observed here will need further study to elucidate regulation mechanisms but certainly put translation regulation in the road map to understand AD dysregulated processes.

ACKNOWLEDGMENTS

We thank members of Sotelo-Silveira lab for the results discussion and intellectual input. We also thank members of Bloom lab Andrés Norambuena and Antonia Silva for their support with wet lab experiments and especially to Dora Bigler-Wang and Nutan Shivange for handling mice and brain dissections.

We would like to acknowledge the following institutions for the financial support received: PhD fellowships from Agencia Nacional de Investigación e Innovación (ANII) to GE (POS_NAC_2016_1_129959), Programa de Desarrollo de las Ciencias Básicas (PEDECIBA) to GE and JRSS, PROLAB travel grant (PABMB/ASBMB/IUBMB) to GE and Owen's Family Foundation and Cure Alzheimer's Fund to GSB.

CONFLICT OF INTEREST

The authors have no conflict of interest to report.

AUTHOR CONTRIBUTIONS

J.R.S-S. and G.S.B. conceived the project, designed and supervised the research. J.S.L. and E.R.S. contributed to the project design and intellectual content. G.E. performed the experiments. G.E. and E.R.S. analyzed data. G.E., J.R.S-S. and G.S.B. wrote the paper. All authors approved the manuscript.

REFERENCES

(At the bottom)

TABLES

Table 1. Genotype description of the transgenic mice used.

Genotype	*Gene(s)*	*Mutations*	*Modification*	*Genetic Background*
CVN	APP, NOS2	APP: K670N/M671L, E693Q, D694N	APP: Transgenic NOS2: Knock-Out	C57/BL6
Tg2576	APP	APP: KM670/671NL	APP: Transgenic	B6;SJL

Table 2. The number of differentially expressed genes for CVN (upper panel) and Tg2576 (lower panel) transgenic mice contrasted to WT animals is shown. Differentially expressed genes, defined by p-adjusted value <0.05, are separated by fold change intervals. For each genotype, comparison at the transcriptome level (RNA-Seq) and translatome level (Ribo-Seq) by *edgeR*; and at the translational efficiency (TE) level by *Xtail*, are shown.

CVN vs WT		*p-adjusted value < 0.05*			
		FC > 1.5	*FC > 1*	*FC < -1.5*	*FC < -1*
edgeR	RNA-Seq	160	282	80	187
	Ribo-Seq	300	830	77	335
Xtail	TE	88	491	56	306

Tg2576 vs WT		*p-adjusted value < 0.05*			
		FC > 1.5	*FC > 1*	*FC < -1.5*	*FC < -1*
edgeR	RNA-Seq	76	194	64	149
	Ribo-Seq	46	66	48	69
Xtail	TE	25	50	25	37

FIGURE LEGENDS

Figure 1. Phenotypical description of the transgenic mice used as AD amyloid-related models and an illustrative representation of the protocol used. (**A**) Phenotype characterization of each transgenic model, CVN and Tg2576, described by the *Alzforum* organization website is shown. Three male, 6 months old mice were used per genotype. (**B**) A brief illustrative description of the experimental approaches used here is presented. *(i)* Brain cortex is dissected and *(ii)* homogenized using a glass Dounce homogenizer. At this point, *(iii. a)* a transcriptome sample is separated to proceed with total RNA isolation and RNA-Seq protocol. In parallel, *(iii. b)* post mitochondrial supernatant is obtained and *(iv. b)* ultracentrifuged to isolate polysomes *(v. b)*. An RNAse protection assay is performed over polysomes *(vi. b)*, where a controlled digestion generates small mRNA fragments. These ribosome footprints are isolated *(vii. b)* and submitted to high-throughput sequencing (Ribo-Seq protocol).

Figure 2. Differential expression analysis performed by *edgeR* for transcriptomes (**A-C**), and by *Xtail* for translational efficiency values (**D-F**), comparing CVN transgenic mice against wild type. Scatter plots comparing normalized CPM expression between genotypes for transcriptome and translational efficiency values, respectively, are shown in (**A**) and (**D**). Volcano plots where the relationship between fold change and p-adjusted values is evidenced for transcriptome and translational efficiency comparison, respectively, are shown in (**B**) and (**E**). Scatter plots comparing translational vs transcriptional fold change are shown in (**C**) and (**F**). In both cases, regulated genes identified in each level are colored. In all plots, colored dots indicates differentially expressed genes (p-adjusted value <0.05) by the following criteria: red up-regulated genes by >1.5 fold, orange up-regulated by >1 fold, blue down-regulated genes by <-1.5 fold and sky-blue down-regulated genes by <-1 fold.

Figure 3. Differential expression analysis performed by *edgeR* for transcriptomes (**A-C**), and by *Xtail* for translational efficiency values (**D-F**), comparing Tg2576 transgenic mice against wild type. Scatter plots comparing normalized CPM expression between genotypes for

transcriptome and translational efficiency values, respectively, are shown in (**A**) and (**D**). Volcano plots where the relationship between fold change and p-adjusted values is evidenced for transcriptome and translational efficiency comparison, respectively, are shown in (**B**) and (**E**). Scatter plots comparing translational vs transcriptional fold change are shown in (**C**) and (**F**). In both cases, regulated genes identified in each level are colored. In all plots, colored dots indicates differentially expressed genes (p-adjusted value <0.05) by the following criteria: red up-regulated genes by >1.5 fold, orange up-regulated by >1 fold, blue down-regulated genes by <-1.5 fold and sky-blue down-regulated genes by <-1 fold.

Figure 4. Heatmap of DEGs (|fold change| >1.5 and p-adjusted value <0.05) at transcriptome compartments (**A** and **C**) and at translational efficiency (**B** and **D**) for CVN (**A-B**) and Tg2576 (**C-D**) transgenic mice models.

Figure 5. Functional enrichment analysis of DEGs. The top10 (z-score) most decreased and increased functional categories are shown for each level (RNA-Seq or transcriptome, Ribo-Seq or translatome, and translational efficiency) and for both transgenic mice, CVN (**A**) and Tg2576 (**B**). Analysis was performed using *IPA* (QIAGEN Inc.) and graphical representation was obtained from *GOplot* R package. See Table S2 to find the complete set of decreased and increased pathway at each level and transgenic mice.

Figure 6. Upstream inferred regulation analysis performed by IPA. The inferred upstream genes marked as inhibited (blue) or activated (red) based on their targets regulation observed is shown for each level: RNA-Seq or transcriptome (**A-B**), Ribo-Seq or translatome (**C-D**), and translational efficiency (**E-F**).

Figure 7. Expression regulation of genes related to Aβ, APP or tau metabolism in the CVN (**A**) or Tg2576 transgenic mice (**B**). Several gene ontology categories of genes, obtained from AmiGO2, were merged to consider all genes related to Aβ, APP or tau metabolism.

Genes were selected by p-adjusted value <0.05 and the expression level of those significant genes is shown as a heatmap.

FIGURES

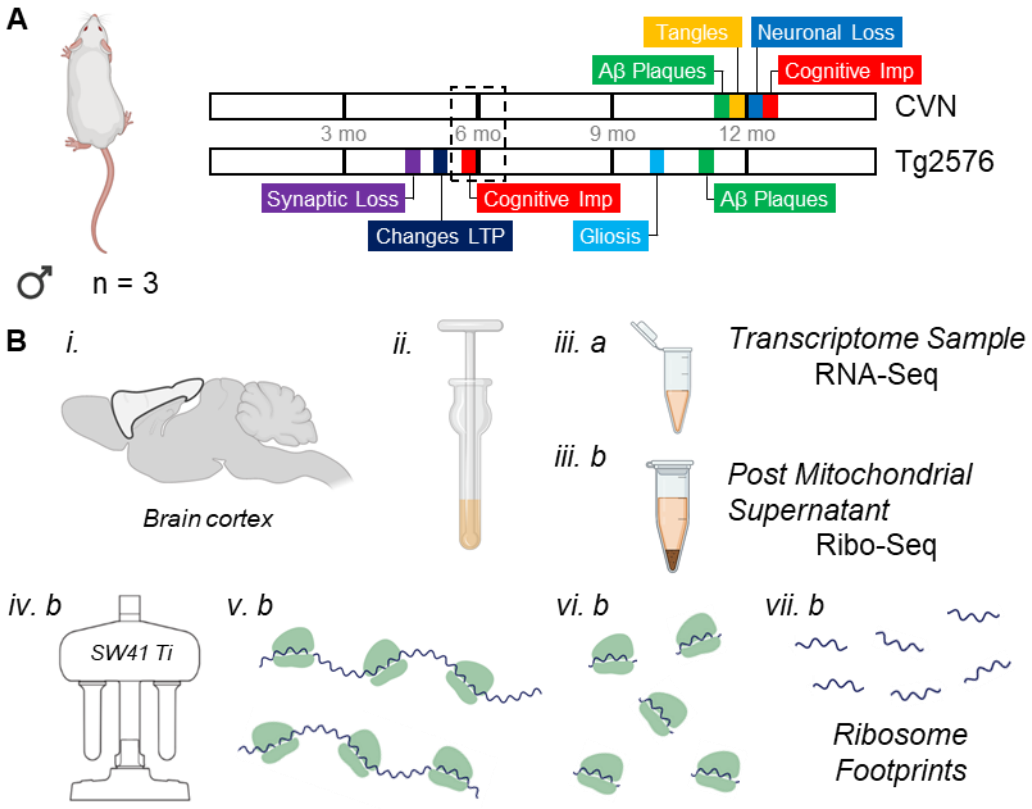

FIGURE 1

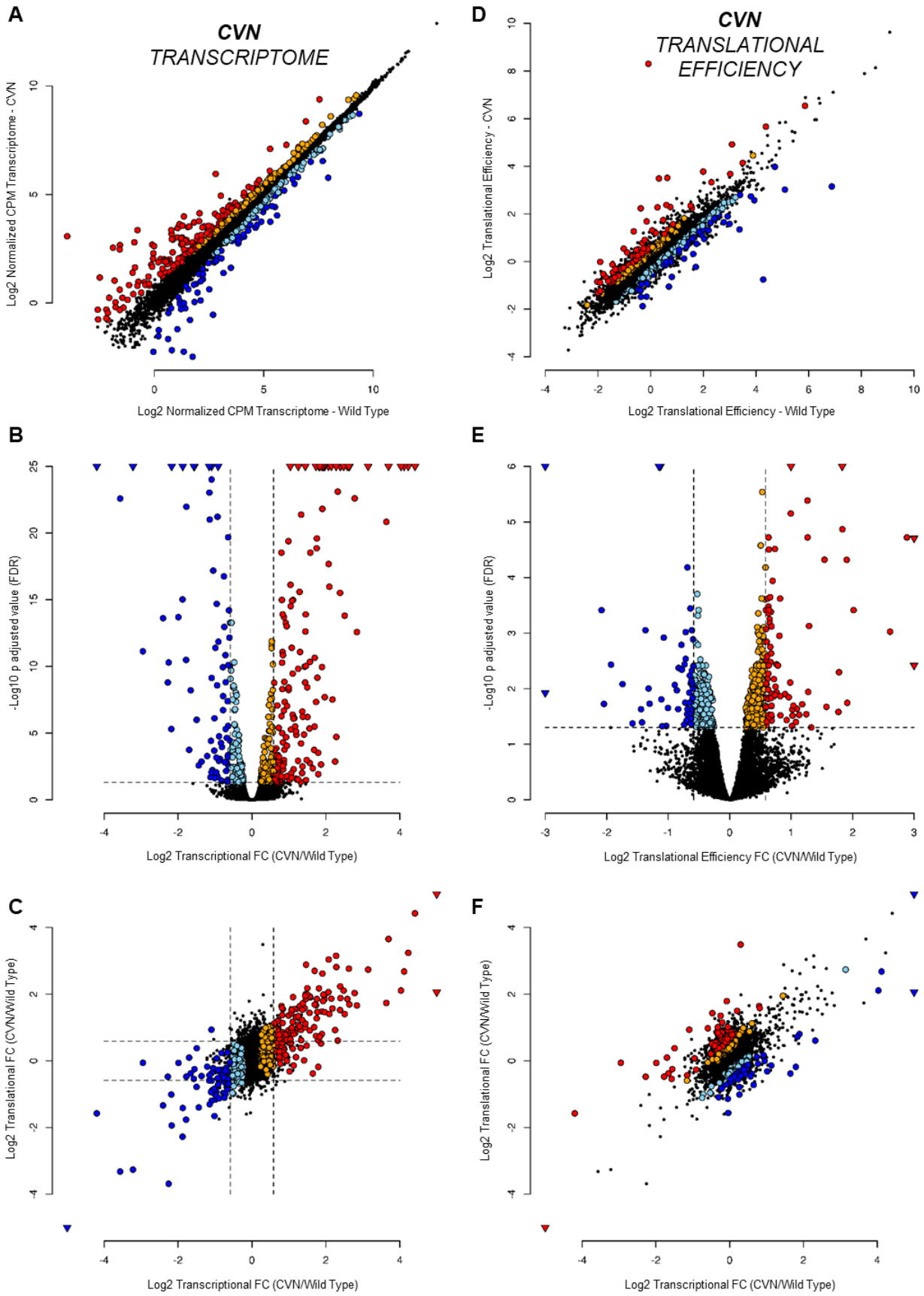
A
CVN
TRANSCRIPTOME
Log2 Normalized CPM Transcriptome - CVN
Log2 Normalized CPM Transcriptome - Wild Type
D
CVN
TRANSLATIONAL
EFFICIENCY
Log2 Translational Efficiency - CVN
Log2 Translational Efficiency - Wild Type
B
-Log10 p adjusted value (FDR)
Log2 Transcriptional FC (CVN/Wild Type)
E
-Log10 p adjusted value (FDR)
Log2 Translational Efficiency FC (CVN/Wild Type)
C
Log2 Translational FC (CVN/Wild Type)
Log2 Transcriptional FC (CVN/Wild Type)
F
Log2 Translational FC (CVN/Wild Type)
Log2 Transcriptional FC (CVN/Wild Type)

FIGURE 2

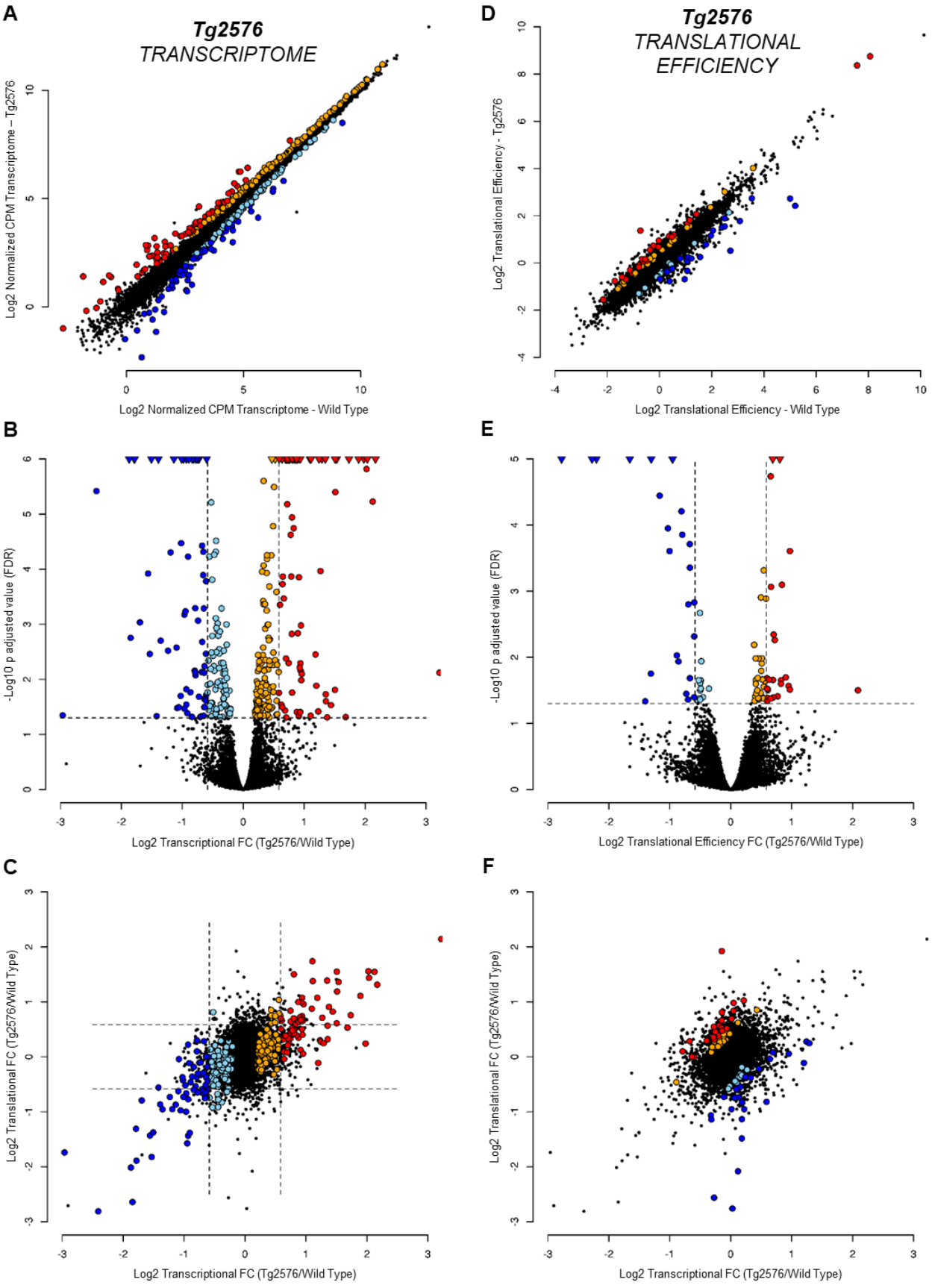
A
Tg2576
TRANSCRIPTOME
Log2 Normalized CPM Transcriptome – Tg2576
Log2 Normalized CPM Transcriptome - Wild Type
D
Tg2576
TRANSLATIONAL
EFFICIENCY
Log2 Translational Efficiency - Tg2576
Log2 Translational Efficiency - Wild Type
B
-Log10 p adjusted value (FDR)
Log2 Transcriptional FC (Tg2576/Wild Type)
E
-Log10 p adjusted value (FDR)
Log2 Translational Efficiency FC (Tg2576/Wild Type)
C
Log2 Translational FC (Tg2576/Wild Type)
Log2 Transcriptional FC (Tg2576/Wild Type)
F
Log2 Translational FC (Tg2576/Wild Type)
Log2 Transcriptional FC (Tg2576/Wild Type)

FIGURE 3

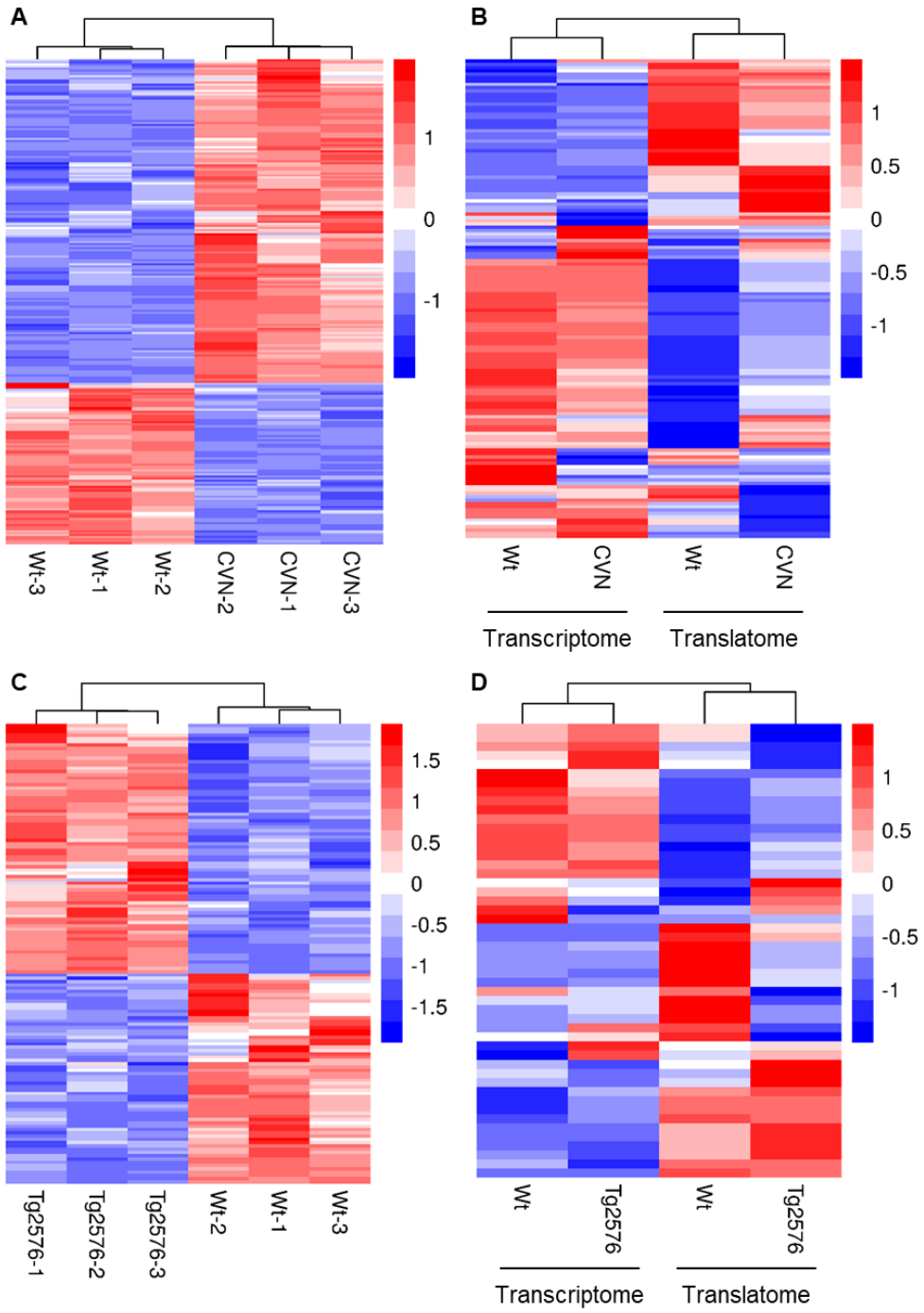
A
1
0
-1
Wt-3
Wt-1
Wt-2
CVN-2
CVN-1
CVN-3
B
1
0.5
0
-0.5
-1
Wt
CVN
Wt
CVN
Transcriptome
Translatome
C
1.5
1
0.5
0
-0.5
-1
-1.5
Tg2576-1
Tg2576-2
Tg2576-3
Wt-2
Wt-1
Wt-3
D
1
0.5
0
-0.5
-1
Wt
Tg2576
Wt
Tg2576
Transcriptome
Translatome

FIGURE 4

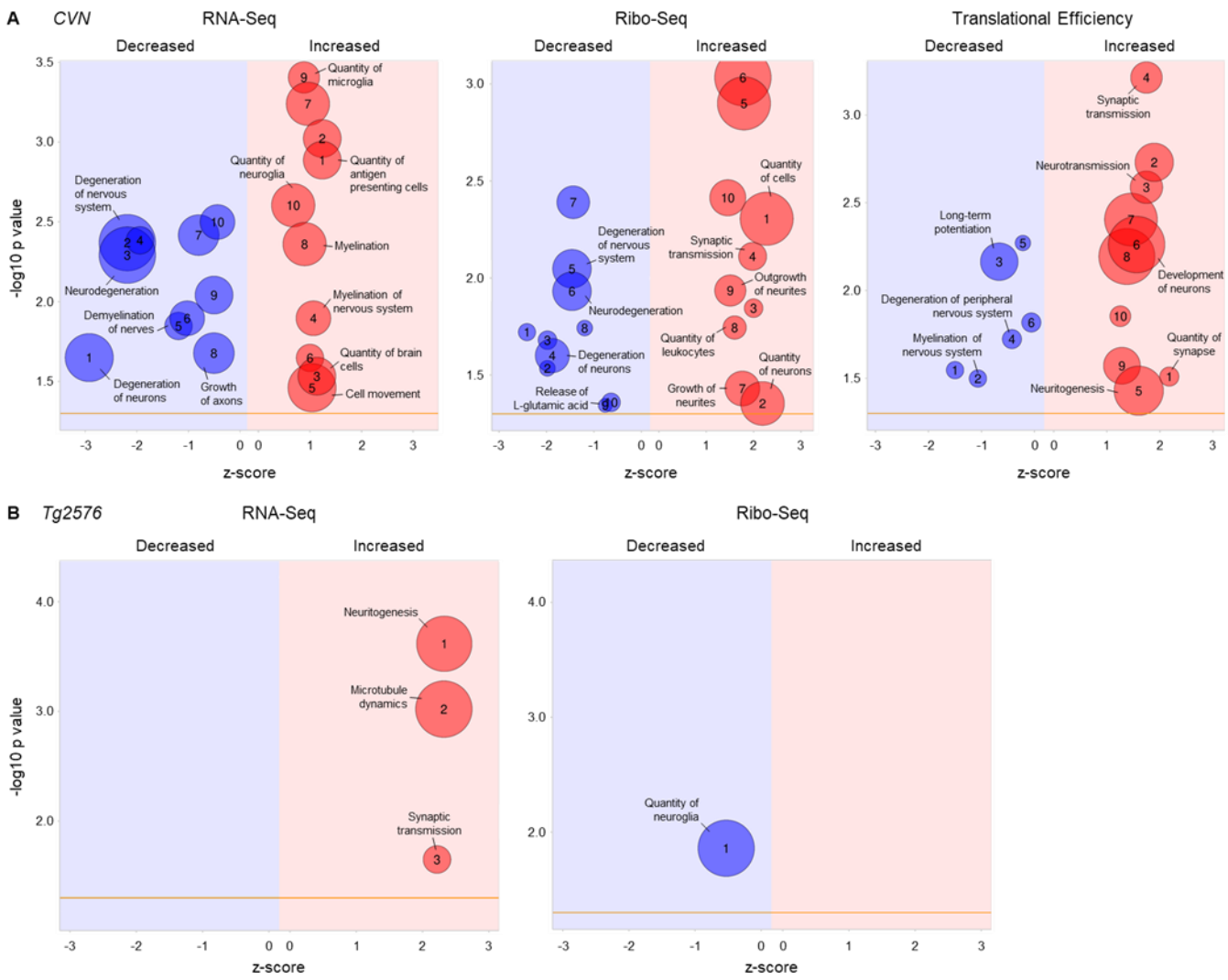
A CVN
RNA-Seq
Ribo-Seq
Translational Efficiency
Decreased
Increased
-log10 p value
z-score
Quantity of microglia
Quantity of antigen presenting cells
Quantity of neuroglia
Myelination
Degeneration of nervous system
Neurodegeneration
Demyelination of nerves
Myelination of nervous system
Quantity of brain cells
Degeneration of neurons
Growth of axons
Cell movement
Quantity of cells
Synaptic transmission
Outgrowth of neurites
Quantity of leukocytes
Quantity of neurons
Release of L-glutamic acid
Growth of neurites
Long-term potentiation
Neurotransmission
Development of neurons
Degeneration of peripheral nervous system
Quantity of synapse
Neuritogenesis
B Tg2576
RNA-Seq
Ribo-Seq
Neuritogenesis
Microtubule dynamics
Synaptic transmission
Quantity of neuroglia

FIGURE 5

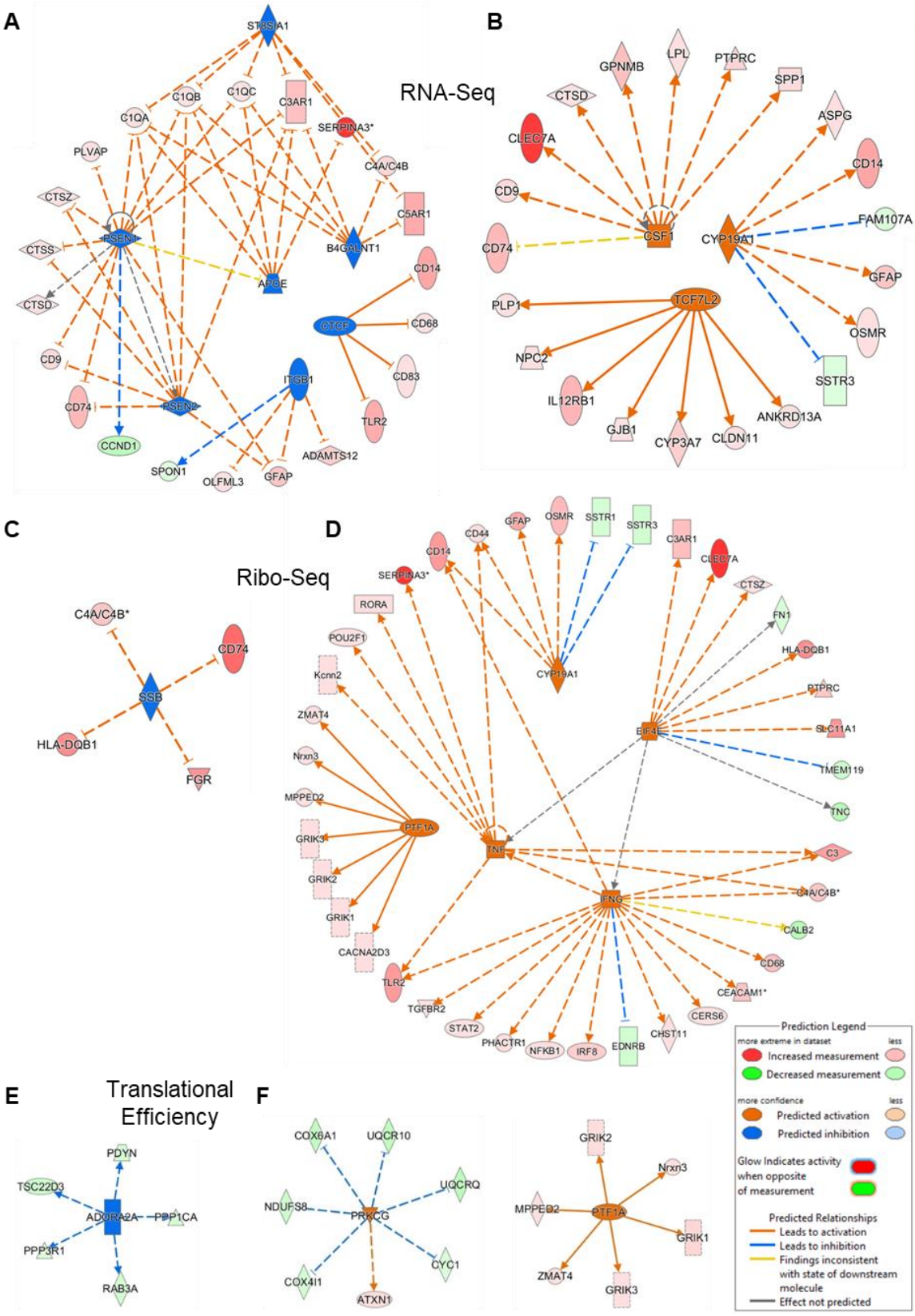
A
RNA-Seq
ST8SIA1
C1QB
C1QC
C3AR1
C1QA
SERPINA3*
PLVAP
C4A/C4B
CTSZ
C5AR1
PSEN1
B4GALNT1
CTSS
APOE
CD14
CTSD
CTCF
CD68
CD9
ITGB1
CD83
CD74
PSEN2
TLR2
CCND1
ADAMTS12
SPON1
OLFML3
GFAP
B
GPNMB
LPL
PTPRC
SPP1
CTSD
ASPG
CLEC7A
CD14
CD9
FAM107A
CSF1
CYP19A1
CD74
GFAP
PLP1
TCF7L2
OSMR
NPC2
SSTR3
IL12RB1
ANKRD13A
GJB1
CYP3A7
CLDN11
C
Ribo-Seq
C4A/C4B*
CD74
SSB
HLA-DQB1
FGR
D
CD14
CD44
GFAP
OSMR
SSTR1
SSTR3
C3AR1
CLEC7A
SERPINA3*
CTSZ
RORA
FN1
POU2F1
HLA-DQB1
CYP19A1
Kcnn2
PTPRC
ZMAT4
EIF4E
SLC11A1
Nrxn3
TMEM119
MPPED2
TNC
PTF1A
GRIK3
TNF
C3
GRIK2
C4A/C4B*
IFNG
GRIK1
CALB2
CACNA2D3
CD68
TLR2
CEACAM1*
TGFBR2
CERS6
STAT2
CHST11
PHACTR1
NFKB1
IRF8
EDNRB
Prediction Legend
more extreme in dataset
less
Increased measurement
Decreased measurement
more confidence
less
Predicted activation
Predicted inhibition
Glow Indicates activity when opposite of measurement
Predicted Relationships
Leads to activation
Leads to inhibition
Findings inconsistent with state of downstream molecule
Effect not predicted
E
Translational Efficiency
PDYN
TSC22D3
ADORA2A
PPP1CA
PPP3R1
RAB3A
F
COX6A1
UQCR10
UQCRQ
NDUFS8
PRKCG
CYC1
COX4I1
ATXN1
GRIK2
Nrxn3
MPPED2
PTF1A
GRIK1
ZMAT4
GRIK3

FIGURE 6

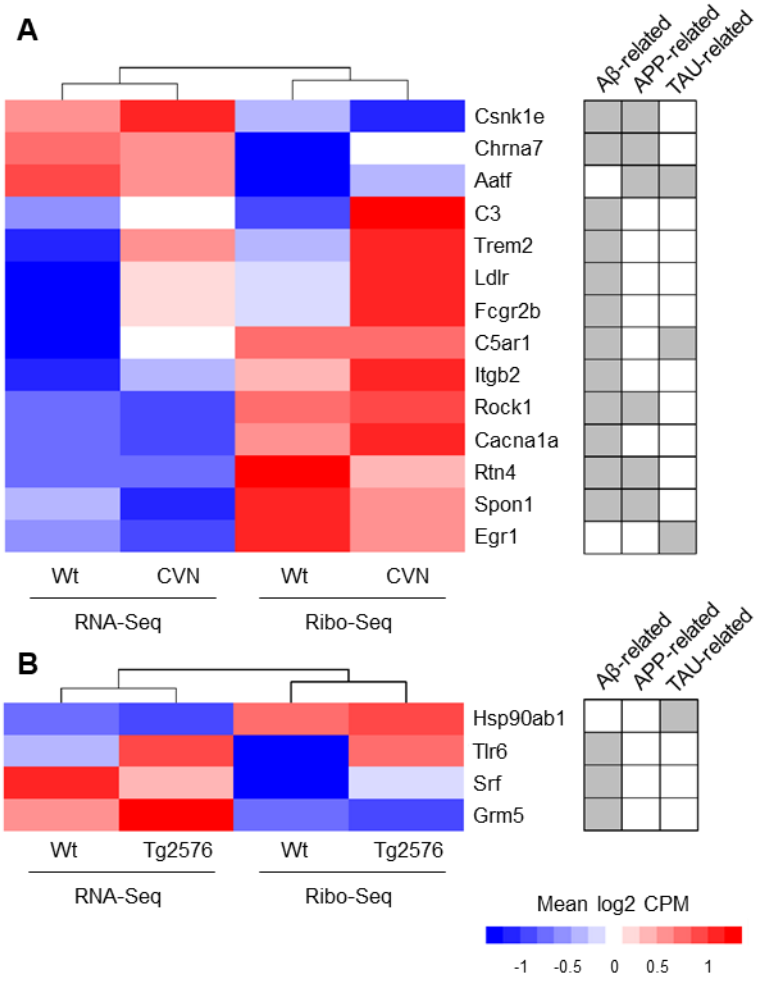
A
Aβ-related
APP-related
TAU-related
Csnk1e
Chrna7
Aatf
C3
Trem2
Ldlr
Fcgr2b
C5ar1
Itgb2
Rock1
Cacna1a
Rtn4
Spon1
Egr1
Wt
CVN
Wt
CVN
RNA-Seq
Ribo-Seq
B
Aβ-related
APP-related
TAU-related
Hsp90ab1
Tlr6
Srf
Grm5
Wt
Tg2576
Wt
Tg2576
RNA-Seq
Ribo-Seq
Mean log2 CPM
-1
-0.5
0
0.5
1

FIGURE 7

SUPPLEMENTARY MATERIAL

Table S1. The number of sequenced and mapped reads is shown for each model for both transcriptome (RNA-Seq; A) and translatome (Ribo-Seq; B) samples.

A

Genotype	#	*Total Reads*	*PE reads mapped concordantly*	*PE reads mapped discordantly*	*Broken PE reads mapped*	*% of map.*	*counting over*			
							mRNAs (21 989)		*genes (46 095)*	
CVN	1	23,135,637	18,253,665	862,612	2,892,742	88.9%	31,934,134	77.7%	36,855,454	89.6%
	2	22,997,533	18,104,983	843,327	2,861,377	88.6%	31,583,039	77.5%	36,571,542	89.7%
	3	23,036,754	17,654,723	874,552	3,003,636	87.0%	30,657,313	76.5%	36,006,497	89.9%
Wt	1	23,263,962	18,347,017	855,608	2,928,713	88.8%	31,856,021	77.1%	37,089,239	89.7%
	2	23,492,421	18,619,340	873,227	2,872,726	89.1%	32,376,097	77.3%	37,628,971	89.9%
	3	23,609,748	18,518,928	834,489	2,968,238	88.3%	32,253,440	77.4%	37,445,618	89.9%
Tg2576	1	23,950,074	18,677,371	900,467	3,185,344	88.4%	32,346,342	76.4%	37,931,132	89.6%
	2	23,656,574	18,517,226	854,470	3,006,279	88.2%	32,233,304	77.2%	37,456,950	89.7%
	3	23,431,043	18,285,070	935,969	3,067,945	88.6%	31,390,282	75.6%	37,346,615	90.0%
Wt Tg2576	1	21,085,032	15,995,496	797,005	2,833,921	86.4%	27,935,114	76.7%	32,647,797	89.6%
	2	22,758,028	17,429,707	871,461	3,029,020	87.1%	31,077,379	78.4%	35,511,353	89.6%
	3	23,032,760	18,036,162	829,500	2,945,435	88.3%	31,337,466	77.0%	36,505,692	89.7%

B

Genotype	#	*Total Reads*	*non rRNA*		*aligned exactly 1 time*	*aligned >1 times*	*counting over*			
							mRNAs (21 989)		*genes (46 095)*	
CVN	1	125,158,118	18,467,165	14.8%	11,294,565	4,039,692	11,817,046	77.1%	12,885,534	84.0%
	2	124,834,868	19,343,288	15.5%	11,757,820	4,071,266	12,333,505	77.9%	13,623,963	86.1%
	3	124,796,265	21,304,049	17.1%	11,469,519	4,897,991	12,138,772	74.2%	13,253,986	81.0%
Wt	1	125,600,184	16,312,016	13.0%	9,756,019	3,647,431	10,303,253	76.9%	11,447,979	85.4%
	2	147,633,148	19,439,215	13.2%	11,483,105	4,298,470	12,055,087	76.4%	13,555,389	85.9%
	3	98,153,015	12,829,605	13.1%	7,729,089	2,643,123	8,050,517	77.6%	8,896,089	85.8%
Tg2576	1	124,934,216	16,796,957	13.4%	10,220,204	3,399,665	10,695,295	78.5%	11,866,137	87.1%

	2	125,030,269	18,376,892	14.7%	11,180,855	3,916,901	11,626,486	77.0%	12,872,033	85.3%
	3	124,656,995	16,552,770	13.3%	9,729,332	3,516,747	10,093,511	76.2%	11,355,864	85.7%
Wt Tg2576	1	125,767,260	14,955,168	11.9%	8,867,825	3,298,156	9,367,092	77.0%	10,254,327	84.3%
	2	126,692,576	18,912,320	14.9%	11,609,538	4,463,051	11,938,808	74.3%	13,162,956	81.9%
	3	125,199,385	15,079,762	12.0%	9,470,651	3,253,477	9,773,898	76.8%	10,773,420	84.7%

Table S2. Complete set of decreased and increased pathway for both transgenic mice at the transcriptome, translatome and translational efficiency level determined by *IPA*.

(Excel file attached)

SUPPLEMENTARY FIGURE LEGENDS

Figure S1. Ribosome footprints purification. (**A**) Polysome fraction digested with Benzonase were separated in a 15% PAGE with 7M Urea. Wells description: 1, 3 and 11 – RNA oligos of 26 and 34 nucleotide in length; 2 an 12 – Ultra Low DNA Ladder (Invitrogen, catalog # 10597012); 4 to 6 – Polysome digestion of WT brain cortex; 8 to 10 – Polysome digestion of CVN brain cortex. Using RNA oligos as markers (indicated in full line boxes), ribosome footprints bands were identified and excised in a dark room under UV light exposure (indicated in slashed line boxes). (**B**) Ribosome footprints quality was evaluated in a 2100 Agilent Bioanalyzer instrument using a Small RNA kit. Electropherograms of unpurified polysome digestion sample (red line) and of purified ribosome footprints sample (blue line) are shown. Ribosome footprints sample consists of RNA fragments around 30 nucleotides in length.

Figure S2. Transcriptome and Translatome detected genes. Venn diagram indicates the number of detected and shared genes for each compartment for CVN (**A**) and Tg2576 transgenic mice (**B**).

Figure S3. Inter-replicate correlation among transcriptomes and translatomes samples for CVN (**A**) and Tg2576 mice (**B**). Pearson correlation value is shown for each pairwise correlation and indicated in a color scheme.

Figure S4. Observed-to-expected ratio of the Ribo-Seq and RNA-Seq derived reads mapping to each of the three nucleotides in codons. Ribo-Seq derived reads 5' ends are preferentially enriched at the first nucleotide of the codon (A), while RNA-Seq derived reads 5' end are distributed more equally among the three nucleotides (B). The same periodicity pattern is observed indistinctly in the CVN and Tg2576 transgenic mice models and their wild type controls. The analysis was performed following the criteria described by Ingolia et al. Science 2009 and Guo et al. Nature 2010.

Figure S5. Distribution of mapped reads among coding sequences (CDS), 5' and 3' untranslated regions (5'-UTR and 3'-UTR). (A) Fraction of mapped reads among mRNA's features is shown for CVN and Tg2576 transgenic mice models and their wild type controls, for the Ribo-Seq and RNA-Seq data sets. Ribo-Seq derived reads map preferentially over CDS and RNA-Seq derived reads are distributed in a more uniform pattern. This difference is not due to a bias in feature length as is shown in (B).

Figure S6. Principal Component Analysis for transcriptomes (**A** and **C**) and translatomes samples (**B** and **D**) of CVN (**A-B**) and Tg2576 (**C-D**) mice model. In each case, a 2D plot of principal component 1 and 2 for transcriptomes or translatomes is shown with the scree plots associated indicating the percentage of explained variation by each dimension of the PCA.

Figure S7. Differential expression analysis performed by *edgeR* for the translatome compartment comparing CVN transgenic mice against wild type. (**A**) Shows a scatter plot comparing normalized CPM expressions at the translatome between genotypes. (**B**) Shows a volcano plot where the relationship between fold change and p-adjusted values is evidenced for translatome comparison. (**C**) Shows a scatter plot comparing translational vs transcriptional fold change, highlighting regulated genes at the translational level. (**D**) Heatmap of differentially expressed genes (|fold change| >1.5 and p-adjusted value <0.05) at the translatome compartment. In (**A-C**), colored dots indicates differentially expressed genes (p-adjusted value <0.05) by the following criteria: red up-regulated genes by >1.5 fold, orange up-regulated by >1 fold, blue down-regulated genes by <-1.5 fold and sky-blue down-regulated genes by <-1 fold.

Figure S8. Differential expression analysis performed by *edgeR* for the translatome compartment comparing Tg2576 transgenic mice against wild type. (**A**) Shows a scatter plot comparing normalized CPM expressions at the translatome between genotypes. (**B**) Shows a volcano plot where the relationship between fold change and p-adjusted values is evidenced for translatome comparison. (**C**) Shows a scatter plot comparing translational vs transcriptional fold change, highlighting regulated genes at the translational level. (**D**) Heatmap of differentially expressed genes (|fold change| >1.5 and p-adjusted value <0.05)

at the translatome compartment. In (**A-C**), colored dots indicates differentially expressed genes (p-adjusted value <0.05) by the following criteria: red up-regulated genes by >1.5 fold, orange up-regulated by >1 fold, blue down-regulated genes by <-1.5 fold and sky-blue down-regulated genes by <-1 fold.

Figure S9. Intersection between DEGs at transcriptome (RNA-Seq), translatome (Ribo-Seq) and translational efficiency (TE) levels for CVN and Tg2576 transgenic models. The Venn diagrams shows the intersection for DEGs up- and down-regulated genes for the CVN model (**A** and **B**, respectively) and for the Tg2576 model (**C** and **D**, respectively).

Figure S10. Modulated pathways in the CVN transgenic model. Regulated pathways showed in Figure 5 are reconstructed here showing affected genes and their relationship. The three compartments are represented: transcriptome (**A**) and (**B**), translatome (**C**) and (**D**), and translational efficiency (**E**) and (**F**), for decreased and increased pathways respectively.

Figure S11. *STRING* network analysis for transcriptome up-regulated genes (160 genes at fold change >1.5 and p-adjusted value <0.05) in CVN transgenic model. Network has significantly more interactions than expected (296 vs 53; p-value <1.0E-16). Red nodes are associated with the immune system process, an enriched biological process (FDR = 2.67E-07). Disconnected nodes are hide and line thickness indicates the strength of data support.

Figure S12. *STRING* network analysis for translatome up-regulated genes (300 genes at fold change >1.5 and p-adjusted value <0.05) in CVN transgenic model. Network has significantly more interactions than expected (431 vs 164; p-value <1.0E-16). Red nodes are associated with the immune system process, an enriched biological process (FDR = 3.44E-07). Disconnected nodes are hide and line thickness indicates the strength of data support.

Figure S13. Differential expression analysis performed by *edgeR* for the transcriptome compartment comparing WT strains (C57/BL6 vs B6;SJL). (**A**) PCA of samples. (**B**) Scatter plot comparing normalized CPM expressions at the transcriptome between genotypes. (**C**) Volcano plot where the relationship between fold change and p-adjusted values is evidenced for transcriptome comparison. (**D**) Functional enrichment analysis of DEGs performed by *g:GOSt* from *g:Profiler*. In (**B**) and (**C**), colored dots indicates differentially expressed genes (p-adjusted value <0.05) by the following criteria: red up-regulated genes by >1.5 fold, orange up-regulated by >1 fold, blue down-regulated genes by <-1.5 fold and sky-blue down-regulated genes by <-1 fold.

Figure S14. Same as Figure S13, but for the translatome compartment comparison between WT strains (C57/BL6 vs B6;SJL). (**A**) PCA of samples. (**B**) Scatter plot comparing normalized CPM expressions at the transcriptome between genotypes. (**C**) Volcano plot where the relationship between fold change and p-adjusted values is evidenced for transcriptome comparison. (**D**) Functional enrichment analysis of DEGs performed by *g:GOSt* from *g:Profiler*. In (**B**) and (**C**), colored dots indicates differentially expressed genes (p-adjusted value <0.05) by the following criteria: red up-regulated genes by >1.5 fold, orange up-regulated by >1 fold, blue down-regulated genes by <-1.5 fold and sky-blue down-regulated genes by <-1 fold.

Figure S15. Gene expression regulation of TYROBP-related immune response in microglial cells in the CVN transgenic mice. Pathway with direct and indirect causal inputs upstream and downstream of TYROBP was obtained from *WikiPathways*, reconstructed from Zhang B. et al. Cell (2013) and Ryu JK. et al. Nat Immunol (2018). Up-regulated genes at p-adjusted value <0.1 for transcriptome or translatome data sets are indicated with red-colored boxes. No significant down-regulated genes were found.

REFERENCES

[1] Bloom GS (2014) Amyloid-β and tau: the trigger and bullet in Alzheimer disease pathogenesis. *JAMA Neurol* **71**, 505–508.

[2] Kapur M, Monaghan CE, Ackerman SL (2017) Regulation of mRNA Translation in Neurons-A Matter of Life and Death. *Neuron* **96**, 616–637.

[3] Delaidelli A, Jan A, Herms J, Sorensen PH (2019) Translational control in brain pathologies: biological significance and therapeutic opportunities. *Acta Neuropathol* **137**, 535–555.

[4] Taymans J-M, Nkiliza A, Chartier-Harlin M-C (2015) Deregulation of protein translation control, a potential game-changing hypothesis for Parkinson's disease pathogenesis. *Trends Mol Med* **21**, 466–472.

[5] Eshraghi M, Karunadharma PP, Blin J, Shahani N, Ricci EP, Michel A, Urban NT, Galli N, Sharma M, Ramírez-Jarquín UN, Florescu K, Hernandez J, Subramaniam S (2021) Mutant Huntingtin stalls ribosomes and represses protein synthesis in a cellular model of Huntington disease. *Nat Commun* **12**, 1461.

[6] Cefaliello C, Penna E, Barbato C, Di Ruberto G, Mollica MP, Trinchese G, Cigliano L, Borsello T, Chun JT, Giuditta A, Perrone-Capano C, Miniaci MC, Crispino M (2020) Deregulated Local Protein Synthesis in the Brain Synaptosomes of a Mouse Model for Alzheimer's Disease. *Mol Neurobiol* **57**, 1529–1541.

[7] Evans HT, Benetatos J, van Roijen M, Bodea L-G, Götz J (2019) Decreased synthesis of ribosomal proteins in tauopathy revealed by non-canonical amino acid labelling. *EMBO J* **38**, e101174.

[8] Li C, Götz J (2017) Somatodendritic accumulation of Tau in Alzheimer's disease is promoted by Fyn-mediated local protein translation. *EMBO J* **36**, 3120–3138.

[9] Banerjee S, Ferdosh S, Ghosh AN, Barat C (2020) Tau protein- induced sequestration of the eukaryotic ribosome: Implications in neurodegenerative disease. *Sci Rep* **10**, 5225.

[10] Ghosh A, Mizuno K, Tiwari SS, Proitsi P, Gomez Perez-Nievas B, Glennon E, Martinez-Nunez RT, Giese KP (2020) Alzheimer's disease-related dysregulation of mRNA translation causes key pathological features with ageing. *Transl Psychiatry* **10**, 192.

[11] Baleriola J, Walker CA, Jean YY, Crary JF, Troy CM, Nagy PL, Hengst U (2014) Axonally synthesized ATF4 transmits a neurodegenerative signal across brain regions. *Cell* **158**, 1159–1172.

[12] Norambuena A, Wallrabe H, McMahon L, Silva A, Swanson E, Khan SS, Baerthlein D, Kodis E, Oddo S, Mandell JW, Bloom GS (2017) mTOR and neuronal cell cycle reentry: How impaired brain insulin signaling promotes Alzheimer's disease. *Alzheimers Dement* **13**, 152–167.

[13] Norambuena A, Wallrabe H, Cao R, Wang DB, Silva A, Svindrych Z, Periasamy A, Hu S, Tanzi RE, Kim DY, Bloom GS (2018) A novel lysosome-to-mitochondria signaling pathway disrupted by amyloid-β oligomers. *EMBO J* **37**,.

[14] Switon K, Kotulska K, Janusz-Kaminska A, Zmorzynska J, Jaworski J (2017) Molecular neurobiology of mTOR. *Neuroscience* **341**, 112–153.

[15] Castanho I, Murray TK, Hannon E, Jeffries A, Walker E, Laing E, Baulf H, Harvey J, Bradshaw L, Randall A, Moore K, O'Neill P, Lunnon K, Collier DA, Ahmed Z, O'Neill MJ, Mill J (2020) Transcriptional Signatures of Tau and Amyloid Neuropathology. *Cell Rep* **30**, 2040–2054.e5.

[16] Wan Y-W, Al-Ouran R, Mangleburg CG, Perumal TM, Lee TV, Allison K, Swarup V, Funk CC, Gaiteri C, Allen M, Wang M, Neuner SM, Kaczorowski CC, Philip VM, Howell GR, Martini-Stoica H, Zheng H, Mei H, Zhong X, Kim JW, Dawson VL, Dawson TM, Pao P-C, Tsai L-H, Haure-Mirande J-V, Ehrlich ME, Chakrabarty P, Levites Y, Wang X, Dammer EB, Srivastava G, Mukherjee S, Sieberts SK, Omberg L, Dang KD, Eddy JA, Snyder P, Chae Y, Amberkar S, Wei W, Hide W, Preuss C, Ergun A, Ebert PJ, Airey DC, Mostafavi S, Yu L, Klein H-U, Accelerating Medicines Partnership-Alzheimer's Disease Consortium, Carter GW, Collier DA, Golde TE, Levey AI, Bennett DA, Estrada K, Townsend TM, Zhang B, Schadt E, De Jager PL, Price ND, Ertekin-Taner N, Liu Z, Shulman JM, Mangravite LM, Logsdon BA (2020) Meta-Analysis of the Alzheimer's Disease Human Brain Transcriptome and Functional Dissection in Mouse Models. *Cell Rep* **32**, 107908.

[17] Keren-Shaul H, Spinrad A, Weiner A, Matcovitch-Natan O, Dvir-Szternfeld R, Ulland TK, David E, Baruch K, Lara-Astaiso D, Toth B, Itzkovitz S, Colonna M, Schwartz M, Amit I (2017) A Unique Microglia Type Associated with Restricting Development of Alzheimer's Disease. *Cell* **169**, 1276–1290.e17.

[18] Pickett EK, Herrmann AG, McQueen J, Abt K, Dando O, Tulloch J, Jain P, Dunnett S, Sohrabi S, Fjeldstad MP, Calkin W, Murison L, Jackson RJ, Tzioras M, Stevenson A, d'Orange M, Hooley M, Davies C, Colom-Cadena M, Anton-Fernandez A, King D, Oren I, Rose J, McKenzie C-A, Allison E, Smith C, Hardt O, Henstridge CM, Hardingham GE, Spires-Jones TL (2019) Amyloid Beta and Tau Cooperate to Cause Reversible Behavioral and Transcriptional Deficits in a Model of Alzheimer's Disease. *Cell Rep* **29**, 3592–3604.e5.

[19] Ingolia NT (2014) Ribosome profiling: new views of translation, from single codons to genome scale. *Nat Rev Genet* **15**, 205–213.

[20] Ingolia NT (2016) Ribosome Footprint Profiling of Translation throughout the Genome. *Cell* **165**, 22–33.

[21] Eastman G, Smircich P, Sotelo-Silveira JR (2018) Following Ribosome Footprints to Understand Translation at a Genome Wide Level. *Comput Struct Biotechnol J* **16**, 167–176.

[22] Wilcock DM, Lewis MR, Van Nostrand WE, Davis J, Previti ML, Gharkholonarehe N, Vitek MP, Colton CA (2008) Progression of amyloid pathology to Alzheimer's disease pathology in an amyloid precursor protein transgenic mouse model by removal of nitric oxide synthase 2. *J Neurosci* **28**, 1537–1545.

[23] Hsiao K, Chapman P, Nilsen S, Eckman C, Harigaya Y, Younkin S, Yang F, Cole G (1996) Correlative memory deficits, Abeta elevation, and amyloid plaques in transgenic mice. *Science* **274**, 99–102.

[24] Ingolia NT, Brar GA, Rouskin S, McGeachy AM, Weissman JS (2012) The ribosome profiling strategy for monitoring translation in vivo by deep sequencing of ribosome-protected mRNA fragments. *Nat Protoc* **7**, 1534–1550.

[25] Smircich P, Eastman G, Bispo S, Duhagon MA, Guerra-Slompo EP, Garat B, Goldenberg S, Munroe DJ, Dallagiovanna B, Holetz F, Sotelo-Silveira JR (2015) Ribosome profiling reveals translation control as a key mechanism generating differential gene expression in Trypanosoma cruzi. *BMC Genomics* **16**, 443.

[26] Andrews S (2015) *FastQC: A Quality Control Tool for High Throughput Sequence Data*.

[27] Langmead B, Salzberg SL (2012) Fast gapped-read alignment with Bowtie 2. *Nat Methods* **9**, 357–359.

[28] Liao Y, Smyth GK, Shi W (2014) featureCounts: an efficient general purpose program for assigning sequence reads to genomic features. *Bioinformatics* **30**, 923–930.

[29] Robinson MD, McCarthy DJ, Smyth GK (2010) edgeR: a Bioconductor package for differential expression analysis of digital gene expression data. *Bioinformatics* **26**, 139–140.
[30] Xiao Z, Zou Q, Liu Y, Yang X (2016) Genome-wide assessment of differential translations with ribosome profiling data. *Nat Commun* **7**, 11194.
[31] Krämer A, Green J, Pollard J Jr, Tugendreich S (2014) Causal analysis approaches in Ingenuity Pathway Analysis. *Bioinformatics* **30**, 523–530.
[32] Szklarczyk D, Franceschini A, Wyder S, Forslund K, Heller D, Huerta-Cepas J, Simonovic M, Roth A, Santos A, Tsafou KP, Kuhn M, Bork P, Jensen LJ, von Mering C (2015) STRING v10: protein-protein interaction networks, integrated over the tree of life. *Nucleic Acids Res* **43**, D447–52.
[33] Raudvere U, Kolberg L, Kuzmin I, Arak T, Adler P, Peterson H, Vilo J (2019) g:Profiler: a web server for functional enrichment analysis and conversions of gene lists (2019 update). *Nucleic Acids Res* **47**, W191–W198.
[34] Carbon S, Ireland A, Mungall CJ, Shu S, Marshall B, Lewis S, AmiGO Hub, Web Presence Working Group (2009) AmiGO: online access to ontology and annotation data. *Bioinformatics* **25**, 288–289.
[35] Walter W, Sánchez-Cabo F, Ricote M (2015) GOplot: an R package for visually combining expression data with functional analysis. *Bioinformatics* **31**, 2912–2914.
[36] Yamaguchi T, Yamauchi Y, Furukawa K, Ohmi Y, Ohkawa Y, Zhang Q, Okajima T, Furukawa K (2016) Expression of B4GALNT1, an essential glycosyltransferase for the synthesis of complex gangliosides, suppresses BACE1 degradation and modulates APP processing. *Sci Rep* **6**, 34505.
[37] Bernardo A, Harrison FE, McCord M, Zhao J, Bruchey A, Davies SS, Jackson Roberts L 2nd, Mathews PM, Matsuoka Y, Ariga T, Yu RK, Thompson R, McDonald MP (2009) Elimination of GD3 synthase improves memory and reduces amyloid-beta plaque load in transgenic mice. *Neurobiol Aging* **30**, 1777–1791.
[38] Yang Y, Quitschke WW, Vostrov AA, Brewer GJ (1999) CTCF is essential for up-regulating expression from the amyloid precursor protein promoter during differentiation of primary hippocampal neurons. *J Neurochem* **73**, 2286–2298.
[39] McGill BE, Barve RA, Maloney SE, Strickland A, Rensing N, Wang PL, Wong M, Head R, Wozniak DF, Milbrandt J (2018) Abnormal Microglia and Enhanced Inflammation-Related Gene Transcription in Mice with Conditional Deletion of in -Expressing Neurons. *J Neurosci* **38**, 200–219.
[40] Silva AC, Lemos C, Gonçalves FQ, Pliássova AV, Machado NJ, Silva HB, Canas PM, Cunha RA, Lopes JP, Agostinho P (2018) Blockade of adenosine A receptors recovers early deficits of memory and plasticity in the triple transgenic mouse model of Alzheimer's disease. *Neurobiol Dis* **117**, 72–81.
[41] Viana da Silva S, Haberl MG, Zhang P, Bethge P, Lemos C, Gonçalves N, Gorlewicz A, Malezieux M, Gonçalves FQ, Grosjean N, Blanchet C, Frick A, Nägerl UV, Cunha RA, Mulle C (2016) Early synaptic deficits in the APP/PS1 mouse model of Alzheimer's disease involve neuronal adenosine A2A receptors. *Nat Commun* **7**, 11915.
[42] Blom ES, Wang Y, Skoglund L, Hansson AC, Ubaldi M, Lourdusamy A, Sommer WH, Mielke M, Hyman BT, Heilig M, Lannfelt L, Nilsson LNG, Ingelsson M (2010) Increased mRNA Levels of TCF7L2 and MYC of the Wnt Pathway in Tg-ArcSwe Mice and Alzheimer's Disease Brain. *Int J Alzheimers Dis* **2011**, 936580.
[43] Kawanishi S, Takata K, Itezono S, Nagayama H, Konoya S, Chisaki Y, Toda Y, Nakata S, Yano Y, Kitamura Y, Ashihara E (2018) Bone-Marrow-Derived Microglia-Like Cells Ameliorate Brain Amyloid Pathology and Cognitive Impairment in a Mouse

Model of Alzheimer's Disease. *J Alzheimers Dis* **64**, 563–585.
[44] Boissonneault V, Filali M, Lessard M, Relton J, Wong G, Rivest S (2009) Powerful beneficial effects of macrophage colony-stimulating factor on beta-amyloid deposition and cognitive impairment in Alzheimer's disease. *Brain* **132**, 1078–1092.
[45] Xiao D, Liu X, Zhang M, Zou M, Deng Q, Sun D, Bian X, Cai Y, Guo Y, Liu S, Li S, Shiang E, Zhong H, Cheng L, Xu H, Jin K, Xiang M (2018) Direct reprogramming of fibroblasts into neural stem cells by single non-neural progenitor transcription factor Ptf1a. *Nat Commun* **9**, 2865.
[46] He Z, Yang Y, Xing Z, Zuo Z, Wang R, Gu H, Qi F, Yao Z (2020) Intraperitoneal injection of IFN-γ restores microglial autophagy, promotes amyloid-β clearance and improves cognition in APP/PS1 mice. *Cell Death Dis* **11**, 440.
[47] Chakrabarty P, Ceballos-Diaz C, Beccard A, Janus C, Dickson D, Golde TE, Das P (2010) IFN-gamma promotes complement expression and attenuates amyloid plaque deposition in amyloid beta precursor protein transgenic mice. *J Immunol* **184**, 5333–5343.
[48] Baron R, Nemirovsky A, Harpaz I, Cohen H, Owens T, Monsonego A (2008) IFN-gamma enhances neurogenesis in wild-type mice and in a mouse model of Alzheimer's disease. *FASEB J* **22**, 2843–2852.
[49] Decourt B, Lahiri DK, Sabbagh MN (2017) Targeting Tumor Necrosis Factor Alpha for Alzheimer's Disease. *Curr Alzheimer Res* **14**, 412–425.
[50] Zheng C, Zhou X-W, Wang J-Z (2016) The dual roles of cytokines in Alzheimer's disease: update on interleukins, TNF-α, TGF-β and IFN-γ. *Transl Neurodegener* **5**, 7.
[51] Argellati F, Domenicotti C, Passalacqua M, Janda E, Melloni E, Marinari UM, Pronzato MA, Ricciarelli R (2009) Protein kinase C-dependent alpha-secretory processing of the amyloid precursor protein is mediated by phosphorylation of myosin II-B. *FASEB J* **23**, 1246–1251.
[52] Sala Frigerio C, Wolfs L, Fattorelli N, Thrupp N, Voytyuk I, Schmidt I, Mancuso R, Chen W-T, Woodbury ME, Srivastava G, Möller T, Hudry E, Das S, Saido T, Karran E, Hyman B, Perry VH, Fiers M, De Strooper B (2019) The Major Risk Factors for Alzheimer's Disease: Age, Sex, and Genes Modulate the Microglia Response to Aβ Plaques. *Cell Rep* **27**, 1293–1306.e6.
[53] Mathys H, Adaikkan C, Gao F, Young JZ, Manet E, Hemberg M, De Jager PL, Ransohoff RM, Regev A, Tsai L-H (2017) Temporal Tracking of Microglia Activation in Neurodegeneration at Single-Cell Resolution. *Cell Rep* **21**, 366–380.
[54] Zhang B, Gaiteri C, Bodea L-G, Wang Z, McElwee J, Podtelezhnikov AA, Zhang C, Xie T, Tran L, Dobrin R, Fluder E, Clurman B, Melquist S, Narayanan M, Suver C, Shah H, Mahajan M, Gillis T, Mysore J, MacDonald ME, Lamb JR, Bennett DA, Molony C, Stone DJ, Gudnason V, Myers AJ, Schadt EE, Neumann H, Zhu J, Emilsson V (2013) Integrated systems approach identifies genetic nodes and networks in late-onset Alzheimer's disease. *Cell* **153**, 707–720.
[55] Audoy-Rémus J, Bozoyan L, Dumas A, Filali M, Lecours C, Lacroix S, Rivest S, Tremblay M-E, Vallières L (2015) GPR84 deficiency reduces microgliosis, but accelerates dendritic degeneration and cognitive decline in a mouse model of Alzheimer's disease. *Brain Behav Immun* **46**, 112–120.
[56] Kamphuis W, Middeldorp J, Kooijman L, Sluijs JA, Kooi E-J, Moeton M, Freriks M, Mizee MR, Hol EM (2014) Glial fibrillary acidic protein isoform expression in plaque related astrogliosis in Alzheimer's disease. *Neurobiol Aging* **35**, 492–510.
[57] Tyagi E, Fiorelli T, Norden M, Padmanabhan J (2013) Alpha 1-Antichymotrypsin, an Inflammatory Protein Overexpressed in the Brains of Patients with Alzheimer's Disease, Induces Tau Hyperphosphorylation through c-Jun N-Terminal Kinase

Activation. *Int J Alzheimers Dis* **2013**, 606083.
[58] Hol EM, Roelofs RF, Moraal E, Sonnemans MAF, Sluijs JA, Proper EA, de Graan PNE, Fischer DF, van Leeuwen FW (2003) Neuronal expression of GFAP in patients with Alzheimer pathology and identification of novel GFAP splice forms. *Mol Psychiatry* **8**, 786–796.
[59] Wirz KTS, Bossers K, Stargardt A, Kamphuis W, Swaab DF, Hol EM, Verhaagen J (2013) Cortical beta amyloid protein triggers an immune response, but no synaptic changes in the APPswe/PS1dE9 Alzheimer's disease mouse model. *Neurobiol Aging* **34**, 1328–1342.
[60] Lim Y-A, Giese M, Shepherd C, Halliday G, Kobayashi M, Takamatsu K, Staufenbiel M, Eckert A, Götz J (2012) Role of hippocalcin in mediating Aβ toxicity. *Biochim Biophys Acta* **1822**, 1247–1257.
[61] Jamieson SE, White JK, Howson JMM, Pask R, Smith AN, Brayne C, Evans JG, Xuereb J, Cairns NJ, Rubinsztein DC, Blackwell JM (2005) Candidate gene association study of solute carrier family 11a members 1 (SLC11A1) and 2 (SLC11A2) genes in Alzheimer's disease. *Neurosci Lett* **374**, 124–128.
[62] Matthes F, Hettich MM, Schilling J, Flores-Dominguez D, Blank N, Wiglenda T, Buntru A, Wolf H, Weber S, Vorberg I, Dagane A, Dittmar G, Wanker E, Ehninger D, Krauss S (2018) Inhibition of the MID1 protein complex: a novel approach targeting APP protein synthesis. *Cell Death Discov* **4**, 4.
[63] Reynolds CH, Garwood CJ, Wray S, Price C, Kellie S, Perera T, Zvelebil M, Yang A, Sheppard PW, Varndell IM, Hanger DP, Anderton BH (2008) Phosphorylation regulates tau interactions with Src homology 3 domains of phosphatidylinositol 3-kinase, phospholipase Cgamma1, Grb2, and Src family kinases. *J Biol Chem* **283**, 18177–18186.
[64] Seward ME, Swanson E, Norambuena A, Reimann A, Cochran JN, Li R, Roberson ED, Bloom GS (2013) Amyloid-β signals through tau to drive ectopic neuronal cell cycle re-entry in Alzheimer's disease. *J Cell Sci* **126**, 1278–1286.
[65] López González I, Garcia-Esparcia P, Llorens F, Ferrer I (2016) Genetic and Transcriptomic Profiles of Inflammation in Neurodegenerative Diseases: Alzheimer, Parkinson, Creutzfeldt-Jakob and Tauopathies. *Int J Mol Sci* **17**, 206.
[66] Diederich K, Sevimli S, Dörr H, Kösters E, Hoppen M, Lewejohann L, Klocke R, Minnerup J, Knecht S, Nikol S, Sachser N, Schneider A, Gorji A, Sommer C, Schäbitz W-R (2009) The role of granulocyte-colony stimulating factor (G-CSF) in the healthy brain: a characterization of G-CSF-deficient mice. *J Neurosci* **29**, 11572–11581.
[67] Rah W-J, Lee Y-H, Moon J-H, Jun H-J, Kang H-R, Koh H, Eom HJ, Lee JY, Lee YJ, Kim JY, Choi Y-Y, Park K, Kim MJ, Kim S-H (2017) Neuroregenerative potential of intravenous G-CSF and autologous peripheral blood stem cells in children with cerebral palsy: a randomized, double-blind, cross-over study. *J Transl Med* **15**, 1–9.
[68] Song S, Kong X, Acosta S, Sava V, Borlongan C, Sanchez-Ramos J (2016) Granulocyte-colony stimulating factor promotes brain repair following traumatic brain injury by recruitment of microglia and increasing neurotrophic factor expression. *Restor Neurol Neurosci* **34**, 415–431.
[69] Martiskainen H, Viswanathan J, Nykänen N-P, Kurki M, Helisalmi S, Natunen T, Sarajärvi T, Kurkinen KMA, Pursiheimo J-P, Rauramaa T, Alafuzoff I, Jääskeläinen JE, Leinonen V, Soininen H, Haapasalo A, Huttunen HJ, Hiltunen M (2015) Transcriptomics and mechanistic elucidation of Alzheimer's disease risk genes in the brain and in vitro models. *Neurobiol Aging* **36**, 1221.e15–28.
[70] Darcy MJ, Jin S-X, Feig LA (2014) R-Ras contributes to LTP and contextual discrimination. *Neuroscience* **277**, 334–342.

[71] Heneka MT, Reyes-Irisarri E, Hüll M, Kummer MP (2011) Impact and Therapeutic Potential of PPARs in Alzheimer's Disease. *Curr Neuropharmacol* **9**, 643–650.
[72] de la Monte SM, Wands JR (2006) Molecular indices of oxidative stress and mitochondrial dysfunction occur early and often progress with severity of Alzheimer's disease. *J Alzheimers Dis* **9**, 167–181.
[73] Malinin NL, Wright S, Seubert P, Schenk D, Griswold-Prenner I (2005) Amyloid-beta neurotoxicity is mediated by FISH adapter protein and ADAM12 metalloprotease activity. *Proc Natl Acad Sci U S A* **102**, 3058–3063.
[74] Ranganathan S, Noyes NC, Migliorini M, Winkles JA, Battey FD, Hyman BT, Smith E, Yepes M, Mikhailenko I, Strickland DK (2011) LRAD3, a novel low-density lipoprotein receptor family member that modulates amyloid precursor protein trafficking. *J Neurosci* **31**, 10836–10846.
[75] Kolev MV, Tediose T, Sivasankar B, Harris CL, Thome J, Morgan BP, Donev RM (2010) Upregulating CD59: a new strategy for protection of neurons from complement-mediated degeneration. *Pharmacogenomics J* **10**, 12–19.
[76] Yang LB, Li R, Meri S, Rogers J, Shen Y (2000) Deficiency of complement defense protein CD59 may contribute to neurodegeneration in Alzheimer's disease. *J Neurosci* **20**, 7505–7509.
[77] Baglietto-Vargas D, Moreno-Gonzalez I, Sanchez-Varo R, Jimenez S, Trujillo-Estrada L, Sanchez-Mejias E, Torres M, Romero-Acebal M, Ruano D, Vizuete M, Vitorica J, Gutierrez A (2010) Calretinin interneurons are early targets of extracellular amyloid-beta pathology in PS1/AbetaPP Alzheimer mice hippocampus. *J Alzheimers Dis* **21**, 119–132.
[78] Pastorino L, Ma SL, Balastik M, Huang P, Pandya D, Nicholson L, Lu KP (2012) Alzheimer's disease-related loss of Pin1 function influences the intracellular localization and the processing of AβPP. *J Alzheimers Dis* **30**, 277–297.
[79] Wang S, Simon BP, Bennett DA, Schneider JA, Malter JS, Wang D-S (2007) The significance of Pin1 in the development of Alzheimer's disease. *J Alzheimers Dis* **11**, 13–23.
[80] Pastorino L, Sun A, Lu P-J, Zhou XZ, Balastik M, Finn G, Wulf G, Lim J, Li S-H, Li X, Xia W, Nicholson LK, Lu KP (2006) The prolyl isomerase Pin1 regulates amyloid precursor protein processing and amyloid-beta production. *Nature* **440**, 528–534.
[81] Pascual-Lucas M, Viana da Silva S, Di Scala M, Garcia-Barroso C, González-Aseguinolaza G, Mulle C, Alberini CM, Cuadrado-Tejedor M, Garcia-Osta A (2014) Insulin-like growth factor 2 reverses memory and synaptic deficits in APP transgenic mice. *EMBO Mol Med* **6**, 1246–1262.
[82] Xie K, Liu Y, Hao W, Walter S, Penke B, Hartmann T, Schachner M, Fassbender K (2013) Tenascin-C deficiency ameliorates Alzheimer's disease-related pathology in mice. *Neurobiol Aging* **34**, 2389–2398.
[83] Stewart CR, Stuart LM, Wilkinson K, van Gils JM, Deng J, Halle A, Rayner KJ, Boyer L, Zhong R, Frazier WA, Lacy-Hulbert A, El Khoury J, Golenbock DT, Moore KJ (2010) CD36 ligands promote sterile inflammation through assembly of a Toll-like receptor 4 and 6 heterodimer. *Nat Immunol* **11**, 155–161.
[84] Mahaman YAR, Huang F, Kessete Afewerky H, Maibouge TMS, Ghose B, Wang X (2019) Involvement of calpain in the neuropathogenesis of Alzheimer's disease. *Med Res Rev* **39**, 608–630.
[85] Ferreira A (2012) Calpain dysregulation in Alzheimer's disease. *ISRN Biochem* **2012**, 728571.
[86] Castro-Alvarez JF, Uribe-Arias SA, Kosik KS, Cardona-Gómez GP (2014) Long- and short-term CDK5 knockdown prevents spatial memory dysfunction and tau pathology

of triple transgenic Alzheimer's mice. *Front Aging Neurosci* **6**, 243.
[87] Zheng Y-L, Kesavapany S, Gravell M, Hamilton RS, Schubert M, Amin N, Albers W, Grant P, Pant HC (2005) A Cdk5 inhibitory peptide reduces tau hyperphosphorylation and apoptosis in neurons. *EMBO J* **24**, 209–220.
[88] Liu F, Su Y, Li B, Zhou Y, Ryder J, Gonzalez-DeWhitt P, May PC, Ni B (2003) Regulation of amyloid precursor protein (APP) phosphorylation and processing by p35/Cdk5 and p25/Cdk5. *FEBS Lett* **547**, 193–196.
[89] Lopes JP, Oliveira CR, Agostinho P (2009) Cdk5 acts as a mediator of neuronal cell cycle re-entry triggered by amyloid-beta and prion peptides. *Cell Cycle* **8**, 97–104.
[90] Li H, Ruberu K, Muñoz SS, Jenner AM, Spiro A, Zhao H, Rassart E, Sanchez D, Ganfornina MD, Karl T, Garner B (2015) Apolipoprotein D modulates amyloid pathology in APP/PS1 Alzheimer's disease mice. *Neurobiol Aging* **36**, 1820–1833.
[91] Martínez E, Navarro A, Ordóñez C, Del Valle E, Tolivia J (2012) Amyloid-β25-35 induces apolipoprotein D Synthesis and growth arrest in HT22 hippocampal cells. *J Alzheimers Dis* **30**, 233–244.
[92] Lee S-J, Seo B-R, Koh J-Y (2015) Metallothionein-3 modulates the amyloid β endocytosis of astrocytes through its effects on actin polymerization. *Mol Brain* **8**, 84.
[93] Manso Y, Carrasco J, Comes G, Meloni G, Adlard PA, Bush AI, Vašák M, Hidalgo J (2012) Characterization of the role of metallothionein-3 in an animal model of Alzheimer's disease. *Cell Mol Life Sci* **69**, 3683–3700.
[94] Balasubramaniam M, Ayyadevara S, Shmookler Reis RJ (2018) Structural insights into pro-aggregation effects of C. elegans CRAM-1 and its human ortholog SERF2. *Sci Rep* **8**, 14891.
[95] van Ham TJ, Holmberg MA, van der Goot AT, Teuling E, Garcia-Arencibia M, Kim H-E, Du D, Thijssen KL, Wiersma M, Burggraaff R, van Bergeijk P, van Rheenen J, Jerre van Veluw G, Hofstra RMW, Rubinsztein DC, Nollen EAA (2010) Identification of MOAG-4/SERF as a regulator of age-related proteotoxicity. *Cell* **142**, 601–612.
[96] Ashby EL, Kehoe PG, Love S (2010) Kallikrein-related peptidase 6 in Alzheimer's disease and vascular dementia. *Brain Res* **1363**, 1–10.
[97] Diamandis EP, Yousef GM, Petraki C, Soosaipillai AR (2000) Human kallikrein 6 as a biomarker of alzheimer's disease. *Clin Biochem* **33**, 663–667.
[98] Kumar U (2005) Expression of somatostatin receptor subtypes (SSTR1-5) in Alzheimer's disease brain: an immunohistochemical analysis. *Neuroscience* **134**, 525–538.
[99] Davies P, Katzman R, Terry RD (1980) Reduced somatostatin-like immunoreactivity in cerebral cortex from cases of Alzheimer disease and Alzheimer senile dementa. *Nature* **288**, 279–280.
[100] Pan Y, Choy KHC, Marriott PJ, Chai SY, Scanlon MJ, Porter CJH, Short JL, Nicolazzo JA (2018) Reduced blood-brain barrier expression of fatty acid-binding protein 5 is associated with increased vulnerability of APP/PS1 mice to cognitive deficits from low omega-3 fatty acid diets. *J Neurochem* **144**, 81–92.
[101] Pan Y, Short JL, Choy KHC, Zeng AX, Marriott PJ, Owada Y, Scanlon MJ, Porter CJH, Nicolazzo JA (2016) Fatty Acid-Binding Protein 5 at the Blood-Brain Barrier Regulates Endogenous Brain Docosahexaenoic Acid Levels and Cognitive Function. *J Neurosci* **36**, 11755–11767.
[102] Nakanishi N, Ryan SD, Zhang X, Khan A, Holland T, Cho E-G, Huang X, Liao F-F, Xu H, Lipton SA, Tu S (2013) Synaptic protein α1-takusan mitigates amyloid-β-induced synaptic loss via interaction with tau and postsynaptic density-95 at postsynaptic sites. *J Neurosci* **33**, 14170–14183.
[103] Tu S, Shin Y, Zago WM, States BA, Eroshkin A, Lipton SA, Tong GG, Nakanishi N

(2007) Takusan: a large gene family that regulates synaptic activity. *Neuron* **55**, 69–85.

[104] Giannuzzi G, Siswara P, Malig M, Marques-Bonet T, NISC Comparative Sequencing Program, Mullikin JC, Ventura M, Eichler EE (2013) Evolutionary dynamism of the primate LRRC37 gene family. *Genome Res* **23**, 46–59.

[105] Jun G, Ibrahim-Verbaas CA, Vronskaya M, Lambert J-C, Chung J, Naj AC, Kunkle BW, Wang L-S, Bis JC, Bellenguez C, Harold D, Lunetta KL, Destefano AL, Grenier-Boley B, Sims R, Beecham GW, Smith AV, Chouraki V, Hamilton-Nelson KL, Ikram MA, Fievet N, Denning N, Martin ER, Schmidt H, Kamatani Y, Dunstan ML, Valladares O, Laza AR, Zelenika D, Ramirez A, Foroud TM, Choi S-H, Boland A, Becker T, Kukull WA, van der Lee SJ, Pasquier F, Cruchaga C, Beekly D, Fitzpatrick AL, Hanon O, Gill M, Barber R, Gudnason V, Campion D, Love S, Bennett DA, Amin N, Berr C, Tsolaki M, Buxbaum JD, Lopez OL, Deramecourt V, Fox NC, Cantwell LB, Tárraga L, Dufouil C, Hardy J, Crane PK, Eiriksdottir G, Hannequin D, Clarke R, Evans D, Mosley TH Jr, Letenneur L, Brayne C, Maier W, De Jager P, Emilsson V, Dartigues J-F, Hampel H, Kamboh MI, de Bruijn RFAG, Tzourio C, Pastor P, Larson EB, Rotter JI, O'Donovan MC, Montine TJ, Nalls MA, Mead S, Reiman EM, Jonsson PV, Holmes C, St George-Hyslop PH, Boada M, Passmore P, Wendland JR, Schmidt R, Morgan K, Winslow AR, Powell JF, Carasquillo M, Younkin SG, Jakobsdóttir J, Kauwe JSK, Wilhelmsen KC, Rujescu D, Nöthen MM, Hofman A, Jones L, IGAP Consortium, Haines JL, Psaty BM, Van Broeckhoven C, Holmans P, Launer LJ, Mayeux R, Lathrop M, Goate AM, Escott-Price V, Seshadri S, Pericak-Vance MA, Amouyel P, Williams J, van Duijn CM, Schellenberg GD, Farrer LA (2016) A novel Alzheimer disease locus located near the gene encoding tau protein. *Mol Psychiatry* **21**, 108–117.

[106] Chang S-H, Hwang C-S, Yin J-H, Chen S-D, Yang D-I (2015) Oncostatin M-dependent Mcl-1 induction mediated by JAK1/2-STAT1/3 and CREB contributes to bioenergetic improvements and protective effects against mitochondrial dysfunction in cortical neurons. *Biochim Biophys Acta* **1853**, 2306–2325.

[107] Kraft AW, Hu X, Yoon H, Yan P, Xiao Q, Wang Y, Gil SC, Brown J, Wilhelmsson U, Restivo JL, Cirrito JR, Holtzman DM, Kim J, Pekny M, Lee J-M (2013) Attenuating astrocyte activation accelerates plaque pathogenesis in APP/PS1 mice. *FASEB J* **27**, 187–198.

[108] Richter F, Meurers BH, Zhu C, Medvedeva VP, Chesselet M-F (2009) Neurons express hemoglobin alpha- and beta-chains in rat and human brains. *J Comp Neurol* **515**, 538–547.

[109] Wu C-W, Liao P-C, Yu L, Wang S-T, Chen S-T, Wu C-M, Kuo Y-M (2004) Hemoglobin promotes Abeta oligomer formation and localizes in neurons and amyloid deposits. *Neurobiol Dis* **17**, 367–377.

[110] Oyama R, Yamamoto H, Titani K (2000) Glutamine synthetase, hemoglobin alpha-chain, and macrophage migration inhibitory factor binding to amyloid beta-protein: their identification in rat brain by a novel affinity chromatography and in Alzheimer's disease brain by immunoprecipitation. *Biochim Biophys Acta* **1479**, 91–102.

[111] Ullrich S, Münch A, Neumann S, Kremmer E, Tatzelt J, Lichtenthaler SF (2010) The novel membrane protein TMEM59 modulates complex glycosylation, cell surface expression, and secretion of the amyloid precursor protein. *J Biol Chem* **285**, 20664–20674.

[112] Liu Z, Ning J, Zheng X, Meng J, Han L, Zheng H, Zhong L, Chen X-F, Zhang X, Luo H, Can D, Xu H, Zhang Y-W (2020) TMEM59 interacts with TREM2 and modulates TREM2-dependent microglial activities. *Cell Death Dis* **11**, 678.

[113] Burgos PV, Mardones GA, Rojas AL, daSilva LLP, Prabhu Y, Hurley JH, Bonifacino JS (2010) Sorting of the Alzheimer's disease amyloid precursor protein mediated by the AP-4 complex. *Dev Cell* **18**, 425–436.
[114] Terrey M, Adamson SI, Gibson AL, Deng T, Ishimura R, Chuang JH, Ackerman SL (2020) GTPBP1 resolves paused ribosomes to maintain neuronal homeostasis. *Elife* **9**,.
[115] Kapur M, Ganguly A, Nagy G, Adamson SI, Chuang JH, Frankel WN, Ackerman SL (2020) Expression of the Neuronal tRNA n-Tr20 Regulates Synaptic Transmission and Seizure Susceptibility. *Neuron* **108**, 193–208.e9.
[116] Das Sharma S, Metz JB, Li H, Hobson BD, Hornstein N, Sulzer D, Tang G, Sims PA (2019) Widespread Alterations in Translation Elongation in the Brain of Juvenile Fmr1 Knockout Mice. *Cell Rep* **26**, 3313–3322.e5.
[117] Hornstein N, Torres D, Das Sharma S, Tang G, Canoll P, Sims PA (2016) Ligation-free ribosome profiling of cell type-specific translation in the brain. *Genome Biol* **17**, 149.
[118] Wang Y, Cella M, Mallinson K, Ulrich JD, Young KL, Robinette ML, Gilfillan S, Krishnan GM, Sudhakar S, Zinselmeyer BH, Holtzman DM, Cirrito JR, Colonna M (2015) TREM2 lipid sensing sustains the microglial response in an Alzheimer's disease model. *Cell* **160**, 1061–1071.
[119] Wang Y, Ulland TK, Ulrich JD, Song W, Tzaferis JA, Hole JT, Yuan P, Mahan TE, Shi Y, Gilfillan S, Cella M, Grutzendler J, DeMattos RB, Cirrito JR, Holtzman DM, Colonna M (2016) TREM2-mediated early microglial response limits diffusion and toxicity of amyloid plaques. *J Exp Med* **213**, 667–675.
[120] Yuan P, Condello C, Keene CD, Wang Y, Bird TD, Paul SM, Luo W, Colonna M, Baddeley D, Grutzendler J (2016) TREM2 Haplodeficiency in Mice and Humans Impairs the Microglia Barrier Function Leading to Decreased Amyloid Compaction and Severe Axonal Dystrophy. *Neuron* **90**, 724–739.
[121] Konishi H, Kiyama H (2018) Microglial TREM2/DAP12 Signaling: A Double-Edged Sword in Neural Diseases. *Frontiers in Cellular Neuroscience* **12**,.
[122] Ulland TK, Song WM, Huang SC-C, Ulrich JD, Sergushichev A, Beatty WL, Loboda AA, Zhou Y, Cairns NJ, Kambal A, Loginicheva E, Gilfillan S, Cella M, Virgin HW, Unanue ER, Wang Y, Artyomov MN, Holtzman DM, Colonna M (2017) TREM2 Maintains Microglial Metabolic Fitness in Alzheimer's Disease. *Cell* **170**, 649–663.e13.
[123] Ryu JK, Rafalski VA, Meyer-Franke A, Adams RA, Poda SB, Rios Coronado PE, Pedersen LØ, Menon V, Baeten KM, Sikorski SL, Bedard C, Hanspers K, Bardehle S, Mendiola AS, Davalos D, Machado MR, Chan JP, Plastira I, Petersen MA, Pfaff SJ, Ang KK, Hallenbeck KK, Syme C, Hakozaki H, Ellisman MH, Swanson RA, Zamvil SS, Arkin MR, Zorn SH, Pico AR, Mucke L, Freedman SB, Stavenhagen JB, Nelson RB, Akassoglou K (2018) Fibrin-targeting immunotherapy protects against neuroinflammation and neurodegeneration. *Nat Immunol* **19**, 1212–1223.
[124] Lee CYD, Daggett A, Gu X, Jiang L-L, Langfelder P, Li X, Wang N, Zhao Y, Park CS, Cooper Y, Ferando I, Mody I, Coppola G, Xu H, Yang XW (2018) Elevated TREM2 Gene Dosage Reprograms Microglia Responsivity and Ameliorates Pathological Phenotypes in Alzheimer's Disease Models. *Neuron* **97**, 1032–1048.e5.

Supplementary Figures

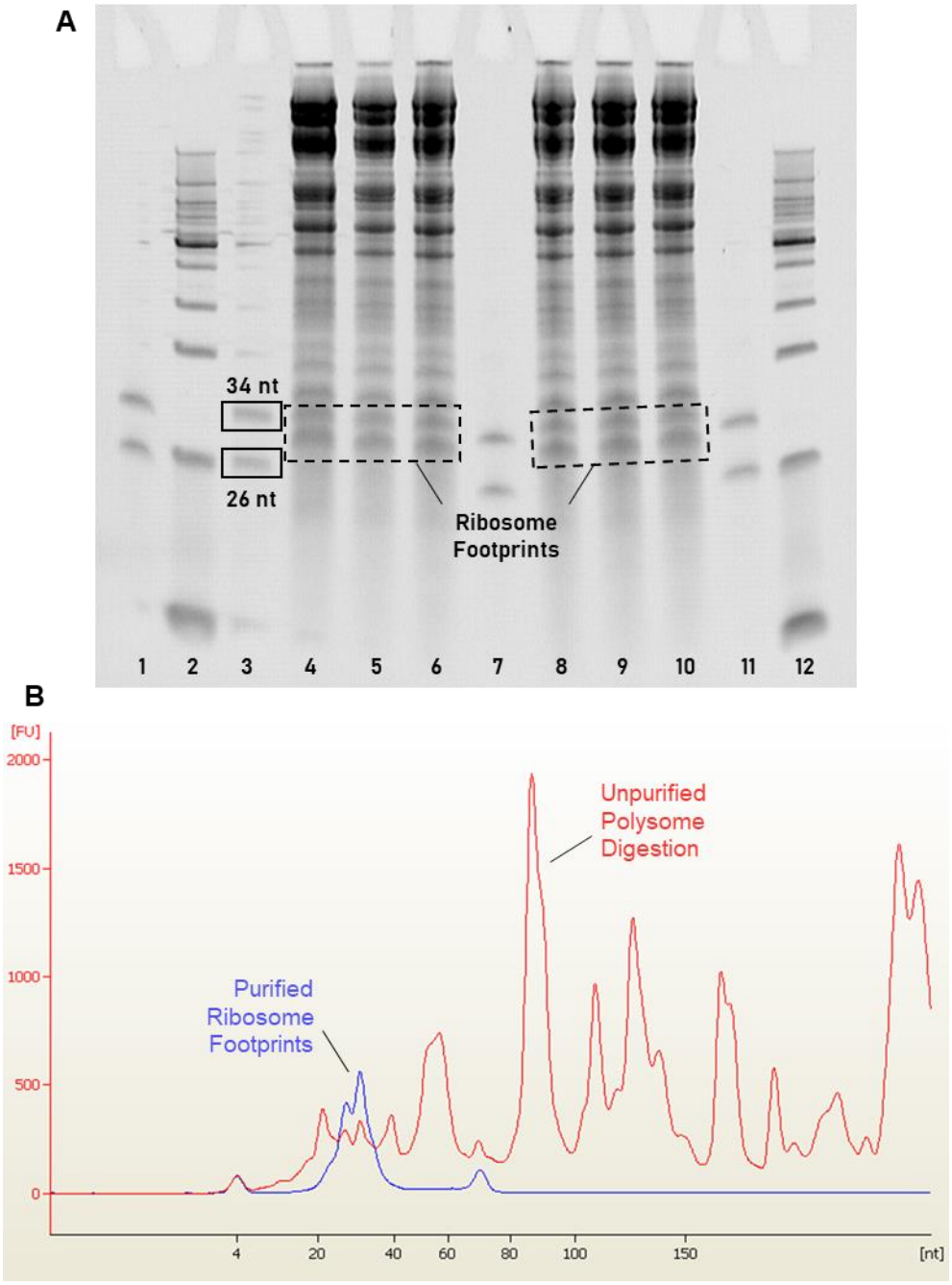

Figure S1

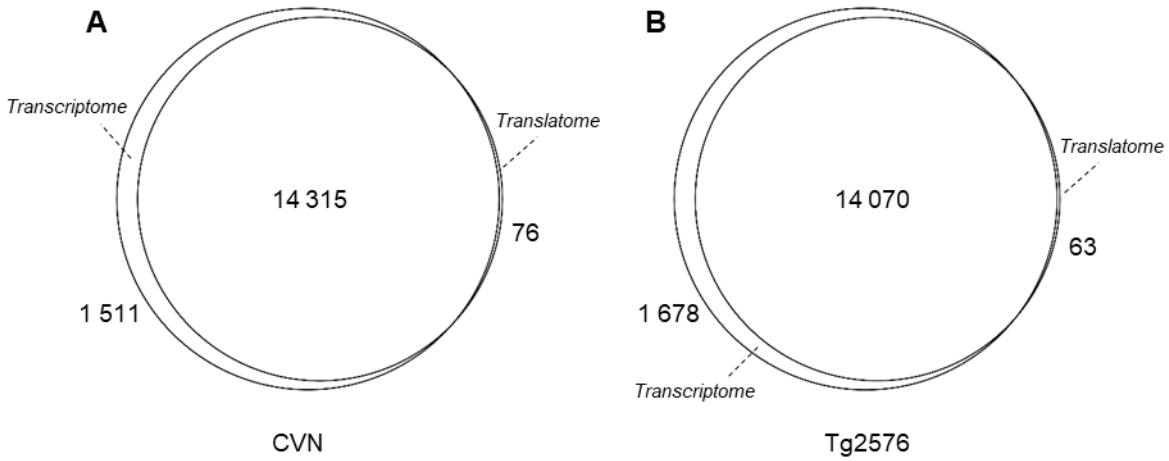
A
Transcriptome
Translatome
14 315
76
1 511
CVN
B
Translatome
14 070
63
1 678
Transcriptome
Tg2576

Figure S2

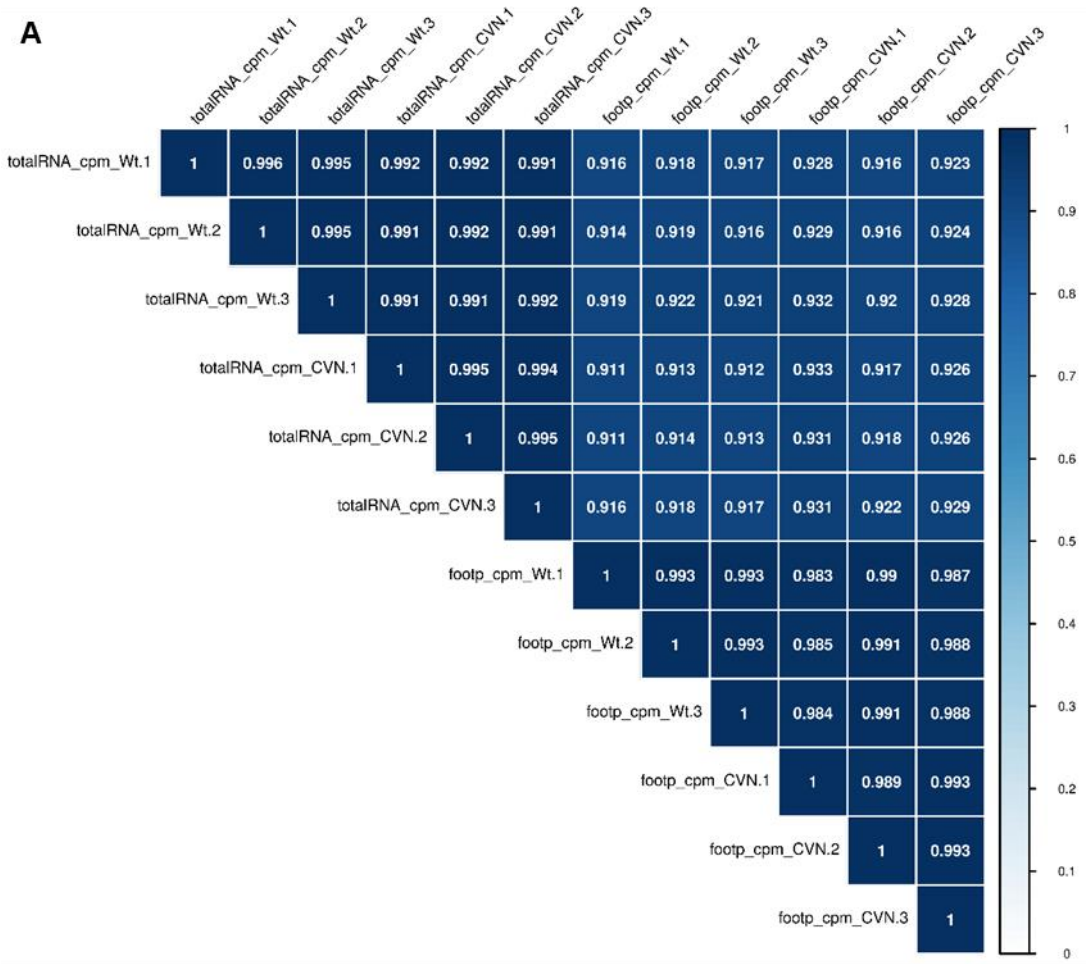
A
totalRNA_cpm_Wt.1
totalRNA_cpm_Wt.2
totalRNA_cpm_Wt.3
totalRNA_cpm_CVN.1
totalRNA_cpm_CVN.2
totalRNA_cpm_CVN.3
footp_cpm_Wt.1
footp_cpm_Wt.2
footp_cpm_Wt.3
footp_cpm_CVN.1
footp_cpm_CVN.2
footp_cpm_CVN.3
1 0.996 0.995 0.992 0.992 0.991 0.916 0.918 0.917 0.928 0.916 0.923
1 0.995 0.991 0.992 0.991 0.914 0.919 0.916 0.929 0.916 0.924
1 0.991 0.991 0.992 0.919 0.922 0.921 0.932 0.92 0.928
1 0.995 0.994 0.911 0.913 0.912 0.933 0.917 0.926
1 0.995 0.911 0.914 0.913 0.931 0.918 0.926
1 0.916 0.918 0.917 0.931 0.922 0.929
1 0.993 0.993 0.983 0.99 0.987
1 0.993 0.985 0.991 0.988
1 0.984 0.991 0.988
1 0.989 0.993
1 0.993
1
1
0.9
0.8
0.7
0.6
0.5
0.4
0.3
0.2
0.1
0

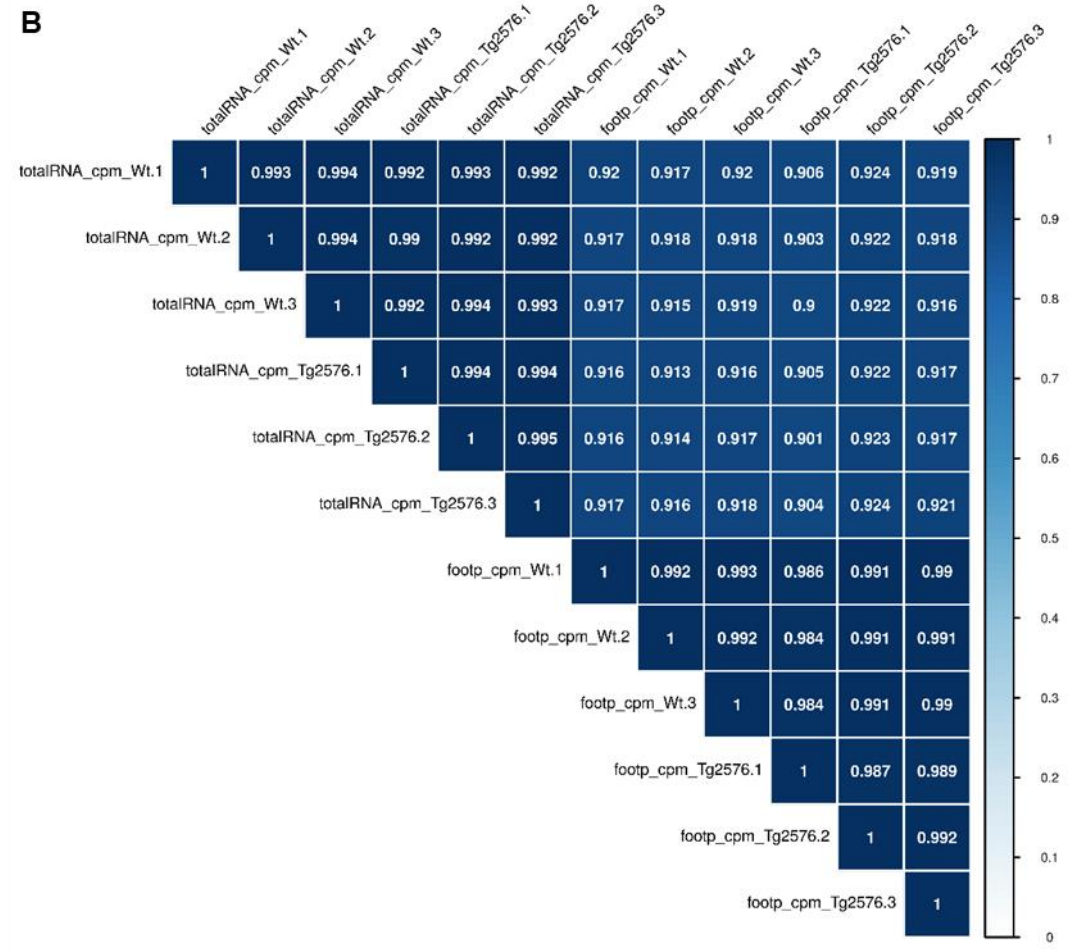
B
totalRNA_cpm_Wt.1
totalRNA_cpm_Wt.2
totalRNA_cpm_Wt.3
totalRNA_cpm_Tg2576.1
totalRNA_cpm_Tg2576.2
totalRNA_cpm_Tg2576.3
footp_cpm_Wt.1
footp_cpm_Wt.2
footp_cpm_Wt.3
footp_cpm_Tg2576.1
footp_cpm_Tg2576.2
footp_cpm_Tg2576.3
1 0.993 0.994 0.992 0.993 0.992 0.92 0.917 0.92 0.906 0.924 0.919
1 0.994 0.99 0.992 0.992 0.917 0.918 0.918 0.903 0.922 0.918
1 0.992 0.994 0.993 0.917 0.915 0.919 0.9 0.922 0.916
1 0.994 0.994 0.916 0.913 0.916 0.905 0.922 0.917
1 0.995 0.916 0.914 0.917 0.901 0.923 0.917
1 0.917 0.916 0.918 0.904 0.924 0.921
1 0.992 0.993 0.986 0.991 0.99
1 0.992 0.984 0.991 0.991
1 0.984 0.991 0.99
1 0.987 0.989
1 0.992
1
1
0.9
0.8
0.7
0.6
0.5
0.4
0.3
0.2
0.1
0

Figure S3

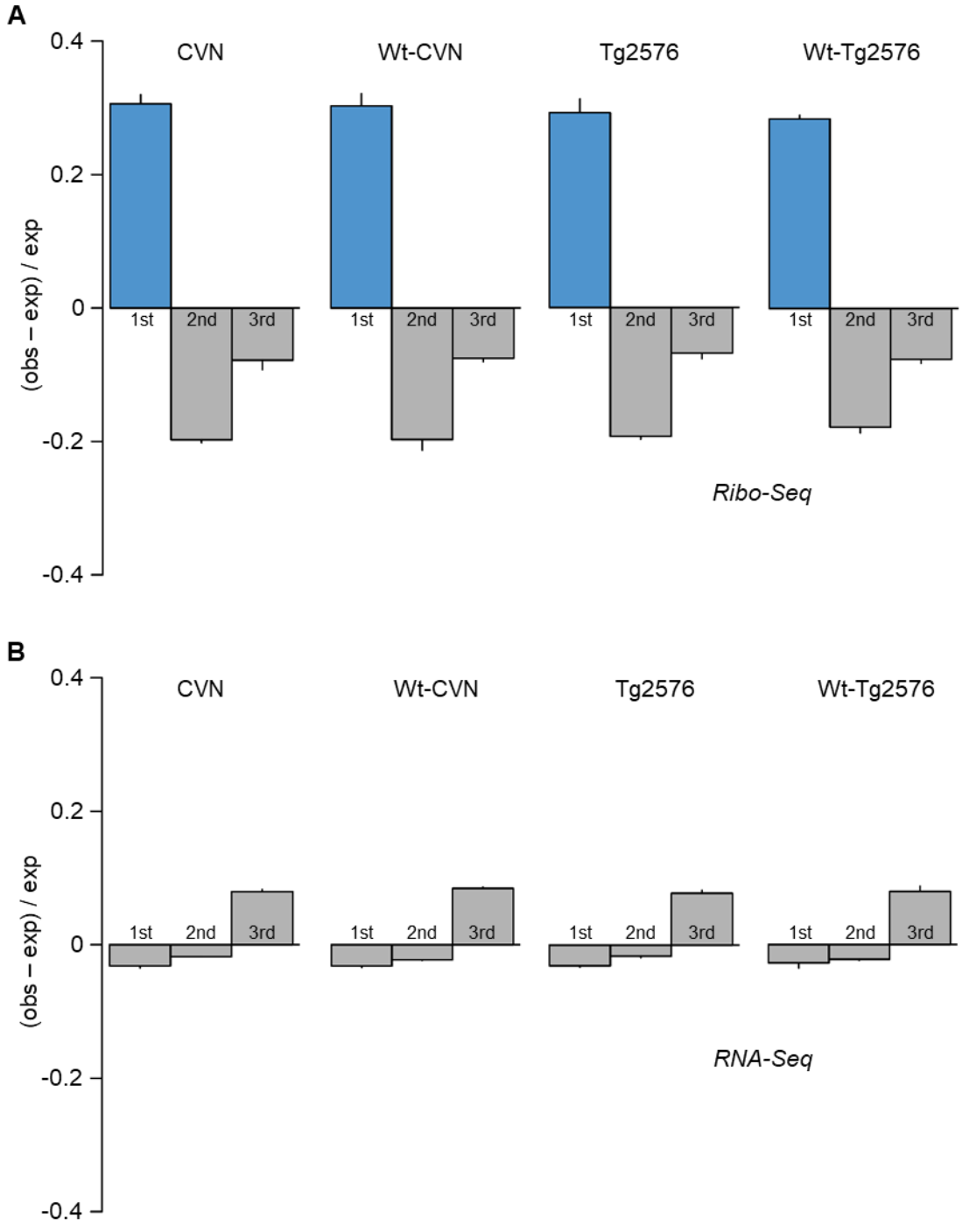
A
CVN
Wt-CVN
Tg2576
Wt-Tg2576
0.4
0.2
0
-0.2
-0.4
(obs – exp) / exp
1st
2nd
3rd
Ribo-Seq
B
CVN
Wt-CVN
Tg2576
Wt-Tg2576
0.4
0.2
0
-0.2
-0.4
(obs – exp) / exp
1st
2nd
3rd
RNA-Seq

Figure S4

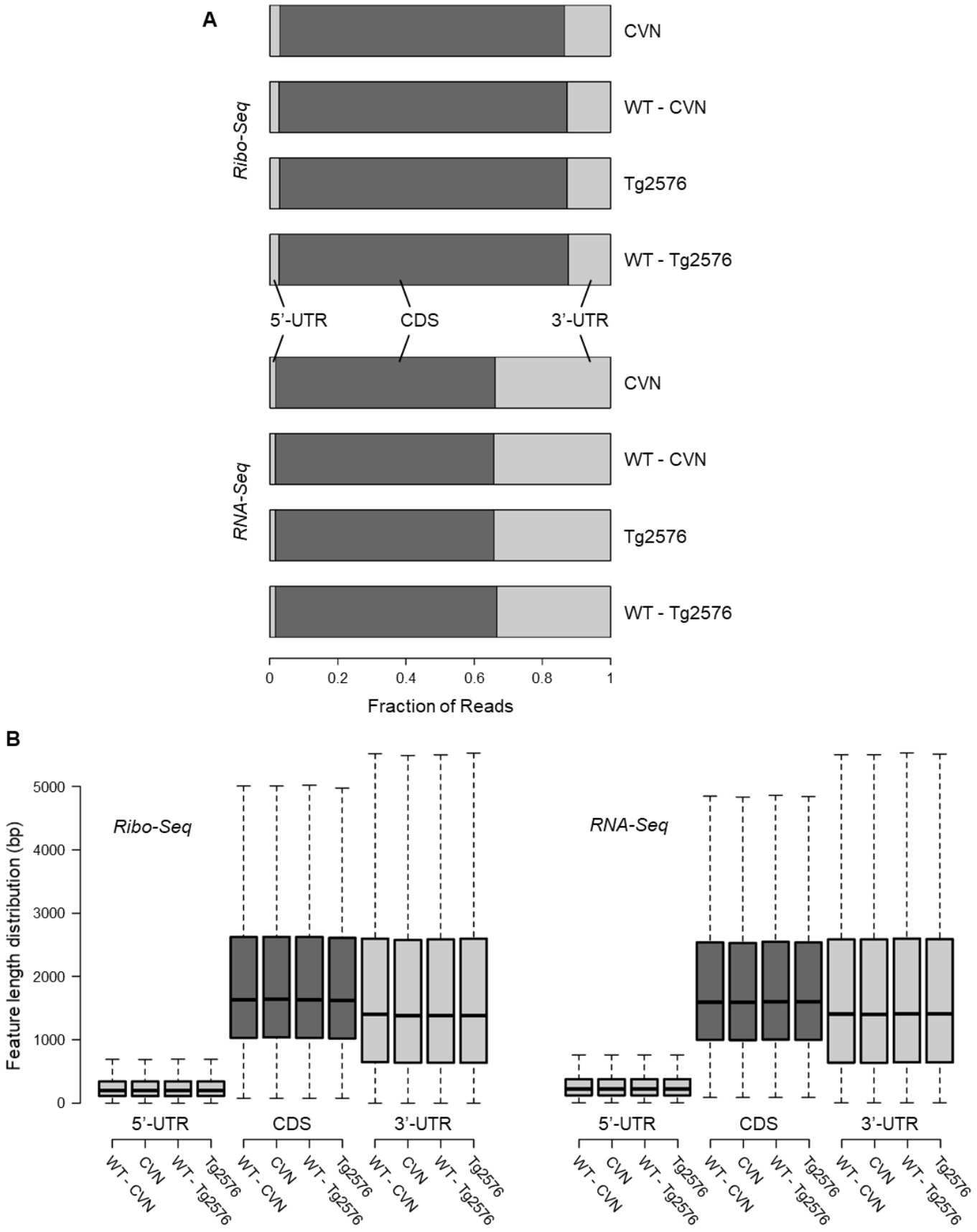
A
Ribo-Seq
CVN
WT - CVN
Tg2576
WT - Tg2576
5'-UTR
CDS
3'-UTR
RNA-Seq
CVN
WT - CVN
Tg2576
WT - Tg2576
0
0.2
0.4
0.6
0.8
1
Fraction of Reads
B
Feature length distribution (bp)
5000
4000
3000
2000
1000
0
Ribo-Seq
RNA-Seq
5'-UTR
CDS
3'-UTR
WT - CVN
CVN
WT - Tg2576
Tg2576

Figure S5

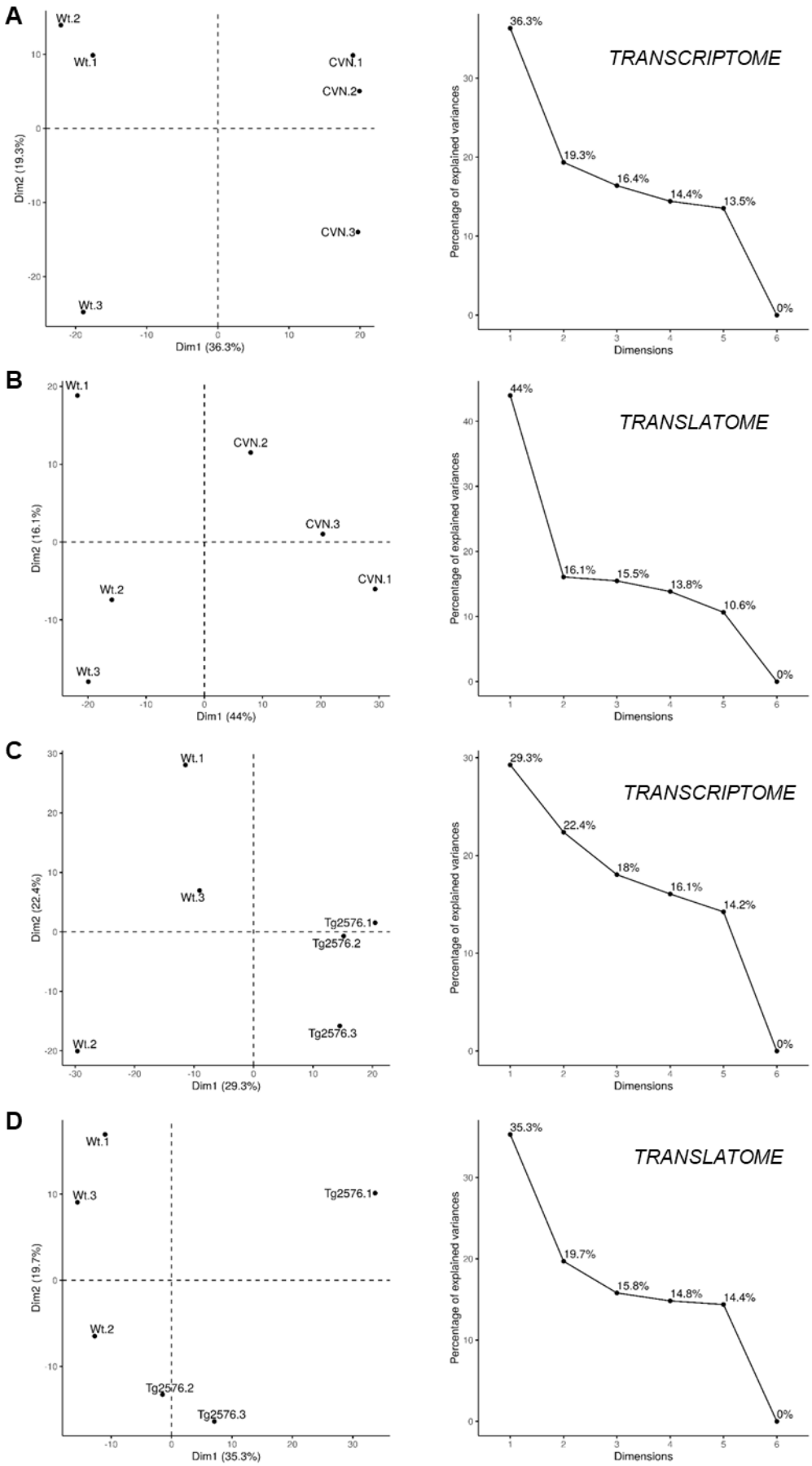
A
Wt.2
Wt.1
CVN.1
CVN.2
CVN.3
Wt.3
Dim2 (19.3%)
Dim1 (36.3%)
TRANSCRIPTOME
36.3%
19.3%
16.4%
14.4%
13.5%
0%
Percentage of explained variances
Dimensions
B
Wt.1
CVN.2
CVN.3
CVN.1
Wt.2
Wt.3
Dim2 (16.1%)
Dim1 (44%)
TRANSLATOME
44%
16.1%
15.5%
13.8%
10.6%
0%
Percentage of explained variances
Dimensions
C
Wt.1
Wt.3
Tg2576.1
Tg2576.2
Tg2576.3
Wt.2
Dim2 (22.4%)
Dim1 (29.3%)
TRANSCRIPTOME
29.3%
22.4%
18%
16.1%
14.2%
0%
Percentage of explained variances
Dimensions
D
Wt.1
Wt.3
Tg2576.1
Wt.2
Tg2576.2
Tg2576.3
Dim2 (19.7%)
Dim1 (35.3%)
TRANSLATOME
35.3%
19.7%
15.8%
14.8%
14.4%
0%
Percentage of explained variances
Dimensions

Figure S6

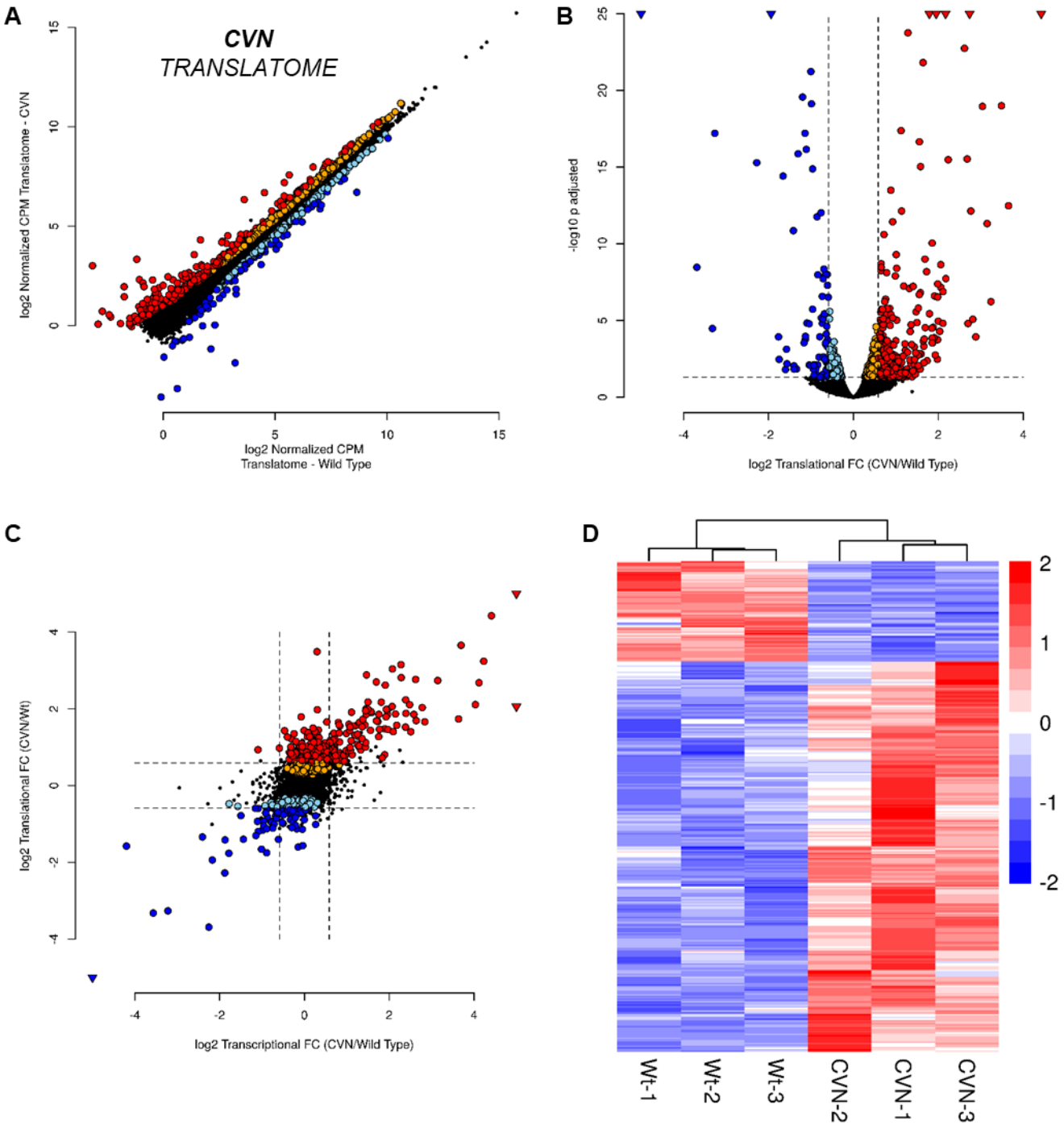
A
CVN
TRANSLATOME
log2 Normalized CPM Translatome - CVN
log2 Normalized CPM
Translatome - Wild Type
B
-log10 p adjusted
log2 Translational FC (CVN/Wild Type)
C
log2 Translational FC (CVN/Wt)
log2 Transcriptional FC (CVN/Wild Type)
D
Wt-1
Wt-2
Wt-3
CVN-2
CVN-1
CVN-3

Figure S7

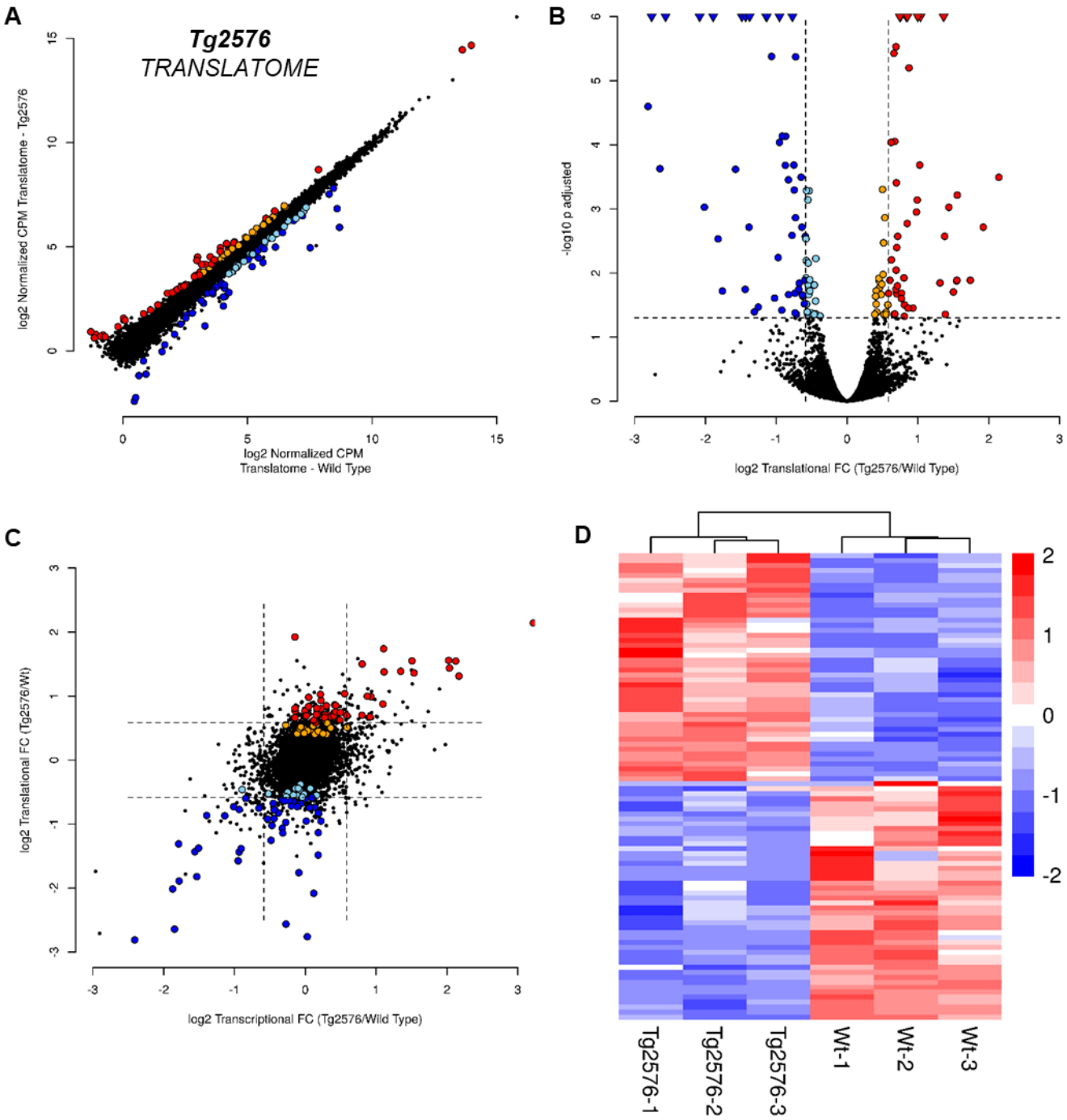
A
Tg2576
TRANSLATOME
log2 Normalized CPM Translatome - Tg2576
log2 Normalized CPM
Translatome - Wild Type
B
-log10 p adjusted
log2 Translational FC (Tg2576/Wild Type)
C
log2 Translational FC (Tg2576/Wt)
log2 Transcriptional FC (Tg2576/Wild Type)
D
Tg2576-1
Tg2576-2
Tg2576-3
Wt-1
Wt-2
Wt-3

Figure S8

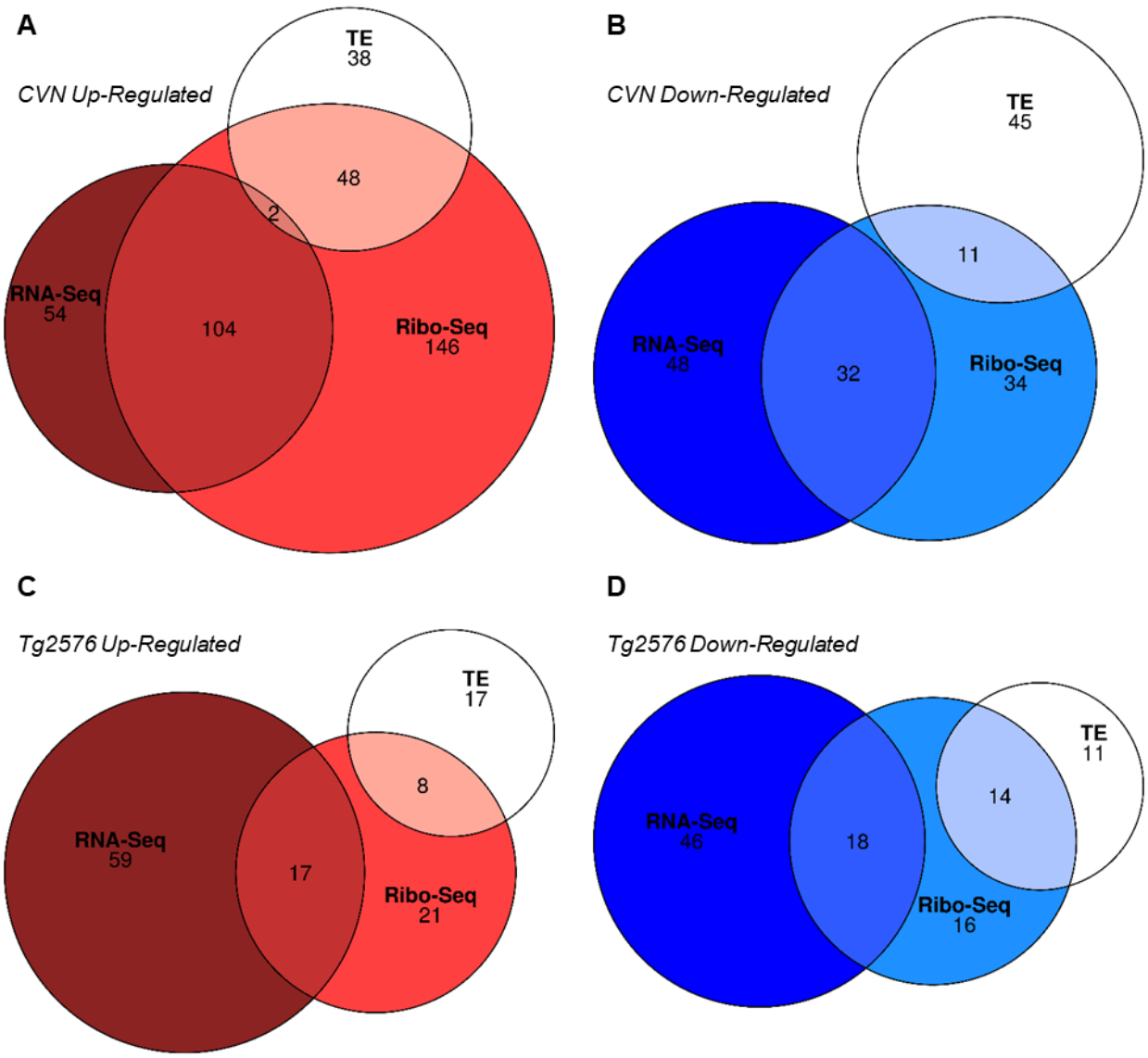
A
CVN Up-Regulated
TE
38
48
2
RNA-Seq
54
104
Ribo-Seq
146
B
CVN Down-Regulated
TE
45
11
RNA-Seq
48
32
Ribo-Seq
34
C
Tg2576 Up-Regulated
TE
17
8
RNA-Seq
59
17
Ribo-Seq
21
D
Tg2576 Down-Regulated
TE
11
14
RNA-Seq
46
18
Ribo-Seq
16

Figure S9

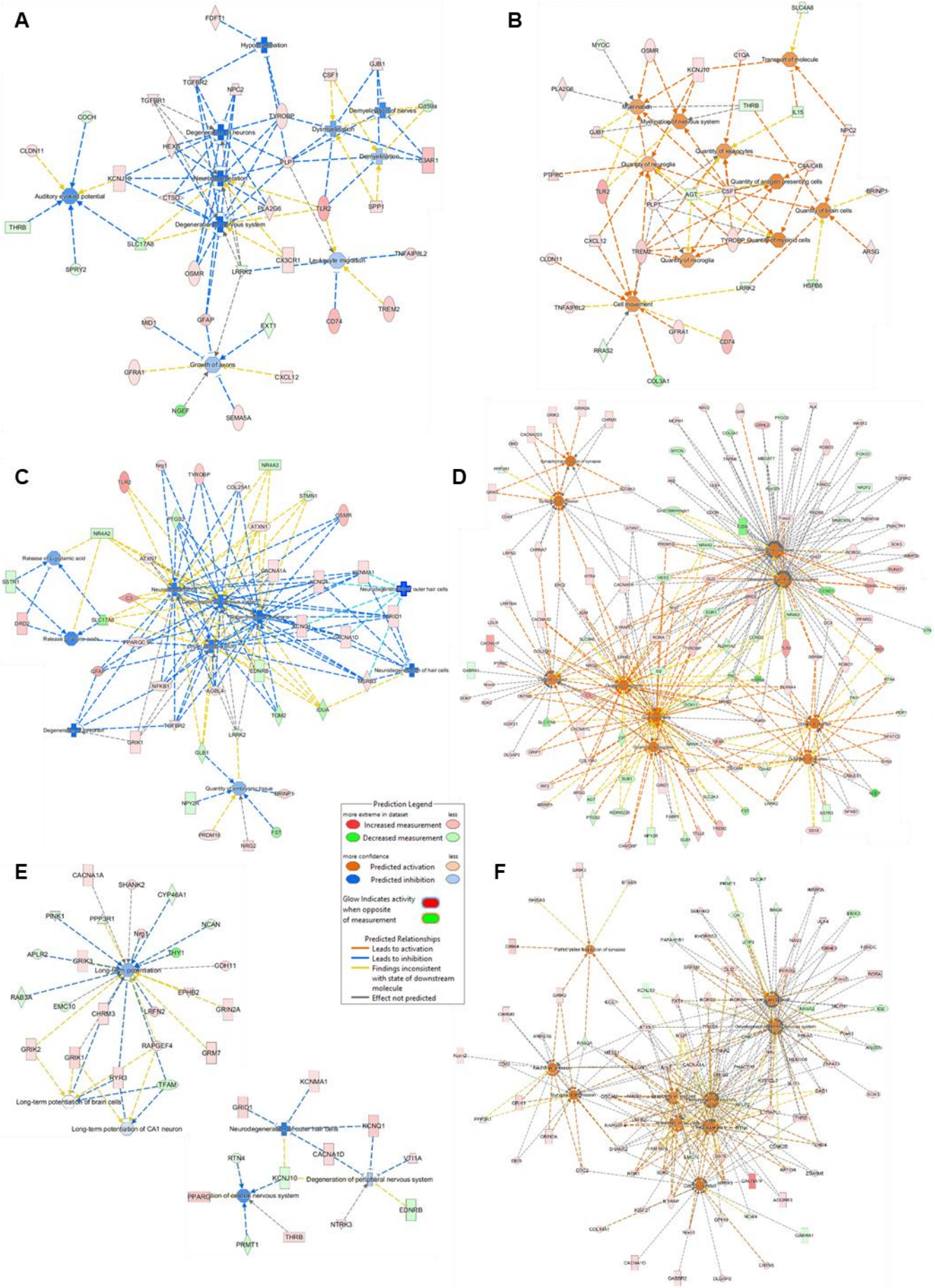
A
B
C
D
E
F
Prediction Legend
more extreme in dataset
less
Increased measurement
Decreased measurement
more confidence
less
Predicted activation
Predicted inhibition
Glow Indicates activity when opposite of measurement
Predicted Relationships
Leads to activation
Leads to inhibition
Findings inconsistent with state of downstream molecule
Effect not predicted

Figure S10

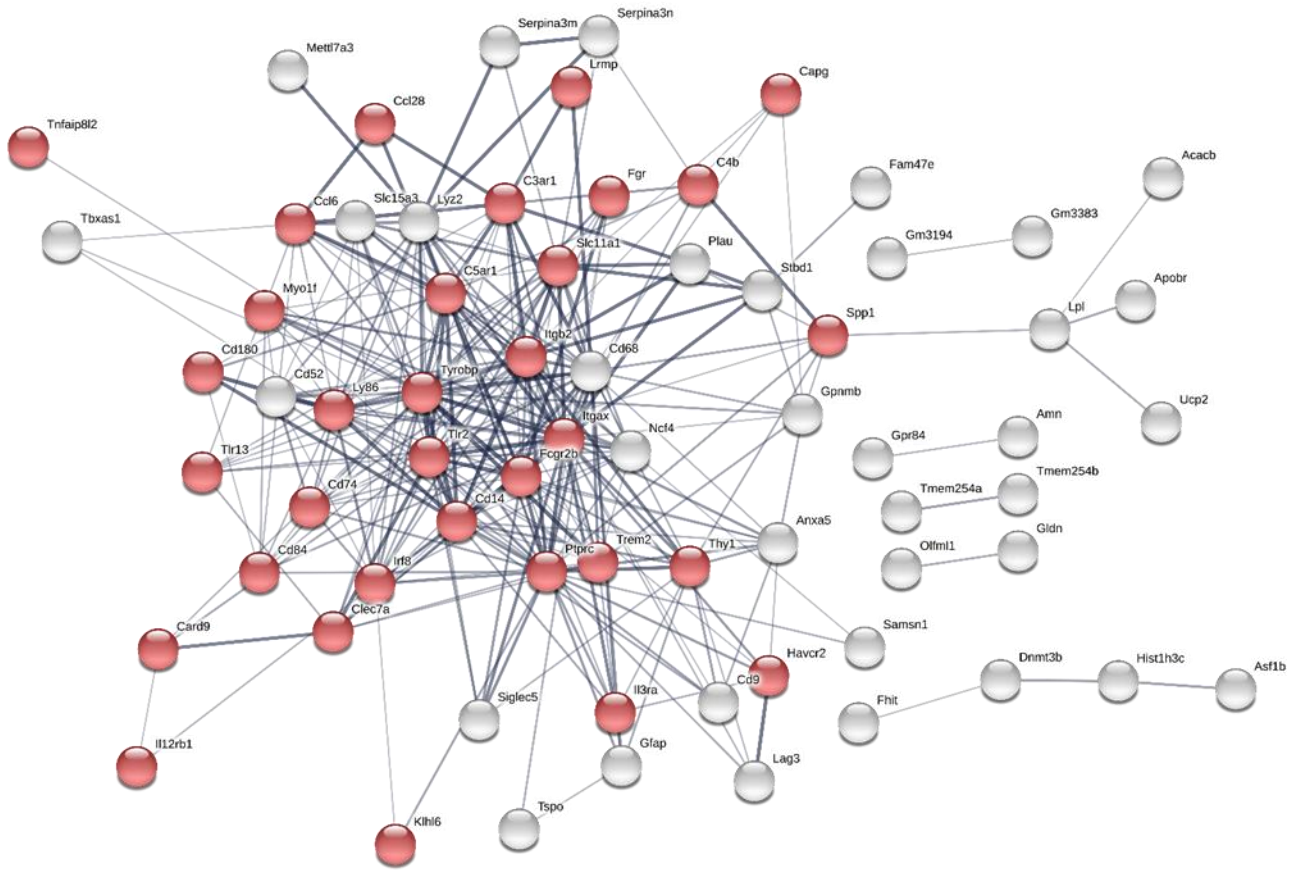
Serpina3m
Serpina3n
Mettl7a3
Lrmp
Capg
Ccl28
Tnfaip8l2
C4b
Fam47e
Acacb
C3ar1
Fgr
Ccl6
Slc15a3
Lyz2
Tbxas1
Gm3383
Gm3194
Slc11a1
Plau
Stbd1
C5ar1
Apobr
Myo1f
Lpl
Spp1
Itgb2
Cd68
Cd180
Cd52
Tyrobp
Ly86
Gpnmb
Ucp2
Itgax
Amn
Ncf4
Tlr2
Gpr84
Tlr13
Fcgr2b
Tmem254b
Tmem254a
Cd74
Cd14
Anxa5
Gldn
Olfml1
Cd84
Ptprc
Trem2
Thy1
Irf8
Clec7a
Samsn1
Card9
Havcr2
Dnmt3b
Hist1h3c
Asf1b
Cd9
Siglec5
Il3ra
Fhit
Il12rb1
Gfap
Lag3
Tspo
Klhl6

Figure S11

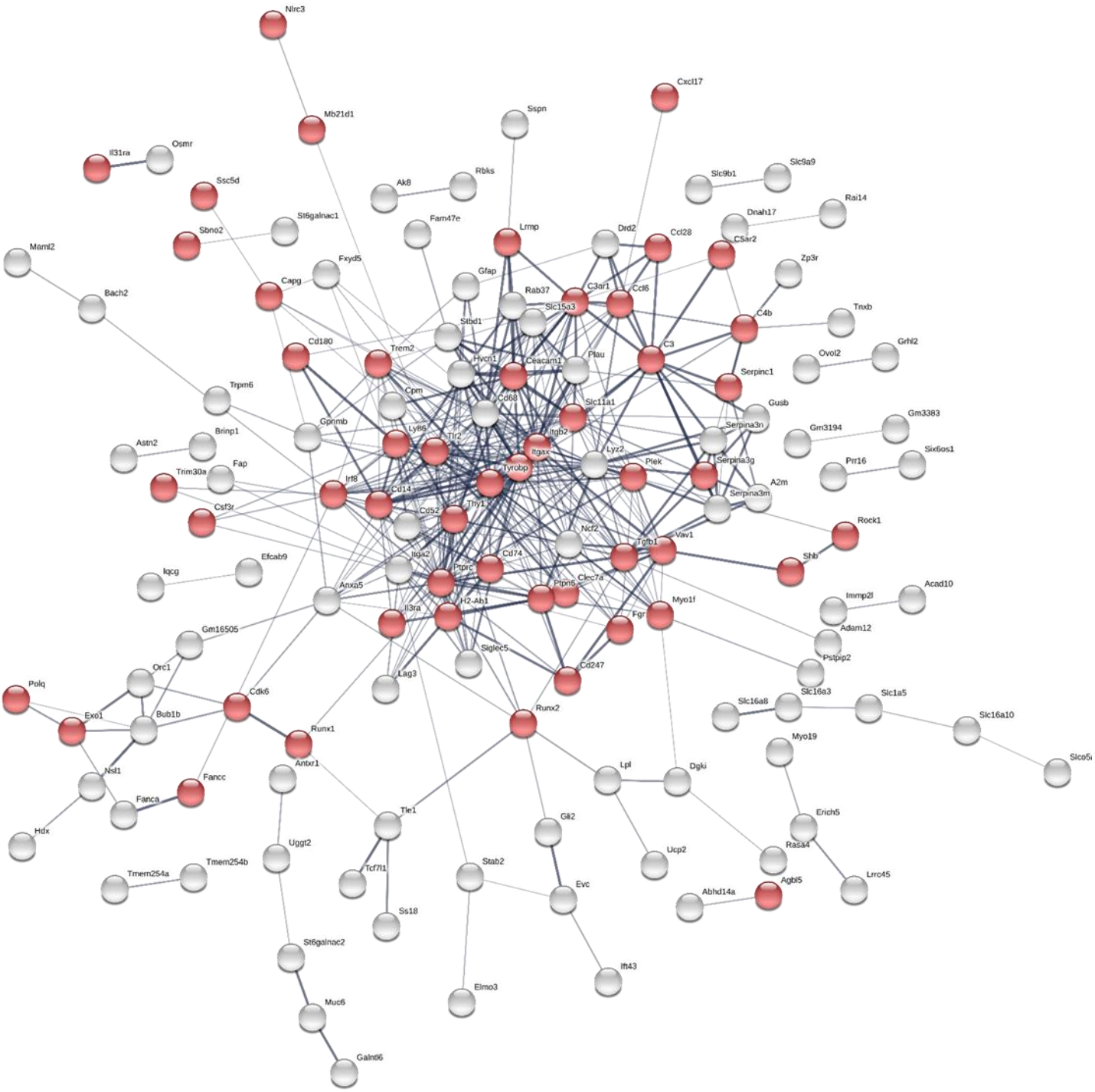
Nlrc3
Mb21d1
Cxcl17
Sspn
Il31ra
Osmr
Ssc5d
Ak8
Rbks
Slc9b1
Slc9a9
Rai14
Dnah17
St6galnac1
Sbno2
Fam47e
Lrmp
Drd2
Ccl28
Csrr2
Zp3r
Maml2
Fxyd5
Gfap
Capg
Rab37
C3ar1
Ccl6
Bach2
Slc15a3
Tnxb
C4b
Sibd1
Cd180
Trem2
Hvcn1
Ceacam1
Plau
C3
Ovol2
Grhl2
Serpinc1
Trpm6
Cpm
Cd68
Slc11a1
Gusb
Gpnmb
Ly86
Tlr2
Itgb2
Serpina3n
Gm3383
Gm3194
Brinp1
Astn2
Itgax
Lyz2
Six6os1
Trim30a
Fap
Tyrobp
Plek
Serpina3g
Prr16
Irf8
Cd14
Thy1
A2m
Serpina3m
Csf3r
Cd52
Ncf2
Rock1
Vav1
Tgfb1
Efcab9
Itga2
Cd74
Shb
Iqcg
Ptprc
Anxa5
Ptpn6
Clec7a
Acad10
Myo1f
Il3ra
H2-Ab1
Fgr
Immp2l
Gm16505
Adam12
Orc1
Siglec5
Pstpip2
Cd247
Lag3
Polq
Cdk6
Runx2
Slc16a8
Slc16a3
Slc1a5
Slc16a10
Exo1
Bub1b
Runx1
Myo19
Antxr1
Lpl
Dgki
Nsl1
Fancc
Fanca
Erich5
Tle1
Gli2
Rasa4
Hdx
Uggt2
Ucp2
Tcf7l1
Stab2
Lrrc45
Tmem254a
Tmem254b
Evc
Agbl5
Abhd14a
Ss18
St6galnac2
Ift43
Elmo3
Muc6
Galnt6

Figure S12

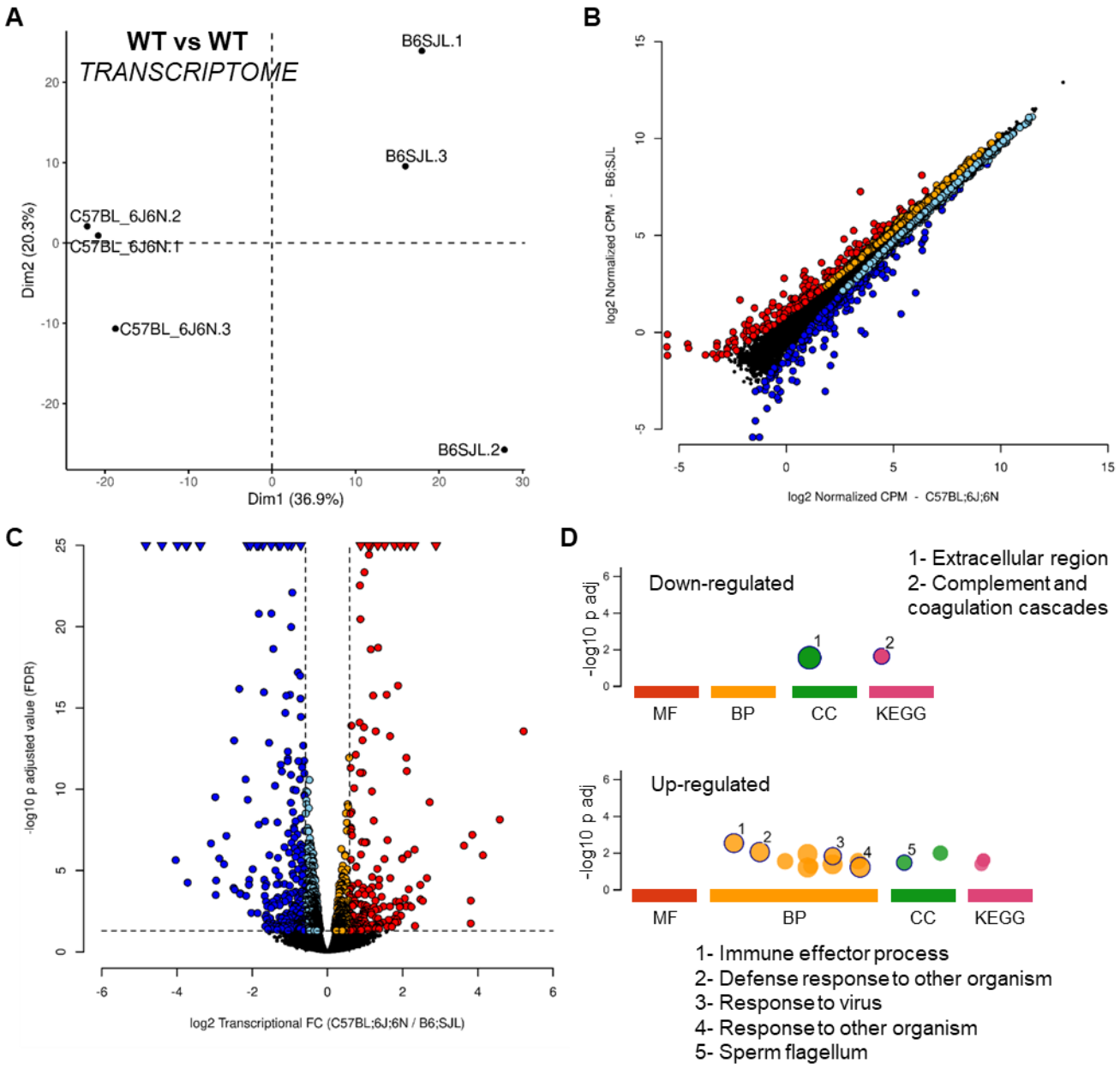
A
WT vs WT
TRANSCRIPTOME
B6SJL.1
B6SJL.3
C57BL_6J6N.2
C57BL_6J6N.1
C57BL_6J6N.3
B6SJL.2
Dim2 (20.3%)
Dim1 (36.9%)
B
log2 Normalized CPM - B6;SJL
log2 Normalized CPM - C57BL;6J;6N
C
-log10 p adjusted value (FDR)
log2 Transcriptional FC (C57BL;6J;6N / B6;SJL)
D
Down-regulated
-log10 p adj
MF
BP
CC
KEGG
1- Extracellular region
2- Complement and coagulation cascades
Up-regulated
1- Immune effector process
2- Defense response to other organism
3- Response to virus
4- Response to other organism
5- Sperm flagellum

Figure S13

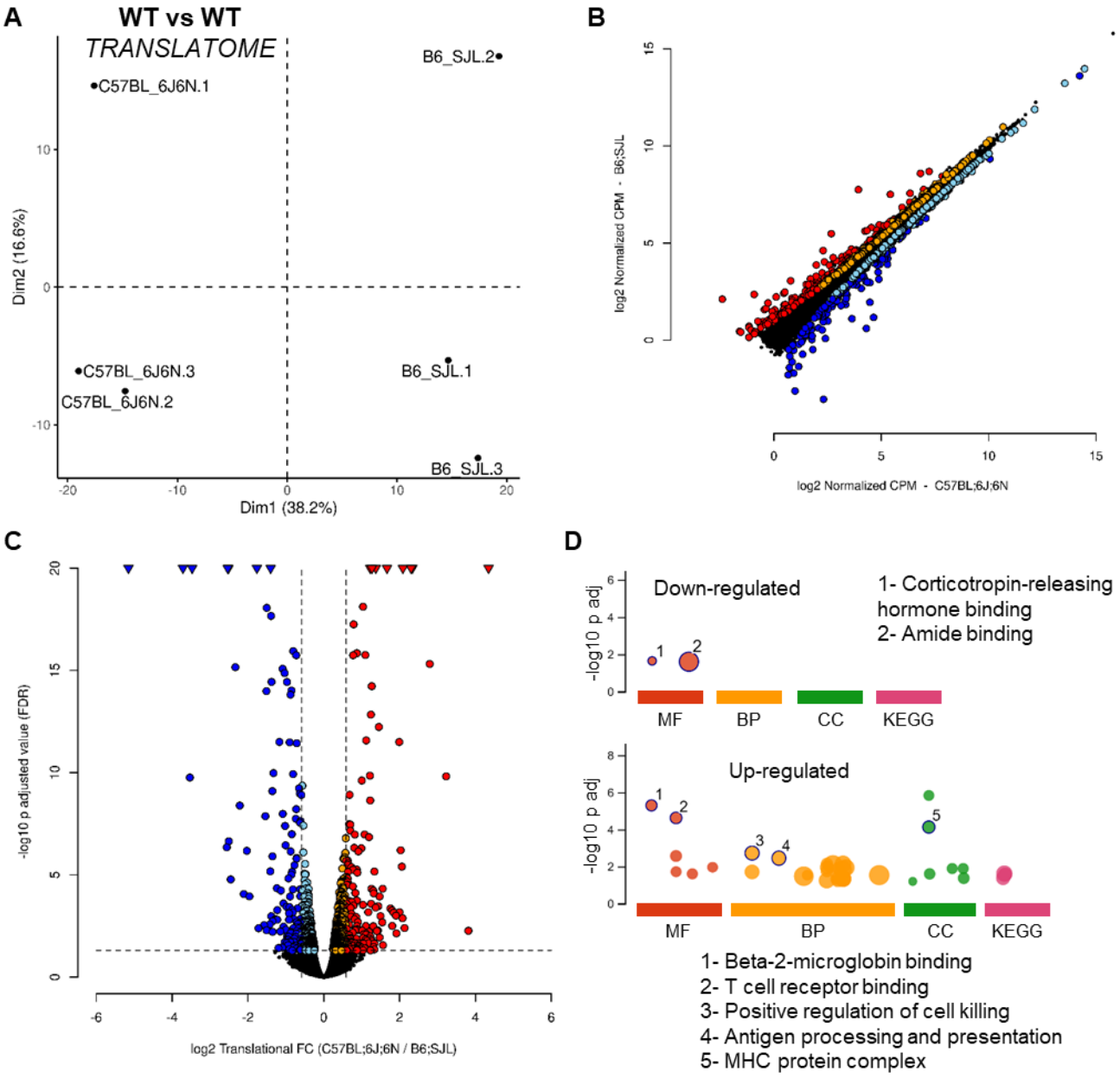
A
WT vs WT
TRANSLATOME
B6_SJL.2
C57BL_6J6N.1
C57BL_6J6N.3
C57BL_6J6N.2
B6_SJL.1
B6_SJL.3
Dim2 (16.6%)
Dim1 (38.2%)
B
log2 Normalized CPM - B6;SJL
log2 Normalized CPM - C57BL;6J;6N
C
-log10 p adjusted value (FDR)
log2 Translational FC (C57BL;6J;6N / B6;SJL)
D
Down-regulated
1- Corticotropin-releasing hormone binding
2- Amide binding
-log10 p adj
MF
BP
CC
KEGG
Up-regulated
1- Beta-2-microglobin binding
2- T cell receptor binding
3- Positive regulation of cell killing
4- Antigen processing and presentation
5- MHC protein complex

Figure S14

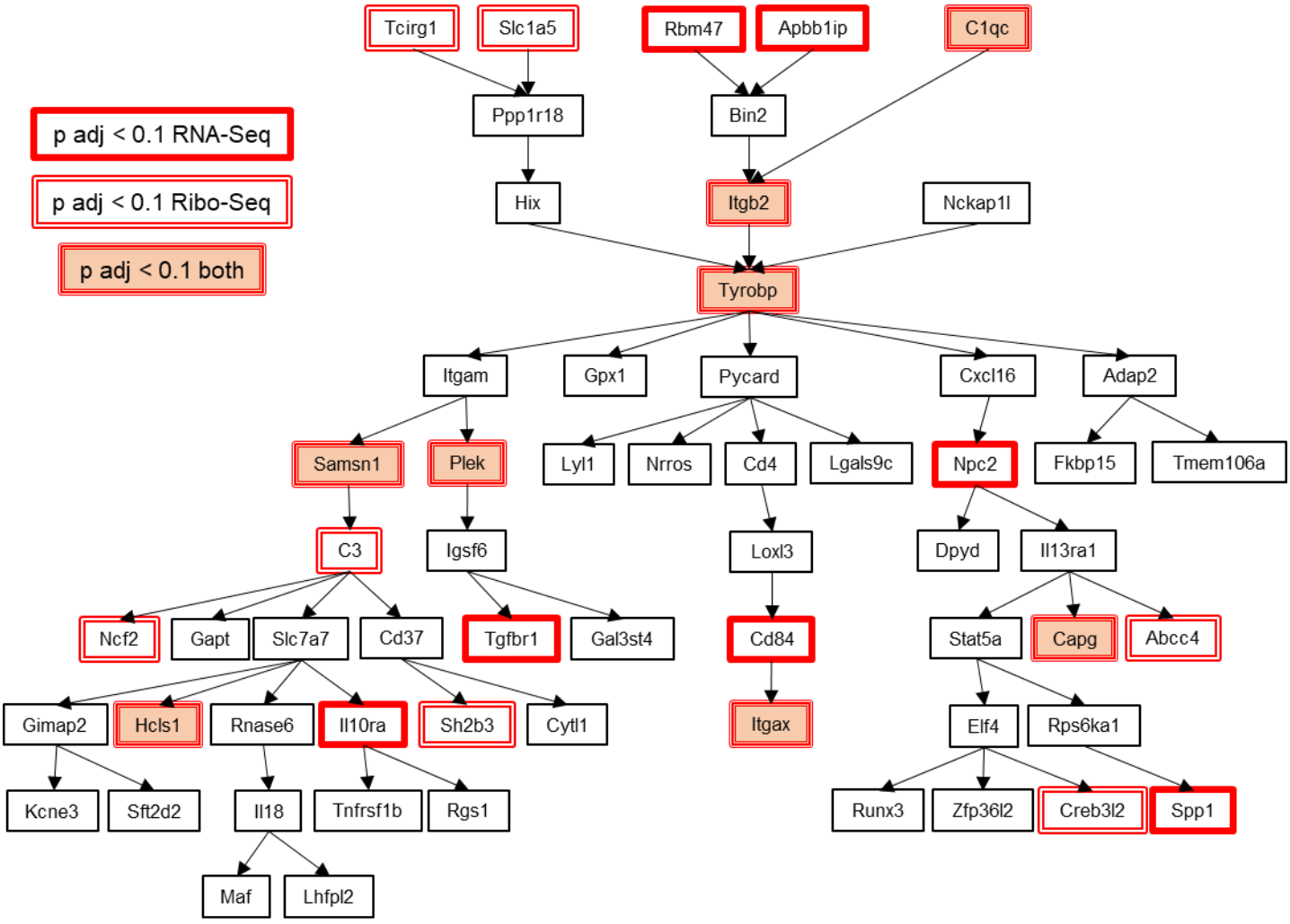
p adj < 0.1 RNA-Seq
p adj < 0.1 Ribo-Seq
p adj < 0.1 both
Tcirg1
Slc1a5
Rbm47
Apbb1ip
C1qc
Ppp1r18
Bin2
Hix
Itgb2
Nckap1l
Tyrobp
Itgam
Gpx1
Pycard
Cxcl16
Adap2
Samsn1
Plek
Lyl1
Nrros
Cd4
Lgals9c
Npc2
Fkbp15
Tmem106a
C3
Igsf6
Loxl3
Dpyd
Il13ra1
Ncf2
Gapt
Slc7a7
Cd37
Tgfbr1
Gal3st4
Cd84
Stat5a
Capg
Abcc4
Gimap2
Hcls1
Rnase6
Il10ra
Sh2b3
Cytl1
Itgax
Elf4
Rps6ka1
Kcne3
Sft2d2
Il18
Tnfrsf1b
Rgs1
Runx3
Zfp36l2
Creb3l2
Spp1
Maf
Lhfpl2

Figure S15

VII. CONCLUSIONES

En la presente tesis nos planteamos como objetivo general contribuir a comprender tanto los mecanismos, como los distintos eventos de regulación de la expresión génica que ocurren a nivel traduccional en modelos neuronales. Para esto, utilizamos principalmente enfoques genómicos y técnicas de secuenciación masiva, como RNA-Seq y Ribo-Seq, sobre diversos sustratos biológicos del tipo neuronal y en diversos contextos. Los resultados obtenidos en la presente tesis nos permiten concluir lo siguiente:

1. La técnica de Ribo-Seq es una valiosa herramienta para el estudio del compartimento traduccional y de los eventos de regulación que en este ocurren. Pudimos optimizar el uso de la misma sobre diversos sustratos biológicos, del tipo neuronal, como: células *in vitro*, cultivos *in vitro* de neuronas embrionarias primarias y tejido nervioso derivado de animales.

2. En todos los casos fuimos capaces de detectar niveles confiables de expresión génica a nivel traduccional para cerca de 10.000 genes. Las huellas ribosomales producidas cumplieron con los controles de calidad esperados: mapeo preferencial sobre regiones codificantes versus regiones no codificantes y periodicidad de mapeo.

3. El factor proteico PDCD4 es capaz de regular la traducción de un conjunto específico de mensajeros (blancos traduccionales) en modelos neuronales. El reporte del conjunto de 267 ARNm blancos traduccionales de PDCD4 es el segundo a la fecha obtenido mediante aproximaciones genómicas y el primero en modelos neuronales.

4. Dentro de los blancos traduccionales reportados se reconoce una firma génica asociada al crecimiento neurítico y/o axonal. Se destaca, por su función biológica sobre el crecimiento neurítico, la regulación que ejerce PDCD4 sobre NFKB2. Dicha regulación fue comprobada mediante técnicas ortogonales como Western blot y cuantificación de ARNm en fracciones polisomales.

5. La elección de la enzima a utilizar en el ensayo de digestión del protocolo de Ribo-Seq es un aspecto relevante. La comparativa entre las enzimas Benzonasa y RNAsa I arrojó algunas diferencias, como esperábamos. De todas maneras, la identidad de los genes observados en el compartimiento traduccional definido por cada enzima es muy similar. En el análisis de expresión génica diferencial, pocos genes diferenciales

parecen estar exclusivamente asociados a una enzima en particular. Los grupos de genes definidos como exclusivamente detectados por una enzima, no superan los 200 miembros y no revelan funciones biológicas particularmente comprometidas, de hecho abundan los genes no codificantes y en particular especies pequeñas de ARN. Por lo tanto, ambas enzimas son adecuadas para la producción de huellas ribosomales y definen traductomas cuyos niveles de expresión son comparables.

6. Las huellas ribosomales producidas con las distintas enzimas difieren en su tamaño, patrones de periodicidad y mapeo, y distribución sobre las distintas regiones codificantes y no codificantes del ARNm. También se observaron diferencias en los fragmentos de ARNr producidos como contaminación y se pudo conocer la secuencia de dichos fragmentos a los efectos de diseñar oligos específicos para su sustracción en futuros experimentos.

7. Existen importantes eventos de regulación de la expresión génica, tanto a nivel transcripcional como traduccional, en la corteza cerebral de modelos murinos transgénicos del mal de Alzheimer, en etapas preferentemente asintomáticas. En particular, el modelo CVN es el que mayor nivel de regulación muestra a nivel traduccional y es completamente asintomático a la edad utilizada.

8. El análisis de las funciones representadas por los genes regulados muestra que, en particular para el modelo CVN, tanto a nivel transcripcional como traduccional, se inhiben procesos asociados a la neurodegeneración mientras que se favorecen procesos de tipo neuroprotector como la cantidad de células neuronales y neurogliales, la transmisión sináptica y la neuritogénesis, entre otros. A su vez, el modelo CVN muestra una firma génica regulada positivamente a nivel transcripcional y traduccional asociada a una subpoblación microglial que responde a la acumulación temprana de Aβ.

9. El análisis individual revela que ambos modelos regulan, tanto a nivel transcripcional como traduccional, la expresión de genes asociados al metabolismo de APP y Aβ, ya sea con funciones neurotóxicas o neuroprotectoras. La regulación temprana de estos procesos ocurre en modelos murinos donde la presencia de placas amiloides no ha sido descrita a la edad aquí utilizada. Además, se describe la regulación a nivel traduccional de estos procesos por primera vez en este tipo de modelos.

10. A pesar de que los dos modelos transgénicos utilizados derivan de distintas cepas de ratón, desarrollan la patología de maneras muy distintas y muestran distintos niveles de regulación en la expresión génica, se observan genes regulados en común entre ambos modelos. Aquí se destacan casos interesantes donde se observan genes asociados a funciones neuroprotectoras que responden a la presencia y acumulación de Aβ.

VIII. PERSPECTIVAS

Con respecto a las perspectivas derivadas de los experimentos realizados y los resultados obtenidos en la presente tesis, surgen principalmente perspectivas tanto a corto, como a mediano y largo plazo. Se presentan a continuación las perspectivas del presente trabajo agrupadas según la organización en capítulos que se utilizó antes.

Respecto de la búsqueda de blancos traduccionales de PDCD4 en modelos neuronales nos parece interesante continuar, a corto plazo, con la validación de los ARNm blancos traduccionales encontrados. Estas confirmaciones se realizarían de la misma manera que se realizó la confirmación particular de NFKB2, tanto mediante cuantificación de la abundancia en fracciones polisomales, como mediante cuantificación de la abundancia proteica por Western blot, en presencia y ausencia de PDCD4. Podríamos agregar también confirmaciones por cuantificación de abundancia proteica mediante estimaciones de intensidad en imágenes de microscopía confocal, una herramienta disponible en el Instituto Clemente Estable con tecnología de punta. También nos resulta interesante estudiar en particular el tipo de regulación que existe entre PDCD4 y sus ARNm blancos. Si dicha regulación es mediada por estructuras secundarias en los 5'-UTRs o si la inhibición ocurre en la etapa de elongación [48]. Podríamos manipular distintas secuencias derivadas de los blancos traduccionales encontrados, estructuradas o no, en el 5'-UTR de un gen reportero como la luciferasa y evaluar su actividad ante la presencia/ausencia de PDCD4. En el escenario de regulación a nivel de la elongación, podríamos seleccionar candidatos a ser regulados en esta etapa y modificar porciones de secuencias a lo largo del CDS hasta evidenciar la regulación.

Nos resulta también interesante diseñar experimentos en los cuales podamos evidenciar la regulación traduccional que ejerce PDCD4 de manera local. Una posibilidad es utilizar cultivos de neuronas derivadas del ganglio de la raíz dorsal en cámaras compartimentalizadas. De esta manera, luego de alcanzar los días de crecimiento *in vitro* necesarios para restablecer altos niveles de expresión de PDCD4, podríamos silenciar dicho factor (como hemos ya realizado en [78]), y así producir huellas ribosomales para determinar eventos de regulación traduccional local específicos de axones.

Explorando posibilidades de más largo aliento, podría ser interesante evaluar el papel de PDCD4 y sus ARNm blancos en modelos *in vivo*. Conocer los blancos traduccionales de PDCD4 en, por ejemplo, fibras de nervio ciático y cómo éstos se modulan en respuesta a la injuria se presenta como una hipótesis desafiante pero sumamente interesante. Hoy en día

se han desarrollado protocolos específicos para la producción de librerías de secuenciación de *small RNAs* (las utilizadas en la secuenciación de huellas ribosomales) a partir de cantidades muy pequeñas de material de partida, como podría ser el caso de la recuperación de polisomas a partir de axoplasma de nervio ciático. Surgen, sin embargo, desafíos adicionales asociados a este tipo de experimento que sin dudas representan aspectos a resolver y optimizar, como la óptima purificación de axoplasma a partir de las fibras y el silenciamiento de PDCD4.

Respecto al uso de Ribo-Seq en otros modelos neuronales descrito en el Capítulo 2, y en conjunción con los objetivos estudiados en el Capítulo 3, surgen varias perspectivas a explorar. En primer lugar, nos parece interesante estudiar el efecto de oligómeros tanto de Aβ, como de TAU, sobre el compartimento traduccional de cultivos *in vitro* de neuronas corticales primarias. Este tipo de cultivos y tratamientos son técnicas utilizadas cotidianamente en el laboratorio de mi co-tutor George Bloom, con lo cual los protocolos para la producción de ambos oligómeros, que suelen ser técnicas desafiantes, se encuentran optimizados. De esta manera podríamos conocer si las dos piezas fundamentales en la patología de Alzheimer tienen un rol sobre el compartimento traduccional en un modelo celular neuronal. Vale recordar que, en particular la acumulación de Aβ, ocurre a nivel extracelular, pero se ha demostrado que es reconocido por diversos receptores disparando vías de señalización diversas, algunas de las cuales convergen en mTOR [73,74], y que además podría tener un rol en la síntesis local en axones *in vitro* [110]. En este sentido, disponemos de algunos resultados preliminares respecto de cómo se ve afectada la traducción *in vitro* de GFP ante la exposición a distintas concentraciones de oligómeros de Aβ y TAU. Aunque los resultados son preliminares, parece existir cierto impacto negativo en los niveles traduccionales ante la exposición, en particular, de oligómeros de TAU.

Por otro lado, considerando el uso del protocolo de Ribo-Seq sobre la corteza cerebral de modelos transgénicos del mal de Alzheimer se derivan también interesantes perspectivas a estudiar. En primer lugar, consideramos que realizar una línea temporal y estudiar los traductomas de las cortezas de los animales a distintas edades representa un trabajo atractivo y desafiante. Lograr establecer dicha línea temporal nos permitiría realizar estudios de redes de co-expresión génica en búsqueda de grupos de genes cuya expresión se vea modificada con el avance en la edad de los ratones, esto es, con el desarrollo de la patología y de alteraciones cognitivas. Es claro que, tanto en los modelos murinos transgénicos de la enfermedad, como en la patología en sí observada en humanos, ocurren procesos dinámicos, con diversos estadíos y particularmente en humanos con un desarrollo lento, progresivo y largo. Este tipo de experimento representa un desafío de gran utilidad no solo para poder comprender los cambios iniciales como intentamos responder en el capítulo 3, sino también

los eventos de regulación que ocurren en distintos estadíos más avanzados. Podemos considerar también, como aspecto adicional, la posibilidad de discernir entre regiones más acotadas del cerebro murino con importancia en la patología, como el hipocampo o la corteza entorrinal [111].

También resulta interesante realizar experimentos similares a los realizados en el Capítulo 3 pero utilizando modelos transgénicos murinos cuya afectación esté asociada a la proteína TAU, y extender el análisis a otros modelos no solo relacionados a APP o Aβ. Existen muchos modelos transgénicos murinos donde el desarrollo de la patología está asociado a manipulaciones genéticas de la proteína TAU. Dos ejemplos, disponibles en el laboratorio del Dr. Bloom, son los ratones hTAU y *tau-knockout*. Los primeros tienen deletado el gen murino *Mapt*, codificante para TAU, pero tienen un transgen para sobreexpresar las 6 isoformas de TAU humano [112]. En cambio, los ratones *tau-knockout*, como su nombre lo indica solamente tienen deletado el gen Mapt [101]. En este sentido, contamos con algunos experimentos y resultados preliminares tanto en el uso del protocolo de Ribo-Seq en corteza de ratones hTau, como en su uso en cultivo de neuronas corticales primarias derivadas de ratones *tau-knockout*.

En último lugar, quisiéramos destacar dos posibles perspectivas más, una principalmente de corto plazo y otra de más largo aliento. Respecto de la primera, en la presente tesis hemos generado una gran cantidad de datos de secuenciación masiva, tanto producidos por RNA-Seq como por Ribo-Seq. Estas secuencias representan un valioso insumo para utilizar en distintos tipos de análisis complementarios a los aquí realizados. Por ejemplo, con los datos derivados de RNA-Seq se podrían realizar ensamblados de los distintos transcriptomas en búsqueda de nuevas o raras isoformas. En el caso de los datos derivados de Ribo-Seq las distintas posibilidades de análisis son aún mayores, por ejemplo: búsqueda de sitios de pausa definidos por grandes picos de mapeo [113,114], búsqueda de marcos de lectura abiertos en los 5'-UTRs (uORFs por sus siglas en inglés; [115,116]), análisis de la preferencia de codón iniciación utilizado [117], búsqueda de eventos de cambio en el marco de lectura [118], entre otros. Con respecto a una segunda perspectiva asociada al trabajo aquí presentado, nos resulta interesante destacar las tecnologías de secuenciación de célula única que se encuentran en un momento de particular desarrollo y uso en la actualidad. Sin embargo, no se conocen al momento protocolos específicos para la construcción de librerías del tipo Ribo-Seq en célula única, aunque varios grupos de investigación se encuentran trabajando en el desarrollo de dichos protocolos. Creemos que, superadas las limitaciones tecnológicas, podrá ser posible conocer el perfil traduccional masivo de una única célula y esto despertará nuevas interrogantes a ser respondidas. En particular, en el contexto de Alzheimer, donde las tecnologías de RNA-Seq de célula única han realizado importantes aportes a la biología de la

enfermedad (ver ejemplos en [119–122]), creemos que la posibilidad de explorar los eventos de regulación traduccional mediante esta técnica de última generación dará paso a nuevos conocimientos que impulsarán el campo hacia nuevos horizontes.

IX. AGRADECIMIENTOS

Esta tesis es sin dudas el corolario de un proceso de formación en el quehacer científico que empezó en el año 2011 cuando ingresé al Instituto a realizar la tesis de grado bajo la orientación de Coya. Durante estos 10 años he compartido con, y aprendido de, mucha gente a la cual debo agradecer. En primer lugar a Coya por recibirme y guiarme durante las distintas etapas, en especial la que aquí culmina. El pensamiento crítico, la búsqueda de la siguiente pregunta y la alegría del trabajo científico son aspectos que aprendí junto a Coya y en el Departamento de Genómica que se formó durante este proceso. A todos los compañeros de Genómica, actuales y anteriores, el agradecimiento por lo aprendido, lo compartido, el apoyo y la compañía durante todos estos años. Quisiera agradecer también al IIBCE, y dentro de él a los compañeros con los cuales compartimos la vocación científica, ya sea colaborando en diversos proyectos o compartiendo IIBCE abiertos. El apoyo institucional recibido también fue un soporte mayor para el pleno desarrollo de esta tesis. Un agradecimiento especial a George, que además de co-orientar esta tesis me recibió en su laboratorio y me dio la total libertad de trabajar a todo vapor en interrogantes biológicas sumamente desafiantes y novedosas.

Quisiera agradecer también a las distintas agencias financiadoras que han apoyado mis estudios de doctorado mediante diversos instrumentos, tanto nacionales (PEDECIBA, ANII, DICYT y D2C2), como internacionales (PROLAB-ASBMB). En especial destaco al PEDECIBA, un programa de posgrado nacional formador de recursos humanos de altísima calidad y cuya estructura da un soporte muy importante al crecimiento del sistema científico nacional.

Agradecer también a los miembros del tribunal por su tiempo y ricos aportes a esta tesis y al trabajo llevado a cabo. También destacar a los miembros de mi CAS por su seguimiento y los aportes que han tenido con mi trabajo durante el desarrollo de esta tesis.

Por último destacar y agradecer el apoyo fundamental de Caro, familia y amigos durante estos años. Cualquier descripción de su apoyo y energía será insuficiente.

X. REFERENCIAS

1. Larsson O, Tian B, Sonenberg N. Toward a genome-wide landscape of translational control. Cold Spring Harb Perspect Biol. 2013;5: a012302.
2. Larsson O, Nadon R. Gene expression - time to change point of view? Biotechnol Genet Eng Rev. 2008;25: 77–92.
3. Kim E, Jung H. Local protein synthesis in neuronal axons: why and how we study. BMB Rep. 2015;48: 139–146.
4. Holt CE, Schuman EM. The central dogma decentralized: new perspectives on RNA function and local translation in neurons. Neuron. 2013;80: 648–657.
5. Perry RB, Fainzilber M. Local translation in neuronal processes--in vivo tests of a “heretical hypothesis.” Dev Neurobiol. 2014;74: 210–217.
6. Wells DG. mRNA translation: regulating an out of soma experience. Curr Opin Cell Biol. 2012;24: 554–557.
7. Crispino M, Chun JT, Cefaliello C, Perrone Capano C, Giuditta A. Local gene expression in nerve endings. Dev Neurobiol. 2014;74: 279–291.
8. Jung H, Yoon BC, Holt CE. Axonal mRNA localization and local protein synthesis in nervous system assembly, maintenance and repair. Nat Rev Neurosci. 2012;13: 308–324.
9. Sotelo-Silveira JR, Calliari A, Kun A, Koenig E, Sotelo JR. RNA trafficking in axons. Traffic. 2006;7: 508–515.
10. Canclini L, Farias J, Di Paolo A, Sotelo-Silveira JR, Folle G, Kun A, et al. Association of microtubules and axonal RNA transferred from myelinating Schwann cells in rat sciatic nerve. PLoS One. 2020;15: e0233651.
11. Sotelo-Silveira JR, Calliari A, Kun A, Elizondo V, Canclini L, Sotelo JR. Localization of mRNA in vertebrate axonal compartments by in situ hybridization. Methods Mol Biol. 2011;714: 125–138.
12. Farias J, Holt CE, Sotelo JR, Sotelo-Silveira JR. Axon microdissection and transcriptome profiling reveals the in vivo RNA content of fully differentiated myelinated motor axons. RNA. 2020;26: 595–612.
13. Sotelo-Silveira J, Crispino M, Puppo A, Sotelo JR, Koenig E. Myelinated axons contain beta-actin mRNA and ZBP-1 in periaxoplasmic ribosomal plaques and depend on cyclic AMP and F-actin integrity for in vitro translation. J Neurochem. 2008;104: 545–557.
14. Kun A, Otero L, Sotelo-Silveira JR, Sotelo JR. Ribosomal distributions in axons of mammalian myelinated fibers. J Neurosci Res. 2007;85: 2087–2098.
15. Sotelo-Silveira JR, Calliari A, Cárdenas M, Koenig E, Sotelo JR. Myosin Va and kinesin II motor proteins are concentrated in ribosomal domains (periaxoplasmic ribosomal plaques) of myelinated axons. J Neurobiol. 2004;60: 187–196.
16. Sotelo-Silveira JR, Calliari A, Kun A, Benech JC, Sanguinetti C, Chalar C, et al. Neurofilament mRNAs are present and translated in the normal and severed sciatic nerve. J Neurosci Res. 2000;62: 65–74.
17. Sotelo JR, Kun A, Benech JC, Giuditta A, Morillas J, Benech CR. Ribosomes and polyribosomes are present in the squid giant axon: an immunocytochemical study. Neuroscience. 1999;90: 705–715.
18. Shahar OD, Schuman EM. Large-scale cell-type-specific imaging of protein synthesis in a vertebrate brain. Elife. 2020;9. doi:10.7554/eLife.50564
19. Biever A, Glock C, Tushev G, Ciirdaeva E, Dalmay T, Langer JD, et al. Monosomes actively translate synaptic mRNAs in neuronal processes. Science. 2020;367. doi:10.1126/science.aay4991
20. Shigeoka T, Koppers M, Wong HH-W, Lin JQ, Cagnetta R, Dwivedy A, et al. On-Site Ribosome Remodeling by Locally Synthesized Ribosomal Proteins in Axons. Cell Rep. 2019;29: 3605–3619.e10.
21. Holt CE, Martin KC, Schuman EM. Local translation in neurons: visualization and

function. Nat Struct Mol Biol. 2019;26: 557–566.
22. Shigeoka T, Jung H, Jung J, Turner-Bridger B, Ohk J, Lin JQ, et al. Dynamic Axonal Translation in Developing and Mature Visual Circuits. Cell. 2016;166: 181–192.
23. Cefaliello C, Penna E, Barbato C, Di Ruberto G, Mollica MP, Trinchese G, et al. Deregulated Local Protein Synthesis in the Brain Synaptosomes of a Mouse Model for Alzheimer's Disease. Mol Neurobiol. 2020;57: 1529–1541.
24. Sahoo PK, Lee SJ, Jaiswal PB, Alber S, Kar AN, Miller-Randolph S, et al. Axonal G3BP1 stress granule protein limits axonal mRNA translation and nerve regeneration. Nat Commun. 2018;9: 3358.
25. Rozenbaum M, Rajman M, Rishal I, Koppel I, Koley S, Medzihradszky KF, et al. Translatome Regulation in Neuronal Injury and Axon Regrowth. eNeuro. 2018;5. doi:10.1523/ENEURO.0276-17.2018
26. Terenzio M, Koley S, Samra N, Rishal I, Zhao Q, Sahoo PK, et al. Locally translated mTOR controls axonal local translation in nerve injury. Science. 2018;359: 1416–1421.
27. Shigeoka T, Jung J, Holt CE, Jung H. Axon-TRAP-RiboTag: Affinity Purification of Translated mRNAs from Neuronal Axons in Mouse In Vivo. Methods Mol Biol. 2018;1649: 85–94.
28. Crispino M, Chun JT, Giuditta A. Squid Giant Axons Synthesize NF Proteins. Mol Neurobiol. 2018;55: 3079–3084.
29. Ingolia NT, Ghaemmaghami S, Newman JRS, Weissman JS. Genome-wide analysis in vivo of translation with nucleotide resolution using ribosome profiling. Science. 2009;324: 218–223.
30. Shibahara K, Asano M, Ishida Y, Aoki T, Koike T, Honjo T. Isolation of a novel mouse gene MA-3 that is induced upon programmed cell death. Gene. 1995;166: 297–301.
31. Lankat-Buttgereit B, Göke R. The tumour suppressor Pdcd4: recent advances in the elucidation of function and regulation. Biol Cell. 2009;101: 309–317.
32. Song X, Zhang X, Wang X, Zhu F, Guo C, Wang Q, et al. Tumor suppressor gene PDCD4 negatively regulates autophagy by inhibiting the expression of autophagy-related gene ATG5. Autophagy. 2013;9: 743–755.
33. Dorrello NV, Peschiaroli A, Guardavaccaro D, Colburn NH, Sherman NE, Pagano M. S6K1- and betaTRCP-mediated degradation of PDCD4 promotes protein translation and cell growth. Science. 2006;314: 467–471.
34. Frampton AE, Castellano L, Colombo T, Giovannetti E, Krell J, Jacob J, et al. MicroRNAs cooperatively inhibit a network of tumor suppressor genes to promote pancreatic tumor growth and progression. Gastroenterology. 2014;146: 268–77.e18.
35. Zhu Q, Wang Z, Hu Y, Li J, Li X, Zhou L, et al. miR-21 promotes migration and invasion by the miR-21-PDCD4-AP-1 feedback loop in human hepatocellular carcinoma. Oncol Rep. 2012;27: 1660–1668.
36. Frankel LB, Christoffersen NR, Jacobsen A, Lindow M, Krogh A, Lund AH. Programmed cell death 4 (PDCD4) is an important functional target of the microRNA miR-21 in breast cancer cells. J Biol Chem. 2008;283: 1026–1033.
37. Asangani IA, Rasheed SAK, Nikolova DA, Leupold JH, Colburn NH, Post S, et al. MicroRNA-21 (miR-21) post-transcriptionally downregulates tumor suppressor Pdcd4 and stimulates invasion, intravasation and metastasis in colorectal cancer. Oncogene. 2008;27: 2128–2136.
38. Bitomsky N, Böhm M, Klempnauer K-H. Transformation suppressor protein Pdcd4 interferes with JNK-mediated phosphorylation of c-Jun and recruitment of the coactivator p300 by c-Jun. Oncogene. 2004;23: 7484–7493.
39. Yang H-S, Knies JL, Stark C, Colburn NH. Pdcd4 suppresses tumor phenotype in JB6 cells by inhibiting AP-1 transactivation. Oncogene. 2003;22: 3712–3720.
40. Leupold JH, Yang H-S, Colburn NH, Asangani I, Post S, Allgayer H. Tumor suppressor Pdcd4 inhibits invasion/intravasation and regulates urokinase receptor (u-PAR) gene expression via Sp-transcription factors. Oncogene. 2007;26: 4550–4562.
41. Shiota M, Izumi H, Tanimoto A, Takahashi M, Miyamoto N, Kashiwagi E, et al. Programmed cell death protein 4 down-regulates Y-box binding protein-1 expression via

a direct interaction with Twist1 to suppress cancer cell growth. Cancer Res. 2009;69: 3148–3156.
42. Bitomsky N, Wethkamp N, Marikkannu R, Klempnauer K-H. siRNA-mediated knockdown of Pdcd4 expression causes upregulation of p21(Waf1/Cip1) expression. Oncogene. 2008;27: 4820–4829.
43. Suzuki C, Garces RG, Edmonds KA, Hiller S, Hyberts SG, Marintchev A, et al. PDCD4 inhibits translation initiation by binding to eIF4A using both its MA3 domains. Proc Natl Acad Sci U S A. 2008;105: 3274–3279.
44. Wedeken L, Ohnheiser J, Hirschi B, Wethkamp N, Klempnauer K-H. Association of Tumor Suppressor Protein Pdcd4 With Ribosomes Is Mediated by Protein-Protein and Protein-RNA Interactions. Genes Cancer. 2010;1: 293–301.
45. Loh PG, Yang H-S, Walsh MA, Wang Q, Wang X, Cheng Z, et al. Structural basis for translational inhibition by the tumour suppressor Pdcd4. EMBO J. 2009;28: 274–285.
46. Waters LC, Strong SL, Ferlemann E, Oka O, Muskett FW, Veverka V, et al. Structure of the tandem MA-3 region of Pdcd4 protein and characterization of its interactions with eIF4A and eIF4G: molecular mechanisms of a tumor suppressor. J Biol Chem. 2011;286: 17270–17280.
47. Fehler O, Singh P, Haas A, Ulrich D, Müller JP, Ohnheiser J, et al. An evolutionarily conserved interaction of tumor suppressor protein Pdcd4 with the poly(A)-binding protein contributes to translation suppression by Pdcd4. Nucleic Acids Res. 2014;42: 11107–11118.
48. Biyanee A, Ohnheiser J, Singh P, Klempnauer K-H. A novel mechanism for the control of translation of specific mRNAs by tumor suppressor protein Pdcd4: inhibition of translation elongation. Oncogene. 2015;34: 1384–1392.
49. Di Paolo A. Análisis de expresión de la proteína Pdcd4 en sistema nervioso. Silveira S JR, editor. Licenciado en Biología, Facultad de Ciencias, UdelaR. 2013.
50. Eastman G. Determinación de blancos traduccionales de PDCD4 (programmed cell death 4) mediante análisis de datos generados por secuenciación masiva de huellas polisomales. Munroe D, Silveira S JR, editors. Magister en Ciencias Biológicas, PEDECIBA, UdelaR. 2016.
51. Gal-Ben-Ari S, Kenney JW, Ounalla-Saad H, Taha E, David O, Levitan D, et al. Consolidation and translation regulation. Learn Mem. 2012;19: 410–422.
52. Sutton MA, Schuman EM. Dendritic protein synthesis, synaptic plasticity, and memory. Cell. 2006;127: 49–58.
53. Malenka RC, Bear MF. LTP and LTD: an embarrassment of riches. Neuron. 2004;44: 5–21.
54. Kandel ER. The molecular biology of memory storage: a dialog between genes and synapses. Biosci Rep. 2001;21: 565–611.
55. Matthies H. In search of cellular mechanisms of memory. Prog Neurobiol. 1989;32: 277–349.
56. Davis HP, Squire LR. Protein synthesis and memory: a review. Psychol Bull. 1984;96: 518–559.
57. Henderson C, Wijetunge L, Kinoshita MN, Shumway M, Hammond RS, Postma FR, et al. Reversal of disease-related pathologies in the fragile X mouse model by selective activation of GABAB receptors with arbaclofen. Sci Transl Med. 2012;4: 152ra128.
58. El Fatimy R, Tremblay S, Dury AY, Solomon S, De Koninck P, Schrader JW, et al. Fragile X mental retardation protein interacts with the RNA-binding protein Caprin1 in neuronal RiboNucleoProtein complexes [corrected]. PLoS One. 2012;7: e39338.
59. Niere F, Wilkerson JR, Huber KM. Evidence for a fragile X mental retardation protein-mediated translational switch in metabotropic glutamate receptor-triggered Arc translation and long-term depression. J Neurosci. 2012;32: 5924–5936.
60. Wang T, Bray SM, Warren ST. New perspectives on the biology of fragile X syndrome. Curr Opin Genet Dev. 2012;22: 256–263.
61. Das Sharma S, Metz JB, Li H, Hobson BD, Hornstein N, Sulzer D, et al. Widespread Alterations in Translation Elongation in the Brain of Juvenile Fmr1 Knockout Mice. Cell

Rep. 2019;26: 3313–3322.e5.
62. Kim JW, Yin X, Jhaldiyal A, Khan MR, Martin I, Xie Z, et al. Defects in mRNA Translation in LRRK2-Mutant hiPSC-Derived Dopaminergic Neurons Lead to Dysregulated Calcium Homeostasis. Cell Stem Cell. 2020;27: 633–645.e7.
63. Taymans J-M, Nkiliza A, Chartier-Harlin M-C. Deregulation of protein translation control, a potential game-changing hypothesis for Parkinson's disease pathogenesis. Trends Mol Med. 2015;21: 466–472.
64. Alzheimer's association. [cited 16 Mar 2021]. Available: https://www.alz.org/alzheimers-dementia/difference-between-dementia-and-alzheimer-s
65. Rademakers R, Cruts M, Van Broeckhoven C. Genetics of early-onset Alzheimer dementia. ScientificWorldJournal. 2003;3: 497–519.
66. Hippius H, Neundörfer G. The discovery of Alzheimer's disease. Dialogues Clin Neurosci. 2003;5: 101–108.
67. Elahi FM, Miller BL. A clinicopathological approach to the diagnosis of dementia. Nat Rev Neurol. 2017;13: 457–476.
68. Nussbaum JM, Schilling S, Cynis H, Silva A, Swanson E, Wangsanut T, et al. Prion-like behaviour and tau-dependent cytotoxicity of pyroglutamylated amyloid-β. Nature. 2012;485: 651–655.
69. Bloom GS. Amyloid-β and tau: the trigger and bullet in Alzheimer disease pathogenesis. JAMA Neurol. 2014;71: 505–508.
70. Li C, Götz J. Somatodendritic accumulation of Tau in Alzheimer's disease is promoted by Fyn-mediated local protein translation. EMBO J. 2017;36: 3120–3138.
71. Banerjee S, Ferdosh S, Ghosh AN, Barat C. Tau protein- induced sequestration of the eukaryotic ribosome: Implications in neurodegenerative disease. Sci Rep. 2020;10: 5225.
72. Evans HT, Benetatos J, van Roijen M, Bodea L-G, Götz J. Decreased synthesis of ribosomal proteins in tauopathy revealed by non-canonical amino acid labelling. EMBO J. 2019;38: e101174.
73. Norambuena A, Wallrabe H, Cao R, Wang DB, Silva A, Svindrych Z, et al. A novel lysosome-to-mitochondria signaling pathway disrupted by amyloid-β oligomers. EMBO J. 2018;37. doi:10.15252/embj.2018100241
74. Norambuena A, Wallrabe H, McMahon L, Silva A, Swanson E, Khan SS, et al. mTOR and neuronal cell cycle reentry: How impaired brain insulin signaling promotes Alzheimer's disease. Alzheimers Dement. 2017;13: 152–167.
75. Switon K, Kotulska K, Janusz-Kaminska A, Zmorzynska J, Jaworski J. Molecular neurobiology of mTOR. Neuroscience. 2017;341: 112–153.
76. Haas A, Nilges BS, Leidel SA, Klempnauer K-H. PDCD4 controls the G1/S-phase transition in a telomerase-immortalized epithelial cell line and affects the expression level and translation of multiple mRNAs. Sci Rep. 2020;10: 2758.
77. Manecka D-L, Mahmood SF, Grumolato L, Lihrmann I, Anouar Y. Pituitary adenylate cyclase-activating polypeptide (PACAP) promotes both survival and neuritogenesis in PC12 cells through activation of nuclear factor κB (NF-κB) pathway: involvement of extracellular signal-regulated kinase (ERK), calcium, and c-REL. J Biol Chem. 2013;288: 14936–14948.
78. Di Paolo A, Eastman G, Mesquita-Ribeiro R, Farias J, Macklin A, Kislinger T, et al. PDCD4 regulates axonal growth by translational repression of neurite growth-related genes and is modulated during nerve injury responses. RNA. 2020;26: 1637–1653.
79. Marcon BH, Holetz FB, Eastman G, Origa-Alves AC, Amorós MA, de Aguiar AM, et al. Downregulation of the protein synthesis machinery is a major regulatory event during early adipogenic differentiation of human adipose-derived stromal cells. Stem Cell Res. 2017;25: 191–201.
80. Smircich P, Eastman G, Bispo S, Duhagon MA, Guerra-Slompo EP, Garat B, et al. Ribosome profiling reveals translation control as a key mechanism generating differential gene expression in Trypanosoma cruzi. BMC Genomics. 2015;16: 443.
81. Angenstein F, Evans AM, Ling S-C, Settlage RE, Ficarro S, Carrero-Martinez FA, et al.

Proteomic characterization of messenger ribonucleoprotein complexes bound to nontranslated or translated poly(A) mRNAs in the rat cerebral cortex. J Biol Chem. 2005;280: 6496–6503.
82. Hornstein N, Torres D, Das Sharma S, Tang G, Canoll P, Sims PA. Ligation-free ribosome profiling of cell type-specific translation in the brain. Genome Biol. 2016;17: 149.
83. Zappulo A, van den Bruck D, Ciolli Mattioli C, Franke V, Imami K, McShane E, et al. RNA localization is a key determinant of neurite-enriched proteome. Nat Commun. 2017;8: 583.
84. Ingolia NT, Brar GA, Rouskin S, McGeachy AM, Weissman JS. The ribosome profiling strategy for monitoring translation in vivo by deep sequencing of ribosome-protected mRNA fragments. Nat Protoc. 2012;7: 1534–1550.
85. Miller MD, Tanner J, Alpaugh M, Benedik MJ, Krause KL. 2.1 A structure of Serratia endonuclease suggests a mechanism for binding to double-stranded DNA. Nat Struct Biol. 1994;1: 461–468.
86. Miller MD, Krause KL. Identification of the Serratia endonuclease dimer: structural basis and implications for catalysis. Protein Sci. 1996;5: 24–33.
87. Spahr PF, Hollingworth BR. Purification and Mechanism of Action of Ribonuclease from Escherichia coli Ribosomes. J Biol Chem. 1961;236: 823–831.
88. Meador J 3rd, Kennell D. Cloning and sequencing the gene encoding Escherichia coli ribonuclease I: exact physical mapping using the genome library. Gene. 1990;95: 1–7.
89. Gerashchenko MV, Gladyshev VN. Ribonuclease selection for ribosome profiling. Nucleic Acids Res. 2017;45: e6.
90. Andrews S. FastQC: A Quality Control Tool for High Throughput Sequence Data. 2010. Available: http://www.bioinformatics.babraham.ac.uk/projects/fastqc/
91. Joshi NA, Fass JN. Sickle: A sliding-window, adaptive, quality-based trimming tool for FastQ files. 2011. Available: https://github.com/najoshi/sickle
92. Langmead B, Trapnell C, Pop M, Salzberg SL. Ultrafast and memory-efficient alignment of short DNA sequences to the human genome. Genome Biol. 2009;10: R25.
93. Langmead B, Salzberg SL. Fast gapped-read alignment with Bowtie 2. Nat Methods. 2012;9: 357–359.
94. Liao Y, Smyth GK, Shi W. featureCounts: an efficient general purpose program for assigning sequence reads to genomic features. Bioinformatics. 2014;30: 923–930.
95. Robinson MD, McCarthy DJ, Smyth GK. edgeR: a Bioconductor package for differential expression analysis of digital gene expression data. Bioinformatics. 2010;26: 139–140.
96. McCarthy DJ, Chen Y, Smyth GK. Differential expression analysis of multifactor RNA-Seq experiments with respect to biological variation. Nucleic Acids Res. 2012;40: 4288–4297.
97. Raudvere U, Kolberg L, Kuzmin I, Arak T, Adler P, Peterson H, et al. g:Profiler: a web server for functional enrichment analysis and conversions of gene lists (2019 update). Nucleic Acids Res. 2019;47: W191–W198.
98. Jensen LJ, Kuhn M, Stark M, Chaffron S, Creevey C, Muller J, et al. STRING 8--a global view on proteins and their functional interactions in 630 organisms. Nucleic Acids Res. 2009;37: D412–6.
99. Li H, Handsaker B, Wysoker A, Fennell T, Ruan J, Homer N, et al. The Sequence Alignment/Map format and SAMtools. Bioinformatics. 2009;25: 2078–2079.
100. Quinlan AR, Hall IM. BEDTools: a flexible suite of utilities for comparing genomic features. Bioinformatics. 2010;26: 841–842.
101. Dawson HN, Ferreira A, Eyster MV, Ghoshal N, Binder LI, Vitek MP. Inhibition of neuronal maturation in primary hippocampal neurons from tau deficient mice. J Cell Sci. 2001;114: 1179–1187.
102. Ingolia NT. Genome-wide translational profiling by ribosome footprinting. Methods Enzymol. 2010;470: 119–142.
103. Keller D, Erö C, Markram H. Cell Densities in the Mouse Brain: A Systematic Review. Front Neuroanat. 2018;12: 83.

104. Lama L, Cobo J, Buenaventura D, Ryan K. Small RNA-seq: The RNA 5'-end adapter ligation problem and how to circumvent it. J Biol Methods. 2019;6. doi:10.14440/jbm.2019.269
105. Eastman G, Smircich P, Sotelo-Silveira JR. Following Ribosome Footprints to Understand Translation at a Genome Wide Level. Comput Struct Biotechnol J. 2018;16: 167–176.
106. Ingolia NT, Lareau LF, Weissman JS. Ribosome profiling of mouse embryonic stem cells reveals the complexity and dynamics of mammalian proteomes. Cell. 2011;147: 789–802.
107. Diament A, Tuller T. Estimation of ribosome profiling performance and reproducibility at various levels of resolution. Biol Direct. 2016;11: 24.
108. Terns MP, Terns RM. Small nucleolar RNAs: versatile trans-acting molecules of ancient evolutionary origin. Gene Expr. 2002;10: 17–39.
109. Liu B, Molinaro G, Shu H, Stackpole EE, Huber KM, Richter JD. Optimization of ribosome profiling using low-input brain tissue from fragile X syndrome model mice. Nucleic Acids Res. 2019;47: e25.
110. Baleriola J, Walker CA, Jean YY, Crary JF, Troy CM, Nagy PL, et al. Axonally synthesized ATF4 transmits a neurodegenerative signal across brain regions. Cell. 2014;158: 1159–1172.
111. Braak H, Braak E. Neuropathological stageing of Alzheimer-related changes. Acta Neuropathol. 1991;82: 239–259.
112. Andorfer C, Kress Y, Espinoza M, de Silva R, Tucker KL, Barde Y-A, et al. Hyperphosphorylation and aggregation of tau in mice expressing normal human tau isoforms. J Neurochem. 2003;86: 582–590.
113. Legendre R, Baudin-Baillieu A, Hatin I, Namy O. RiboTools: a Galaxy toolbox for qualitative ribosome profiling analysis. Bioinformatics. 2015;31: 2586–2588.
114. Kumari R, Michel AM, Baranov PV. PausePred and Rfeet: webtools for inferring ribosome pauses and visualizing footprint density from ribosome profiling data. RNA. 2018;24: 1297–1304.
115. Bazzini AA, Johnstone TG, Christiano R, Mackowiak SD, Obermayer B, Fleming ES, et al. Identification of small ORFs in vertebrates using ribosome footprinting and evolutionary conservation. EMBO J. 2014;33: 981–993.
116. Calviello L, Mukherjee N, Wyler E, Zauber H, Hirsekorn A, Selbach M, et al. Detecting actively translated open reading frames in ribosome profiling data. Nat Methods. 2016;13: 165–170.
117. Michel AM, Andreev DE, Baranov PV. Computational approach for calculating the probability of eukaryotic translation initiation from ribo-seq data that takes into account leaky scanning. BMC Bioinformatics. 2014;15: 380.
118. Michel AM, Choudhury KR, Firth AE, Ingolia NT, Atkins JF, Baranov PV. Observation of dually decoded regions of the human genome using ribosome profiling data. Genome Res. 2012;22: 2219–2229.
119. Castanho I, Murray TK, Hannon E, Jeffries A, Walker E, Laing E, et al. Transcriptional Signatures of Tau and Amyloid Neuropathology. Cell Rep. 2020;30: 2040–2054.e5.
120. Mathys H, Adaikkan C, Gao F, Young JZ, Manet E, Hemberg M, et al. Temporal Tracking of Microglia Activation in Neurodegeneration at Single-Cell Resolution. Cell Rep. 2017;21: 366–380.
121. Sala Frigerio C, Wolfs L, Fattorelli N, Thrupp N, Voytyuk I, Schmidt I, et al. The Major Risk Factors for Alzheimer's Disease: Age, Sex, and Genes Modulate the Microglia Response to Aβ Plaques. Cell Rep. 2019;27: 1293–1306.e6.
122. Keren-Shaul H, Spinrad A, Weiner A, Matcovitch-Natan O, Dvir-Szternfeld R, Ulland TK, et al. A Unique Microglia Type Associated with Restricting Development of Alzheimer's Disease. Cell. 2017;169: 1276–1290.e17.

XI. ANEXOS

Notas

Nota 1: En todos los casos, los cultivos *in vitro* de neuronas corticales primarias fueron generados por la técnica del laboratorio de George Bloom, Nutan Shivange. En mi caso, solo me encargué del mantenimiento y uso de los mismos para los experimentos mencionados.

Nota 2: En todos los casos, el manejo de animales de laboratorio así como su anestesia, sacrificio y extracción de cerebro, fue siempre realizado por las técnicas del laboratorio de George Bloom, Nutan Shivange y Dora Bigler Wang. En mi caso, me encargué de la disección de la corteza y los pasos posteriores mencionados en la sección.

Apoyo Financiero

La presente tesis doctoral contó con el apoyo financiero de las siguientes agencias y organizaciones:

- ANII, beca de posgrado (doctorado) llamado 2016: POS_NAC_2016_1_129959
- ANII, SNI llamado 2019: Ingreso categoría Iniciación, Ciencias Naturales y Exactas
- PEDECIBA, apoyo a estudiantes mediante alícuotas
- PEDECIBA, apoyo a pasantías en el exterior llamado 2017
- DICYT, programa de movilidad 2017
- D2C2, convocatorio Tocó Salir-I 2019
- ASBMB, becas PROLAB llamado 2017

Figuras Suplementarias

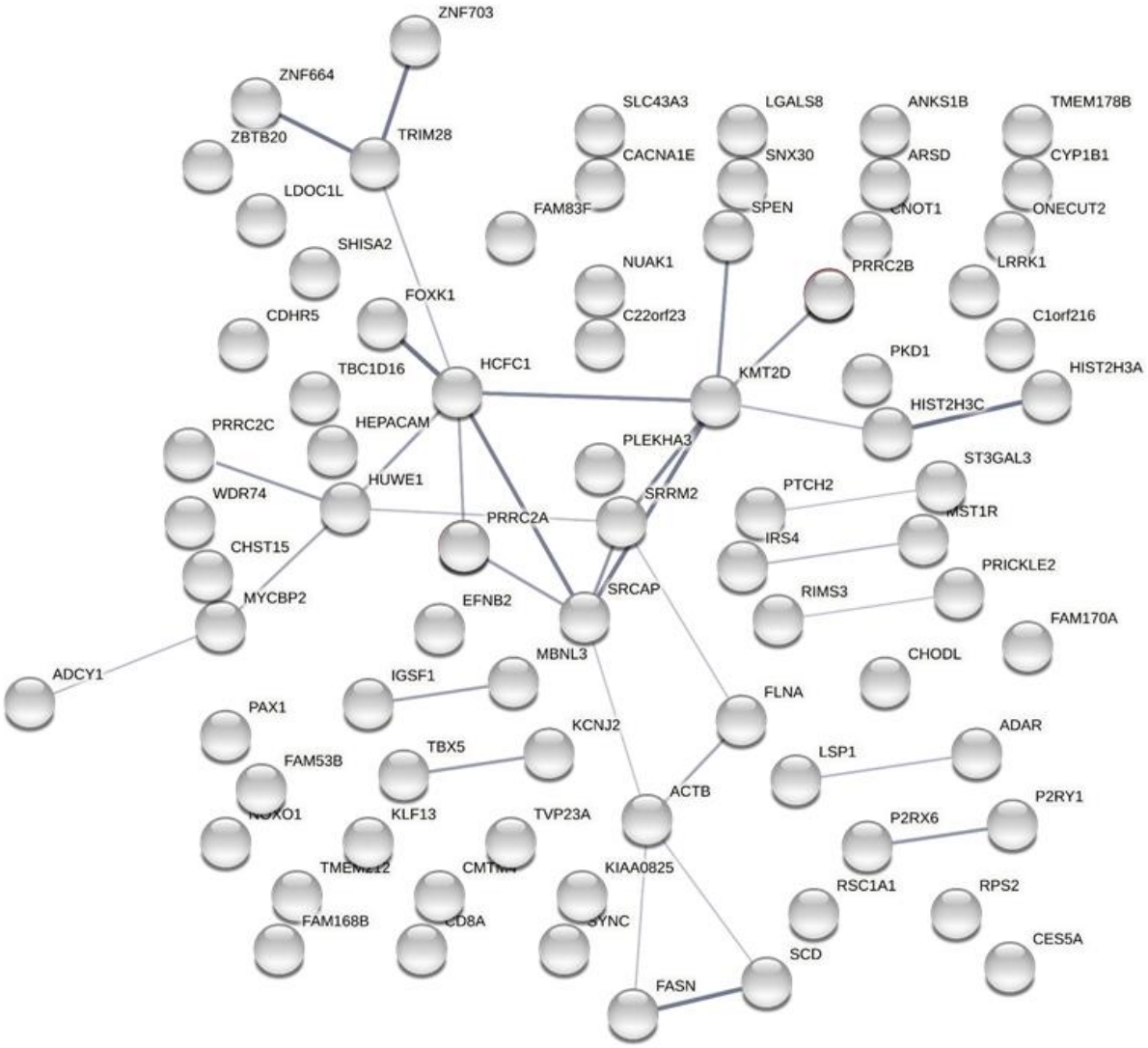

Figura Suplementaria XI.1. Red de asociación funcional de genes codificantes asociados a la Benzonasa. No se observan vías KEGG sobrerrepresentadas. Red obtenida con la herramienta STRING.

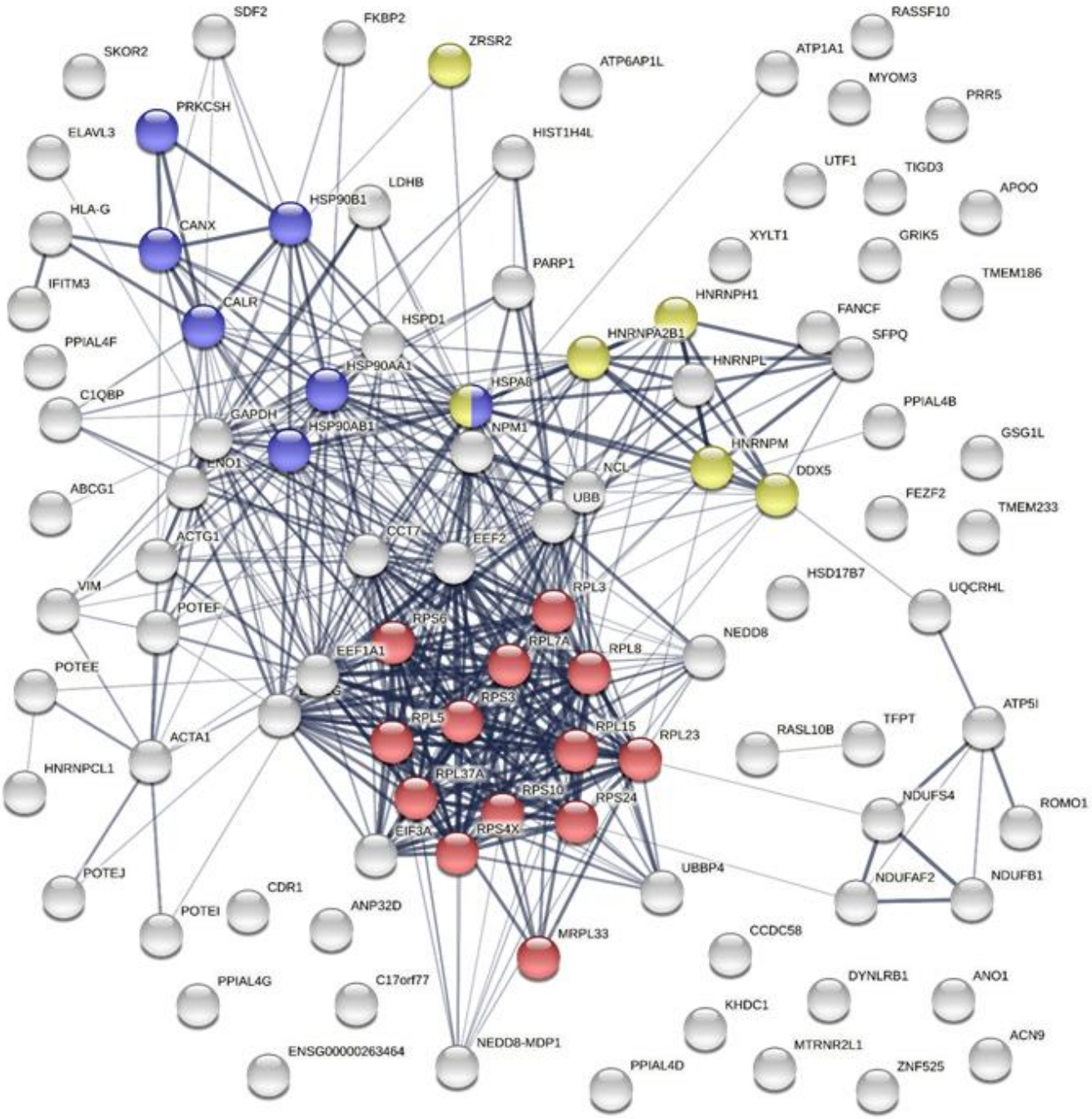

Figura Suplementaria XI.2. Red de asociación funcional de genes codificantes asociados a la RNAsa I. Las vías KEGG sobrerrepresentadas encontradas en el análisis se muestran en el siguiente esquema de colores: en rojo, ribosoma; en azul, procesamiento de proteínas del retículo endoplásmico y en verde, espliceosoma. Red obtenida con la herramienta STRING.

Tabla Suplementaria XI.I. Resultado completo del análisis de ontología génica realizado con los genes asociados a la RNAsa I. Se muestra la salida de la herramienta g:GOSt del g:Profiler indicando los términos sobrerrepresentados clasificados por ontología en funciones moleculares, procesos biológicos, componentes celulares y vías KEGG. Tabla asociada a la Figura V.9 D.

---

source	term_name	term_id	adjusted_p_value	term_size	query_size	intersection_size
GO:MF	RNA binding	GO:0003723	2.09E-14	1946	100	43
GO:MF	structural constituent of ribosome	GO:0003735	3.86E-09	170	100	13
GO:MF	cyclosporin A binding	GO:0016018	4.36E-09	20	100	7
GO:MF	peptidyl-prolyl cis-trans isomerase activity	GO:0003755	4.49E-08	44	100	8
GO:MF	cis-trans isomerase activity	GO:0016859	7.85E-08	47	100	8
GO:MF	drug binding	GO:0008144	1.07E-07	73	100	9
GO:MF	rRNA binding	GO:0019843	1.03E-06	64	100	8
GO:MF	unfolded protein binding	GO:0051082	4.71E-06	111	100	9
GO:MF	nucleic acid binding	GO:0003676	3.15E-05	4353	100	48
GO:MF	structural molecule activity	GO:0005198	9.49E-05	698	100	17
GO:MF	isomerase activity	GO:0016853	1.80E-04	169	100	9
GO:MF	peptide binding	GO:0042277	4.18E-04	305	100	11
GO:MF	amide binding	GO:0033218	5.04E-04	379	100	12
GO:MF	enzyme binding	GO:0019899	2.17E-03	1866	100	26
GO:MF	heterocyclic compound binding	GO:1901363	2.22E-03	6302	100	56
GO:MF	ubiquitin protein ligase binding	GO:0031625	2.78E-03	300	100	10
GO:MF	organic cyclic compound binding	GO:0097159	3.52E-03	6387	100	56
GO:MF	ubiquitin-like protein ligase binding	GO:0044389	4.64E-03	318	100	10
GO:MF	mRNA binding	GO:0003729	4.68E-03	554	100	13
GO:MF	5S rRNA binding	GO:0008097	1.40E-02	11	100	3
GO:MF	pre-mRNA binding	GO:0036002	2.61E-02	37	100	4
GO:MF	MHC class II protein complex binding	GO:0023026	4.65E-02	16	100	3
GO:BP	protein folding	GO:0006457	8.77E-11	224	96	16
GO:BP	SRP-dependent cotranslational protein targeting to membrane	GO:0006614	1.90E-10	96	96	12
GO:BP	translation	GO:0006412	2.26E-10	763	96	25

GO:BP	cotranslational protein targeting to membrane	GO:0006613	3.54E-10	101	96	12
GO:BP	peptide biosynthetic process	GO:0043043	4.64E-10	788	96	25
GO:BP	protein targeting to ER	GO:0045047	1.55E-09	114	96	12
GO:BP	protein localization to endoplasmic reticulum	GO:0070972	1.59E-09	147	96	13
GO:BP	biological process involved in symbiotic interaction	GO:0044403	1.75E-09	996	96	27
GO:BP	establishment of protein localization to endoplasmic reticulum	GO:0072599	2.36E-09	118	96	12
GO:BP	mRNA catabolic process	GO:0006402	3.03E-09	386	96	18
GO:BP	peptide metabolic process	GO:0006518	3.31E-09	941	96	26
GO:BP	nuclear-transcribed mRNA catabolic process, nonsense-mediated decay	GO:0000184	3.89E-09	123	96	12
GO:BP	viral gene expression	GO:0019080	4.05E-09	197	96	14
GO:BP	mRNA metabolic process	GO:0016071	4.93E-09	877	96	25
GO:BP	translational initiation	GO:0006413	4.97E-09	200	96	14
GO:BP	RNA catabolic process	GO:0006401	1.51E-08	425	96	18
GO:BP	amide biosynthetic process	GO:0043604	1.69E-08	928	96	25
GO:BP	viral transcription	GO:0019083	2.13E-08	180	96	13
GO:BP	viral process	GO:0016032	2.23E-08	940	96	25
GO:BP	establishment of protein localization to organelle	GO:0072594	4.99E-08	589	96	20
GO:BP	protein peptidyl-prolyl isomerization	GO:0000413	1.26E-07	44	96	8
GO:BP	nuclear-transcribed mRNA catabolic process	GO:0000956	1.98E-07	215	96	13
GO:BP	protein targeting	GO:0006605	2.65E-07	441	96	17
GO:BP	protein localization to organelle	GO:0033365	6.83E-07	1014	96	24
GO:BP	cellular amide metabolic process	GO:0043603	1.08E-06	1223	96	26
GO:BP	protein targeting to membrane	GO:0006612	1.41E-06	203	96	12
GO:BP	nucleobase-containing compound catabolic process	GO:0034655	1.60E-06	566	96	18
GO:BP	peptidyl-proline modification	GO:0018208	2.23E-06	62	96	8
GO:BP	heterocycle catabolic process	GO:0046700	4.12E-06	601	96	18
GO:BP	cellular nitrogen compound catabolic process	GO:0044270	4.70E-06	606	96	18
GO:BP	establishment of protein localization to membrane	GO:0090150	6.02E-06	342	96	14
GO:BP	aromatic compound catabolic process	GO:0019439	7.07E-06	622	96	18
GO:BP	organic cyclic compound catabolic process	GO:1901361	1.40E-05	650	96	18

GO:BP	intracellular protein transport	GO:0006886	1.77E-05	1195	96	24
GO:BP	organonitrogen compound biosynthetic process	GO:1901566	2.37E-05	1854	96	30
GO:BP	biological process involved in interspecies interaction between organisms	GO:0044419	1.81E-04	2272	96	32
GO:BP	peptide transport	GO:0015833	4.37E-04	1989	96	29
GO:BP	amide transport	GO:0042886	6.33E-04	2024	96	29
GO:BP	cellular macromolecule catabolic process	GO:0044265	6.93E-04	1237	96	22
GO:BP	establishment of protein localization	GO:0045184	7.80E-04	2044	96	29
GO:BP	protein transport	GO:0015031	9.96E-04	1946	96	28
GO:BP	protein stabilization	GO:0050821	1.42E-03	191	96	9
GO:BP	posttranscriptional regulation of gene expression	GO:0010608	1.74E-03	897	96	18
GO:BP	protein localization	GO:0008104	1.97E-03	2789	96	34
GO:BP	intracellular transport	GO:0046907	2.10E-03	1777	96	26
GO:BP	cellular protein localization	GO:0034613	2.21E-03	2024	96	28
GO:BP	cellular macromolecule localization	GO:0070727	2.46E-03	2035	96	28
GO:BP	cellular protein metabolic process	GO:0044267	2.57E-03	5225	96	50
GO:BP	establishment of localization in cell	GO:0051649	3.01E-03	2840	96	34
GO:BP	protein localization to membrane	GO:0072657	3.47E-03	660	96	15
GO:BP	macromolecule catabolic process	GO:0009057	3.61E-03	1477	96	23
GO:BP	regulation of RNA splicing	GO:0043484	4.03E-03	161	96	8
GO:BP	protein metabolic process	GO:0019538	4.16E-03	5806	96	53
GO:BP	negative regulation of gene expression	GO:0010629	5.85E-03	2516	96	31
GO:BP	mRNA splicing, via spliceosome	GO:0000398	6.09E-03	362	96	11
GO:BP	RNA splicing, via transesterification reactions with bulged adenosine as nucleophile	GO:0000377	6.09E-03	362	96	11
GO:BP	regulation of mRNA splicing, via spliceosome	GO:0048024	6.19E-03	120	96	7
GO:BP	RNA splicing, via transesterification reactions	GO:0000375	6.60E-03	365	96	11
GO:BP	ribonucleoprotein complex biogenesis	GO:0022613	7.28E-03	445	96	12
GO:BP	regulation of cellular amide metabolic process	GO:0034248	8.06E-03	531	96	13
GO:BP	regulation of protein stability	GO:0031647	8.21E-03	302	96	10
GO:BP	protein refolding	GO:0042026	1.09E-02	23	96	4
GO:BP	regulation of translation	GO:0006417	1.09E-02	463	96	12

GO:BP	response to organic substance	GO:0010033	1.29E-02	3459	96	37
GO:BP	nitrogen compound transport	GO:0071705	1.31E-02	2347	96	29
GO:BP	cellular response to organic substance	GO:0071310	2.08E-02	2812	96	32
GO:BP	macromolecule localization	GO:0033036	2.09E-02	3238	96	35
GO:BP	protein folding in endoplasmic reticulum	GO:0034975	3.02E-02	10	96	3
GO:BP	cellular response to chemical stimulus	GO:0070887	3.02E-02	3438	96	36
GO:BP	regulation of mRNA metabolic process	GO:1903311	3.44E-02	356	96	10
GO:BP	regulation of mRNA processing	GO:0050684	3.92E-02	159	96	7
GO:BP	ribosome assembly	GO:0042255	4.03E-02	64	96	5
GO:BP	organic substance transport	GO:0071702	4.91E-02	2790	96	31
GO:CC	ribonucleoprotein complex	GO:1990904	3.25E-15	693	99	28
GO:CC	ribosome	GO:0005840	4.99E-11	245	99	16
GO:CC	cytosolic ribosome	GO:0022626	1.32E-10	109	99	12
GO:CC	ribosomal subunit	GO:0044391	3.82E-10	191	99	14
GO:CC	extracellular vesicle	GO:1903561	8.95E-10	2266	99	39
GO:CC	extracellular organelle	GO:0043230	9.20E-10	2268	99	39
GO:CC	extracellular exosome	GO:0070062	6.41E-09	2180	99	37
GO:CC	extracellular space	GO:0005615	1.32E-07	3598	99	46
GO:CC	protein-containing complex	GO:0032991	3.71E-07	5556	99	58
GO:CC	polysome	GO:0005844	1.31E-06	73	99	8
GO:CC	focal adhesion	GO:0005925	1.36E-06	418	99	15
GO:CC	cell-substrate junction	GO:0030055	1.75E-06	426	99	15
GO:CC	large ribosomal subunit	GO:0015934	3.72E-06	119	99	9
GO:CC	cytosolic large ribosomal subunit	GO:0022625	5.65E-06	57	99	7
GO:CC	extracellular region	GO:0005576	1.29E-04	4602	99	47
GO:CC	vesicle	GO:0031982	6.62E-04	4071	99	42
GO:CC	small ribosomal subunit	GO:0015935	8.78E-04	76	99	6
GO:CC	cytosolic small ribosomal subunit	GO:0022627	1.40E-03	47	99	5
GO:CC	anchoring junction	GO:0070161	2.23E-03	843	99	16
GO:CC	pigment granule	GO:0048770	5.72E-03	105	99	6
GO:CC	melanosome	GO:0042470	5.72E-03	105	99	6
GO:CC	lumenal side of membrane	GO:0098576	7.91E-03	33	99	4
GO:CC	nucleolus	GO:0005730	8.34E-03	938	99	16

GO:CC	spliceosomal complex	GO:0005681	1.99E-02	191	99	7
GO:CC	cytoplasm	GO:0005737	2.26E-02	11888	99	80
GO:CC	inner mitochondrial membrane protein complex	GO:0098800	3.63E-02	146	99	6
GO:CC	endocytic vesicle lumen	GO:0071682	4.58E-02	20	99	3
KEGG	Ribosome	KEGG:03010	2.18E-09	154	56	13
KEGG	Coronavirus disease - COVID-19	KEGG:05171	3.59E-06	231	56	12
KEGG	Antigen processing and presentation	KEGG:04612	6.45E-04	70	56	6
KEGG	Protein processing in endoplasmic reticulum	KEGG:04141	1.30E-02	170	56	7
KEGG	Spliceosome	KEGG:03040	4.57E-02	150	56	6
KEGG	Legionellosis	KEGG:05134	5.00E-02	57	56	4

Tabla Suplementaria XI.2. Genes de alta expresión seleccionados para comparar los perfiles de mapeos entre las enzimas. La tabla muestra el nombre del gen, su largo, su posición en el ranking de mayor expresión (#Rank) y la cantidad de lecturas mapeadas en cada caso para las dos enzimas utilizadas y sus dos réplicas.

Gen	Largo	Benzonasa-1		Benzonasa-2		RNAsa I-1		RNAsa I-2	
		#Rank	Lecturas	#Rank	Lecturas	#Rank	Lecturas	#Rank	Lecturas
EEF1A1	3.512	2	132.404	3	67.475	3	66.130	3	85.264
ACTB	1.812	5	55.393	7	33.817	25	20.351	29	24.730
GAPDH	1.285	6	55.083	5	35.568	11	34.756	11	42.149
ENO1	1.781	9	50.415	10	28.507	6	43.389	6	51.240
TUBA1B	1.627	10	48.969	11	28.139	16	27.293	19	32.242